

SOUND PRODUCED BY ENTROPIC AND COMPOSITIONAL INHOMOGENEITIES



ERWAN OLUWASHEI ROLLAND
CORPUS CHRISTI COLLEGE
UNIVERSITY OF CAMBRIDGE

THIS DISSERTATION IS SUBMITTED FOR THE DEGREE OF
DOCTOR OF PHILOSOPHY
OCTOBER 2017

©2017 – ERWAN OLUWASHEI ROLLAND
ALL RIGHTS RESERVED.

This dissertation describes the work conducted in the Department of Engineering at the University of Cambridge in fulfilment of the requirements for the degree of Doctor of Philosophy. I hereby declare that except where specific reference is made to the work of others, the contents of this dissertation are original and have not been submitted in whole or in part for consideration for any degree or diploma or other qualification in this, or any other university or similar institution. This dissertation is the result of my own work and contains nothing which is the outcome of work done in collaboration with others, except as specified in the text and Acknowledgements. This dissertation contains fewer than 65,000 words including appendices, bibliography, footnotes, tables and equations and has fewer than 150 figures.

Erwan Oluwasheyi Rolland
October 2017

SOUND PRODUCED BY ENTROPIC AND COMPOSITIONAL INHOMOGENEITIES

ABSTRACT

Combustion noise is central to several efforts to curb aircraft emissions. Indeed, acoustic waves originating in the combustor are a major contributor to aircraft noise. Moreover, they can act as a trigger for thermoacoustic instabilities, the consequences of which may range from decreased efficiency to outright failure. Modern engines designed to lower NO_x emissions are particularly susceptible to this phenomenon.

Unsteady combustion generates acoustic waves — direct noise — as well as convected flow disturbances, such as entropic, vortical or compositional inhomogeneities. These disturbances generate additional acoustic waves — indirect noise — if they are accelerated. The main objectives of this thesis are to examine the validity of current theoretical models for indirect noise, and to propose new ones where needed.

First, a one-dimensional theoretical framework for the direct and indirect noise produced in a reflective environment is presented. The direct noise produced by the addition of mass, momentum and energy to a flow is determined analytically. A model for the entropic and compositional noise generated at a compact nozzle is then derived, accounting for nozzles with non-uniform entropy. Finally, the effect of reverberation (i.e. repeated acoustic reflections) is determined analytically. This enables direct and indirect acoustic sources to be identified and separated within experimental data, while eliminating the effect of acoustic reflections.

The framework is applied to a model experiment — the Cambridge Wave Generator — in which direct, entropic and compositional noise are generated. Direct and indirect noise models are validated using experimental measurements of the sound field resulting from air injection and extraction, heat addition and helium injection. For the first time, direct, entropic and compositional noise are clearly identified in the experimental data, and shown to be in line with theoretical predictions.

The results provide the first experimental demonstration of the compositional noise mechanism, and show that isentropic nozzle models are inadequate in predicting the indirect noise generated at nozzles with substantial losses.

ASSOCIATED PUBLICATIONS

Journal publications

1. **Rolland, E. O.**, De Domenico, F., Hochgreb, S. (2017). Direct and indirect noise generated by injected entropic and compositional inhomogeneities, *Journal of Engineering for Gas Turbines and Power*, (in press).
2. **Rolland, E. O.**, De Domenico, F., Hochgreb, S. (2017). Theory and application of reverberated direct and indirect noise, *Journal of Fluid Mechanics*, 819, 435–464.
3. De Domenico, F., **Rolland, E. O.**, Hochgreb, S. (2017). Detection of direct and indirect noise generated by synthetic hot spots in a duct, *Journal of Sound and Vibration*, 394, 220–236.

Conference publications

1. De Domenico, F., **Rolland, E. O.**, Hochgreb, S. (2017). Acoustic and entropic transfer functions of a generalised subsonic nozzle, *24th International Congress on Sound and Vibration, London*.
2. Hochgreb, S., **Rolland, E. O.**, De Domenico, F. (2017). Low frequency generation, transmission and reflection of direct and indirect perturbations through nozzle, *24th International Congress on Sound and Vibration, London*.
3. **Rolland, E. O.**, De Domenico, F., Hochgreb, S. (2017). Direct and indirect noise generated by injected entropic and compositional inhomogeneities, *ASME Turbo Expo 2017 : Turbomachinery Technical Conference and Exposition*.

4. De Domenico, F, **Rolland, E. O.**, Hochgreb, S. (2017). Measurements Of The Effect Of Boundary Conditions On The Upstream And Downstream Noise Arising From Entropy Spots, *ASME Turbo Expo 2017 : Turbomachinery Technical Conference and Exposition*.
5. De Domenico, F, **Rolland, E. O.** , Hochgreb, S. (2016). Detection of direct and indirect noise generated by synthetic hot spots in a duct, *International Symposium on Thermoacoustic Instabilities in Gas Turbines and Rocket Engines: Industry meets Academia*.

In preparation

1. De Domenico, F, **Rolland, E. O.** , Hochgreb, S., A generalised model for acoustic and entropic transfer function of nozzles with losses, *Journal of Sound and Vibration*, (submitted).
2. **Rolland, E. O.**, De Domenico, F, Hochgreb, S., System identification in reverberating systems, (in preparation).
3. **Rolland, E. O.**, Rodrigues J., De Domenico, F, Hochgreb, S., Measurements of anisotropic nozzle transfer functions for entropic and compositional noise, (in preparation).

*Je dédie cette thèse à mes grands-parents
and to my grandparents.*

ACKNOWLEDGEMENTS

First and foremost, I would like to thank my supervisor Simone Hochgreb — not by convention, but because she has been a formidable source of wisdom and support. It is no exaggeration to say that she has made this Ph.D. more gratifying and exciting than I ever thought it could be. Her unwavering patience and counsel have been invaluable, and I count myself lucky to have been her student.

I am also indebted to Francesca De Domenico, for providing much of the data and know-how I drew from to put this thesis together. I feel very much obliged to Luca Magri, for taking the time to discuss some of the finer points of compositional noise, as well as Peter Benie for saving me from my own computer in extremis on more than one occasion. I am very thankful for the weekly thermoacoustics meetings Matthew Juniper took the time to organise, which provided me with a broader perspective on the topic (with a therapeutic twist). I am also very grateful to the Engineering and Physical Sciences Research Council for funding this research.

My thanks also goes out to those whose presence made the Hopkinson Lab such a pleasant place to work in (and to avoid work in). Francesca, Nick, Jocelino, Anh Khoa, Jose, Georgios, Alessandro, Luca, Hans, Jack and many others — thank you.

I am especially grateful to the friends I made in Cambridge, for providing the solace, laughter and joie de vivre that kept me afloat for three years. Joris, Amy, Stéphane, Thomas, Jiří, Patrick, Karla and others from the MCR — thank you for making my time in Cambridge unforgettable. Special thanks go to Julia — for her constant affection and words of encouragement.

Finally, I would like to thank my family for their unfaltering love and support, and for encouraging me to believe in myself.

TABLE OF CONTENTS

LIST OF FIGURES	xix
LIST OF TABLES	xxix
NOMENCLATURE	xxxii
INTRODUCTION	1
I STATE OF THE ART	9
I.1 Acoustics of combustion	9
I.2 Analytical models for entropic noise	14
I.3 Analytical models for compositional noise	17
I.4 Indirect noise in combustion systems	19
I.5 Model experiments on indirect noise	23
I.6 Conclusion	27
II WAVES GENERATED BY IMPOSED FLOW PERTURBATIONS	29
II.1 Wave field	29
II.2 Jump conditions at a compact wave source	31
II.3 Waves generated at a compact source	33
II.4 Special cases	35
III TRANSFER FUNCTIONS OF COMPACT NOZZLES	41
III.1 Isentropic nozzle	41
III.2 Anisentropic nozzle	47
III.3 Effect of anisentropicity	52

TABLE OF CONTENTS

IV	REVERBERATION	61
IV.1	Unicameral reverberation	62
IV.2	Bicameral reverberation	71
V	DIRECT AND INDIRECT NOISE MODEL	79
V.1	Unicameral model	80
V.2	Bicameral model	82
V.3	Limit cases	85
V.4	Source and system identification	94
VI	THE CAMBRIDGE WAVE GENERATOR	97
VI.1	Experimental set-up	97
VI.2	Wave generators	101
VI.3	Data acquisition and processing	105
VI.4	Simulation and source identification	107
VII	AIR INJECTION – DIRECT NOISE	111
VII.1	Long configuration	111
VII.2	Short configuration	118
VII.3	Comparison to the direct noise model	123
VIII	HEAT ADDITION – ENTROPIC NOISE	125
VIII.1	Long configuration	125
VIII.2	Short configuration – choked nozzle	129
VIII.3	Short configuration – orifice	135
VIII.4	Comparison to the entropic noise models	142
IX	HELIUM INJECTION – COMPOSITIONAL NOISE	143
IX.1	Long configuration	143
IX.2	Short configuration	146
IX.3	Short extended configuration	151
IX.4	Comparison to compositional noise models	158
	CONCLUSIONS AND FUTURE WORK	161

TABLE OF CONTENTS

APPENDIX A	NOZZLE TRANSFER FUNCTIONS	169
A.1	Matrix permutations	169
A.2	Supersonic compact isentropic nozzle	169
A.3	Anisentropic compact nozzle	172
APPENDIX B	BICAMERAL TRANSFER FUNCTIONS	185
B.1	First chamber	185
B.2	Second chamber	186
REFERENCES		189

LIST OF FIGURES

1	Examples of damage sustained on the Rocketdyne F-1 engine due to combustion instabilities in (a) 1958 and (b) 1963 ⁶⁵	2
2	Direct and indirect noise mechanisms in a typical gas turbine combustor. Inspired by Dowling & Mahmoudi ²¹ and Magri et al. ⁵⁹	5
II.1	Flow variables upstream [0] and downstream [1] of a wave source with changes in mass (ϕ_m), momentum (ϕ_M), energy (ϕ_e) and composition (ϕ_Z).	31
II.2	Forward and backward acoustic (π^+ , π^-), entropic σ and compositional waves ξ upstream [0] and downstream [1] of a wave source.	33
II.3	Forward and backward acoustic (π^+ , π^-), entropic σ and compositional waves ξ generated by a wave source.	34
II.4	Direct acoustic waves π_d^+ and π_d^- and entropic wave σ generated by a compact heat source.	36
II.5	Direct acoustic waves π_d^+ and π_d^- generated by a compact ambient temperature air injection.	37
II.6	Direct acoustic waves π_d^+ and π_d^- , entropic wave σ and compositional wave ξ generated by a helium injection.	38
III.1	Flow fluctuations upstream [1] and downstream [2] of a compact nozzle.	42
III.2	Forward and backward acoustic (π^+ , π^-), entropic (σ) and compositional waves (ξ) upstream [1] and downstream [2] of a subsonic compact nozzle. Ingoing waves (solid arrows), outgoing waves (dashed arrows).	44
III.3	Non-zero mode transfer mechanisms between acoustic (π), entropic (σ) and compositional waves (ξ) at the inlet and outlet of a subsonic isentropic compact nozzle.	47

III.4 Diagram of flow areas at the inlet (A_1), throat (A_t), jet mixing location (A_j) and outlet (A_2) of an anisentropic nozzle, with streamlines for illustration. 48

III.5 Jump locations for (a) an isentropic nozzle with $\Lambda = 0$, (b) an orifice plate with $\Lambda = 1$ (c) a converging nozzle with $\Lambda = 1$ and $A_2 \rightarrow \infty$ and (d) a nozzle with partial losses with $0 < \Lambda < 1$ 49

III.6 Flow fluctuations upstream [1], at the jet mixing location [j] and downstream [2] of a compact anisentropic nozzle. 50

III.7 Non-zero mode transfer mechanisms between acoustic (π), entropic (σ) and compositional waves (ξ) at the inlet and outlet of a subsonic anisentropic compact nozzle. 52

III.8 (a) Inlet Mach number \bar{M}_1 , (b) outlet Mach number \bar{M}_2 and (c) inlet mean pressure \bar{p}_1 as a function of the throat Mach number \bar{M}_t . Ten values of Λ are shown, ranging from isentropic with $\Lambda = 0$ (—) to fully anisentropic with $\Lambda = 1$ (—), with intermediate cases where $0 < \Lambda < 1$ (---). 54

III.9 (a) Acoustic transmission coefficient T_1 , (b) acoustic reflection coefficient R_1 as a function of the throat Mach number \bar{M}_t . Ten values of Λ are shown, ranging from $\Lambda = 0$ (—) to $\Lambda = 1$ (—), with intermediate cases where $0 < \Lambda < 1$ (---). The limit case of an isentropic choked nozzle is also shown (●). 55

III.10 (a) Acoustic reflection coefficient R_2 , (b) acoustic transmission coefficient T_2 as a function of the throat Mach number \bar{M}_t . Ten values of Λ are shown, ranging from $\Lambda = 0$ (—) to $\Lambda = 1$ (—), with intermediate cases where $0 < \Lambda < 1$ (---). The limit case of an isentropic choked nozzle is also shown (●). 56

III.11 (a) Entropic-acoustic transmission coefficient T_σ , (b) entropic-acoustic reflection coefficient R_σ as a function of the throat Mach number \bar{M}_t . Ten values of Λ are shown, ranging from $\Lambda = 0$ (—) to $\Lambda = 1$ (—), with intermediate cases where $0 < \Lambda < 1$ (---). The limit case of an isentropic choked nozzle is also shown (●). 57

LIST OF FIGURES

III.12 (a) Compositional-acoustic transmission coefficient T_ξ , (b) compositional-acoustic reflection coefficient R_ξ as a function of the throat Mach number \bar{M}_t . Ten values of Λ are shown, ranging from $\Lambda = 0$ (—) to $\Lambda = 1$ (—), with intermediate cases where $0 < \Lambda < 1$ (- - -). The limit case of an isentropic choked nozzle is also shown (●). 58

III.13 (a) Acoustic-entropic coefficient $(\bar{p}_2/\bar{p}_1)\sigma_2/\pi_1^+$, (b) acoustic-entropic coefficient σ_2/π_2^- as a function of the throat Mach number \bar{M}_t . Ten values of Λ are shown, ranging from $\Lambda = 0$ (—) to $\Lambda = 1$ (—), with intermediate cases where $0 < \Lambda < 1$ (- - -). The limit case of an isentropic choked nozzle is also shown (●). 59

III.14 (a) Entropic-entropic coefficient σ_2/σ_1 , (b) Compositional-entropic coefficient σ_2/ξ_1 as a function of the throat Mach number \bar{M}_t . Ten values of Λ are shown, ranging from $\Lambda = 0$ (— or —) to $\Lambda = 1$ (— or —), with intermediate cases where $0 < \Lambda < 1$ (- - - or - - -) for (a) and (b) respectively. The limit case of an isentropic choked nozzle is also shown (●, ●). 60

IV.1 Unicameral system: an acoustic source at a location x_s generates forward- and backward-propagating waves $\pi_s^+(t)$ and $\pi_s^-(t)$ 63

IV.2 The forward-propagating wave π_s^+ generated by the acoustic source is successively reflected at the inlet and outlet of the unicameral system. 64

IV.3 The forward and backward-propagating waves of amplitude π_s after the acoustic source has been deactivated. 66

IV.4 (a) Non-rectangular acoustic wave (b) Non-rectangular acoustic wave (.....) and rectangular approximation (—) for $\delta t = 20$ ms, (c) Non-rectangular acoustic wave and rectangular approximation for $\delta t = 10$ ms. 68

IV.5 Bicameral system: an upstream acoustic source at a location x_{s1} generates forward- and backward-propagating waves $\pi_{s1}^+(t)$ and $\pi_{s1}^-(t)$ 71

IV.6 The forward-propagating wave π_{s1}^+ generated by the upstream acoustic source is successively reflected at the inlet and outlet of the second chamber, effectively resulting in several reflections. 72

IV.7 The forward-propagating wave π_{s1}^+ generated by the upstream acoustic source is successively reflected at the inlet and outlet of the first chamber, effectively resulting in several transmissions. 74

IV.8	Bicameral system: a downstream acoustic source at a location x_{s2} generates forward- and backward-propagating waves $\pi_{s2}^+(t)$ and $\pi_{s2}^-(t)$	75
V.1	A one-dimensional wave generator generates forward and backward direct acoustic waves π_d^- and π_d^+ along with entropic and compositional waves σ and ξ . The convected waves generate corresponding forward and backward indirect acoustic waves ($\pi_\sigma^+, \pi_\sigma^-, \pi_\xi^+$ and π_ξ^-) as they are convected through the nozzle.	79
V.2	Unicameral system: a wave generator produces direct noise and convected waves, which produce indirect noise after propagating across a convective length L_c	80
V.3	Block diagram representing the analytical model for a unicameral reverberating system.	82
V.4	Bicameral system: a wave generator produces direct noise and convected waves, which produce indirect noise after propagating through a convective length L_c	83
V.5	Block diagram representing the analytical model for the upstream pressure in a bicameral reverberating system.	84
V.6	Block diagram representing the analytical model for the downstream pressure in a bicameral reverberating system.	84
V.7	Acoustic pressure history $p'/\gamma\bar{p}$ at $x = 2$ m (—) and case I results (for reference) (—). (a) case I: Anechoic (b) case II: Fully reflective (c) case III: Open-ended.	86
V.8	Acoustic pressure history $p'/\gamma\bar{p}$ at $x = 2$ m and case I results (for reference) (—). (a) case IV: arbitrary source signal for $R_o = 0.25$ (⋯⋯), $R_o = 0.5$ (- - -), and $R_o = 0.75$ (—), (b) case IV: full expressions for a rectangular pulse, (c) case IV: simplified expression for a rectangular pulse.	88
V.9	Acoustic pressure history $p'/\gamma\bar{p}$ at $x = 2$ m of total noise (—), direct noise (—) and indirect noise (—). (a) case V: Anechoic (low Mach) (b) case VI: Partial reflections (low Mach) (c) case VII: Partial reflections.	89
V.10	Acoustic pressure history $p'/\gamma\bar{p}$ at $x = 2$ m for case VIII (—) with acoustic forcing signal (—) obtained with (a) the arbitrary source signal model (b) rectangular approximation for $\delta t = 20$ ms and (c) rectangular approximation for $\delta t = 5$ ms.	90

LIST OF FIGURES

V.11	Upstream and downstream indirect to direct noise ratios χ_1 and χ_2 with $\bar{M}_1 = 0.025$ (—), $\bar{M}_1 = 0.05$ (- - -), $\bar{M}_1 = 0.1$ (.....), and wave ratio η_2 for comparison with $\bar{M}_1 = 0.025$ (●), $\bar{M}_1 = 0.05$ (●), $\bar{M}_1 = 0.1$ (●).	93
VI.1	The Cambridge Wave Generator: air flows through a duct fitted with wave generation modules and a nozzle.	98
VI.2	Section views of the CWG in its (a) long, (b) short and (c) short extended configurations with upstream length L_1 , downstream length L_2 , wave source location x_s and convective length L_c	99
VI.3	Three nozzles used in the Cambridge Wave Generator: (a) orifice plate, (b) choked converging nozzle, (c) subsonic converging nozzle.	100
VI.4	Section views of the gas injector/extractor.	102
VI.5	Flow lines for air/helium injection with (1) pressure gauge, (2) valve, (3) air tank, (4) helium bottle, (5) pressure regulator, (6) mass flow meter, (7) mass flow controller and (8) fast response valve.	103
VI.6	Flow lines for air extraction.	103
VI.7	Exploded view of the heating device.	104
VI.8	Example of pressure transducers and thermocouples mounted on the CWG.	105
VI.9	Example of acoustic pressure signal conditioning: (a) raw signal, (b) averaged signal (over 100 pulses), (c) averaged and filtered signal.	106
VII.1	Long tube configuration with wave module A: air is injected/extracted into a duct with reflections at the inlet and outlet.	112
VII.2	Experimental pressure fluctuation $p'(x, t)$ for (a) case A1 and (b) case A4 with $\dot{m}_i = 0.2$ (—), 0.4 (—), 0.6 (—), 0.8 (—), 1.0 g s^{-1} (—). The valve timing signal is shown for reference (- - -).	113
VII.3	Experimental pressure fluctuation $p'(x, t)$ for (a) case A5 with $\dot{m}_i = 0.2$ (—), 0.4 (—), 0.6 (—), 0.8 (—), 1.0 g s^{-1} (—) and (b) cases A8 (—), A9 (—) and A10 (—). The valve timing signal is shown for reference (- - -).	114
VII.4	Measured acoustic attenuation α as a function of mean Mach number \bar{M}_1 for cases A1 (●), A2 (●), A3 (●), A5-A7 (●) and A8-A10 (●).	115
VII.5	Analytical (—) and experimental (—) results for (a) case A1 with $\dot{m}_i = 1 \text{ g s}^{-1}$ and (b) case A3 with $\dot{m}_i = 1 \text{ g s}^{-1}$	116

VII.6	Analytical (—) and experimental (—) results for (a) case A5 with $\dot{m}_i = 1 \text{ g s}^{-1}$ and (b) case A8.	116
VII.7	Direct acoustic wave π_d^+ extracted from experimental data (—), computed theoretically (—) and normalised experimental acoustic pressure (⋯⋯) for (a) case A6 with $\dot{m}_i = 1 \text{ g s}^{-1}$ and (b) case A9.	117
VII.8	Short tube configuration with wave module A: air is injected/extracted into a duct with reflections at the inlet and outlet.	118
VII.9	Experimental pressure fluctuation $p'(x, t)$ for case A11 with $\dot{m}_i = 0.2$ (—), 0.4 (—), 0.6 (—), 0.8 (—), 1.0 g s^{-1} (—). The valve timing signal is shown for reference (---).	119
VII.10	Experimental pressure fluctuation $p'(x, t)$ for cases A14 (—), A15 (—) and A16 (—). The valve timing signal is shown for reference (---).	120
VII.11	Analytical (—) and experimental (—) pressure fluctuation $p'(x, t)$ for (a) case A13 with $\dot{m}_i = 1 \text{ g s}^{-1}$ and (b) case A14.	120
VII.12	Direct acoustic wave π_d^+ extracted from experimental data (—), computed theoretically (—) for (a) case A12 with $\dot{m}_i = 1 \text{ g s}^{-1}$ and (b) case A16.	121
VII.13	Experimental acoustic pressure (⋯⋯) and theoretical decay for $R_o = 0.982$ (—), $R_o = 0.985$ (—) and $R_o = 0.988$ (—) for (a) case A12 with $\dot{m}_i = 1 \text{ g s}^{-1}$ and (b) case A16.	122
VII.14	Analytical (—) and experimental results for the peak direct noise pressure $p' = \gamma \bar{p} (\pi_d^+ + \pi_d^-)$ for cases A1-A4 (○), A5-A7 (●), A8-A10 (●), A11-A13 (▲) and A14-A16 (▲).	123
VIII.1	Long tube configuration with wave module B: heat is generated in a duct with reflections at the inlet and outlet.	126
VIII.2	Experimental temperature fluctuation ΔT_d downstream of the heating device for (a) cases B1 (—), B2 (—), B3 (—) and (b) cases B4 (—), B5 (—), B6 (—). The heating device signal is shown for reference (---).	127
VIII.3	Experimental pressure fluctuation $p'(x, t)$ for (a) cases B1 (—), B2 (—), B3 (—) and (b) cases B4 (—), B5 (—), B6 (—). The heating device signal is shown for reference (---).	128
VIII.4	Analytical (—) and experimental results (—) for the pressure fluctuation $p'(x, t)$ for (a) case B1 (b) case B4.	129

LIST OF FIGURES

VIII.5 Short tube configuration with wave module B: heat is generated in a duct with reflections at the inlet and outlet. An entropic wave is generated at the heating device and convected through the duct. 130

VIII.6 Experimental temperature fluctuations downstream of the heating device and upstream of the nozzle ($\Delta T_d, \Delta T_n$) for (a) cases B7 (—, ····), B8 (—,····), B9 (—,····) and (b) cases B10 (—, ····), B11 (—,····), B12 (—,····). The convective time delay (---) and heating device signal (---) are shown for reference. 131

VIII.7 Experimental pressure fluctuation $p'(x, t)$ for (a) cases B7 (—), B8 (—), B9 (—) and (b) cases B10 (—), B11 (—), B12 (—). The convective time delay (---) and heating device signal are shown for reference (---). 132

VIII.8 Analytical (—) and experimental results (—) for the pressure fluctuation $p'(x, t)$: (a) case B7 (b) case B10. Contributions of direct (····) and entropic (····) noise to the overall analytical pressure (—) for (c) case B7 and (d) case B10. 133

VIII.9 Acoustic source $\pi/2$ for direct (—) and entropic acoustic waves (—) generated for (a) case B7 and (b) case B10. Convective time delay τ_c (---). 134

VIII.10 Experimental temperature fluctuations downstream of the heating device and upstream of the nozzle ($\Delta T_d, \Delta T_n$) for cases B12 (—,····) to B20 (—, ····). The heating device signal is shown for reference (---). 136

VIII.11 Experimental pressure fluctuations $p'(x, t)$ for cases B12 (—) to B20 (—). The heating device signal is shown for reference (---). 137

VIII.12 Upstream mean pressure \bar{p}_1 as a function of the throat Mach number \bar{M}_t . Experimental measurements for cases B13–B20 (●), isentropic limit case for $\Lambda = 0$ (····), orifice limit case for $\Lambda = 1$ (····). 138

VIII.13 Reflection coefficients of the orifice (—) and of an isentropic convergent nozzle of identical dimensions (—). Values corresponding to cases B13–B20 (●,●). 139

VIII.14 Acoustic pressure fluctuation $p'(x, t)$ for cases B13 (—) to B20 (—): (a) Experimental measurements (b) analytical results with the isentropic nozzle model. 139

VIII.15	Acoustic pressure fluctuation $p'(x, t)$ for cases B13 (—) to B20 (—): (a) Experimental measurements (b) analytical results with the anisentropic nozzle model.	140
VIII.16	Cases B13 to B20: (a) Overall acoustic source π (— to —), (b) direct and entropic acoustic sources π_d^+ (— to —) and π_σ^- (..... to).	141
VIII.17	(a) Entropic sound wave $ \pi_\sigma^- $ for cases B7–B9 (●) and cases B10–B12 (●) compared to the isentropic model (—) and (b) Entropic-acoustic transfer function $ R_\sigma = \pi_1^- / \sigma_1 $ for cases B13–B20 (●) compared to the anisentropic orifice model (—) and isentropic model (—).	142
IX.1	Long tube configuration with wave module C: helium is injected into a duct with reflections at the inlet and outlet.	144
IX.2	Experimental pressure fluctuation $p'(x, t)$ for (a) case C1 and (b) case C4, with $\dot{m}_i = 0.027$ (—), 0.055 (—), 0.082 (—), 0.109 (—), 0.136 g s ⁻¹ (—). 145	145
IX.3	(a) Analytical (—) and experimental (—) results for case C6 with $\dot{m}_i = 0.136$ g/s and (b) Experimental peak pressure fluctuation: for cases C2 (Δ), C3 (▲) with linear fit (.....), and C5 (○), C6 (●) with linear fit (- - -) and analytical prediction of direct noise (—).	146
IX.4	Long tube configuration with wave module C: helium is injected into a duct with reflections at the inlet and outlet.	147
IX.5	Experimental pressure fluctuation $p'(x, t)$ for (a) case C7 and (b) case C10, with $\dot{m}_i = 0.027$ (—), 0.055 (—), 0.082 (—), 0.109 (—), 0.136 g s ⁻¹ (—). Convective time delay τ_c (- - -).	148
IX.6	Analytical (—) and experimental results (—) for the pressure fluctuation $p'(x, t)$: (a) case C7 (b) case C10. Contributions of direct (.....), entropic (.....) and compositional (.....) noise to the overall analytical pressure (—) for (c) case C7 and (d) case C10.	149
IX.7	Dereverberated experimental signal for direct (π_d^+ , —) and indirect acoustic waves ($\pi_i^- = \pi_\sigma^- + \pi_\xi^-$,) generated for $\dot{m}_i = 0.027$ (—), 0.055 (—), 0.082 (—), 0.109 (—), 0.136 g s ⁻¹ (—) in (a) case C7 and (b) case C10. Convective time delay τ_c (- - -).	151
IX.8	Short extended configuration with wave module C: helium is injected/extracted into a duct with reflections at the inlet and outlet.	151

LIST OF FIGURES

IX.9	Experimental pressure fluctuations (a) $p'(x_1)$ upstream of the nozzle and (b) $p'(x_2)$ downstream of the nozzle for cases C13 (—), C14 (—), C15 (—), C16 (—), C17 (—) and (c) $p'(x_1)$ upstream of the nozzle and (d) $p'(x_2)$ downstream of the nozzle for cases C18 (—), C19 (—), C20 (—), C21 (—), C22 (—). The valve timing signal is shown for reference (---).	153
IX.10	Upstream mean pressure \bar{p}_1 as a function of the throat Mach number \bar{M}_t . Experimental measurements for cases C13–C22 (●), isentropic limit case for $\Lambda = 0$ (⋯⋯), fully dissipative limit case for $\Lambda = 1$ (⋯⋯) and best fit for $\Lambda = 0.9988$ (⋯⋯).	155
IX.11	Case C14: (a) Upstream experimental acoustic pressure $p'(x_1)$ (⋯⋯) and theoretical decay for $R_{o1} = 0.870$ (—), $R_{o1} = 0.873$ (—) and $R_{o1} = 0.867$ (—) and (b) downstream experimental acoustic pressure $p'(x_2)$ (⋯⋯) and theoretical upstream transmission for $T_{o1} = 0.131$ (—), $T_{o1} = 0.141$ (—) and $T_{o1} = 0.121$ (—).	156
IX.12	(a) Acoustic transmission coefficient T_{o1} and (b) acoustic reflection coefficient R_{o1} extracted from experimental data (●), and computed using the anisentropic nozzle model (—).	156
IX.13	Dereverberated experimental signal for direct (π_d^+ , —) and indirect acoustic waves (π_i^- , ⋯⋯) generated for (a) cases C13 (—), C14 (—), C15 (—), C16 (—), C17 (—) and (b) cases C18 (—), C19 (—), C20 (—), C21 (—), C22 (—).	157
IX.14	(a) Downstream pressure $p'/\gamma\bar{p}(x_2)$ (⋯⋯), transmitted upstream pressure $p'/\gamma\bar{p}(x_1) T_{o1}/(1 + R_{o1})$ (⋯⋯) and resulting indirect sound wave π_i^+ (—) for case C21. (b) Indirect sound wave π_i^+ for cases C13 (—), C14 (—), C15 (—), C16 (—), C17 (—).	158
IX.15	Indirect sound wave $ \pi_\xi^- + \pi_\sigma^- $ for cases C10 (●), C11 (●) and C12 (●) compared to the isentropic model (—).	159
IX.16	Indirect noise transfer functions (a) $ \pi_\xi^+ + \pi_\sigma^+ /\xi_1$ and (b) $ \pi_\xi^- + \pi_\sigma^- /\xi_1$ for cases C13–C17 (●) compared to the anisentropic nozzle model for $\Lambda = 0.9988$ (—).	159

LIST OF TABLES

I.1	Flow variables affected (●) and unaffected (-) by the four canonical wave types.	12
III.1	Anisentropicity levels Λ and corresponding effect jet area diameters d_j for ten nozzles.	53
IV.1	Amplitudes, distances travelled and time delays associated to the forward-propagating acoustic wave π_s^+ and its first three reflections.	64
IV.2	Amplitudes, distances travelled and time delays associated to the backward-propagating acoustic wave π_s^- and its first three reflections.	65
IV.3	Amplitudes, distances travelled and time-delays associated to the first four reflections of the forward-propagating acoustic wave π_{s1}^+	73
IV.4	Amplitudes, distances travelled and time delays associated to the first four transmissions of the forward-propagating acoustic wave π_{s1}^+	74
IV.5	Amplitudes, distances travelled and time-delays associated to the first four transmissions of the backward-propagating acoustic wave π_{s2}^-	76
IV.6	Amplitudes, distances travelled and time-delays associated to the first four reflections of the backward-propagating acoustic wave π_{s2}^-	77
V.1	Description of limit cases I-IV with corresponding inlet and outlet reflection coefficients R_i and R_o	86
V.2	Description of limit cases V-VII with corresponding reflection coefficients R_i and R_o and Mach number \bar{M}	89
VI.1	Noise types measured (●) and not measured (-) in each configuration of the Cambridge Wave Generator.	100

VI.2	Wave types generated (●) and not generated (-) by each wave generation module.	101
VII.1	Experimental cases for wave module A (air injection/extraction) in the long configuration with outlet type, mean pressure \bar{p} , mean Mach number \bar{M}_1 , primary mass flow rate \dot{m} and injected mass flow rate \dot{m}_i	112
VII.2	Experimental cases for wave module A (air injection/extraction) in the short configuration with outlet type, mean pressure \bar{p} , mean Mach number \bar{M}_1 , primary mass flow rate \dot{m} and injected mass flow rate \dot{m}_i	118
VIII.1	Experimental cases for wave module B (heat addition) in the long configuration with outlet type, mean pressure \bar{p} , mean Mach number \bar{M}_1 , primary mass flow rate \dot{m} and average grid temperature fluctuation ΔT_d	126
VIII.2	Experimental cases for wave module B (heat addition) in the short configuration with a choked nozzle, convective length L_c , mean pressure \bar{p} , mean Mach number \bar{M}_1 , primary mass flow rate \dot{m} , average grid temperature fluctuation ΔT_d and average nozzle temperature fluctuation ΔT_n	130
VIII.3	Experimental cases for wave module B (heat addition) in the short configuration with the orifice, convective length L_c , mean pressure \bar{p} , mean Mach number \bar{M}_1 , orifice throat Mach number \bar{M}_t , primary mass flow rate \dot{m} , average grid temperature fluctuation ΔT_d and average nozzle temperature fluctuation ΔT_n	135
IX.1	Experimental cases for wave module C (helium injection) in the long configuration with outlet type, mean pressure \bar{p} , mean Mach number \bar{M}_1 , primary mass flow rate \dot{m} and injected helium mass flow rate \dot{m}_i	144
IX.2	Experimental cases for wave module C (helium injection) in the short configuration with a choked nozzle, convective length L_c , mean pressure \bar{p} , mean Mach number \bar{M}_1 , primary mass flow rate \dot{m} and injected helium mass flow rate \dot{m}_i	147
IX.3	Experimental cases for wave module C (helium injection) in the short extended configuration with a subsonic convergent nozzle: convective length L_c , mean pressure \bar{p} , mean Mach number \bar{M}_1 , mean throat Mach number \bar{M}_t , primary mass flow rate \dot{m} and injected helium mass flow rate \dot{m}_i	152

NOMENCLATURE

ROMAN SYMBOLS

A	cross-sectional area	m^2
c	sound speed	m s^{-1}
c_p	specific heat capacity	$\text{J K}^{-1} \text{kg}^{-1}$
g	Gibbs free energy	J kg^{-1}
h	specific enthalpy	J kg^{-1}
He	Helmholtz number	-
L	section length	m
\dot{m}	mass flow rate	g s^{-1}
M	Mach number	-
p	pressure	Pa
Q	heat release rate	$\text{J m}^{-2} \text{s}^{-1}$
q	normalised heat release rate	-
R	acoustic reflection coefficient	-
s	specific entropy	$\text{J K}^{-1} \text{kg}^{-1}$
T	acoustic transmission coefficient	-
T	temperature	K
u	velocity	m s^{-1}

NOMENCLATURE

W	molar mass	kg mol^{-1}
x	axial location	m
Y	mass fraction	-
Z	mixture fraction	-
GREEK SYMBOLS		
α	acoustic attenuation coefficient	m^{-1}
Γ	vena contracta factor	-
γ	heat capacity ratio	-
Λ	anisotropicity parameter	-
μ	chemical potential	J mol^{-1}
Ω	vorticity	s^{-1}
Φ_e	energy flux perturbation	$\text{J m}^{-2} \text{s}^{-1}$
Φ_M	momentum flux perturbation	$\text{kg m}^{-1} \text{s}^{-2}$
Φ_m	mass flux perturbation	$\text{kg m}^{-2} \text{s}^{-1}$
Φ_Z	mass fraction perturbation	-
Ψ	chemical potential function	-
ρ	density	kg m^{-3}
σ	entropic wave amplitude	-
τ	acoustic time delay	ms
τ_c	convective time delay	ms
τ_p	pulse duration	ms
φ_e	normalised energy flux perturbation	-
φ_M	normalised momentum flux perturbation	-
φ_m	normalised mass flux perturbation	-

NOMENCLATURE

φ_Z normalised mass fraction perturbation -

ξ compositional wave amplitude -

SUPERSCRIPTS

$(\bar{\cdot})$ mean component

$(\cdot)^-$ backward-propagating

$(\cdot)^+$ forward-propagating

$(\cdot)'$ fluctuating component

$(\cdot)^*$ augmented reflection/transmission

SUBSCRIPTS

$(\cdot)_0$ upstream of the wave generator

$(\cdot)_1$ upstream of the nozzle (in the first chamber)

$(\cdot)_2$ downstream of the nozzle (in the second chamber)

$(\cdot)_{\text{air}}$ relating to the air flow

$(\cdot)_d$ direct

$(\cdot)_{\text{He}}$ relating to the helium flow

$(\cdot)_i$ indirect, inlet or injected

$(\cdot)_j$ at the nozzle jet location

$(\cdot)_o$ outlet

$(\cdot)_s$ source

$(\cdot)_\sigma$ entropic

$(\cdot)_t$ at the nozzle throat

$(\cdot)_\xi$ compositional

INTRODUCTION

In 1858, Leconte famously recounted his attendance of a tea party at which several of Beethoven's grand trios were performed⁴⁹. He noticed something peculiar about one of the burning gas lights near the piano. As the music was playing, the burner was pulsating in rhythm with the music; each note was accompanied by a synchronous flare in the flame. This is a thermoacoustic effect — an interaction between heat and sound. Leconte was right: the flame was responding to the sound created by the musical instruments. In his own words, 'a deaf man might have seen the harmony'.

Thermoacoustic effects are more than mere scientific curiosities; they are relevant in many modern technologies. In particular, heat-sound interactions are known to occur in combustion devices such as aircraft and rocket engines. While the response of a small flame to a Beethoven trio might be harmonious, the same erratic behaviour observed in a 7,000 kilonewton rocket engine is more worrying. Nevertheless, this is precisely what occurs if an engine is subject to a thermoacoustic instability.

Thermoacoustic instabilities

Thermoacoustic instabilities result from a resonant coupling between heat and sound. They arise in combustion chambers because flames generate acoustic waves (pressure fluctuations). These waves can be reflected at the boundaries of the system, return to the flame location and affect its heat release, in turn producing yet more acoustic waves. In certain conditions, this amounts to a positive feedback loop, whereby acoustic waves are amplified, leading to violent pressure oscillations at specific frequencies. The consequences of these instabilities can be extremely serious.

An example of this is the chaotic development of the F-1 engine destined to equip the Saturn V rocket. During a performance test in 1962, the engine exploded less than half a second

after ignition; this was attributed to a combustion instability⁶. These instabilities would occur repeatedly during tests, at frequencies determined by the geometry of the injector and of the combustion chamber. Low frequency instabilities would affect overall performance and cause explosions, while high frequency instabilities could prevent cooling and cause the engine to melt⁸⁷. Examples of such damage are shown in figure 1. These instabilities were eventually eliminated at great expense through trial and error, by building hundreds of chamber geometries and injector designs⁶. The Saturn V rocket would go on to fly astronauts to the moon.

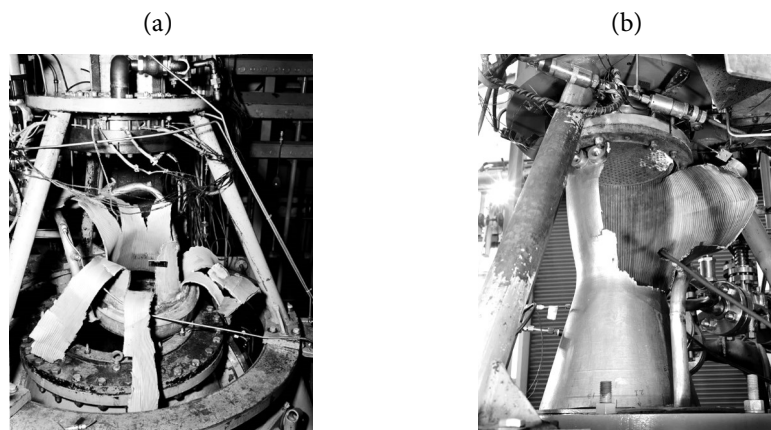


Figure 1: Examples of damage sustained on the Rocketdyne F-1 engine due to combustion instabilities in (a) 1958 and (b) 1963⁶⁵.

Clearly, avoiding thermoacoustic instabilities using trial and error is neither economical nor practical. Ideally, one would like to predict the onset of a thermoacoustic instability during the early phases of design. This requires a detailed understanding of the phenomenon, explaining why and how such instabilities occur. In his seminal 1877 treatise, 'A Theory of Sound', Rayleigh⁸¹ proposed such an explanation:

If heat be periodically communicated to, and abstracted from, a mass of air vibrating (for example) in a cylinder bounded by a piston, the effect produced will depend upon the phase of the vibration at which the transfer of heat takes place. If heat be given to the air at the moment of greatest condensation, or be taken from it at the moment of greatest rarefaction, the vibration is encouraged. On the other hand, if heat be given at the moment of greatest rarefaction, or abstracted at the moment of greatest condensation, the vibration is discouraged.

In other words, the growth of a thermoacoustic instability depends on the relative phase of the heat release and pressure oscillations. If both are in phase, an amplification effect occurs,

INTRODUCTION

and an instability will arise (notwithstanding losses in the system).

In combustion systems, several mechanisms can lead to a coupling of heat release and acoustic pressure fluctuations. Generally speaking, changes in heat release generate acoustic waves which can affect the flow upstream of the flame (local flow rate, equivalence ratio, mixing, flow structures, thermodynamic properties etc.). As these perturbations are convected into the flame, they provoke a further heat release fluctuation^{23,11}. If these processes occur with the appropriate time delays and overcome the acoustic losses in the system, an unstable feedback loop may be formed, leading to a self-sustained thermoacoustic instability^{12,78}. In each case, the noise generated by the combustion process plays an essential role in the development of an instability.

Combustion noise in aeroengines

While combustion noise and thermoacoustic effects are present in many combustion devices, they are of particular concern in aero engines. This is because they play an important role in two forms of aircraft pollution. The first is the emission of gases such as carbon dioxide (CO₂) and nitrogen oxides (NO_x), which deteriorate local air quality, and contribute to climate change⁵⁰. The other is noise pollution, which is particularly pronounced in zones surrounding airports, with health effects ranging from mild hearing loss to increased cardiovascular risk³⁴.

Several steps have been taken to mitigate these harmful emissions, and modern aircraft are drastically less polluting than their predecessors¹⁴. Despite this, technological advances are being outpaced by the growth in global air traffic, which has risen continuously in the past decade. This trend shows no sign of stopping — according to the International Civil Aviation Organization, global air traffic is likely to double over the next 20 years⁴³. This realisation has made reducing aircraft emissions a matter of urgency; technological innovations are desperately needed.

One such innovation has come in the form of new aircraft engine designs. Specifically, the necessity of reducing NO_x emissions has encouraged the development of lean-premixed gas turbines. These engines can run at unprecedentedly low temperatures, which in turn reduces NO_x production¹⁴. These improvements have come at a cost however, as lean-premixed combustors are particularly prone to thermoacoustic instabilities²². To predict and avoid these instabilities, we must first understand how the combustion process generates acoustic waves (i.e. combustion noise).

Combustion noise is also relevant in the context of aircraft noise pollution. Prompted by increasingly stringent noise-emission regulations, significant progress has been made in the areas of jet noise and fan noise. As a result, the noise stemming from the gas turbine combustor now represents an important contribution to the overall aircraft noise. For both of the reasons outlined above, furthering our understanding of combustion noise is a crucial step in view of reducing aircraft pollutant emissions.

The noise generated by the combustion process is generally divided into two categories – direct and indirect combustion noise, in reference to their generation mechanism. Direct combustion noise refers to the acoustic waves generated in the reactive region. These are the result of the volumetric expansion and contraction brought about by the flame’s unsteady heat release⁸. Flames can also act as a source of non-acoustic perturbations in the flow. For example, they may generate entropic waves — pockets of gas with a different temperature than their surroundings. Similarly, they may produce small local changes in chemical composition (compositional waves), or in the velocity field (vortical waves). These disturbances are convected downstream with the flow, generating no acoustic waves in general¹³. If the flow is accelerated or decelerated however — as is often the case in practice — these convected waves generate acoustic waves, referred to as indirect noise^{28,67,18,58}. Indirect noise is further categorised as entropic, compositional or vortical, depending on the type of flow perturbation it arises from.

In a gas turbine combustor the flow is accelerated downstream of the flame, first at the nozzle guide vanes at the outlet of the combustor, as well as further downstream as the flow passes through several turbine stages. As such, a gas turbine generates both direct and indirect combustion noise, as shown in figure 2.

The term ‘combustion noise’ is sometimes used to refer exclusively to the downstream noise radiated through the turbine stages to the engine exhaust, which contributes to overall aircraft noise. In this thesis we also use the term in reference to the upstream propagating noise, which is reflected into the combustor where it may lead to the onset of a thermoacoustic instability^{33,79}. Specifically, several studies have shown that reflected indirect noise may trigger or sustain an instability^{9,33,36,70}, and it is considered to be one of the key feedback mechanisms for very low frequency instabilities^{62,93}.

The relative importance of direct and indirect noise has long been a topic of debate⁸⁶. Indeed, while direct combustion noise is now relatively well understood¹⁰, several aspects of the indirect noise mechanism remain nebulous⁶⁸. This is due in large part to the scarcity of ex-

INTRODUCTION

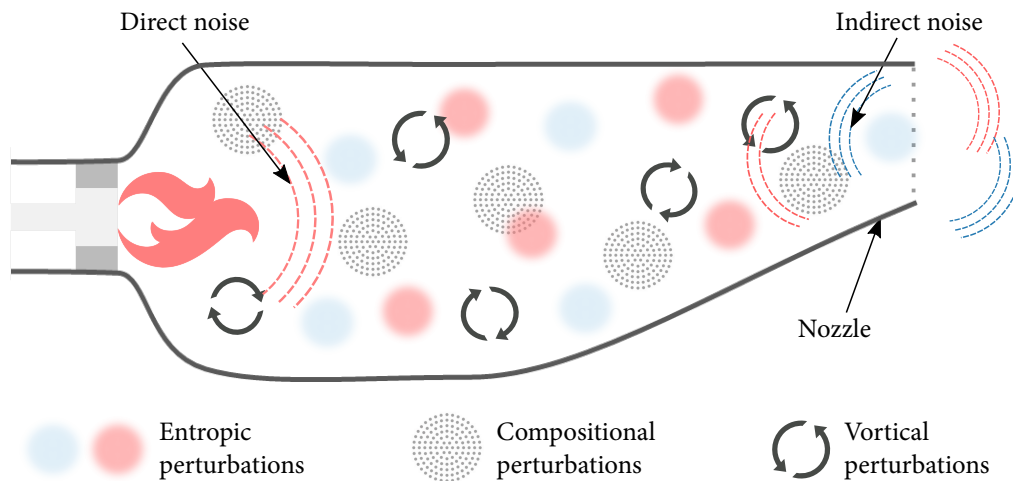


Figure 2: Direct and indirect noise mechanisms in a typical gas turbine combustor. Inspired by Dowling & Mahmoudi²¹ and Magri et al.⁵⁹.

perimental data, which are required to validate, refute or inform current theoretical models²¹. In fact, while there is some experimental evidence supporting the existence of entropic and vortical noise, no such data exist for compositional noise.

The indirect noise generation process can be thought of as a chain of three successive events, each of which must be well understood for the same to be said about the overall mechanism. First, entropic, compositional and vortical waves are generated by a flame or otherwise. Second, these waves are convected through the combustor, diffusing and dispersing along the way. Thirdly, the waves are accelerated at the outlet of the combustor, producing indirect noise. This final step has garnered considerable interest from researchers in recent years, and is the focus of the present work.

Thesis outline

The objective of this thesis is to shed a light on the validity of current theoretical models for the generation of entropic and compositional noise, and to propose new ones where needed. Emphasis is laid on low-frequency noise in the infra-sound range, for which analytical and experimental results can be most readily obtained. A one-dimensional analytical framework for direct and indirect noise generation and reflection is developed, building on existing theoretical models. This framework is then directly compared to experimental data obtained

with the Cambridge Wave Generator, in which acoustic, entropic and compositional waves are generated and accelerated, leading to direct and indirect noise.

In chapter I, the literature concerning the generation of indirect combustion noise is presented. The main analytical, numerical and experimental efforts to gain insights into indirect noise are reviewed, identifying gaps in our current understanding of the phenomenon.

A one-dimensional analytical model for the generation of waves at a flow discontinuity is derived in chapter II. It enables the production of acoustic waves (direct noise), as well as entropic and compositional waves to be computed quantitatively in a variety of scenarios, including heat addition (as is the case for a flame or a heater), or mass, momentum, energy and species addition (the general case).

The theoretical response of compact nozzles to acoustic, entropic and compositional waves is derived in chapter III. The common assumption of an isentropic nozzle is relaxed, offering analytical predictions in situations in which entropy is not conserved, as is often the case in real systems.

Chapter IV presents an analytical approach to account for the effect of repeated acoustic reflections (reverberation) on acoustic sources in a one-dimensional system. The results of these analyses lead to the definition of reverberation and transmission transfer functions for unicameral and bicameral systems. These transfer functions provide a two-way link between the acoustic pressure one can measure in a system and the acoustic sources within it.

The models in chapters II–IV are combined to form a complete theoretical framework for the generation of direct, entropic and compositional noise, which is presented in chapter V. Reverberation and transmission transfer functions are implemented to show how direct and indirect acoustic sources can be recovered from simple pressure measurements (de-reverberation).

A new experimental facility to study direct and indirect noise, the Cambridge Wave Generator, is described in chapter VI. The experimental set-up and wave generation methods used to obtain the results in chapters VII–IX are presented.

In chapter VII, experimental results concerning the generation of direct noise by air injection and extraction are shown. These are compared to the theoretical framework developed in chapters II–IV. This provides a simple test case for the reverberation and de-reverberation models, and enables the validity of the direct noise model to be examined.

The detection and measurement of entropic noise produced by convected temperature fluctuations is reported in chapter VIII. The upstream-propagating entropic noise generated at

INTRODUCTION

isentropic and anisentropic nozzles is measured for the first time. Finally, the response of nozzles to impinging entropic waves is characterised and compared to analytical predictions.

In chapter IX, compositional noise is introduced as an additional source of indirect noise. This is achieved by accelerating a helium-air mixture through nozzles of varying levels of anisentropy. The resulting entropic and compositional noise is once again measured and compared to the theoretical framework, this time measuring both upstream- and downstream-propagating components.

STATE OF THE ART

This chapter serves as a summary of current research on indirect combustion noise and its relevance in modern combustion systems. The governing equations for reacting flows are briefly presented, highlighting the mechanisms driving the generation of direct and indirect noise. The literature concerning the indirect mechanism is explored, covering the main theoretical, numerical and experimental results. Particular attention is given to the sound generated by the interaction of flow inhomogeneities with nozzles, which is the focus of this thesis.

I.1 Acoustics of combustion

I.1.1 Governing equations

To understand how the combustion process gives rise to acoustic waves, one can start from the equations of motion of a reacting multicomponent gas. For a viscous compressible flow with no external forces, the conservation of mass and momentum are given by the Navier-Stokes equations:

$$\frac{D\rho}{Dt} + \rho\nabla \cdot \mathbf{u} = 0, \quad (\text{I.1})$$

$$\rho \frac{D\mathbf{u}}{Dt} = -\nabla p + \nabla \cdot \boldsymbol{\tau}, \quad (\text{I.2})$$

where ρ is the density, p is the pressure, \mathbf{u} is the velocity and $\boldsymbol{\tau}$ is the viscous stress tensor. The material derivative is $D/Dt = \partial/\partial t + \mathbf{u} \cdot \nabla$. These equations are complemented by the ideal gas law, which relates the pressure to the gas density and temperature T :

$$p = \rho RT, \quad (\text{I.3})$$

where R is the gas constant, which is a function of the mixture composition. Since we are dealing with a flame which generates heat, we must also consider the balance of energy:

$$\rho \frac{Dh}{Dt} = \frac{Dp}{Dt} + q + \nabla \cdot (k\nabla T) + \boldsymbol{\tau} : \nabla \mathbf{u}, \quad (\text{I.4})$$

where h is the specific enthalpy, q is the heat release rate per unit volume and k is the thermal conductivity. We must also account for the conservation of chemical species:

$$\rho \frac{DY}{Dt} = \rho \dot{\boldsymbol{\omega}} - \nabla \cdot \mathbf{j}, \quad (\text{I.5})$$

where \mathbf{Y} is the vector of the mass fractions Y_i of the N species composing the gas (such that $\sum_{i=1}^N Y_i = 1$), $\dot{\boldsymbol{\omega}}$ is the vector of species production rates, and \mathbf{j} is the vector of diffusive mass fluxes.

These equations are closed with Gibbs' relation for a multicomponent gas:

$$dh = T ds + (1/\rho) dp + \sum_{i=1}^N \frac{\mu_i}{W_i} dY_i, \quad (\text{I.6})$$

where s is the entropy and W_i is the molar mass of one of N species. The chemical potential of each species is defined as $\mu_i = W_i \frac{\partial h}{\partial Y_i}$. This enables us recast equation (I.4) as:

$$\rho T \frac{Ds}{Dt} = q + \nabla \cdot (k\nabla T) + \boldsymbol{\tau} : \nabla \mathbf{u} - \rho \sum_{i=1}^N \frac{\mu_i}{W_i} \frac{DY_i}{Dt}, \quad (\text{I.7})$$

which shows that the production of entropy is driven by heat addition q , as well as thermal gradients, viscous heating, compositional gradients, and chemical reactions.

Together, equations (I.1)-(I.7) can be used to fully describe the flow. Nevertheless, we are interested mainly in the acoustic component of the flow, which appears physically as small fluctuations in the variables p , ρ , T and \mathbf{u} . As such, we decompose flow variables into their mean and fluctuating components, denoted with an over-bar and a prime respectively (e.g. $\beta(x, t) = \bar{\beta}(x) + \beta'(x, t)$). Furthermore, we consider linear fluctuations; their amplitude is small relative to the mean quantity (e.g. $\beta' \ll \bar{\beta}$). If we consider small perturbations to the inviscid flow of a non-reacting perfect gas, we can derive linearised governing equations:

$$\frac{D\bar{\rho}'}{Dt} = -\bar{\rho} \nabla \cdot \mathbf{u}', \quad (\text{I.8})$$

I. STATE OF THE ART

$$\frac{\bar{D}\mathbf{u}'}{Dt} = -\frac{1}{\bar{\rho}}\nabla p', \quad (\text{I.9})$$

$$\frac{\bar{D}s'}{Dt} = \frac{q'}{\bar{\rho}\bar{T}}, \quad (\text{I.10})$$

$$\frac{\bar{D}\boldsymbol{\Omega}'}{Dt} = 0, \quad (\text{I.11})$$

$$\frac{\bar{D}\mathbf{Y}'}{Dt} = 0, \quad (\text{I.12})$$

where $\boldsymbol{\Omega} = \nabla \times \mathbf{u}$ is the vorticity, and $\bar{D}/Dt = \partial/\partial t + \bar{\mathbf{u}} \cdot \nabla$.

Combining (I.8)-(I.11) and making use of the ideal gas law leads to the inhomogeneous acoustic wave equation:

$$\frac{1}{\bar{c}^2} \frac{\bar{D}^2 p'}{Dt^2} - \nabla^2 p' = \frac{\gamma - 1}{\bar{c}^2} \frac{\bar{D}q'}{Dt}, \quad (\text{I.13})$$

where $c = \sqrt{\gamma RT}$ is the speed of sound, and γ is the heat capacity ratio. The equation above shows that heat release fluctuations q' directly drive the generation of acoustic waves, here manifested as pressure perturbations p' . This reveals one way in which combustion noise may be generated. Additional insight can be obtained by separating acoustic fluctuations from other types of disturbances.

I.1.2 Flow decomposition

Considering equations (I.8)-(I.12), we see that any linear perturbation can be described as the sum of four canonical disturbances: acoustic, entropic, vortical and compositional^{13,54,57}. Assuming a uniform mean flow with no unsteady heat input ($q' = 0$), these disturbances are independent from each other, and do not interact⁵⁷.

The acoustic disturbance is isentropic and irrotational. Setting $s' = 0$ and $\boldsymbol{\Omega}' = \mathbf{0}$ in equations (I.8)-(I.11) leads to the acoustic wave equation:

$$\frac{1}{\bar{c}^2} \frac{\bar{D}^2 p'}{Dt^2} - \nabla^2 p' = 0. \quad (\text{I.14})$$

For a one-dimensional flow, the solution to this equation corresponds to the superposition of forward and backward travelling acoustic waves. These waves travel at the speed of sound \bar{c} relative to the mean flow speed \bar{u} .

Similarly, the entropic disturbance is incompressible and irrotational:

$$\frac{\bar{D}s'}{Dt} = 0, \quad (\text{I.15})$$

which shows that entropic fluctuations are simply convected with the flow. This can be thought of as an entropic wave propagating at the mean flow speed \bar{u} .

The vorticity perturbation is incompressible and isentropic, and we have:

$$\frac{\bar{D}\boldsymbol{\Omega}'}{Dt} = \mathbf{0}, \quad (\text{I.16})$$

showing that the vortical disturbance manifests itself as a vortical wave convected with the mean flow.

Finally, the compositional perturbation is incompressible, isentropic, irrotational and is also convected with the flow:

$$\frac{\bar{D}\mathbf{Y}'}{Dt} = \mathbf{0}. \quad (\text{I.17})$$

Each one of these canonical waves (or modes) manifests itself physically as a set of fluctuations in the flow variables, as shown in table I.1. For example, an entropic wave is observable as a fluctuation of both temperature and density.

	Acoustic wave	Entropic wave	Vortical wave	Compositional wave
Pressure p	●	-	-	-
Velocity \mathbf{u}	●	-	●	-
Density ρ	●	●	-	-
Temperature T	●	●	-	-
Vorticity $\boldsymbol{\Omega}$	-	-	●	-
Entropy s	-	●	-	●
Composition \mathbf{Y}	-	-	-	●

Table I.1: Flow variables affected (●) and unaffected (-) by the four canonical wave types.

I.1.3 Mode conversion

For a uniform mean flow, Chu & Kovásznyai¹³ showed that the interactions between acoustic, vortical and entropic waves only have a second order effect (i.e. $\mathcal{O}(p'^2)$). Magri⁵⁷ showed compositional waves are also uncoupled in the first-order equations. However, these perturbations can be coupled in the presence of a gradient in the mean flow, where different types of waves may interact. Example of these interactions are shown in figure I.1, and include (a) acoustic waves impinging on an orifice plate generating vortical waves⁷³, (b) entropic waves impinging on an aerofoil cascade generating acoustic waves¹⁷ and (c) compositional waves impinging on a nozzle generating acoustic waves^{44,58}. These couplings are sometimes described as mode conversion mechanisms⁷⁶.

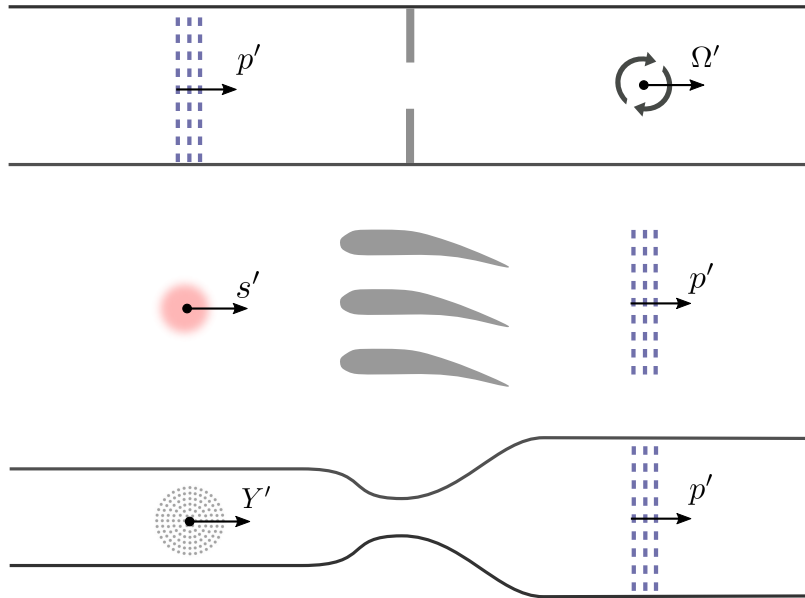


Figure I.1: Examples of mode conversion mechanisms between acoustic (p'), vortical (Ω'), entropic (s') and compositional (Y') perturbations.

As we have shown in (I.10), unsteady heat release can be a source of entropic waves, which if convected through a nozzle may then lead to the generation of acoustic waves. In that sense, mode conversion consists of an indirect link through which unsteady heat release (characteristic of combustion) may generate acoustic waves. This is in addition to the direct link shown in (I.13).

Indirect noise generation can be thought of as a set of three mode conversion mechanisms, whereby accelerated or decelerated entropic, vortical or compositional waves produce acoustic

waves^{40,61,58}. Vortical noise is often considered to be less prevalent than entropic noise in gas turbines. Indeed, high gas temperatures result in an elevated viscosity, which tends to dissipate turbulent vortical structures before they reach the nozzle⁶⁸. For this reason, the entropic and compositional mechanisms have garnered the most attention from researchers.

I.2 Analytical models for entropic noise

Entropic noise has been the topic of numerous studies since it was theorised in the sixties¹⁵. One of the first investigations on the topic was carried out in 1973 by Morfey⁶⁷, who refined Lighthill's theory for jet noise⁵⁵ to account for the 'excess jet noise' generated by density inhomogeneities. He showed that this excess noise could be understood by considering the excess density ρ_e , defined as:

$$\rho_e = \rho' - \frac{1}{\bar{c}^2} p'. \quad (\text{I.18})$$

This excess density corresponds to the density fluctuation not related to isentropic acoustic fluctuations. In fact, for an ideal gas, the excess density is directly related to the entropic fluctuation:

$$\frac{\rho_e}{\bar{\rho}} = \frac{\rho'}{\bar{\rho}} - \frac{p'}{\gamma \bar{p}} = -\frac{s'}{\bar{c}_p}. \quad (\text{I.19})$$

where c_p is the specific heat capacity at constant pressure.

This extension of Lighthill's theory was further developed by Howe^{38, 37} and Ffowcs-Williams²⁸, who used Green's functions approaches to determine the entropic noise generated in low Mach number flows. Bailly et al.¹ derived several acoustic analogies for reacting flows with reference to entropic noise.

In parallel to these developments, Marble & Candel⁶¹ developed a different approach to examine the coupling between entropic and acoustic fluctuations. They considered the quasi one-dimensional flow through an isentropic nozzle, assuming that (1) the flow is adiabatic, (2) composed of a homogeneous gas, (3) thermodynamically perfect (γ is constant) and (4) viscous effects are negligible. In this scenario, the linearised Euler equations are:

$$\frac{\bar{D}}{Dt} \left(\frac{p'}{\gamma \bar{p}} \right) + \bar{u} \frac{\partial}{\partial x} \left(\frac{u'}{\bar{u}} \right) = 0, \quad (\text{I.20})$$

$$\frac{\bar{D}}{Dt} \left(\frac{u'}{\bar{u}} \right) + \frac{\bar{c}^2}{\bar{u}} \frac{\partial}{\partial x} \left(\frac{p'}{\gamma \bar{p}} \right) + \left[2 \frac{u'}{\bar{u}} + (1 - \gamma) \frac{p'}{\gamma \bar{p}} \right] \frac{d\bar{u}}{dx} = \frac{s'}{\bar{c}_p} \frac{d\bar{u}}{dx}, \quad (\text{I.21})$$

I. STATE OF THE ART

$$\frac{\bar{D}}{Dt} \left(\frac{s'}{\bar{c}_p} \right) = 0. \quad (\text{I.22})$$

If the mean flow gradient is zero ($d\bar{u}/dx = 0$), then combining equations (I.20) and (I.21) enables one to recover (I.14), which simply describes acoustic propagation. The presence of a mean flow gradient ($d\bar{u}/dx \neq 0$) has two effects. First, terms representing refraction and reflection appear (third term of (I.21)). Secondly, entropic fluctuations s'/\bar{c}_p appear as a dipole source term in the wave equation (on the right hand side of (I.21), revealing the entropic noise generation mechanism.

I.2.1 Compact models

Marble & Candel⁶¹ examined the case of a compact nozzle, meaning that the length of the nozzle is negligible compared to the wavelength of acoustic and entropic disturbances. This limits the analysis to low frequency acoustic and entropic waves, which are assumed to propagate quasi-steadily through an abrupt area change. Under these conditions, the normalised fluctuations in mass flow $\dot{m}'/\bar{\dot{m}}$, total temperature T'_t/\bar{T}_t and entropy s'/\bar{c}_p are matched across the area change. This can be formulated as a jump condition for the acoustic and entropic waves on either side of the nozzle. This enabled them to determine transfer functions for the waves generated at a subsonic or supersonic nozzle (shown in §III.1). These transfer functions enable one to calculate the amplitude of acoustic waves generated in response to impinging entropic or acoustic waves.

Marble & Candel⁶¹ also considered the interaction of an entropic wave with a normal shock downstream of the nozzle. Moase et al.⁶⁶ extended their approach to a more general case: by applying the Rankine-Hugoniot conditions across the shock, they were able to derive acoustic-acoustic and entropic-acoustic transfer functions for compact nozzles with a shock.

Cumpsty & Marble¹⁷ applied the concept of the compact nozzle to the case of an entropic fluctuation convected through a series of compact turbine blade rows, showing that the generated entropic noise could be calculated analytically.

I.2.2 Non-linear models

Most indirect noise models assume a linear flow regime in which flow perturbations are small relative to the mean. In practical situations, perturbations may not always be linear. In the presence of a combustion instability for example – during which flow perturbations are un-

usually large – entropic fluctuations generated at the flame may fall outside of the linear range (e.g. above 100 K for a 1000 K average temperature). In this scenario, nonlinear effects must be considered.

Huet & Giauque⁴² modelled the response of subsonic and supersonic nozzles to impinging nonlinear acoustic and nonlinear entropic perturbations. This was later extended by Huet⁴¹ to nozzles with shocks, producing both second-order and fully nonlinear models. Their results show that the nozzle response to nonlinear acoustic fluctuations is identical to the first-order solution. In other words, the nonlinear acoustic-acoustic nozzle transfer functions are identical to the linear ones derived by Marble & Candel⁶¹.

In contrast, the response of nozzles to nonlinear entropic fluctuations shows that additional noise is generated compared to the first-order (linear) model. In most cases, the nonlinear solution can be well approximated (to within 1%) by the second-order model⁴². For subsonic diverging nozzles where both the inlet and outlet Mach numbers are high, the discrepancy can be substantial (up to 70%), although this is not representative of a gas turbine combustor, in which the outlet Mach number is high but the inlet Mach number is typically low.

I.2.3 Non-compact models

Compact nozzle models are valid in the limit of low Helmholtz numbers $He = \omega L/c$ (where ω is the perturbation frequency, L is the characteristic length of the nozzle and c is the speed of sound). In this sense, a strictly compact nozzle is a nozzle with zero-length, or subjected to zero-frequency perturbations. If the perturbation frequency and nozzle length are larger than zero, the actual response of the nozzle is no longer predicted by the compact model. The most important difference between compact and non-compact nozzles is that in the former, there is no phase shift between the inlet and outlet. For the latter, a phase shift occurs, modifying the nozzle response as a function of frequency both in terms of amplitude and phase.

Leyko et al.⁵³ investigated the importance of non-compactness by solving the quasi one-dimensional Euler equations ((I.20)-(I.22)) numerically, and comparing the result to the compact nozzle models. Their results show that the compact assumption remains accurate up to $He \approx 0.2$, but that non-compactness becomes important at higher Helmholtz numbers. In that case, the finite length of the nozzle must be taken into account. Similarly, Leyko et al.⁵¹ showed that compact blade row models are unsuitable beyond $He \approx 0.1$.

In their original study, Marble & Candel⁶¹ also considered the response of finite-length nozzles with a linear mean velocity profile. Their work was extended to account for more

I. STATE OF THE ART

complex nozzle geometries with piece-wise linear velocity distributions by Moase et al.⁶⁶ and Giauque et al.²⁹. These analytical results were validated with numerical simulations of the Euler equations.

A different approach was taken by Stow et al.⁸⁵, who accounted for finite-length nozzles by introducing a phase-correction to the boundary conditions established in the compact case. This work was continued by Goh & Morgans³², who introduced the concept of effective lengths as a way to determine phase predictions of the nozzle response. These effective lengths are dependent on the type of disturbance and on the nozzle geometry.

Finally, Duran & Moreau²⁴ derived analytical expressions for the acoustic and entropic transfer functions of subsonic and choked finite-length nozzles of arbitrary geometries. They solved the linearised Euler equations ((I.20)-(I.22)) using the Magnus expansion. Their results apply to subsonic and supersonic nozzles of arbitrary geometries for any perturbation frequency. Their solution can be used to predict the response of nozzles to impinging acoustic or entropic waves. Their predictions of the acoustic response is in excellent agreement with experimental measurements of acoustic-acoustic response by Zinn et al.⁹⁶ for converging-diverging choked nozzles over a large range of frequencies. Such a validation has not yet been carried out for the entropic-acoustic response due to a lack of experimental data. In general, their numerical results suggest that amplitude of the entropic noise generated at a choked nozzle decreases as the Helmholtz number increases. There seems to be no such general rule for a subsonic nozzle, which may produce more or less entropic noise than the compact equivalent depending on the Helmholtz number.

I.3 Analytical models for compositional noise

Much of the literature on indirect noise assumes a homogeneous gas with uniform composition. In reality, the flow in a combustor is comprised of a range of chemical species, which may result in compositional inhomogeneities (due to imperfect mixing or dilution for example). Ihme⁴⁴ and Magri et al.⁵⁸ examined compositional heterogeneities as a contributor to indirect noise. They assumed a chemically frozen multi-component gas, uniquely describing compositional variations using the mixture fraction Z , such that $\mathbf{Y} = \mathbf{Y}(Z)$. In this scenario, Magri⁵⁷ showed that the excess density can be expressed as:

$$\frac{\rho_e}{\bar{\rho}} = -\frac{s'}{\bar{c}_p} - \Psi Z', \quad (\text{I.23})$$

where Ψ is the chemical potential function:

$$\Psi = \frac{1}{\bar{c}_p \bar{T}} \sum_{i=1}^N \frac{\mu_i}{W_i} \frac{dY_i}{dZ}. \quad (\text{I.24})$$

Comparing (I.19) and (I.23) reveals that in a multi-component gas, fluctuations in composition Z' act as a contributor to the excess density in addition to entropic fluctuations s'/\bar{c}_p . This suggests that convected compositional fluctuations also generate indirect noise.

Linearising the Euler equations as in (I.20)-(I.22) without assuming a homogeneous gas, one obtains⁵⁷:

$$\frac{\bar{D}}{Dt} \left(\frac{u'}{\bar{u}} \right) + \frac{\bar{c}^2}{\bar{u}} \frac{\partial}{\partial x} \left(\frac{p'}{\gamma \bar{p}} \right) + \left[2 \frac{u'}{\bar{u}} + (1 - \gamma) \frac{p'}{\gamma \bar{p}} \right] \frac{d\bar{u}}{dx} = \left(\frac{s'}{\bar{c}_p} + \Psi Z' \right) \frac{d\bar{u}}{dx}, \quad (\text{I.25})$$

which shows that compositional fluctuations Z' appear as a dipole acoustic source in the presence of a mean flow gradient.

I.3.1 Compact model

Ihme⁴⁴ and Magri et al.⁵⁸ extended the compact nozzle approach developed by Marble & Candel⁶¹ to include the effect of impinging compositional waves. In addition to the jump conditions assumed in the original study (conservation of fluctuating mass, total temperature and entropy), they considered that the compositional fluctuation Z' was conserved across the nozzle.

They obtained the analytical response of subsonic and supersonic nozzles to impinging acoustic, entropic and compositional fluctuations. Their study also accounts for the presence of a shock wave downstream of the supersonic nozzle. Their derivation (shown in §III) enables one to recover the acoustic-acoustic and entropic-acoustic transfer functions previously obtained by Marble & Candel⁶¹, with the addition of compositional-acoustic transfer functions.

I.3.2 Non-compact model

As with the entropic noise models, the assumption of nozzle compactness must be relaxed to obtain realistic solutions for nozzles of finite lengths and non-zero frequency impinging waves.

I. STATE OF THE ART

Magri et al.⁶⁰ performed a numerical integration of the linearised Euler equations accounting for compositional fluctuations ((I.20), (I.22) and (I.25)). They considered several subsonic and supersonic nozzle geometries, showing that the response of a nozzle to compositional waves is frequency-dependent. Magri⁵⁷ solved these equations analytically using asymptotic expansions. Generally speaking, the compositional noise produced at a choked nozzle decreases monotonically as the Helmholtz number increases. In other words, a choked nozzle of finite length produces less compositional noise than the equivalent compact nozzle. This trend is similar but not strictly identical to that of entropic noise.

I.4 Indirect noise in combustion systems

The analytical indirect noise models in §I.2-I.3 enable one to compute the acoustic waves generated by entropic or compositional waves impinging on a nozzle or turbine blade row. Nevertheless, this is not enough to gain an in-depth understanding of indirect noise in real combustion systems. Specifically, the importance of indirect noise compared to direct noise and its effect on the thermoacoustic stability of a combustor are of immediate practical interest. To obtain such a level of insight, one must rely either on experimental data, or on studies in which theoretical and numerical models are applied to realistic configurations.

I.4.1 Experimental investigations of indirect noise generation

In 1977, Cumpsty & Marble¹⁶ used their compact stator row model to predict the indirect noise produced by a gas turbine. Their predictions were in good agreement with acoustic power measurements carried out for three commercial jet engines (Rolls Royce Olympus 593, Rolls Royce Olympus 512 and Pratt and Whitney FT8D-9). This comparison provided some circumstantial evidence for the validity of the compact indirect noise model. In spite of this, the authors admitted that the data did not provide conclusive evidence on the predominance of either direct or indirect noise, and that definite validation could only be achieved by separating direct and indirect noise sources in the experimental data¹⁶. In practice, this is difficult: since both direct and indirect noise arise from the same heat release fluctuations at the flame, they tend to be highly correlated.

Such a separation was attempted by Muthukrishnan et al.⁷² in 1978 using partial coherence analysis. They measured combustion noise using several pressure transducers located inside

and outside a combustor taken from a Boeing 502-7D gas turbine unit. When the combustor was operated without an outlet nozzle, the radiated noise was found to be due to the direct noise mechanism. Conversely, when the combustor was fitted with a choked outlet nozzle, entropic noise was found to be the dominant sound source. The results also suggested that other sound sources were present in the combustor – potentially vortical noise (as suggested by the authors), or compositional noise.

Another approach used to distinguish direct and indirect noise in experimental conditions is a time delay analysis. One of the distinctions between direct and indirect noise is the location at which they are generated. Since direct noise is generated at the flame and indirect noise is generated at the outlet nozzle, they are separated by a convective time delay of L/\bar{u} where L is the length of the combustor and \bar{u} is the mean flow speed. This approach was favoured by Miles⁶², who developed a source location technique based on adjusting an effective time delay to maximise the coherence between interior and far-field pressure measurements. By applying this technique to measurements from a Honeywell TECH977 turbofan engine, he showed that the indirect noise mechanism was the dominant sound source in the range 0-200 Hz while direct noise dominated at higher frequencies^{62,64,63}.

Schemel et al.⁸⁴ and Bake et al.^{3,2} used yet another method to identify the indirect noise produced in a laboratory combustor fitted with an outlet nozzle. They excited the flame with a fuel pulse to produce direct noise, followed by indirect noise after a convective time delay. The resulting pressure measurements could be phase averaged over several pulses and analysed in the time domain. The results were consistent with the generation of direct and indirect noise separated by a convective time delay. Nevertheless, the relative amplitudes of these noise sources could not be measured directly, and the results were not compared to theoretical models.

Finally, Tam et al.⁸⁸ investigated the indirect noise produced by a Honeywell RE220 auxiliary power unit. They performed a theoretical study to analyse the frequency ranges over which indirect noise was most likely to be generated, and attempted to find corresponding peaks in the acoustic spectra measured experimentally. Their comparison suggested that indirect noise may be a contributor to the overall measured noise, though by their own admission the supporting evidence was not very strong.

I.4.2 Theoretical investigations of indirect noise generation

Given the difficulty of separating and evaluating direct and indirect noise in an experimental context, several studies have attempted to do so by applying theoretical models to realistic combustor configurations.

Leyko et al.⁵³ estimated the direct and entropic noise produced in a combustor terminated with a nozzle. They assumed a cold flame (generating only fluctuations in heat release with no mean heat addition), and used compact direct and indirect noise models derived by Cumpsty¹⁸ and Marble & Candel⁶¹ respectively. They showed that the direct to entropic noise ratio depends on the Mach number in the combustor and in the outlet nozzle. They concluded that direct noise would be the main sound source in laboratory combustors (where the nozzle is usually subsonic), but that entropic noise could be an order of magnitude larger than direct noise in aeroengines (where the outlet nozzle is typically choked).

Leyko et al.⁵³ also considered the effect of the Helmholtz number on direct and entropic noise by integrating the Euler equations numerically. Their results also show that the ratio of direct to entropic noise increases with the Helmholtz number; in other words entropic noise is most relevant at low frequencies. This was confirmed by an analytical study of the same case by Duran & Moreau²⁴.

Indirect noise corresponds to entropic noise, vortical noise and compositional noise. Most studies have focused on the relative amplitude of entropic and direct noise, usually overlooking vortical and compositional contributions. Vortical noise is often considered to be less important than entropic and compositional noise in combustion flows, since it is suspected that large vortical structures generated at the flame location dissipate before reaching the outlet of the combustor⁶⁸. The relative importance of compositional and entropic noise is not clear; they cannot be separated experimentally given that they typically arise from the same flow structures. For the time being, insight into the relative importance of entropic and compositional mechanisms can only be reached through theoretical considerations.

Estimating the relative importance of compositional and entropic noise is difficult, since the compositional mechanism depends on the chemical composition of combustion products⁷⁵. Magri et al.⁵⁸ estimated the compositional noise generated by the convection of combustion products through a compact subsonic or supersonic nozzle. The combustion products corresponded to those resulting from a series of one-dimensional strained diffusion flames using a kerosene surrogate (*n*-Dodecane $C_{12}H_{26}$) as a fuel. They found that compositional noise could be comparable, and even exceed direct and entropic noise for supersonic nozzles and

lean mixtures. This suggests that compositional noise is particularly relevant for low-emissions gas turbine combustors, in which the mixture is lean and the outlet is choked.

I.4.3 Influence of indirect noise on thermoacoustics

Indirect noise generated at the outlet of a combustor is transmitted downstream towards the engine exhaust, as well as reflected upstream back into the combustor. The reflected component of indirect noise is thought to be a potential source of thermoacoustic instabilities. Specifically, entropic noise is often considered to be responsible for ‘rumble’ – low frequency instabilities in the range of 50 to 150 Hz²¹. This has been the topic of several experimental^{30,36} and numerical studies^{45,95,79,22,33,70}.

Goh & Morgans³³ carried out an analytical study to examine the effect of entropic noise on the thermoacoustic stability of a set of model combustors. They found that entropic noise could (1) stabilise previously unstable modes, (2) destabilise previously stable modes or (3) change which mode was the most unstable. Their study showed that one of the determining factors concerning the influence of entropic noise was the convection of entropic waves across the combustor. Indeed, entropic waves are generated at the flame, and are convected with the main flow towards the outlet nozzle, dissipating, dispersing and diffusing along the way. The amplitude of the upstream propagating entropic noise depends as much on this convection process as it does on the nozzle transfer function. The same is true of compositional noise.

Sattelmayer⁸³ proposed an analytical model for the dispersion of equivalence ratio and entropic waves across a combustor. Their model is based on a distribution of residence times from the flame to the outlet, which can be obtained from a flow field simulation or experimental data. They used experimental data from a laboratory burner, showing that while dispersion of equivalence ratio waves was modest, entropic waves were strongly dispersed even at low frequencies. These findings were corroborated by Eckstein & Sattelmayer²⁷, who found that entropic waves were likely to disperse before reaching the outlet of the combustor.

Morgans et al.⁶⁹ revisited the topic of entropic wave transport. Modelling the transport process as in (I.7), they performed a direct numerical simulation of an entropic wave propagating in a turbulent channel flow. They found that dissipation was negligible, and that dispersion was driven by shear mixing due to the mean velocity profile rather than turbulent mixing. They produced an analytical transport model for entropic waves in good agreement with their numerical data for channel flow. By applying this model to a turbulent velocity profile typical of a gas turbine combustor, they concluded that low-frequency entropic waves could survive

I. STATE OF THE ART

to the outlet of the combustor, and thus generate entropic noise. This is in contrast to the findings of Sattelmayer⁸³ and Eckstein & Sattelmayer²⁷.

Wassmer et al.⁹² also modelled the transport of entropic waves, showing that shear dispersion due to the velocity profile could be modelled as an effective diffusivity (i.e. Taylor dispersion⁹¹). They validated their model using experimental measurements of entropic waves propagating downstream of a premixed flame.

I.5 Model experiments on indirect noise

Notwithstanding the findings described in §I.4.1, quantitative experimental measurements of indirect noise have been difficult to obtain. Specifically, separating the contributions of direct and indirect noise has proven to be particularly arduous, as these tend to be highly correlated and hard to distinguish⁸⁹. To make matters worse, precise measurements are particularly hard to obtain in the harsh environment of a combustor. This is problematic: robust experimental data is the only way by which theoretical models can be confirmed or refuted.

One way to circumvent these difficulties is to carry out a model experiment, in which indirect noise is generated artificially rather than by a flame. The aim of such an experiment is not to measure combustion noise per se (which in itself is a complex phenomenon involving flame dynamics, turbulence, directionality etc.), but rather to measure indirect noise in simplified conditions.

Early experiments carried out in the 1970s by Zukoski & Auerbach⁹⁷ and Bohn⁷ attempted to generate entropic waves artificially using electrical heaters. However, the amplitude of the temperature fluctuation generated by the heaters ($T' \approx 1$ K) was very low, making it difficult for entropic noise to be clearly identified. In addition, data processing capabilities available at the time were insufficient to draw meaningful conclusions from the data⁷.

I.5.1 Entropy and Vorticity Wave Generators

The Entropy Wave Generator (EWG) rig developed at the Deutsches Zentrum für Luft- und Raumfahrt (DLR) overcame these limitations⁴. Entropic waves were generated in a duct using an electric heater consisting of 6 rings gridded with 25 μm platinum wire, acting as a 200 W time-dependent heat source. The heater could be operated at low frequencies (of the order of 1 Hz), achieving temperature fluctuations up $T' \approx 11$ K (corresponding to entropic fluctuations

of $s'/\bar{c}_p \approx 0.035$). The entropic waves thus generated were accelerated through a subsonic or supersonic nozzle, and the resulting acoustic pressure measured further downstream⁴. The duct downstream of the nozzle was fitted with an anechoic outlet designed to prevent any additional acoustic reflections. The upstream-propagating entropic noise (which may play a role in thermoacoustic instabilities) was not measured.

The temperature fluctuation generated by the electric heater was found to generate direct noise, meaning that the pressure measurements were actually a combination of direct and indirect noise²⁹. Due to the small convective time delay, the individual contributions of direct and entropic noise to the total acoustic signal could not be determined. Furthermore, the anechoic outlet was found to be reflective in the frequency range of the experiment, meaning that a portion of the measured pressure signal was a result of acoustic reflections. This made conclusive interpretation of the experimental results even more challenging: to this day there it is still unclear to which extent the EWG measurements correspond to direct or indirect noise⁵⁶. The overall noise produced by the EWG was found to increase in line with the induced temperature fluctuation T' , which is consistent with both the direct and indirect noise models¹⁸.

Computational simulations of the EWG experiment were carried out both for the subsonic and supersonic cases^{71,52,25}. They showed that the acoustic reflections at the boundaries of the system had a very large influence on the measured pressure. The simulations could be made to match the experimental data only if a fitted acoustic reflection coefficient was employed for the anechoic termination, effectively acting as a low-pass filter.

The transfer-function of the pressure transducers used in the experiments (G.R.A.S., type 40BP) does not appear to have been taken into account. De Domenico et al.²⁰ showed that the response of these transducers corresponds to a high-pass filter, producing a non-physical ringing similar to the one present in the EWG data. This effect is important in the low frequency range of the EWG experiment. This suggests that the experimental data is affected both by acoustic reflections and the response of the pressure transducer, making it difficult to draw definite conclusions from the measured pressure signal.

Simulations carried out for the EWG based on compact nozzle models showed good agreement with experimental results (provided the effects described above were taken into account)^{52,25}. While direct and indirect noise sources could not be identified experimentally, these contributions could be computed separately using analytical models and compared. In the subsonic case, Duran et al.²⁵ found that the majority of the noise measured in the experiment was actually direct noise and that entropic noise was negligible. In this sense, the subsonic EWG

I. STATE OF THE ART

experiment cannot be used as a validation for entropic noise models.

A similar approach was taken by Kings & Bake⁴⁶ to study the vortical noise mechanism experimentally. They developed a Vorticity Wave Generator (VWG), in which vortical waves were produced by injecting air into a flow duct at an angle (at a frequency of the order of 1 Hz). Vortical noise was successfully measured, though once again the results were not compared to theoretical models. Once more, the transfer function of the pressure transducers (G.R.A.S., type 40BP) was not taken into account, meaning that the amplitude and shape of the measured signal may not be due solely to acoustics.

I.5.2 Hot Acoustic Test rig

Following these efforts, the Hot Acoustic Test rig (HAT) was developed at DLR to investigate entropic noise⁴⁸. The HAT consists of a duct fitted with a choked nozzle and terminated with an anechoic end. Entropic waves were generated at low frequencies (of the order of 1 Hz) upstream of the nozzle by injecting cold air into a flow of heated air (i.e. cold spots). Using this method, temperature fluctuations of up to $T' \approx -20$ K (corresponding to entropic fluctuations of $s'/\bar{c}_p \approx -0.025$) could be achieved at the nozzle.

The injection of cold air into the hot air flow was found to generate direct noise. By varying the distance between the injector and the nozzle, Knobloch et al.⁴⁸ showed using a time delay analysis that entropic noise was produced at the nozzle as the cold spots were convected through the nozzle. The entropic noise was found to increase in line with the temperature fluctuation associated to the cold spots being convected through the nozzle. As with the original EWG experiment however, the results were not directly compared to analytical models for entropic noise, meaning that the validity of theoretical entropic noise models is still unverified. As with the other DLR experiments, the effect of the pressure transducer transfer functions does not appear to have been taken into account.

I.5.3 High-pressure turbine stage

In an effort to build a model experiment closer to the real operating conditions of a gas turbine, a model high-pressure turbine stage rig was built in Politecnico di Milano⁴⁷. The rig consists of a single-stage high-pressure turbine, which can be operated in subsonic and transonic conditions with static pressures ranging from 1.3 to 1.9 bar. Acoustic, entropic and vortical waves

can be generated and convected through the rotor stage. The resulting noise is measured using large arrays of microphones placed upstream and downstream of the rotor.

Entropic waves are generated by alternately injecting hot and cold air at frequencies of up to 100 Hz, achieving temperature fluctuations up $T' \approx 30$ K (corresponding to entropic fluctuations of $s'/\bar{c}_p \approx 0.1$)⁷⁷. Vortical waves can be generated at the same frequency by pulse injecting ambient air into the rig with a high momentum.

In order to identify the effect of air injection associated to the entropic wave generation method, the rig was operated in two configurations: (A) injection of hot/cold air to produce entropic waves and injection noise, and (B) injection of ambient air to produce only injection noise. By comparing the acoustic power measured in these two configurations, Knobloch et al.⁴⁷ found that upstream of the rotor, configuration (B) generated more noise than configuration (A), while the opposite was true downstream of the rotor. No explanation was offered for this result in the original study⁴⁷. One hypothesis is that this result is due to a combination of constructive and destructive interference between injection noise and entropic noise. However, since only the acoustic power was measured, it is not possible to validate this hypothesis using experimental data alone. The experimental measurements have not been compared to theoretical results.

I.5.4 Temperature and Acoustic Fluctuation Generator

One of the shortcomings of the model experiments presented above is that the results they produce cannot be directly compared to theoretical models. Indeed, these rigs typically produce a combination of direct and indirect noise, but it is not usually known what proportion of the signal corresponds to one or the other.

Tao et al.⁹⁰ attempted to address this issue by building the Temperature and Acoustic Fluctuation Generator (TAGF). The TAGF consists of a tube fitted with a converging nozzle. Entropic waves are generated by injecting hot air into the tube. The injection process is driven by a loudspeaker generating acoustic waves, meaning acoustic and entropic waves are generated simultaneously and at the same frequency (from 20 to 100 Hz). Using this method, temperature fluctuations of up to $T' \approx 10$ K can be achieved, corresponding to entropic fluctuations of $s'/\bar{c}_p \approx 0.033$. The entropic waves are accelerated through the nozzle, meaning that the overall acoustic signal is a combination of direct and indirect noise. The fluctuating pressure and temperature are measured just upstream of the nozzle using microphones and a two-thermocouple sensor.

I. STATE OF THE ART

Tao et al.⁹⁰ derived an analytical method to extract the acoustic-acoustic and entropic-acoustic nozzle transfer functions from the experimental data. The acoustic reflection coefficient was recovered from the pressure measurements, and found to be in good agreement with the compact nozzle model of Marble & Candel⁶¹. Due to the poor signal to noise ratio and the low amount of entropic noise produced in the experiment, the entropic reflection coefficient of the nozzle could not be recovered.

I.6 Conclusion

Indirect noise arises from the acceleration of entropic, vortical or compositional perturbations. In gas turbines, indirect noise is produced at the nozzle guide vane and turbine rows. It is thought to contribute to the onset or sustenance of low-frequency thermoacoustic instabilities.

Several theoretical models have been produced for the generation of indirect noise at nozzles and turbine stages. In general, these are formulated as nozzle transfer functions, relating the amplitudes of acoustic, entropic and compositional waves impinging and generated at a subsonic or supersonic nozzle. The compact nozzle models produced by Marble & Candel⁶¹ and Magri et al.⁵⁸ have been extended to the more general case of a finite length nozzle^{24,60}.

Several experimental studies have been carried out in order to measure indirect noise in combustion systems. Broadly speaking, the results of these experiments have been difficult to interpret. One major difficulty is the separation of direct and indirect noise within the measured acoustic signal.

To circumvent these complications, simplified experiments were set up to generate and measure entropic and vortical noise in model conditions. These experiments have demonstrated the existence of entropic and vortical noise. As with combustion experiments however, the separation of direct and indirect noise remains an issue. In addition, acoustic reflections have been shown to have a determining effect on the measured signals. For these reasons, no experimental study has provided a quantitative measurement of indirect noise which could be directly compared to theoretical models. As a result, the analytical models for entropic and vortical noise have not been validated. Finally, the compositional noise mechanism has yet to be demonstrated experimentally.

For both entropic and compositional noise, there is a need for unambiguous experimental measurements to confirm or refute theoretical predictions. These are the main objectives of this thesis.

In this work, the difficulties associated to measuring indirect noise are overcome by carrying out careful experiments on a specially designed modular rig – the Cambridge Wave Generator. The dimensions, boundary conditions and type of waves generated inside the rig can be modified from one test to the next. In one set of tests, air is injected at ambient temperatures to generate direct noise only. This is used as a baseline for further tests using heat addition (generating direct noise and entropic noise) and helium injection (generating direct, entropic and compositional noise). The resulting measurements are compared to reveal the effect of these changes on the measured pressure signal. The data are then analysed using a one-dimensional theoretical framework, which is used to (1) eliminate the effect of repeated acoustic reflections inside the rig and (2) separate the contributions of direct and indirect acoustic sources.

II

WAVES GENERATED BY IMPOSED FLOW PERTURBATIONS

A flame generates direct noise, as well as vortical, entropic and compositional flow perturbations. Direct noise is conventionally defined as the acoustic waves produced by an unsteady heat flux. Here, we define direct noise more generally as the noise generated by a ‘wave source’, which produces unsteady perturbations in the flow’s mass, momentum, and energy fluxes, as well as mixture fraction. This enables us to examine the effect of heat addition, but also of gas injection, which is of particular interest for the experiments presented in this thesis, as well as a realistic model for the effect of cooling or secondary air in combustors.

In this section, we present a one-dimensional model for the acoustic, entropic and compositional waves generated by a compact wave source. Vortical waves are not considered.

II.1 Wave field

We consider the one-dimensional flow of a gas mixture in a duct. The mixture can be assumed to be a perfect gas, so that the heat capacity c_p changes only with the mixture composition. The gas is composed of N species, each with a mass fraction Y_i such that $\sum_{i=1}^N Y_i = 1$. The mixture is characterised by its pressure p , density ρ , temperature T , sensible enthalpy $h = \sum_{i=1}^N h_i Y_i$ and specific entropy $s = \sum_{i=1}^N s_i Y_i$. The flow is non-reacting and we assume that the mixture composition is uniquely described with a mixture fraction Z such that $\mathbf{Y} = \mathbf{Y}(Z)$. This is the case for a mixture of two species, which is of primary interest for this thesis.

Flow variables can be separated into their mean and fluctuating components (denoted with an over-bar and a prime respectively): $\beta(x, t) = \bar{\beta}(x) + \beta'(t)$. Furthermore, we assume linear

II. WAVES GENERATED BY IMPOSED FLOW PERTURBATIONS

fluctuations; their amplitude is small relative to the mean quantity (i.e. $\beta' \ll \bar{\beta}$).

In this scenario, flow perturbations can be decomposed as the combination of acoustic, entropic, and compositional waves⁵⁷. The forward- and backward-propagating acoustic waves propagate at the speed of sound relative to the flow speed ($\bar{c} + \bar{u}$ and $\bar{c} - \bar{u}$) respectively, while compositional and entropic waves are convected with the flow speed \bar{u} . The amplitudes of the forward- and backward-propagating acoustic waves π^+ and π^- are given by:

$$\pi^+ = \frac{1}{2} \left(\frac{p'}{\gamma \bar{p}} + \frac{u'}{\bar{c}} \right), \quad \pi^- = \frac{1}{2} \left(\frac{p'}{\gamma \bar{p}} - \frac{u'}{\bar{c}} \right). \quad (\text{II.1})$$

The amplitude of the compositional wave ξ is given by the mixture fraction fluctuation:

$$\xi = Z', \quad (\text{II.2})$$

and the entropic wave amplitude σ is given by:

$$\sigma = \frac{s'}{\bar{c}_p}. \quad (\text{II.3})$$

To express the entropic wave amplitude in terms of other flow variables, we start with Gibbs' relation for a multicomponent gas:

$$dh = T ds + \frac{dp}{\rho} + \sum_{i=1}^N \frac{\mu_i}{W_i} dY_i, \quad (\text{II.4})$$

Combining the above with the definition of the entropic wave gives us:

$$\sigma = \frac{T'}{T} + \frac{c'_p}{\bar{c}_p} + (\gamma - 1) \frac{p'}{\gamma \bar{p}} - \frac{1}{\bar{c}_p T} \sum_{i=1}^N \frac{\mu_i}{W_i} \frac{dY_i}{dZ} Z', \quad (\text{II.5})$$

where W_i is the molecular weight of each chemical species, and μ_i is the chemical potential defined as $\mu_i = W_i \partial h_i / \partial Y_i|_{p,T}$, and we have taken advantage of the fact that $Y'_i = (dY_i/dZ) Z'$. Combining (II.5) with the linearised ideal gas law ($p'/\bar{p} = \rho'/\bar{\rho} + R'/\bar{R} + T'/\bar{T}$) and noting that $R'/\bar{R} = c'_p/\bar{c}_p$ (since γ is constant) yields a new definition of the entropic wave:

$$\sigma = \frac{p'}{\gamma \bar{p}} - \frac{\rho'}{\bar{\rho}} - \Psi Z', \quad (\text{II.6})$$

where Ψ is the chemical potential function as defined in (I.24). This reveals that the entropic

II. WAVES GENERATED BY IMPOSED FLOW PERTURBATIONS

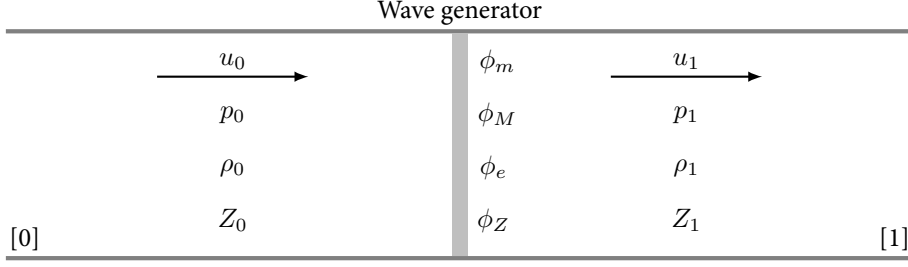


Figure II.1: Flow variables upstream [0] and downstream [1] of a wave source with changes in mass (ϕ_m), momentum (ϕ_M), energy (ϕ_e) and composition (ϕ_Z).

wave amplitude depends on the local compositional fluctuation, since the specific entropy is tied to the local gas composition.

II.2 Jump conditions at a compact wave source

We consider the case of a compact wave source, meaning that its length is negligible compared to the wavelength of the disturbances of interest. This is equivalent to assuming that we are dealing with the limit of zero-frequency waves. In this scenario, the wave source is essentially a discontinuity; there is no delay or distortion between the inlet and outlet.

In order to capture the effect of the wave source on the flow variables, jump conditions may be applied, whereby mass, momentum and energy fluxes (ϕ_m , ϕ_M and ϕ_e respectively), as well as a change in mixture fraction (ϕ_Z) are added to the flow at a discontinuity. This situation is depicted in figure II.1.

To satisfy the conservation of mass, momentum, energy and species, the flow variables directly upstream and downstream of the wave source must satisfy:

$$\left. \begin{aligned} [\rho u]_0^1 &= \phi_m, \\ [p + \rho u^2]_0^1 &= \phi_M, \\ [\rho u h]_0^1 &= \phi_e, \\ [Z]_0^1 &= \phi_Z, \end{aligned} \right\} \quad (\text{II.7})$$

where the notation $[\beta]_0^1$ denotes the difference between the flow variables immediately upstream [0] and downstream [1] of the discontinuity, such that $[\beta]_0^1 = \beta_1 - \beta_0$.

We assume that the added fluxes are small, and that their mean component is negligible

II. WAVES GENERATED BY IMPOSED FLOW PERTURBATIONS

($\bar{\phi} = 0$, $\phi = \phi'$), so that mean flow properties are conserved across the discontinuity. The flow perturbations on either side of the discontinuity can be related to the added fluxes ϕ'_m , ϕ'_M , ϕ'_e and ϕ'_Z :

$$\left. \begin{aligned} [\rho'\bar{u} + \bar{\rho}u']_0^1 &= \phi'_m, \\ [p' + \rho'\bar{u}^2 + 2\bar{\rho}\bar{u}u']_0^1 &= \phi'_M, \\ [\bar{c}_p\bar{T}(\rho'\bar{u} + \bar{\rho}u') + \bar{\rho}\bar{u}(\bar{c}_pT' + c'_p\bar{T} + \bar{u}u')]_0^1 &= \phi'_e, \\ [Z']_0^1 &= \phi'_Z. \end{aligned} \right\} \quad (\text{II.8})$$

Normalising (II.8) gives:

$$\left. \begin{aligned} \left[\left(\frac{\rho'}{\bar{\rho}} \right) + \frac{1}{\bar{M}} \left(\frac{u'}{\bar{c}} \right) \right]_0^1 &= \varphi'_m, \\ \left[\frac{1}{\bar{M}^2} \left(\frac{p'}{\gamma\bar{p}} \right) + \left(\frac{\rho'}{\bar{\rho}} \right) + \frac{2}{\bar{M}} \left(\frac{u'}{\bar{c}} \right) \right]_0^1 &= \varphi'_M, \\ \left[\gamma \left(\frac{p'}{\gamma\bar{p}} \right) + \left(\frac{1}{\bar{M}} + (\gamma - 1)\bar{M} \right) \left(\frac{u'}{\bar{c}} \right) \right]_0^1 &= \varphi'_e, \\ [Z']_0^1 &= \varphi'_Z, \end{aligned} \right\} \quad (\text{II.9})$$

where φ'_m , φ'_M , φ'_e and φ'_Z are the normalised changes in mass, momentum, energy, and mixture fraction:

$$\varphi'_m = \frac{\phi'_m}{\bar{\rho}\bar{u}}, \quad \varphi'_M = \frac{\phi'_M}{\bar{\rho}\bar{u}^2}, \quad \varphi'_e = \frac{\phi'_e}{\bar{\rho}\bar{u}\bar{c}_p\bar{T}}, \quad \varphi'_Z = \phi'_Z. \quad (\text{II.10})$$

The flow variables upstream and downstream of the discontinuity can be decomposed into a combination of forward- and backward-propagating acoustic waves (π^+ and π^-), an entropic wave σ , and a compositional wave ξ as shown in figure II.2. Decomposing (II.9) in terms of wave amplitudes gives us a jump condition for the waves just upstream and downstream of

II. WAVES GENERATED BY IMPOSED FLOW PERTURBATIONS

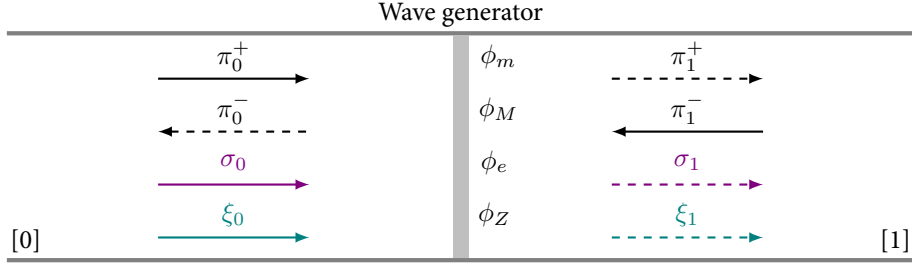


Figure II.2: Forward and backward acoustic (π^+ , π^-), entropic σ and compositional waves ξ upstream [0] and downstream [1] of a wave source .

the wave source:

$$\left. \begin{aligned} \left[\left(1 + \frac{1}{\bar{M}}\right) \pi^+ + \left(1 - \frac{1}{\bar{M}}\right) \pi^- - \sigma - \Psi \xi \right]_0^1 &= \varphi'_m \\ \left[\left(1 + \frac{1}{\bar{M}}\right)^2 \pi^+ + \left(1 - \frac{1}{\bar{M}}\right)^2 \pi^- - \sigma - \Psi \xi \right]_0^1 &= \varphi'_M \\ \left[\left((\gamma - 1) \bar{M} + \gamma + \frac{1}{\bar{M}} \right) \pi^+ + \left(-(\gamma - 1) \bar{M} + \gamma - \frac{1}{\bar{M}} \right) \pi^- \right]_0^1 &= \varphi'_e \\ [\xi]_0^1 &= \varphi'_Z, \end{aligned} \right\} \quad (\text{II.11})$$

II.3 Waves generated at a compact source

If the flow is subsonic, the ingoing waves (propagating towards the wave source) are π_0^+ , π_1^- , σ_0 and ξ_0 and the outgoing waves are π_1^+ , π_0^- , σ_1 and ξ_1 . Ingoing waves can be imposed, while outgoing waves are transmitted or generated at the wave source. Equation (II.11) may be pivoted and inverted to obtain the outgoing waves:

$$\begin{bmatrix} \pi_1^+ \\ \pi_0^- \\ \sigma_1 \\ \xi_1 \end{bmatrix} = \begin{bmatrix} \pi_0^+ \\ \pi_1^- \\ \sigma_0 \\ \xi_0 \end{bmatrix} + \begin{bmatrix} \frac{1}{2} \frac{(\gamma - 1) \bar{M}^3 - \bar{M}^2}{\bar{M} + 1} & \frac{1}{2} \frac{(1 - \gamma) \bar{M}^3 + \bar{M}^2}{\bar{M} + 1} & \frac{1}{2} \frac{\bar{M}}{1 + \bar{M}} & 0 \\ \frac{1}{2} \frac{(1 - \gamma) \bar{M}^3 - \bar{M}^2}{\bar{M} - 1} & \frac{1}{2} \frac{(\gamma - 1) \bar{M}^3 + \bar{M}^2}{\bar{M} - 1} & \frac{1}{2} \frac{\bar{M}}{1 - \bar{M}} & 0 \\ (\gamma - 1) \bar{M}^2 - 1 & (1 - \gamma) \bar{M}^2 & 1 & -\Psi \\ 0 & 0 & 0 & 1 \end{bmatrix} \begin{bmatrix} \varphi'_m \\ \varphi'_M \\ \varphi'_e \\ \varphi'_Z \end{bmatrix} \quad (\text{II.12})$$

II. WAVES GENERATED BY IMPOSED FLOW PERTURBATIONS

Equation (II.12) enables the amplitude of acoustic, entropic and compositional waves generated at the jump location to be computed directly based on the added mass, momentum, energy and compositional fluxes ϕ'_m , ϕ'_M , ϕ'_e and ϕ'_Z .

If there are no added fluxes ($\phi'_m = \phi'_M = \phi'_e = \phi'_Z = 0$), then we recover the trivial case of flow in a one-dimensional duct, and waves simply propagate across the wave source with no change in their amplitude.

In the scenario where there are no incoming waves ($\pi_0^+ = \pi_1^- = \sigma_0 = \xi_0 = 0$), the wave source produces forward- and backward-propagating acoustic waves $\pi_d^+ = \pi_1^+$ and $\pi_d^- = \pi_0^-$ (direct noise), as well as forward-propagating entropic and compositional waves $\sigma = \sigma_1$ and $\xi = \xi_1$.

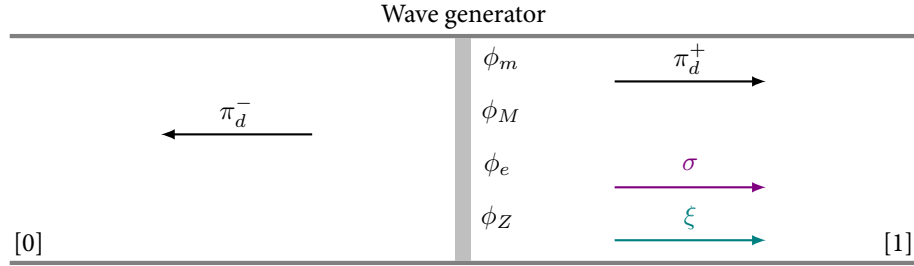


Figure II.3: Forward and backward acoustic (π^+ , π^-), entropic σ and compositional waves ξ generated by a wave source.

An overall measure of the sound generated at the discontinuity is the acoustic pressure p'_d , which is the pressure fluctuation corresponding to the passage of the direct acoustic waves π_d^+ and π_d^- :

$$\frac{p'_d}{\gamma \bar{p}} = \pi_d^+ + \pi_d^- = \frac{\gamma \bar{M}^3}{1 - \bar{M}^2} (\phi'_m - \phi'_M) + \frac{\bar{M}}{1 - \bar{M}^2} \phi'_e, \quad (\text{II.13})$$

which reveals that the generation of direct noise can be driven by an energy perturbation ϕ'_e , but also by a mismatch in the normalised mass and momentum perturbations (if $\phi'_m \neq \phi'_M$). The energy mechanism is dominant at low Mach numbers ($\bar{M} \ll 1$). If the higher order terms \bar{M}^2 and \bar{M}^3 are neglected, then the forward and backward waves are related such that $\pi_d^+ / \pi_d^- = (1 - \bar{M}) / (1 + \bar{M})$. The acoustic pressure fluctuation can then be expressed simply as:

$$p'_d = \frac{\gamma - 1}{\bar{c}} \phi'_e, \quad (\text{II.14})$$

which shows that the generated acoustic pressure fluctuation is directly proportional to the energy flux perturbation ϕ'_e . Notably, p'_d is completely independent of the pressure and Mach

II. WAVES GENERATED BY IMPOSED FLOW PERTURBATIONS

number. This suggests that even if there is no flow ($\bar{M} = 0$), an energy perturbation still generates acoustic waves in the duct.

The entropic wave σ generated at the discontinuity can be expressed as:

$$\sigma = (\varphi'_e - \varphi'_m) + (\gamma - 1)\bar{M}^2(\varphi'_m - \varphi'_M) - \Psi\varphi'_Z, \quad (\text{II.15})$$

which reveals that the production of an entropic wave is driven by three mechanisms. First, entropy is generated if there is a mismatch between the energy and mass perturbations (if $\varphi'_e \neq \varphi'_m$). This is physically intuitive: if energy is added with no mass to carry it, the local specific entropy increases. Second, if a mass perturbation φ'_m is imposed without a matching momentum perturbation φ'_M , entropy is generated. Third, changes in the flow composition φ'_Z can modify the entropy: this is because the gases composing the mixture may have different entropies.

Finally, the generated compositional wave is simply:

$$\xi = \varphi'_Z. \quad (\text{II.16})$$

II.4 Special cases

The general wave source considered in §II.1-II.3 can be simplified to recover three special cases: heat addition, air injection and helium injection. These special cases correspond to wave generation methods employed in previous wave generators (see §I.5), as well as in the Cambridge Wave Generator described in §VI.

II.4.1 Unsteady heat source

In the Entropy Wave Generator developed at the DLR, entropic waves were induced using electric heaters immersed in the flow⁴. The heaters can be modelled as an unsteady heat source. This also corresponds to the ‘cold flame’ with no mean heat release considered by Cumpsty¹⁸ and Leyko et al.⁵¹ in their theoretical predictions of direct and indirect noise.

Unsteady heat release can be modelled as an added energy flux $\phi'_e = Q'$. In practice, heaters immersed in the flow can be expected to lead to a loss of momentum due to drag. If the heater is sufficiently small the effect of drag on the mean flow properties will be small. Here we simply assume that the mean component of drag is negligible. The fluctuating component of the drag

II. WAVES GENERATED BY IMPOSED FLOW PERTURBATIONS

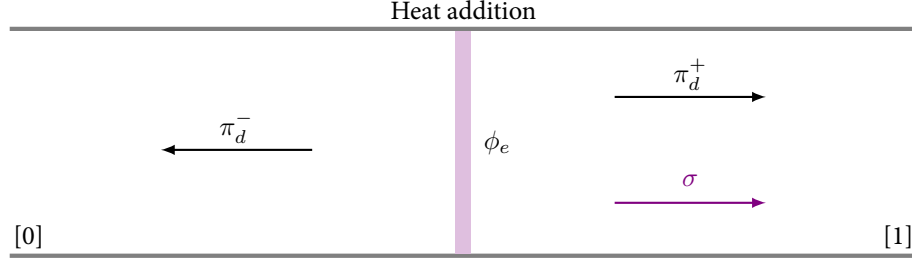


Figure II.4: Direct acoustic waves π_d^+ and π_d^- and entropic wave σ generated by a compact heat source.

could be considered as a fluctuating momentum flux term $\varphi_M \neq 0$. This term is assumed to be negligible here for simplicity. Therefore, the added mass, momentum and compositional fluxes can be considered to be zero, and we have:

$$\varphi_m = 0, \quad \varphi_M = 0, \quad \varphi_e = q', \quad \varphi_Z = 0, \quad (\text{II.17})$$

where $q' = Q'/\bar{\rho}\bar{u}\bar{c}_p\bar{T}$ is the normalised heat release rate. From (II.12), the waves generated by unsteady heat addition are:

$$\pi_d^+ = \frac{1}{2} \frac{\bar{M}}{1 + \bar{M}} q', \quad \pi_d^- = \frac{1}{2} \frac{\bar{M}}{1 - \bar{M}} q', \quad \sigma = q'. \quad (\text{II.18})$$

These results are identical to those obtained by Cumpsty¹⁸ and Leyko et al.⁵¹.

II.4.2 Unsteady air injection

In certain configurations of the high-pressure turbine stage developed by Knobloch et al.⁴⁷, air is injected into a tube at ambient temperatures. This case can be modelled by considering an unsteady injection of air with a mass flow rate \dot{m}'_i , as shown in figure II.5.

Since we are considering a one-dimensional flow, if the injection is carried out perpendicular to the flow then the added momentum flux can be considered to be zero, and we have:

$$\varphi_m = \frac{\dot{m}'_i}{\dot{m}}, \quad \varphi_M = 0, \quad \varphi_e = \frac{\dot{m}'_i}{\dot{m}}, \quad \varphi_Z = 0. \quad (\text{II.19})$$

From (II.12), an unsteady air injection generates direct noise, as well as an entropic wave. For low Mach flows ($\bar{M} \ll 1$), the direct noise is associated to energy addition, and negligible

II. WAVES GENERATED BY IMPOSED FLOW PERTURBATIONS

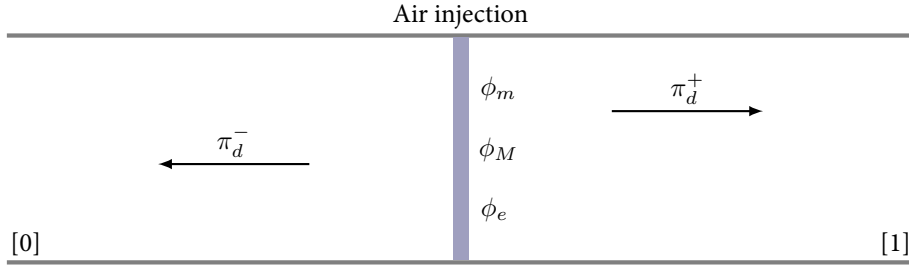


Figure II.5: Direct acoustic waves π_d^+ and π_d^- generated by a compact ambient temperature air injection.

entropy is generated:

$$\pi_d^+ = \frac{1}{2} \frac{\bar{M}}{1 + \bar{M}} \frac{\dot{m}'_i}{\bar{m}}, \quad \pi_d^- = \frac{1}{2} \frac{\bar{M}}{1 - \bar{M}} \frac{\dot{m}'_i}{\bar{m}}, \quad \sigma = 0. \quad (\text{II.20})$$

In the HAT rig⁴⁸ and turbine-stage model experiment⁷⁷, entropic waves are generated by injecting air at a temperature \bar{T}_i higher or lower than the mean flow temperature \bar{T} . This can be modelled as:

$$\varphi_m = \frac{\dot{m}'_i}{\bar{m}}, \quad \varphi_M = 0, \quad \varphi_e = \frac{\dot{m}'_i \bar{T}_i}{\bar{m} \bar{T}}, \quad \varphi_Z = 0. \quad (\text{II.21})$$

For low Mach flows, the injection of hot or cold air generates direct noise as well as an entropic wave:

$$\pi_d^+ = \frac{1}{2} \frac{\bar{M}}{1 + \bar{M}} \frac{\dot{m}'_i \bar{T}_i}{\bar{m} \bar{T}}, \quad \pi_d^- = \frac{1}{2} \frac{\bar{M}}{1 - \bar{M}} \frac{\dot{m}'_i \bar{T}_i}{\bar{m} \bar{T}}, \quad \sigma = \frac{\dot{m}'_i \bar{T}_i - \bar{T}}{\bar{m} \bar{T}}. \quad (\text{II.22})$$

The amplitude of the entropic wave is driven by the temperature difference $\bar{T}_i - \bar{T}$. If hot air is injected ($\bar{T}_i > \bar{T}$), more direct noise is generated than for the ambient air injection (the opposite is true for cold air).

II.4.3 Helium injection

In the Cambridge Wave Generator described in §VI, entropic and compositional waves can be induced in a flow by carrying out unsteady injection of helium (with a mass flow rate \dot{m}'_{He}) at ambient temperatures. Since we have only two species (helium and air), we can simply define the mixture fraction Z as the mass fraction of helium generated by the injection

II. WAVES GENERATED BY IMPOSED FLOW PERTURBATIONS

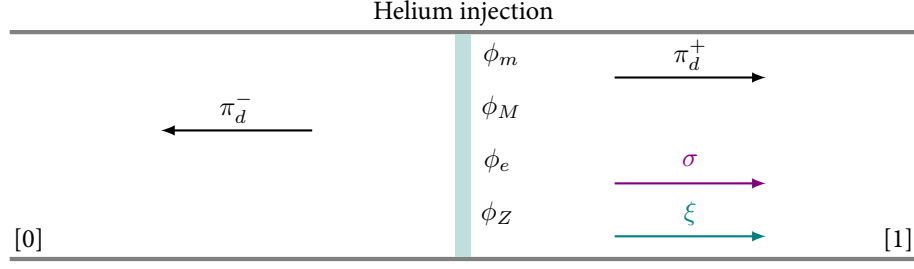


Figure II.6: Direct acoustic waves π_d^+ and π_d^- , entropic wave σ and compositional wave ξ generated by a helium injection.

Y_{He} :

$$Z = Y_{\text{He}} = \frac{\dot{m}_{\text{He}}}{\dot{m}}, \quad (\text{II.23})$$

and the mass fraction of air is $Y_{\text{air}} = 1 - Y_{\text{He}} = 1 - Z$. The unsteady helium injection can be modelled as:

$$\varphi_m = \frac{\dot{m}'_{\text{He}}}{\dot{m}}, \quad \varphi_M = 0, \quad \varphi_e = \frac{\dot{m}'_{\text{He}} \bar{c}_{p,\text{He}}}{\dot{m} \bar{c}_p}, \quad \varphi_Z = \frac{\dot{m}'_{\text{He}}}{\dot{m}}, \quad (\text{II.24})$$

where $\bar{c}_{p,\text{He}}$ is the specific heat capacity of helium. The resulting acoustic waves are:

$$\pi_d^+ = \frac{1}{2} \frac{\bar{M}}{1 + \bar{M}} \frac{\dot{m}'_{\text{He}} \bar{c}_{p,\text{He}}}{\dot{m} \bar{c}_p}, \quad \pi_d^- = \frac{1}{2} \frac{\bar{M}}{1 - \bar{M}} \frac{\dot{m}'_{\text{He}} \bar{c}_{p,\text{He}}}{\dot{m} \bar{c}_p}, \quad (\text{II.25})$$

and the entropic and compositional waves are:

$$\sigma = \left(\frac{\bar{c}_{p,\text{He}} - \bar{c}_p}{\bar{c}_p} - \Psi \right) \frac{\dot{m}'_{\text{He}}}{\dot{m}}, \quad \xi = \frac{\dot{m}'_{\text{He}}}{\dot{m}}. \quad (\text{II.26})$$

To recover a more familiar expression for the entropic wave amplitude, we start by expressing the chemical potential function Ψ in terms of species' heat capacities and specific entropies:

$$\Psi = \frac{1}{\bar{c}_p \bar{T}} \sum_{i=1}^N \bar{g}_i \frac{dY_i}{dZ} = \frac{1}{\bar{c}_p} \sum_{i=1}^N (\bar{c}_{p_i} - \bar{s}_i) \frac{dY_i}{dZ}, \quad (\text{II.27})$$

where $g_i = h_i - T s_i$ is the specific Gibbs energy of a species. Combining (II.26) and (II.27), we can express the entropic and compositional wave amplitudes as:

$$\sigma = \left(\frac{\bar{s}_{\text{air}} - \bar{s}_{\text{He}}}{\bar{c}_p} \right) Y'_{\text{He}}, \quad \xi = Y'_{\text{He}}, \quad (\text{II.28})$$

II. WAVES GENERATED BY IMPOSED FLOW PERTURBATIONS

which reveals that the entropic wave is simply driven by the difference in the entropies of pure helium and pure air, multiplied by the proportion of helium in the flow.

It should be noted that the acoustic model described here does not take into account all noise sources associated to the injection of helium in a duct. Indeed, while the effects of mass, momentum and energy addition are taken into account, other aspects of the injection (formation of a jet, vorticity generation) are not considered since the model is one dimensional. Furthermore, depending on the operating conditions, the velocity and pressure of the helium may change as it is injected into the system and adjusts to the mean flow in the duct. This may lead to a change in the chemical potential function Ψ and Mach number, which drives the generation of entropic and compositional noise (see §III). As such, the noise generated at the injection location is likely to be a sum of several types of noise not accounted for here.

III

TRANSFER FUNCTIONS OF COMPACT NOZZLES

The entropic and compositional noise generated by the corresponding convected waves is typically computed using nozzle transfer functions. These transfer functions relate impinging acoustic, entropic and compositional waves to outgoing ones. The transfer functions of subsonic compact isentropic nozzles originally obtained by Marble & Candel⁶¹, Magri et al.⁵⁸ and Ihme⁴⁴ are rederived here for reference. The derivation for the supersonic case is shown in Appendix A. The assumption of isentropicity is then relaxed to consider nozzles with losses (including the limit case of a jet). Much of this work is based on results obtained by Francesca de Domenico¹⁹, who derived acoustic and entropic transfer functions for subsonic anisentropic nozzles based on an orifice plate model by Durrieu et al.²⁶. Here, these results are recast in a non-dimensional form comparable to other models in the literature, and extended to include the effects of impinging compositional fluctuations. The theoretical transfer functions of isentropic and anisentropic nozzles are then compared for a range of operating conditions.

III.1 Isentropic nozzle

The response of a compact nozzle to compositional perturbations can be derived with the method presented by Marble & Candel⁶¹ and Magri et al.⁵⁸. The assumptions are identical to those in §II, except that the flow is now quasi-one dimensional to allow for a change in cross sectional area.

Here, the compactness assumption means that the length of the nozzle is negligible compared to the disturbance wavelengths. Acoustic, entropic and compositional are assumed to propagate quasi-steadily through the nozzle. The nozzle is essentially a discontinuity; there is no delay or distortion between the inlet and outlet.

III. TRANSFER FUNCTIONS OF COMPACT NOZZLES

The flow can be described in terms of the fluctuating pressure p' , velocity u' , density ρ' and mixture fraction Z' upstream and downstream of the nozzle, denoted with the subscripts 1 and 2 respectively. This is shown in figure III.1.

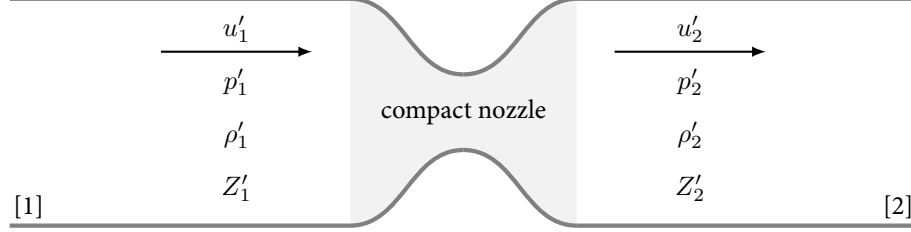


Figure III.1: Flow fluctuations upstream [1] and downstream [2] of a compact nozzle.

III.1.1 Jump conditions

Fluctuations in mass flow rate (\dot{m}), total temperature (T_t), entropy (s) and species (Z) are conserved across the nozzle. This can be formulated as a set of jump conditions, relating the flow variables upstream and downstream of the nozzle discontinuity⁵⁸:

$$\left. \begin{aligned} [\rho u A]_1^2 &= 0, \\ \left[T \left(1 + \frac{\gamma - 1}{2} M^2 \right) \right]_1^2 &= 0, \\ [s]_1^2 &= 0, \\ [Z]_1^2 &= 0, \end{aligned} \right\} \quad (\text{III.1})$$

which can be linearised and normalised to obtain:

$$\left. \begin{aligned} \left[\frac{\dot{m}'}{\dot{m}} \right]_1^2 &= \left[\frac{1}{M} \frac{u'}{\bar{c}} + \frac{\rho'}{\bar{\rho}} \right]_1^2 = 0, \\ \left[\frac{T_t'}{T_t} \right]_1^2 &= \left[\frac{1}{1 + \frac{\gamma - 1}{2} M^2} \left(\frac{T'}{\bar{T}} + (\gamma - 1) M \frac{u'}{\bar{c}} + \frac{1}{\bar{c}_p} \frac{d\bar{c}_p}{dZ} Z' \right) \right]_1^2 = 0, \\ \left[\frac{s'}{\bar{c}_p} \right]_1^2 &= \left[\frac{T'}{\bar{T}} - (\gamma - 1) \frac{p'}{\gamma \bar{p}} + \left(\frac{1}{\bar{c}_p} \frac{d\bar{c}_p}{dZ} - \Psi \right) Z' \right]_1^2 = 0, \\ [Z']_1^2 &= [Z']_1^2 = 0. \end{aligned} \right\} \quad (\text{III.2})$$

Flow perturbations in (III.2) can be decomposed as a combination of acoustic, entropic and compositional waves defined in §II.1. This enables us to derive jump conditions for the wave

III. TRANSFER FUNCTIONS OF COMPACT NOZZLES

amplitudes on either side of the nozzle:

$$\left. \begin{aligned} \left[\left(1 + \frac{1}{\bar{M}}\right) \pi^+ + \left(1 - \frac{1}{\bar{M}}\right) \pi^- - \sigma - \Psi \xi \right]_1^2 &= 0, \\ \left[\frac{\gamma - 1}{1 + \frac{\gamma - 1}{2} \bar{M}^2} \left((1 + \bar{M}) \pi^+ + (1 - \bar{M}) \pi^- + \frac{\sigma}{\gamma - 1} + \frac{\Psi \xi}{\gamma - 1} \right) \right]_1^2 &= 0, \\ [\sigma]_1^2 &= 0, \\ [\xi]_1^2 &= 0. \end{aligned} \right\} \quad (\text{III.3})$$

Equation (III.3) can be recast in matrix form as:

$$[\mathbf{X} \mathbf{w}]_1^2 = 0, \quad (\text{III.4})$$

where \mathbf{w} is the vector of wave amplitudes:

$$\mathbf{w} = \begin{bmatrix} \pi^+ \\ \pi^- \\ \sigma \\ \xi \end{bmatrix}, \quad (\text{III.5})$$

and \mathbf{X} is a transfer matrix:

$$\mathbf{X} = \begin{bmatrix} 1 + \frac{1}{\bar{M}} & 1 - \frac{1}{\bar{M}} & -1 & -\Psi \\ \frac{(\gamma - 1)(1 + \bar{M})}{1 + \frac{\gamma - 1}{2} \bar{M}^2} & \frac{(\gamma - 1)(1 - \bar{M})}{1 + \frac{\gamma - 1}{2} \bar{M}^2} & \frac{1}{1 + \frac{\gamma - 1}{2} \bar{M}^2} & \frac{\Psi}{1 + \frac{\gamma - 1}{2} \bar{M}^2} \\ 0 & 0 & 1 & 0 \\ 0 & 0 & 0 & 1 \end{bmatrix}. \quad (\text{III.6})$$

III.1.2 Transfer functions

The jump condition in (III.4) relates the acoustic, entropic and compositional waves immediately upstream and downstream of the nozzle, shown in figure III.2.

To solve the system, it is practical to recast the problem in terms of known and unknown

III. TRANSFER FUNCTIONS OF COMPACT NOZZLES

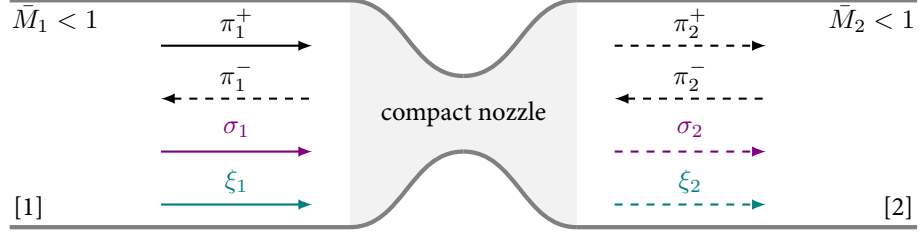


Figure III.2: Forward and backward acoustic (π^+ , π^-), entropic (σ) and compositional waves (ξ) upstream [1] and downstream [2] of a subsonic compact nozzle. Incoming waves (solid arrows), outgoing waves (dashed arrows).

waves. Since we are interested in the response of the nozzle to incoming perturbations, we can recast (III.4) in terms of incoming waves (subscript i) and outgoing waves (subscript o) to solve for the latter:

$$\mathbf{X}_i \mathbf{w}_i = \mathbf{X}_o \mathbf{w}_o, \quad (\text{III.7})$$

where \mathbf{w}_i and \mathbf{w}_o are the ingoing and outgoing waves for a subsonic nozzle:

$$\mathbf{w}_i = \begin{bmatrix} \pi_1^+ \\ \pi_2^- \\ \sigma_1 \\ \xi_1 \end{bmatrix}, \quad \mathbf{w}_o = \begin{bmatrix} \pi_2^+ \\ \pi_1^- \\ \sigma_2 \\ \xi_2 \end{bmatrix}, \quad (\text{III.8})$$

and \mathbf{X}_i and \mathbf{X}_o are permutations of the upstream and downstream transfer matrices \mathbf{X}_1 and \mathbf{X}_2 described in Appendix A. Equation (III.4) can be inverted to yield the outgoing waves \mathbf{w}_o generated by acoustic and entropic waves propagating towards the compact nozzle:

$$\mathbf{w}_o = \mathbf{X}_o^{-1} \mathbf{X}_i \mathbf{w}_i = \mathbf{T} \mathbf{w}_i. \quad (\text{III.9})$$

Here, \mathbf{T} is the matrix of subsonic nozzle transfer functions, which relate incoming waves to

III. TRANSFER FUNCTIONS OF COMPACT NOZZLES

outgoing ones:

$$\mathbf{T} = \begin{bmatrix} \frac{\pi_2^+}{\pi_1^+} & \frac{\pi_2^+}{\pi_2^-} & \frac{\pi_2^+}{\sigma_1} & \frac{\pi_2^+}{\xi_1} \\ \frac{\pi_1^-}{\pi_1^+} & \frac{\pi_1^-}{\pi_2^-} & \frac{\pi_1^-}{\sigma_1} & \frac{\pi_1^-}{\xi_1} \\ \frac{\sigma_2}{\pi_1^+} & \frac{\sigma_2}{\pi_2^-} & \frac{\sigma_2}{\sigma_1} & \frac{\sigma_2}{\xi_1} \\ \frac{\xi_2}{\pi_1^+} & \frac{\xi_2}{\pi_2^-} & \frac{\xi_2}{\sigma_1} & \frac{\xi_2}{\xi_1} \end{bmatrix}. \quad (\text{III.10})$$

The coefficients of the matrix are reflection and transmission coefficients. For example, π_2^+/π_1^+ is the acoustic-acoustic transmission coefficient of the nozzle. It enables one to compute the amplitude of the acoustic wave π_2^+ generated downstream of the nozzle due to an impinging upstream wave π_1^+ :

$$\frac{\pi_2^+}{\pi_1^+} = \left(\frac{2\bar{M}_2}{1 + \bar{M}_2} \right) \left(\frac{1 + \bar{M}_1}{\bar{M}_1 + \bar{M}_2} \right) \frac{1 + \frac{\gamma-1}{2}\bar{M}_2^2}{1 + \frac{\gamma-1}{2}\bar{M}_1\bar{M}_2}. \quad (\text{III.11})$$

Similarly, π_1^-/π_1^+ is the acoustic-acoustic reflection coefficient which gives the reflected upstream wave π_1^- :

$$\frac{\pi_1^-}{\pi_1^+} = \left(\frac{\bar{M}_2 - \bar{M}_1}{1 - \bar{M}_1} \right) \left(\frac{1 + \bar{M}_1}{\bar{M}_1 + \bar{M}_2} \right) \frac{1 - \frac{\gamma-1}{2}\bar{M}_1\bar{M}_2}{1 + \frac{\gamma-1}{2}\bar{M}_1\bar{M}_2}. \quad (\text{III.12})$$

The matrix also contains the acoustic responses to an incoming entropic wave σ_1 . These transfer functions π_2^+/σ_1 and π_1^-/σ_1 describe the entropic-acoustic interaction responsible for reflected and transmitted entropic noise. The entropic-acoustic transmission coefficient is:

$$\frac{\pi_2^+}{\sigma_1} = \frac{1}{2} \left(\frac{\bar{M}_2 - \bar{M}_1}{1 + \bar{M}_2} \right) \frac{\bar{M}_2}{1 + \frac{\gamma-1}{2}\bar{M}_1\bar{M}_2}, \quad (\text{III.13})$$

and the entropic-acoustic reflection coefficient is:

$$\frac{\pi_1^-}{\sigma_1} = -\frac{1}{2} \left(\frac{\bar{M}_2 - \bar{M}_1}{1 - \bar{M}_1} \right) \frac{\bar{M}_1}{1 + \frac{\gamma-1}{2}\bar{M}_1\bar{M}_2}. \quad (\text{III.14})$$

These coefficients show that the generation of entropic noise is driven by the change in Mach number from \bar{M}_1 to \bar{M}_2 . In theory, if a compact nozzle has the same Mach number at

III. TRANSFER FUNCTIONS OF COMPACT NOZZLES

the inlet and outlet ($\bar{M}_1 = \bar{M}_2$), then no entropic noise is generated regardless of the changes in Mach number within the nozzle.

Finally, we have $\sigma_2/\pi_1^+ = \sigma_2/\pi_2^- = 0$ meaning that incoming acoustic waves do not generate entropic fluctuations downstream of the nozzle.

The expressions for the acoustic-acoustic, entropic-acoustic and acoustic-entropic transfer functions are the same as those derived by Marble & Candel⁶¹. The elements new to the analysis by Magri et al.⁵⁸ are those describing the effect of an impinging compositional wave on the acoustic waves upstream and downstream of the nozzle. The compositional-acoustic transmission coefficient is:

$$\frac{\pi_2^+}{\xi_1} = \frac{(\Psi_1 - \Psi_2) (\bar{M}_2 - (\gamma - 1) \bar{M}_2^2)}{(1 + \bar{M}_2) (\gamma - 1) (\bar{M}_1 + \bar{M}_2)} - \frac{\bar{M}_2 (\bar{M}_1 - \bar{M}_2) (\Psi_1 (1 + \frac{1}{2} \bar{M}_2) - \Psi_2 (1 - \frac{1}{2} \bar{M}_1))}{(1 + \bar{M}_2) (\bar{M}_1 + \bar{M}_2) (1 + \frac{\gamma-1}{2} \bar{M}_1 \bar{M}_2)}. \quad (\text{III.15})$$

and the compositional-acoustic reflection coefficient is:

$$\frac{\pi_1^-}{\xi_1} = \frac{(\Psi_1 - \Psi_2) (\bar{M}_1 + (\gamma - 1) \bar{M}_1^2)}{(\bar{M}_1 - 1) (\gamma - 1) (\bar{M}_1 + \bar{M}_2)} - \frac{\bar{M}_1 (\bar{M}_1 - \bar{M}_2) (\Psi_1 (1 + \frac{1}{2} \bar{M}_2) - \Psi_2 (1 - \frac{1}{2} \bar{M}_1))}{(\bar{M}_1 - 1) (\bar{M}_1 + \bar{M}_2) (1 + \frac{\gamma-1}{2} \bar{M}_1 \bar{M}_2)}. \quad (\text{III.16})$$

These coefficients show that the generation of compositional noise is driven by the change in the chemical potential function from $\Psi_1 = f(\bar{T}_1, \bar{p}_1)$ to $\Psi_2 = f(\bar{T}_2, \bar{p}_2)$ as the compositional wave is convected through the nozzle, as well as the change in Mach number from \bar{M}_1 to \bar{M}_2 .

There are no acoustic-compositional and entropic-compositional interactions since compositional waves cannot be generated at the nozzle: $\xi_2/\pi_1^+ = \xi_2/\pi_2^- = \xi_2/\sigma_1 = 0$.

The nozzle transfer functions can be thought of as the set of possible mode transfer mechanisms. The non-zero mode transfer mechanisms of a subsonic isentropic nozzle are shown diagrammatically in figure III.3.

III. TRANSFER FUNCTIONS OF COMPACT NOZZLES

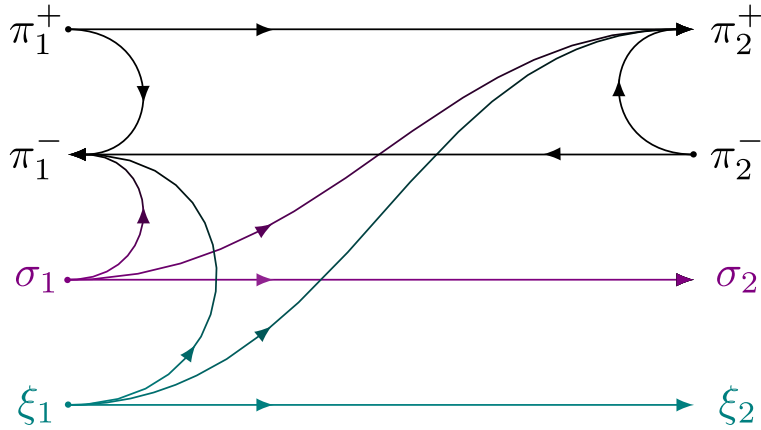


Figure III.3: Non-zero mode transfer mechanisms between acoustic (π), entropic (σ) and compositional waves (ξ) at the inlet and outlet of a subsonic isentropic compact nozzle.

III.2 Anisentropic nozzle

One of the assumptions usually made for the derivation of nozzle transfer functions is that the flow inside the nozzle is isentropic, i.e. reversible and adiabatic (apart from an eventual shock, see §I.2-I.3). In real systems, entropy is not necessarily conserved across the nozzle.

For example, diabatic systems where heat exchange occurs are anisentropic (i.e. not isentropic). In a gas turbine, significant heat is transferred from the flow to the cooled nozzle and turbine blades. Similarly, irreversible processes such as wall friction or flow separation will lead to an anisentropic flow. While nozzle guide vanes are designed to avoid large irreversibilities, some losses can be expected to occur. This source of anisentropy can be modelled as a drop in the stagnation pressure.

The acoustic reflection and transmission of anisentropic flow elements were considered by Durrieu et al.²⁶ (orifice plate in a duct), as well as Howe³⁹ and Bechert⁵ (converging nozzle terminating a duct). Nevertheless, the entropic-acoustic and compositional-acoustic transfer functions of an anisentropic nozzle have not yet been examined.

In this section, the acoustic, entropic and compositional transfer functions of a compact adiabatic anisentropic nozzle are derived. These are obtained by introducing a loss parameter Λ to capture the full range of nozzle behaviours, ranging between the limit cases of a fully isentropic expansion ($\Lambda=0$) to a fully dissipative jet mixing region ($\Lambda=1$). The formulation of this parametric approach for the acoustic and entropic transfer functions was carried out by Francesca De Domenico¹⁹. Here, her approach is extended to include the effect of impinging

compositional fluctuations.

III.2.1 Anisentropic subsonic nozzle

The anisentropic nozzle model considered here is shown in figure III.4. It is defined by the cross sections at the inlet A_1 , throat A_t and outlet A_2 . Since we are considering a compact nozzle (i.e. low frequency perturbations), the nozzle shape between these areas has no effect on the model. It should be noted that the throat area A_t refers to the area at which the flow is most narrow, which does not necessarily correspond to the smallest geometrical area of the nozzle A_g . Indeed, if flow separation occurs at the nozzle throat, the narrowest flow area is at the vena contracta some distance downstream of the throat. These two areas are related by a vena contracta factor Γ such that $A_t = \Gamma A_g$.

Generally speaking, the accelerating flow upstream of the throat area can be considered to be isentropic, regardless of the shape of the convergent section^{26,22}.

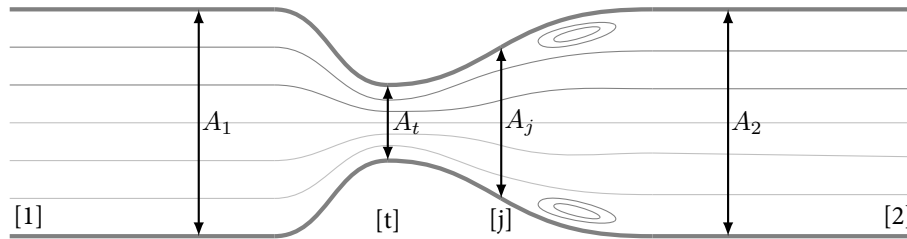


Figure III.4: Diagram of flow areas at the inlet (A_1), throat (A_t), jet mixing location (A_j) and outlet (A_2) of an anisentropic nozzle, with streamlines for illustration.

In the divergent section, we can consider that the flow is somewhere between isentropic and anisentropic depending on the nozzle and flow characteristics. This can be modelled by defining an effective jet mixing area A_j , assuming that the flow is isentropic from A_t to A_j , and that an anisentropic jet is formed thereafter (from A_j to A_2). Physically, the jet mixing area A_j can be thought of as the area at which flow separation occurs within the diverging nozzle. Nevertheless, A_j can be also be used conceptually to represent other types of anisentropic behaviours, since it enables us to model the full range between an isentropic divergent section ($A_j = A_2$), and a fully anisentropic divergent section ($A_j = A_t$). In that sense, A_j is an measure of the level of anisentropy within the divergent nozzle, rather than a physical area.

III. TRANSFER FUNCTIONS OF COMPACT NOZZLES

We can define an anisentropicity parameter Λ :

$$\Lambda = \frac{A_2 - A_j}{A_2 - A_t}, \quad (\text{III.17})$$

where $\Lambda = 0$ means that the nozzle is fully isentropic, $\Lambda = 1$ means that the divergent section is fully anisentropic, and $0 < \Lambda < 1$ describes a nozzle somewhere between these limit cases.

As such, anisentropic nozzles can be defined as a succession of two jumps. The location at which this jump transition occurs determines the type of nozzle being considered, as shown in figure III.5.

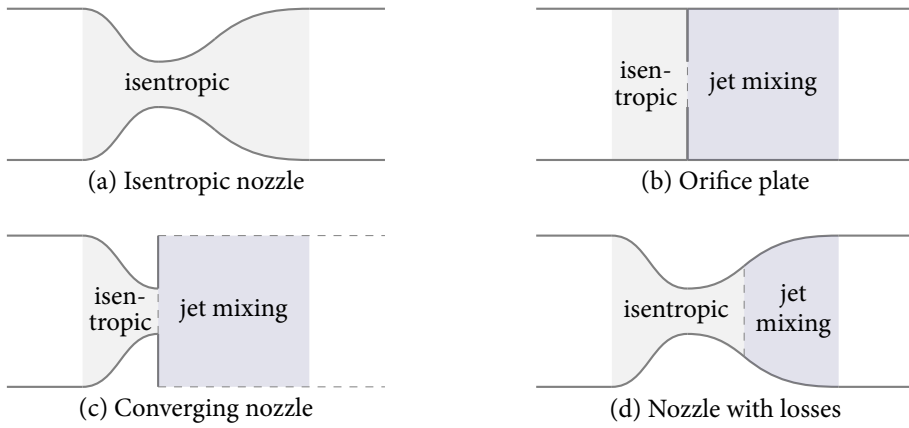


Figure III.5: Jump locations for (a) an isentropic nozzle with $\Lambda = 0$, (b) an orifice plate with $\Lambda = 1$ (c) a converging nozzle with $\Lambda = 1$ and $A_2 \rightarrow \infty$ and (d) a nozzle with partial losses with $0 < \Lambda < 1$.

The case of an isentropic nozzle considered by Marble & Candel⁶¹, Magri et al.⁵⁸ and Ihme⁴⁴ is recovered for $A_j = A_2$ (i.e. there is no jet mixing). For the orifice plate in a duct considered by Durrieu et al.²⁶, we can define $A_j = A_t$ since the jet is formed at the throat. A converging nozzle terminating a duct (as studied Howe³⁹ and Bechert⁵) can be modelled as $A_j = A_t$ with $A_2 \rightarrow \infty$. Finally, a nozzle with partial losses can be defined with an area A_j such that $A_t < A_j < A_2$.

In general, the effective jet mixing area A_j and the anisentropicity parameter Λ are not known a priori. They can be retrieved if the mean flow properties upstream and downstream of a given nozzle are known (e.g. if they are measured experimentally). In that case, the mean components of (III.1) and (III.19) can be solved numerically to extract the values of A_j and Λ corresponding to the known mean flow properties.

III.2.2 Jump conditions

The flow properties upstream and downstream of the nozzle can be related using jump conditions as in §III.1. For the isentropic section (from A_1 to A_j) the jump conditions are those describing mass, total temperature, entropy and species as in (III.1).

For the section of the nozzle in which a jet is formed (from A_j to A_2), instead of entropy conservation we can consider the change in momentum, which is increased by the axial force on the walls:

$$A_2 p_2 + A_2 \rho_2 u_2^2 = A_2 p_j + A_j \rho_j u_j^2, \quad (\text{III.18})$$

which results in the following jump conditions:

$$\left. \begin{aligned} [\rho u A]_j^2 &= 0, \\ \left[T \left(1 + \frac{\gamma - 1}{2} M^2 \right) \right]_j^2 &= 0, \\ [A(p + \rho u^2)]_j^2 &= (A_2 - A_j) p_j, \\ [Z]_j^2 &= 0. \end{aligned} \right\} \quad (\text{III.19})$$

The nozzle can be thought of as two successive jumps, as shown in figure III.6.

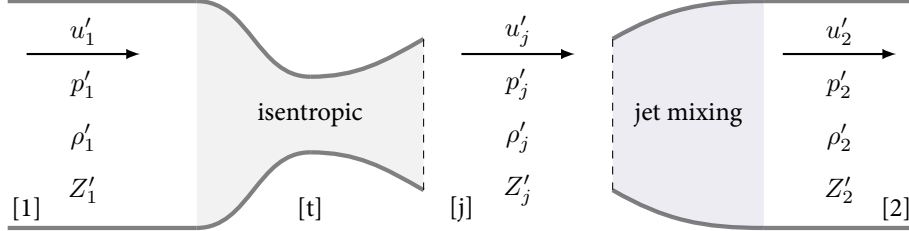


Figure III.6: Flow fluctuations upstream [1], at the jet mixing location [j] and downstream [2] of a compact anisentropic nozzle.

Linearising the momentum jump condition between the jet mixing transition location and the outlet in (III.20) gives:

$$\begin{aligned} \frac{A_2}{A_j} \frac{\bar{c}_j}{\bar{M}_j} \left(\frac{p'_j}{\gamma \bar{p}_j} \right) - \bar{M}_j \bar{c}_j \left(\frac{\rho'_j}{\bar{\rho}_j} \right) + 2 \bar{c}_j \left(\frac{u'_j}{\bar{c}_j} \right) \\ = \frac{c_2}{M_2} \left(\frac{p'_2}{\gamma \bar{p}_2} \right) - \bar{M}_2 \bar{c}_2 \left(\frac{\rho'_2}{\bar{\rho}_2} \right) + 2 \bar{c}_2 \left(\frac{u'_2}{\bar{c}_2} \right), \end{aligned} \quad (\text{III.20})$$

which can be decomposed as a balance of acoustic, entropic and compositional waves. The

III. TRANSFER FUNCTIONS OF COMPACT NOZZLES

jump conditions for mass, total temperature and species are the same as in the isentropic case (see (III.3)), and the entropy conservation condition is replaced by (III.20).

III.2.3 Transfer functions

The anisentropic jump from the jet mixing area to the outlet can expressed in matrix form as:

$$\mathbf{Y}_j \mathbf{w}_j = \mathbf{Y}_2 \mathbf{w}_2, \quad (\text{III.21})$$

where \mathbf{w}_j and \mathbf{w}_2 are the wave vectors at the jet interface and outlet, and \mathbf{Y}_j and \mathbf{Y}_2 are transfer matrices of the form:

$$\mathbf{Y} = \begin{bmatrix} 1 + \frac{1}{\bar{M}} & 1 - \frac{1}{\bar{M}} & -1 & -\Psi \\ \frac{(\gamma - 1)(1 + \bar{M})}{1 + \frac{\gamma-1}{2}\bar{M}^2} & \frac{(\gamma - 1)(1 - \bar{M})}{1 + \frac{\gamma-1}{2}\bar{M}^2} & \frac{1}{1 + \frac{\gamma-1}{2}\bar{M}^2} & \frac{\Psi}{1 + \frac{\gamma-1}{2}\bar{M}^2} \\ \bar{c} \left(\frac{A_2}{A} \frac{1}{M} + 2 + \bar{M} \right) & \bar{c} \left(\frac{A_2}{A} \frac{1}{M} - 2 + \bar{M} \right) & -\bar{M}\bar{c} & -\Psi\bar{M}\bar{c} \\ 0 & 0 & 0 & 1 \end{bmatrix}. \quad (\text{III.22})$$

The isentropic jump from the inlet to the jet transition can be described as in §III.1, with:

$$[\mathbf{X}\mathbf{w}]_1^j = 0, \quad (\text{III.23})$$

where \mathbf{w}_1 and \mathbf{w}_j are the wave vectors at the inlet and jet interface, and \mathbf{X} is the isentropic transfer matrix from (III.6).

To obtain a relationship between the waves at the inlet and outlet of the nozzle \mathbf{w}_1 and \mathbf{w}_2 , we can write:

$$\mathbf{X}_1 \mathbf{w}_1 = \mathbf{X}_j \mathbf{Y}_j^{-1} \mathbf{Y}_2 \mathbf{w}_2, \quad (\text{III.24})$$

or in terms of ingoing and outgoing waves \mathbf{w}_i and \mathbf{w}_o :

$$\mathbf{X}_i \mathbf{w}_i = \mathbf{X}_o \mathbf{w}_o, \quad (\text{III.25})$$

where \mathbf{X}_i and \mathbf{X}_o are permutations of \mathbf{X}_1 and $\mathbf{X}_j \mathbf{Y}_j^{-1} \mathbf{Y}_2$ respectively.

The overall matrix of nozzle transfer functions is $\mathbf{T} = \mathbf{X}_o^{-1} \mathbf{X}_i$. Explicit expressions for

the nozzle transfer functions contained in \mathbf{T} can be readily obtained, but these are too long to provide much physical insight and are therefore presented in Appendix A.

Unlike a compact isentropic nozzle, the anisotropic compact nozzle exhibits acoustic-entropic and compositional-entropic couplings, with $\sigma_2/\pi_1^+ \geq 0$, $\sigma_2/\pi_2^- \leq 0$ and $\sigma_2/\xi_1 \geq 0$. Furthermore, entropic fluctuations are not necessarily conserved, and we have $\sigma_2/\sigma_1 \leq 1$. The range of possible couplings between acoustic, entropic and compositional modes at a subsonic compact anisentropic nozzle are shown in figure III.7.

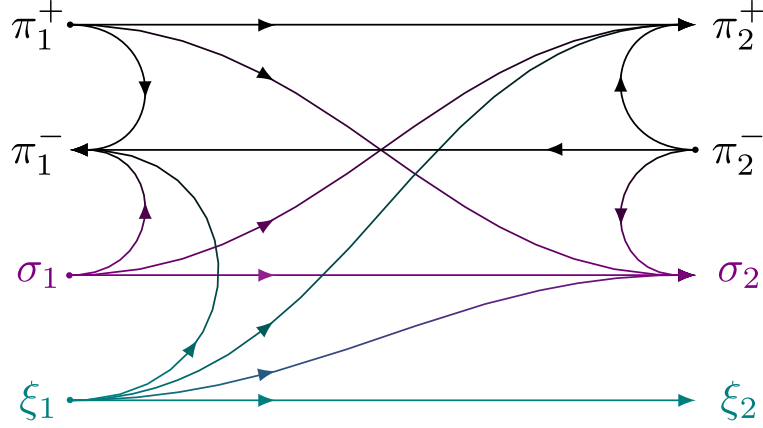


Figure III.7: Non-zero mode transfer mechanisms between acoustic (π), entropic (σ) and compositional waves (ξ) at the inlet and outlet of a subsonic anisentropic compact nozzle.

III.3 Effect of anisentropicity

The effect of anisentropicity on nozzle transfer functions is examined in this section. We consider a subsonic nozzle of dimensions based on the Cambridge Wave Generator described in §VI. The nozzle has an identical flow area at the inlet and outlet ($A_1 = A_2 \approx 1.425 \times 10^{-3} \text{ m}^2$), corresponding to a circular cross section of diameter $d = 42.6 \text{ mm}$. The throat area $A_t \approx 3.42 \times 10^{-5} \text{ m}^2$ corresponds to a circular cross section of diameter $d_t = 6.6 \text{ mm}$. The effect of a vena contracta is neglected here for simplicity.

Based on these dimensions, we define ten nozzles with varying levels of anisentropicity. This is set by selecting a value of $\Lambda \in [0, 1]$, which in turn defines an effective jet mixing area A_j . This jet area can be related to an effective jet diameter d_j . These are shown for the ten nozzles considered here in III.1. In reality, one can expect the anisentropicity Λ of a given nozzle to vary with the mass flow rate; this is not considered here.

III. TRANSFER FUNCTIONS OF COMPACT NOZZLES

Nozzle	1	2	3	4	5	6	7	8	9	10
Λ	0	0.85	0.9	0.93	0.95	0.97	0.98	0.99	0.998	1
d_j (mm)	42.6	17.59	14.86	12.94	11.49	9.83	8.89	7.83	6.86	6.6

Table III.1: Anisentropicity levels Λ and corresponding effect jet area diameters d_j for ten nozzles.

For all the results presented here, the outlet operating conditions are set to atmospheric ($\bar{p}_2 = 101,325$ Pa, $\bar{\rho}_2 = 1.204$ kg m⁻³, $\bar{T}_2 = 293.15$ K). For a given mass flow rate \dot{m} and Λ , we calculate the corresponding mean flow variables at the jet location, at the throat and at the inlet. This is achieved by solving the mean flow jump conditions in (III.1) and (III.19) numerically. By repeating this process for a range of mass flow rates (up to 16 g s⁻¹ of air), we can obtain nozzle transfer functions for the full subsonic range (with the throat Mach number \bar{M}_t ranging from 0 to 1). The resulting inlet and outlet mean Mach numbers \bar{M}_1 and \bar{M}_2 and inlet pressure \bar{p}_1 are shown as a function of the throat Mach number \bar{M}_t in figure III.8.

The inlet Mach number $\bar{M}_1(\bar{M}_t)$ does not depend on Λ . Conversely, the outlet Mach number \bar{M}_2 increases with Λ ; the difference is particularly pronounced at high values of \bar{M}_t . This can be explained by the fact that the inlet pressure \bar{p}_1 increases in line with Λ , while \bar{p}_2 is constant. Indeed, a pressure difference $\bar{p}_1 - \bar{p}_2$ is required to overcome the total pressure losses in the divergent nozzle for anisentropic cases. For the isentropic case ($\Lambda = 0$) considered by Marble & Candel⁶¹ and Magri et al.⁵⁸, \bar{p}_1 is simply equal to \bar{p}_2 since there are no total pressure losses across the nozzle and we have $A_1 = A_2$. Consequently, we have $\bar{M}_1 = \bar{M}_2$ only in the fully isentropic case, and $\bar{M}_1 < \bar{M}_2$ otherwise. This is equivalent to a Fanno line process, in which the generation of entropy due to wall friction leads to the acceleration of the flow⁷⁴.

Once the mean flow variables have been obtained, the nozzle transfer functions can be computed using the method shown in §III.2.1.

III.3.1 Acoustic-acoustic transfer functions

An impinging upstream acoustic wave π_1^+ leads to the generation of a reflected wave π_1^- and a transmitted wave π_2^+ . The corresponding reflection and transmission coefficients are:

$$T_1 = \frac{\bar{p}_2 \pi_2^+}{\bar{p}_1 \pi_1^+}, \quad R_1 = \frac{\pi_1^-}{\pi_1^+}, \quad (\text{III.26})$$

III. TRANSFER FUNCTIONS OF COMPACT NOZZLES

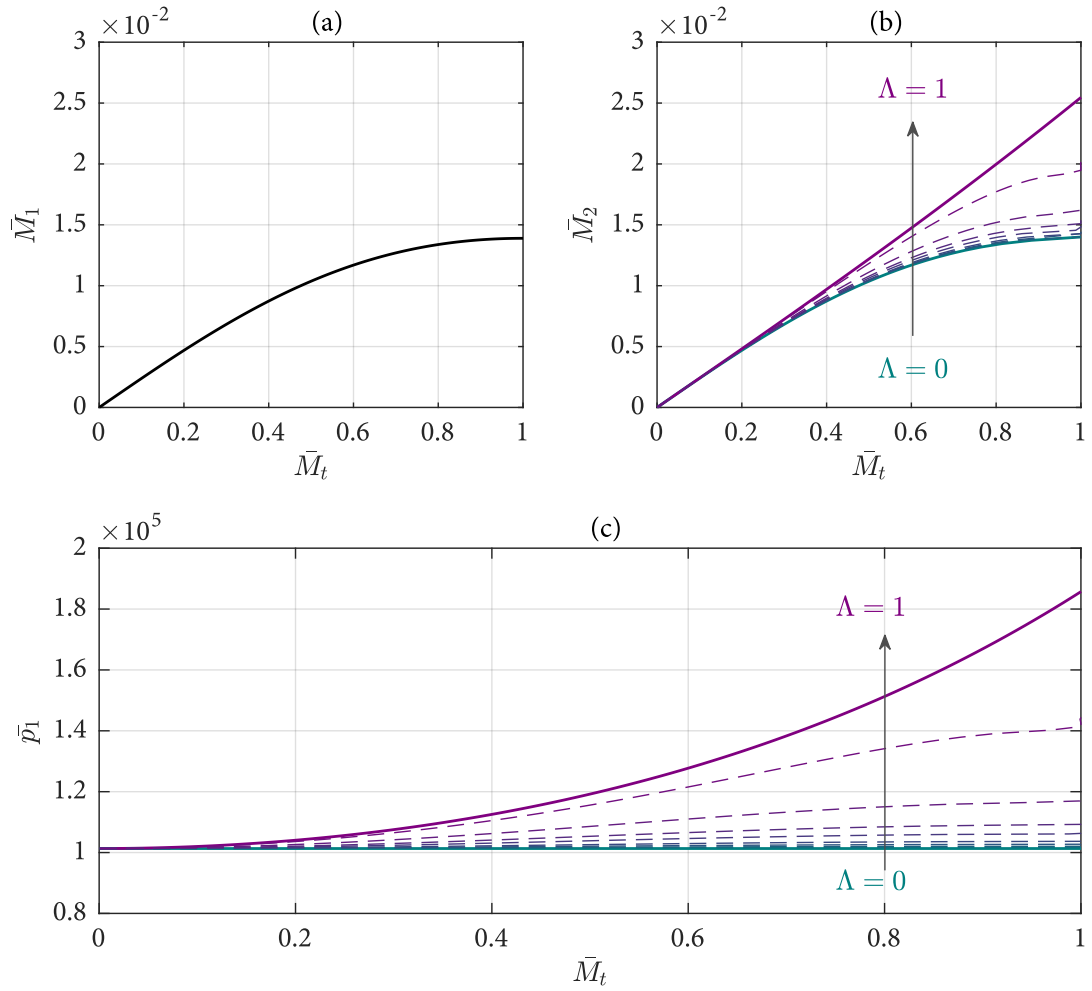


Figure III.8: (a) Inlet Mach number \bar{M}_1 , (b) outlet Mach number \bar{M}_2 and (c) inlet mean pressure \bar{p}_1 as a function of the throat Mach number \bar{M}_t . Ten values of Λ are shown, ranging from isentropic with $\Lambda = 0$ (—) to fully anisentropic with $\Lambda = 1$ (—), with intermediate cases where $0 < \Lambda < 1$ (- -).

III. TRANSFER FUNCTIONS OF COMPACT NOZZLES

where the pressure factor \bar{p}_2/\bar{p}_1 is introduced to account for the change in pressure across the nozzle in the anisentropic cases. The coefficients are plotted in figure III.9. The limit case of a isentropic choked nozzle ($\bar{M}_t = 1$) is also shown for comparison.

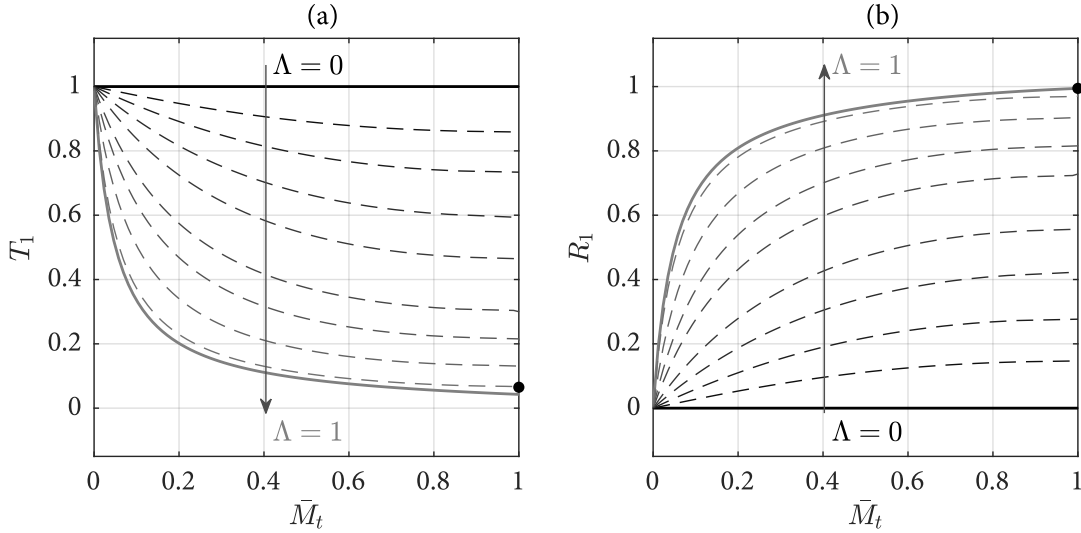


Figure III.9: (a) Acoustic transmission coefficient T_1 , (b) acoustic reflection coefficient R_1 as a function of the throat Mach number \bar{M}_t . Ten values of Λ are shown, ranging from $\Lambda = 0$ (—) to $\Lambda = 1$ (---), with intermediate cases where $0 < \Lambda < 1$ (- - -). The limit case of an isentropic choked nozzle is also shown (●).

In the isentropic limit case ($\Lambda = 0$), the wave is fully transmitted ($T_1 = 1$) with no reflection ($R_1 = 0$). For the anisentropic cases, this is no longer the case: the wave is only partially transmitted ($T_1 < 1$), and a reflection occurs ($R_1 > 0$). These effects become more pronounced as the level of anisentropicity Λ and the throat Mach number \bar{M}_t increase.

When the nozzle is choked (at $\bar{M}_t = 1$), the isentropic transfer functions jump from $T_1 = 1$ to $T_1 \approx 0.07$ and from $R_1 = 0$ to $R_1 \approx 0.99$. This change in behaviour is explained by the fact that upstream propagating waves downstream of the throat can no longer propagate into the upstream section of the nozzle in choked conditions. In the anisentropic cases, a similar jump occurs.

Notably, in the case of a fully dissipative divergent section ($\Lambda = 1$), there is no large jump in the reflection coefficient R_1 for $\bar{M}_t \rightarrow 1$. This is because in choked conditions, R_1 depends solely on the converging section of the nozzle, which is always modelled as isentropic. For $\Lambda = 1$ and $\bar{M}_t \rightarrow 1$, the acoustic energy in the divergent nozzle is dissipated, and contributes very little to the acoustics in the convergent. Conversely, the transmission coefficient T_1 of a

III. TRANSFER FUNCTIONS OF COMPACT NOZZLES

fully dissipative anisentropic nozzle for $\bar{M}_t \rightarrow 1$ is slightly lower than for an isentropic choked nozzle. This is because in the anisentropic case, a portion of the acoustic energy is dissipated in the divergent nozzle.

An impinging downstream acoustic wave π_2^- leads to the generation of a reflected wave π_2^+ and a transmitted wave π_1^- . The corresponding reflection and transmission coefficients are:

$$T_2 = \frac{\bar{p}_1 \pi_1^-}{\bar{p}_2 \pi_2^-}, \quad R_2 = \frac{\pi_2^+}{\pi_2^-}, \quad (\text{III.27})$$

and are shown in figure III.10.

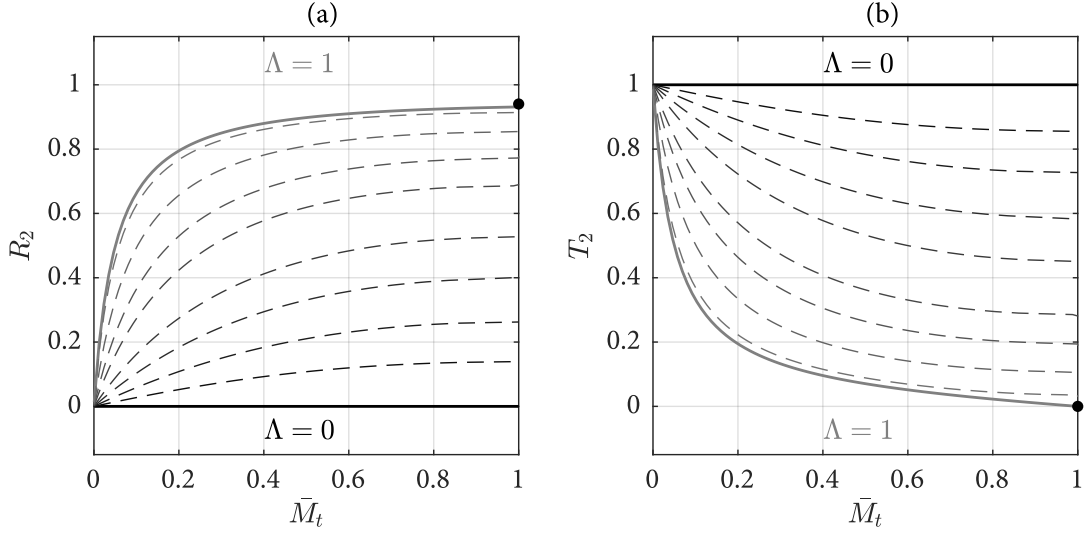


Figure III.10: (a) Acoustic reflection coefficient R_2 , (b) acoustic transmission coefficient T_2 as a function of the throat Mach number \bar{M}_t . Ten values of Λ are shown, ranging from $\Lambda = 0$ (—) to $\Lambda = 1$ (—), with intermediate cases where $0 < \Lambda < 1$ (- - -). The limit case of an isentropic choked nozzle is also shown (●).

As before, the impinging acoustic wave is fully transmitted in the isentropic case ($T_2 = 1$) with no reflection ($R_2 = 0$). The transmission and reflection coefficients increase and decrease (respectively) as Λ and \bar{M}_t increase. For a choked nozzle, the transmission jumps to $T_2 = 0$ since waves cannot propagate past the throat with $\bar{M}_t = 1$. This limit is recovered for $\Lambda = 1$ (fully dissipative divergent nozzle) as $\bar{M}_t \rightarrow 1$. Similarly, the isentropic reflection coefficient jumps to $R_1 \approx 0.94$ as the nozzle becomes choked. For $\Lambda = 1$ and $\bar{M}_t \rightarrow 1$, we obtain a slightly lower value, since some acoustic energy is dissipated in the divergent section.

III. TRANSFER FUNCTIONS OF COMPACT NOZZLES

III.3.2 Entropic-acoustic transfer functions

The entropic noise mechanism is governed by entropic-acoustic transfer functions. An impinging entropic wave σ_1 gives rise to a ‘reflected’ acoustic wave π_1^- , as well as a ‘transmitted’ acoustic wave π_2^+ . Their amplitudes are related by the entropic-acoustic transmission and reflection coefficients:

$$T_\sigma = \frac{\bar{p}_2}{\bar{p}_1} \frac{\pi_2^+}{\sigma_1}, \quad R_\sigma = \frac{\pi_1^-}{\sigma_1}, \quad (\text{III.28})$$

which are plotted in figure III.11.

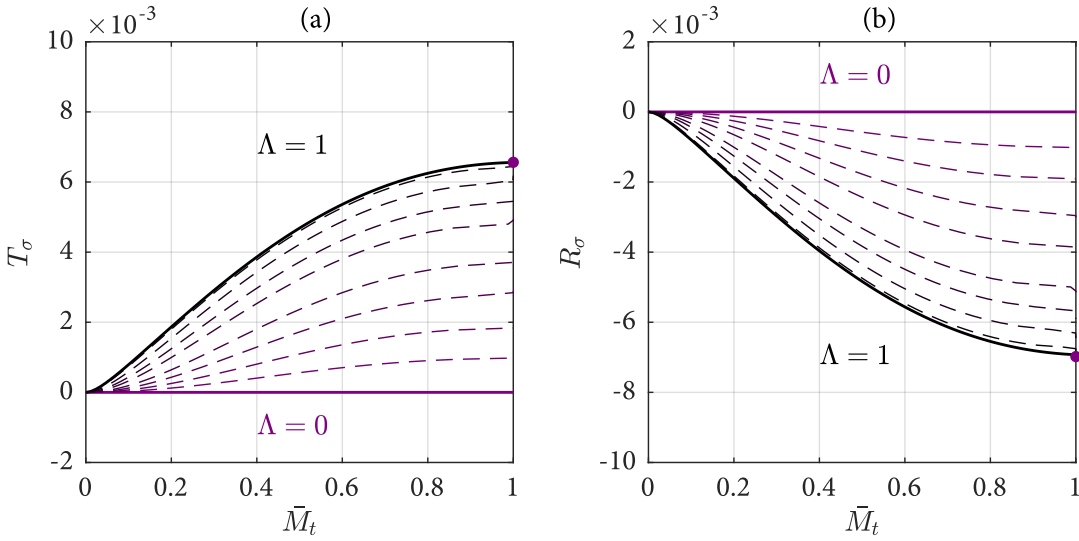


Figure III.11: (a) Entropic-acoustic transmission coefficient T_σ , (b) entropic-acoustic reflection coefficient R_σ as a function of the throat Mach number \bar{M}_t . Ten values of Λ are shown, ranging from $\Lambda = 0$ (—) to $\Lambda = 1$ (---), with intermediate cases where $0 < \Lambda < 1$ (· · ·). The limit case of an isentropic choked nozzle is also shown (●).

For the fully isentropic case, there is no entropic noise, since $\bar{M}_1 = \bar{M}_2$. Entropic noise is produced for the anisentropic cases ($\Lambda > 0$), reaching extreme values of $T_\sigma \approx 6.55 \times 10^{-3}$ and $R_\sigma \approx -6.92 \times 10^{-3}$ for $\Lambda = 1$.

It should be noted that this difference cannot be wholly attributed due to the fact that $\bar{M}_1 < \bar{M}_2$ for anisentropic cases ($\Lambda > 0$). Indeed, taking the case with largest acceleration (from $\bar{M}_1 \approx 0.0139$ to $\bar{M}_2 \approx 0.0253$), we obtain $T_\sigma \approx 1.40 \times 10^{-4}$ and $R_\sigma \approx -8.03 \times 10^{-5}$ in the isentropic case. This shows that the majority of the additional entropic noise for $\Lambda > 0$ is indeed driven by anisentropicity rather than small changes in Mach numbers.

As with the acoustic-acoustic transfer functions, there is a discontinuity at the choking point

(for $\bar{M}_t = 1$). The transfer functions at that operating condition are similar to those for the fully anisentropic divergent section with $\Lambda = 1$ and $\bar{M}_t \rightarrow 1$.

III.3.3 Compositional-acoustic transfer functions

The compositional noise mechanism is governed by compositional-acoustic reflection and transmission coefficients:

$$T_\xi = \frac{\bar{p}_2}{\bar{p}_1} \frac{\pi_2^+}{\xi_1}, \quad R_\xi = \frac{\pi_1^-}{\xi_1}, \quad (\text{III.29})$$

which are plotted in figure III.12 for constant $\Psi = -10$.

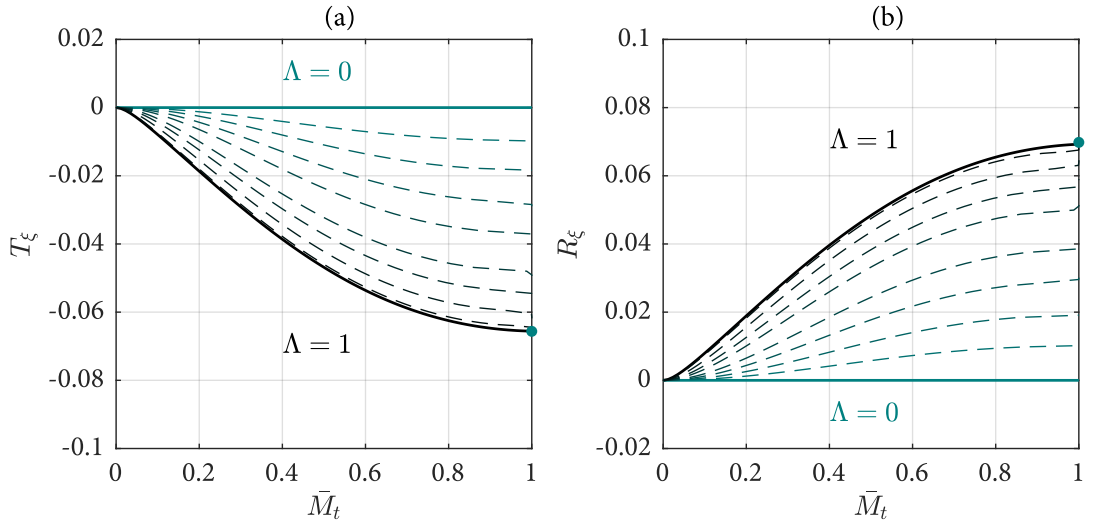


Figure III.12: (a) Compositional-acoustic transmission coefficient T_ξ , (b) compositional-acoustic reflection coefficient R_ξ as a function of the throat Mach number \bar{M}_t . Ten values of Λ are shown, ranging from $\Lambda = 0$ (—) to $\Lambda = 1$ (---), with intermediate cases where $0 < \Lambda < 1$ (- - -). The limit case of an isentropic choked nozzle is also shown (●).

In the isentropic case, compositional noise is driven by changes in the Mach number and in the chemical potential function Ψ . Here we have fixed the value of Ψ (such that $\Psi_1 = \Psi_t = \Psi_j = \Psi_2 = -10$). This is not entirely realistic since in practice the chemical potential function changes with the local flow pressure and temperature. However, this special case enables us to recover an interesting limit:

$$T_\xi = \Psi T_\sigma, \quad (\text{III.30})$$

which was previously shown to be the case for $\Lambda = 0$ by Ihme⁴⁴. The results presented here

III. TRANSFER FUNCTIONS OF COMPACT NOZZLES

show that this result also holds for an anisentropic nozzle where $\Lambda \in [0, 1]$ (this can also be demonstrated analytically). Though this was not originally considered by Ihme⁴⁴, we can also write:

$$R_\xi = \Psi R_\sigma. \quad (\text{III.31})$$

These relationships tell us that in the case where the chemical potential function Ψ is constant, then the ratio of the compositional to entropic noise transfer functions is simply Ψ .

III.3.4 Generation of entropic waves

For an isentropic nozzle, there are no acoustic-entropic interactions, since entropic perturbations are conserved across the nozzle. In the anisentropic case however, such a coupling occurs, and impinging acoustic waves π_1^+ and π_2^- generate an entropic wave σ_2 as shown in figure III.13. An impinging upstream wave generates a positive entropic fluctuation ($\sigma_2 > 0$), while an impinging downstream wave generates a negative entropic fluctuation ($\sigma_2 < 0$)

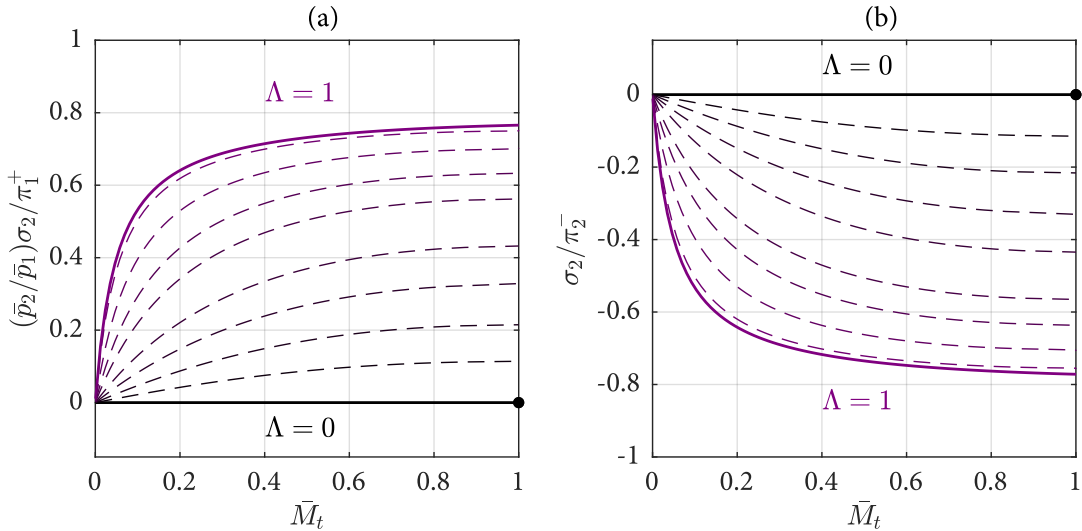


Figure III.13: (a) Acoustic-entropic coefficient $(\bar{p}_2/\bar{p}_1)\sigma_2/\pi_1^+$, (b) acoustic-entropic coefficient σ_2/π_2^- as a function of the throat Mach number \bar{M}_t . Ten values of Λ are shown, ranging from $\Lambda = 0$ (—) to $\Lambda = 1$ (---), with intermediate cases where $0 < \Lambda < 1$ (· · ·). The limit case of an isentropic choked nozzle is also shown (●).

Finally, if entropic fluctuations are not conserved across the nozzle ($\sigma_1 \neq \sigma_2$), an impinging compositional wave may also generate an entropic wave. This is shown in figure III.14.

III. TRANSFER FUNCTIONS OF COMPACT NOZZLES

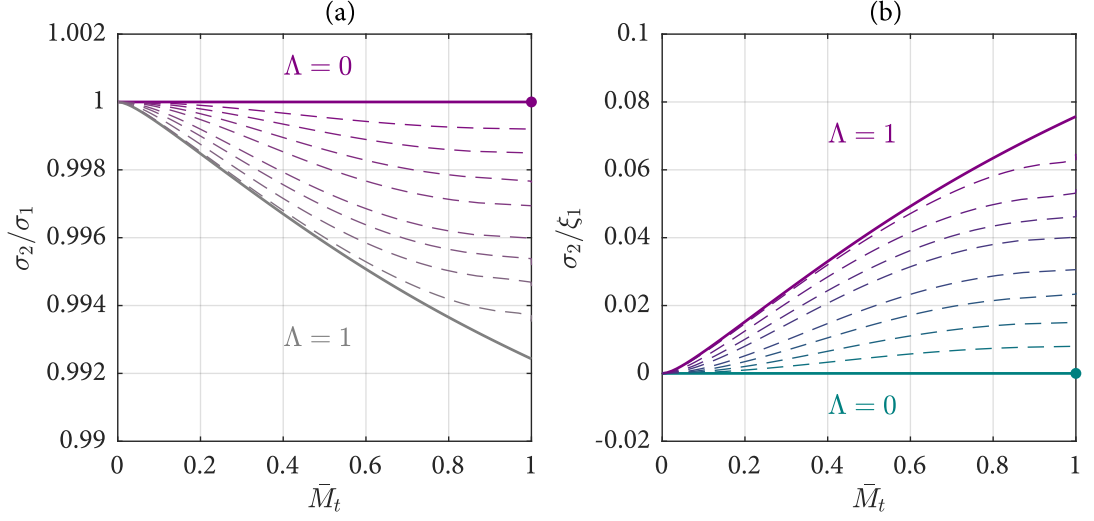


Figure III.14: (a) Entropic-entropic coefficient σ_2/σ_1 , (b) Compositional-entropic coefficient σ_2/ξ_1 as a function of the throat Mach number \bar{M}_t . Ten values of Λ are shown, ranging from $\Lambda = 0$ (—or —) to $\Lambda = 1$ (—or —), with intermediate cases where $0 < \Lambda < 1$ (- - -or - - -) for (a) and (b) respectively. The limit case of an isentropic choked nozzle is also shown (●, ●).

We see that as the anisotropy increases, the amplitude of the convected entropic fluctuation decreases ($\sigma_2 < \sigma_1$). An impinging compositional fluctuation generates an entropic fluctuation of the same sign (for $\Psi < 0$).

Once again, for a constant value of Ψ across the nozzle, we find analytically that:

$$\frac{\sigma_2}{\xi_1} = \Psi \left(1 - \frac{\sigma_2}{\sigma_1} \right). \quad (\text{III.32})$$

IV

REVERBERATION

The objective of this thesis is to compare theoretical models of direct and indirect noise to experimental measurements. The theoretical framework presented in §II–III enables the amplitude of generated direct and indirect acoustic waves to be computed for several operating conditions. Nevertheless, the relation between these waves and the acoustic pressure fluctuations one measures in an experiment is not always straightforward.

For a one-dimensional system, the acoustic pressure at a time t is obtained by considering the amplitudes of the forward and backward propagating acoustic waves at a particular axial location x :

$$\frac{p'}{\gamma \bar{p}}(x, t) = \pi^+(x, t) + \pi^-(x, t). \quad (\text{IV.1})$$

When considering the amplitude of direct and indirect noise, it may be tempting to substitute π^+ and π^- for the acoustic waves amplitudes π_d , π_σ and π_ξ , for which analytical expressions have been obtained. This would not usually provide an accurate result however, as real systems typically present substantial acoustic reflections which are measured along with the original sound waves, thus modifying both the shape and amplitude of the pressure signal. In this chapter, the effect of repeated acoustic reflections inside a one-dimensional duct is determined analytically.

In the first instance, we examine the case of a unicameral system (i.e. consisting of one chamber) containing an acoustic source. We start by considering the reflections of a rectangular acoustic pulse, in the case where the acoustic wavelength is substantially longer than the system itself (i.e. low-frequency sound). In that scenario, reverberation occurs, whereby sound is sustained even after the acoustic source is switched off. A time-domain approach is used to obtain expressions for the corresponding acoustic pressure.

Following this, an analogous method is used to obtain expressions for the reverberation of arbitrary acoustic pulses at arbitrary frequencies, in both the time and frequency domains. The results can be formulated to define reverberation transfer functions for a given reflective system, relating acoustic source signals to the resulting acoustic pressure.

In the second instance, we consider a bicameral system, consisting of two reverberating chambers separated by an interface (e.g. a nozzle). The influence of sound sources upstream and downstream of the interface on the acoustic pressure is determined analytically using reverberation transfer functions.

IV.1 Unicameral reverberation

IV.1.1 Rectangular source

We start by considering a one-dimensional unicameral system consisting of a single chamber of length L . Acoustic reflections occur at the inlet and outlet with reflection coefficients R_i and R_o respectively. The acoustic pressure is measured using a pressure transducer at a distance x downstream of the inlet.

The acoustic pressure inside the duct is attributed to acoustic waves generated by one or more acoustically compact sources producing forward- and backward-propagating waves. Owing to the superposition principle, the total acoustic pressure is a sum of the acoustic pressures due to each one of these sources.

As such, we can consider the effect of a single acoustic source located at a distance x_s downstream of the inlet, producing forward- and backward-propagating acoustic waves $\pi_s^+(t)$ and $\pi_s^-(t)$ as shown in figure IV.1. The entire acoustic field can be recovered by considering the superposition of several of these sources.

We start by examining the case where the pressure transducer is located downstream of the acoustic source ($x > x_s$). The source signal is taken to be a rectangular pulse, which means that it is activated at $t = 0$ and deactivated at $t = t_e$ with no rise time or decay:

$$\pi_s^-(t) = \begin{cases} \pi_s^- & \text{if } t \in [0, t_e] \\ 0 & \text{if } t \in [t_e, +\infty[\end{cases}, \quad \pi_s^+(t) = \begin{cases} \pi_s^+ & \text{if } t \in [0, t_e] \\ 0 & \text{if } t \in [t_e, +\infty[\end{cases}. \quad (\text{IV.2})$$

For the following analysis, we consider acoustic reflections of waves occurring during the

IV. REVERBERATION

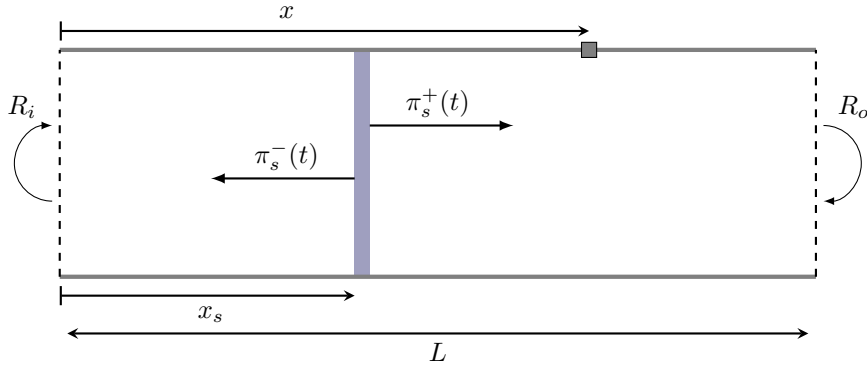


Figure IV.1: Unicameral system: an acoustic source at a location x_s generates forward- and backward-propagating waves $\pi_s^+(t)$ and $\pi_s^-(t)$.

pulse ($0 \leq t \leq t_e$), and after the pulse ($t > t_e$).

During the pulse

When the acoustic source is active, acoustic waves of amplitudes π_s^- and π_s^+ are being continuously generated. At first, the only waves in the duct are those propagating away from the acoustic source. As these waves reach the inlet and outlet of the system, they are reflected, giving rise to waves propagating in the opposite direction, with amplitudes $R_o\pi_s^+$ and $R_i\pi_s^-$. These reflected waves propagate through the duct, and are once again reflected at the opposite ends as $R_oR_i\pi_s^-$ and $R_iR_o\pi_s^+$. The successive reflections of π_s^+ are shown diagrammatically in figure IV.2. As this process repeats itself until the end of the pulse, the overall amplitudes π^+ and π^- of the acoustic waves in the duct change, and the acoustic pressure inside the system is modified accordingly, as shown in equation (IV.1).

Each reflection of π_s^- and π_s^+ is measured with an acoustic time delay, which is the time taken for the wave to travel from its origin at location x_s to the transducer at location x . These time delays are related to the time taken for a wave to propagate either forward or backward across a given distance. For example, the time delays associated to a given length l are:

$$\tau_l^+ = \frac{l}{\bar{c} + \bar{u}}, \quad \tau_l^- = \frac{l}{\bar{c} - \bar{u}}, \quad (\text{IV.3})$$

where τ_l^+ and τ_l^- are the times taken for an acoustic wave to propagate with and against the flow over a distance l . In (IV.3), l can be substituted by x or x_s depending on the length of

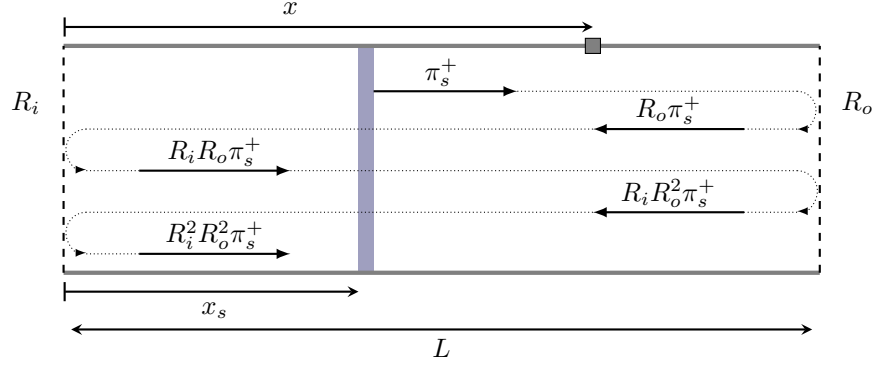


Figure IV.2: The forward-propagating wave π_s^+ generated by the acoustic source is successively reflected at the inlet and outlet of the unicameral system.

Amplitude	Distance travelled	Time-delay
π_s^+	$(x - x_s) = l_p$	$\tau_x^+ - \tau_{x_s}^+ = \tau_p$
$R_o \pi_s^+$	$(L - x_s) + (L - x) = l_q$	$\tau - \tau_x^- - \tau_{x_s}^+ = \tau_q$
$R_o R_i \pi_s^+$	$(x - x_s) + 2L = l_p + 2L$	$\tau_x^+ - \tau_{x_s}^+ + \tau = \tau_p + \tau$
$R_o^2 R_i \pi_s^+$	$(L - x_s) + (L - x) + 2L = l_q + 2L$	$\tau - \tau_x^- - \tau_{x_s}^+ + \tau = \tau_q + \tau$
\vdots	\vdots	\vdots

Table IV.1: Amplitudes, distances travelled and time delays associated to the forward-propagating acoustic wave π_s^+ and its first three reflections.

interest. In addition, we define the acoustic round-trip time τ :

$$\tau = \frac{L}{\bar{c} + \bar{u}} + \frac{L}{\bar{c} - \bar{u}}, \quad (\text{IV.4})$$

which is the time delay for a wave to reflect at both ends of the duct, and propagate back to its original position.

The amplitudes, distances travelled, and time delays associated to each reflection of the acoustic waves π^+ and π_s^- are shown in tables IV.1 and IV.2 respectively. If we consider that the pulse duration is longer than the acoustic time-scale ($t_e > \tau$), then the acoustic signal is reverberated, and acoustic reflections occur while the original wave is still being generated.

The successive reflections of π_s^- and π_s^+ correspond to the sum of the terms of two geometric series of ratio $R_i R_o$, and in which each term is separated by a time delay τ . The general formula for the sum S_k of the first k terms of a geometric series is:

IV. REVERBERATION

Amplitude	Distance travelled	Time-delay
$R_i \pi_s^-$	$(x_s + x) = l_s$	$\tau_{x_s}^- + \tau_x^+ = \tau_s$
$R_i R_o \pi_s^-$	$(L + x_s) + (L - x) = l_r + 2L$	$\tau_{x_s}^- - \tau_x^- = \tau_r$
$R_i^2 R_o \pi_s^-$	$(x_s + x) + 2L = l_s + 2L$	$\tau_{x_s}^- + \tau_x^+ + \tau = \tau_s + \tau$
$R_i^2 R_o^2 \pi_s^-$	$(L + x_s) + (L - x) + 2L = l_r + 4L$	$\tau_{x_s}^- - \tau_x^- + \tau = \tau_r + \tau$
\vdots	\vdots	\vdots

Table IV.2: Amplitudes, distances travelled and time delays associated to the backward-propagating acoustic wave π_s^- and its first three reflections.

$$S_k = \frac{a(1 - r^k)}{1 - r} \quad (\text{IV.5})$$

where r is the ratio and a is the first term of the series. This enables us to express the acoustic pressure due to the acoustic source as:

$$\begin{aligned} \frac{p'}{\gamma \bar{p}} \Big|_s (x, t \leq t_e) = & \overbrace{\pi_s^+ \frac{1 - (R_i R_o)^{\lfloor \frac{t - \tau_p + \tau}{\tau} \rfloor}}{1 - R_i R_o}}^{\text{for } t \geq \tau_p} + \overbrace{R_o \pi_s^+ \frac{1 - (R_i R_o)^{\lfloor \frac{t - \tau_q + \tau}{\tau} \rfloor}}{1 - R_i R_o}}^{\text{for } t \geq \tau_q} + \\ & \underbrace{R_i \pi_s^- \frac{1 - (R_i R_o)^{\lfloor \frac{t - \tau_s + \tau}{\tau} \rfloor}}{1 - R_i R_o}}_{\text{for } t \geq \tau_s} + \underbrace{R_i R_o \pi_s^- \frac{1 - (R_i R_o)^{\lfloor \frac{t - \tau_r + \tau}{\tau} \rfloor}}{1 - R_i R_o}}_{\text{for } t \geq \tau_r}. \end{aligned} \quad (\text{IV.6})$$

where $\lfloor \beta \rfloor$ denotes the floor function, which gives the greatest integer which is less than or equal to β . The time delays τ_p , τ_q , τ_r and τ_s are defined in tables IV.1 and IV.2.

In a typical real system we have $|R_i R_o| < 1$, and equation (IV.6) converges. If the acoustic time-scale τ is significantly shorter than the pulse duration t_e , then the acoustic pressure will quickly converge towards:

$$\lim_{t \rightarrow \infty} \frac{p'}{\gamma \bar{p}} \Big|_s = (R_i \pi_s^- + \pi_s^+) \frac{1 + R_o}{1 - R_i R_o}. \quad (\text{IV.7})$$

After the pulse

Once the acoustic source is deactivated at $t = t_e$, it no longer generates acoustic waves. The only contributions to the acoustic pressure come from pre-existing waves propagating and reflecting at the boundaries of the system.

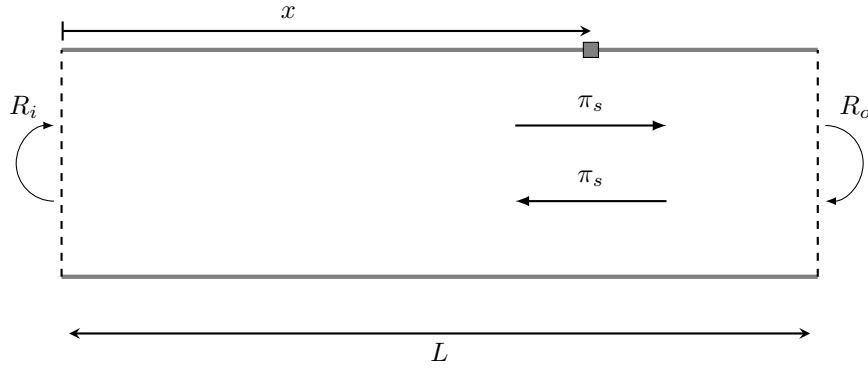


Figure IV.3: The forward and backward-propagating waves of amplitude π_s after the acoustic source has been deactivated.

The acoustic pressure immediately after the source is deactivated is $p'/\gamma\bar{p}|_s(x, t_e)$. We make the simplifying assumption that the acoustic field is comprised of a forward and a backward propagating wave, both of equal amplitude π_s , as shown in figure IV.3. The wave amplitude π_s must satisfy equation (IV.1) and can be assumed to be:

$$\pi_s = \frac{1}{2} \frac{p'}{\gamma\bar{p}} \Big|_s (x, t_e). \quad (\text{IV.8})$$

The amplitudes and time delays associated to each wave passing at the pressure measurement location x can be determined as in tables IV.1 and IV.2. The successive reflections of π_s correspond to the terms of four geometric sequences with ratios $R_i R_o$, and in which each term is separated by a time delay τ . If we consider the successive terms of two of these four sequences, the acoustic pressure in the tube can be approximated as:

$$\frac{p'}{\gamma\bar{p}} \Big|_s (t > t_e) = \pi_s (R_i R_o)^{\lfloor \frac{t-t_e}{\tau} \rfloor} + R_o \pi_s (R_i R_o)^{\lfloor \frac{t-(t_e+\tau-\tau_x^+-\tau_x^-)}{\tau} \rfloor}. \quad (\text{IV.9})$$

The accuracy of this approximation is examined in §V.3 (limit case IV).

Effect of acoustic attenuation

Acoustic attenuation occurs in the tube due to turbulence, mixing, viscous effects as well as losses at the walls. The amplitude change of a acoustic wave due to attenuation can be expressed as:

$$\pi(l) = \pi_0 e^{-\alpha l} \quad (\text{IV.10})$$

IV. REVERBERATION

where π_0 is the original amplitude of the wave, $\pi(l)$ is the amplitude of the wave at a distance l from its origin, and α is the attenuation coefficient. The effect of acoustic attenuation can be included in the results presented in the previous section. Consider the case of a wave π_s^+ generated at the wave generator. If acoustic attenuation is neglected, the wave propagates towards the outlet, and returns with an amplitude $\pi_s^+ R_o$. If acoustic attenuation is taken into account, the wave is attenuated over a distance $2(L - x_s)$, and returns with an amplitude $\pi_s^+ R_o e^{-2\alpha(L-x_s)}$.

Including attenuation terms of the form $e^{-\alpha l}$ throughout the derivation in §IV.1.1 –IV.1.1 yields modified expressions for the acoustic pressure due to reverberation. These modified expressions can be easily obtained by substituting R_i with $R_i e^{-2\alpha x}$ and R_o by $R_o e^{-2\alpha(L-x)}$ in equations (IV.6) and (IV.9). For example, (IV.6) becomes:

$$\begin{aligned} \left. \frac{p'}{\gamma \bar{p}} \right|_s (x, t \leq t_e) = & \overbrace{\pi_s^+ \frac{1 - (R_i R_o e^{-2\alpha L})^{\lfloor \frac{t - \tau_p + \tau}{\tau} \rfloor}}{1 - R_i R_o e^{-2\alpha L}}}_{\text{for } t \geq \tau_p} + \overbrace{R_o e^{-2\alpha(L-x)} \pi_s^+ \frac{1 - (R_i R_o e^{-2\alpha L})^{\lfloor \frac{t - \tau_q + \tau}{\tau} \rfloor}}{1 - R_i R_o e^{-2\alpha L}}}_{\text{for } t \geq \tau_q} \\ & + \overbrace{R_i e^{-2\alpha x} \pi_s^- \frac{1 - (R_i R_o e^{-2\alpha L})^{\lfloor \frac{t - \tau_s + \tau}{\tau} \rfloor}}{1 - R_i R_o e^{-2\alpha L}}}_{\text{for } t \geq \tau_s} + \overbrace{R_i R_o e^{-2\alpha L} \pi_s^- \frac{1 - (R_i R_o e^{-2\alpha L})^{\lfloor \frac{t - \tau_r + \tau}{\tau} \rfloor}}{1 - R_i R_o e^{-2\alpha L}}}_{\text{for } t \geq \tau_r}. \end{aligned} \quad (\text{IV.11})$$

Extension to arbitrary sources using Riemann rectangles

One of the limitations of the reverberation model outlined above is that it requires the acoustic source signal to be rectangular in time. In real systems this is not usually the case. However, the acoustic pressure resulting from the reverberation of non-rectangular acoustic signals can be closely approximated analytically by discretising the acoustic signal.

Indeed, an acoustic signal of arbitrary shape can be approximated as the succession of rectangular pulses of varying amplitudes and of duration δt . As δt is decreased, the approximation of the arbitrary signal becomes increasingly accurate. In this sense, any acoustic signal can be closely approximated as a train of several successive rectangular acoustic waves. This is shown in figure IV.4 in the case where the acoustic pulse is a raised sine wave (of the form $\sin^2(\omega t)$) lasting $t_e = 200$ ms with an amplitude $\pi_s^+ = 10^{-5}$. The acoustic wave is shown in (a), and rectangular approximations for $\delta t = 20$ ms and $\delta t = 10$ ms are shown in (b) and (c) respectively.

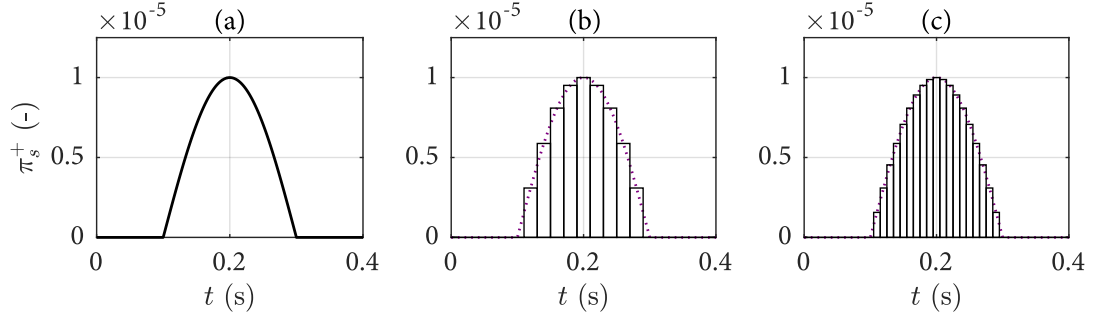


Figure IV.4: (a) Non-rectangular acoustic wave (b) Non-rectangular acoustic wave (⋯⋯) and rectangular approximation (—) for $\delta t = 20$ ms, (c) Non-rectangular acoustic wave and rectangular approximation for $\delta t = 10$ ms.

The acoustic pressure resulting from the reverberation of the non-rectangular signal can then be estimated as the sum of the acoustic pressures due to each of the rectangular waves used to construct it. This can be calculated analytically by using the reverberation model presented in equations (V.2), (V.3) and (V.4). In principle, the accuracy of this approximation can be improved by decreasing δt as required. Note that if the rectangular pulse width δt is smaller than the acoustic time-scale τ , the ‘floored’ terms $[\cdot]$ must be replaced by (\cdot) to recover a physical solution.

IV.1.2 Arbitrary source signal

The results shown up to this point are restricted to cases where the acoustic pulse duration is long compared to the acoustic time-scale of the system ($t_e \gg \tau$). This effectively limits the analysis to low-frequency acoustic sources. Furthermore, the expressions describing the acoustic pressure (V.2)–(V.4) are piece-wise defined, which complicates their manipulation.

Using a similar approach to the one employed above, we derive new equations for the reverberation of arbitrary acoustic signals $\pi_s^+(t)$ and $\pi_s^-(t)$. The reverberation process can be formulated in the frequency domain, which enables one to obtain acoustic transfer functions, which are a two-way link between acoustic sources and the acoustic pressure in the system.

Time-domain analysis

We consider a unicameral one-dimensional system as shown in figure IV.1. The source generates forward- and backward-propagating waves $\pi_s^+(t)$ and $\pi_s^-(t)$, the amplitudes of which vary with time. Once again, we start by examining only the effect of a forward-propagating

IV. REVERBERATION

wave $\pi_s^+(t)$, in the case where the pressure transducer is located downstream of the acoustic source ($x > x_s$).

The amplitudes, distances travelled, and time delays associated to each reflection of the acoustic wave π_s^+ are shown in table IV.1. The amplitudes of successive reflections correspond to two alternating geometric sequences (where successive terms are multiplied by $R_i R_o$). The time delays associated to these waves correspond to two alternating arithmetic sequences (where each term is separated by τ). The acoustic pressure at the microphone location $p'/\gamma\bar{p}|_s(x, t)$ corresponds to the sum of all the acoustic waves passing at x at a time t :

$$\begin{aligned} \frac{p'}{\gamma\bar{p}} \Big|_s (x, t) = & \pi_s^+(t - \tau_p) + R_o \pi_s^+(t - \tau_q) + R_i R_o \pi_s^+(t - \tau_p - \tau) \\ & + R_i R_o^2 \pi_s^+(t - \tau_q - 2\tau) + R_i^2 R_o^2 \pi_s^+(t - \tau_p - 2\tau) + \dots \end{aligned} \quad (\text{IV.12})$$

where $\tau_p = \tau_x^+ - \tau_{x_s}^+$ and $\tau_q = \tau - \tau_x^- - \tau_{x_s}^+$. By defining $\pi_s^+(t < 0) = 0$, the sum can be recast as:

$$\frac{p'}{\gamma\bar{p}} \Big|_s (x, t) = \sum_{n=0}^{\infty} (R_i R_o)^n [\pi_s^+(t - (\tau_p + n\tau)) + R_o \pi_s^+(t - (\tau_q + n\tau))] \quad (\text{IV.13})$$

In practice it is sufficient to compute the sum up to $n = N$, where N is a number of acoustic reflections occurring up to given point in time $t = N\tau$.

Similarly, the acoustic pressure due to the reflections of the backward-propagating wave $\pi_s^-(t)$ can be expressed as:

$$\frac{p'}{\gamma\bar{p}} \Big|_s (x, t) = \sum_{n=1}^{\infty} (R_i R_o)^n [\pi_s^-(t - (\tau_r + (n+1)\tau))] + \sum_{n=0}^{\infty} (R_i R_o)^n [R_i \pi_s^-(t - (\tau_s + n\tau))] \quad (\text{IV.14})$$

where $\tau_r = \tau_{x_s}^- - \tau_x^-$ and $\tau_s = \tau_{x_s}^- + \tau_x^+$.

Frequency-domain analysis

The Fourier transform of the acoustic pressure $p'/\gamma\bar{p}|_s(x, t)$ expressed in (IV.13) is:

$$\widehat{\frac{p'}{\gamma\bar{p}}} \Big|_s (x, \omega) = \sum_{n=0}^{\infty} (R_i R_o)^n e^{-i\omega n\tau} [e^{-i\omega\tau_p} + R_o e^{-i\omega\tau_q}] \widehat{\pi_s^+}(\omega) \quad (\text{IV.15})$$

where $\widehat{\pi_s^+}(\omega)$ is the Fourier transform of the acoustic wave $\pi_s^+(t)$. For $|R_i R_o| < 1$ (which is true in a physical system), the series in (IV.15) is convergent, and we can write:

$$\left. \frac{\widehat{p}'}{\gamma \widehat{p}} \right|_s(x, \omega) = \frac{e^{-i\omega\tau_p} + R_o e^{-i\omega\tau_q}}{1 - R_i R_o e^{-i\omega\tau}} \widehat{\pi_s^+}. \quad (\text{IV.16})$$

The transfer function \mathcal{R}^+ between the Fourier transforms of the acoustic wave amplitude $\pi_s^+(t)$ and the resulting acoustic pressure fluctuation $p'/\gamma\bar{p}|_s(x, t)$ is given by:

$$\mathcal{R}^+(x, \omega) = \frac{\widehat{p}'/\gamma\bar{p}|_s}{\widehat{\pi_s^+}} = \frac{e^{-i\omega\tau_p} + R_o e^{-i\omega\tau_q}}{1 - R_i R_o e^{-i\omega\tau}}. \quad (\text{IV.17})$$

Note that \mathcal{R}^+ is a function of the measurement and acoustic source locations x and x_s . Similarly, we can define the transfer function \mathcal{R}^- between the Fourier transforms of the backward acoustic wave $\pi_s^-(t)$ and the resulting acoustic pressure $p'/\gamma\bar{p}(x, t)$:

$$\mathcal{R}^-(x, \omega) = \frac{\widehat{p}'/\gamma\bar{p}|_s}{\widehat{\pi_s^-}} = \frac{R_i R_o e^{-i\omega(\tau_r + \tau)} + R_i e^{-i\omega\tau_s}}{1 - R_i R_o e^{-i\omega\tau}}. \quad (\text{IV.18})$$

Reverberation transfer functions

We have derived frequency-dependent acoustic transfer functions $\mathcal{R}^+(\omega)$ and $\mathcal{R}^-(\omega)$, relating acoustic source signals $\widehat{\pi_s^+}(\omega)$ and $\widehat{\pi_s^-}(\omega)$ to the resulting acoustic pressures. The overall acoustic pressure is then simply:

$$\left. \frac{\widehat{p}'}{\gamma \widehat{p}} \right|_s = \mathcal{R}^+ \widehat{\pi_s^+} + \mathcal{R}^- \widehat{\pi_s^-}. \quad (\text{IV.19})$$

We can also introduce the effect of acoustic attenuation as in §IV.1.1. The resulting transfer functions are:

$$\mathcal{R}^+ = \frac{e^{-i\omega\tau_p - \alpha l_p} + R_o e^{-i\omega\tau_q - \alpha l_q}}{1 - R_i R_o e^{-i\omega\tau - 2\alpha L}}, \quad (\text{IV.20})$$

$$\mathcal{R}^- = \frac{R_i R_o e^{-i\omega(\tau_r + \tau) - \alpha(l_r + 2L)} + R_i e^{-i\omega\tau_s - \alpha l_s}}{1 - R_i R_o e^{-i\omega\tau - 2\alpha L}}. \quad (\text{IV.21})$$

Until now we have focused on the case where the pressure transducer is located downstream of the acoustic source ($x > x_s$). Alternative transfer functions can be derived in the same way

IV. REVERBERATION

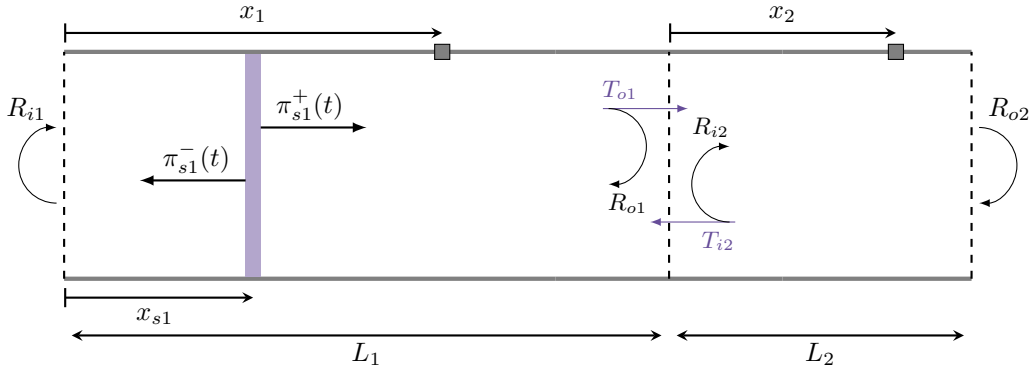


Figure IV.5: Bicameral system: an upstream acoustic source at a location x_{s1} generates forward- and backward-propagating waves $\pi_{s1}^+(t)$ and $\pi_{s1}^-(t)$.

for the opposite case:

$$\mathcal{R}^+ = \frac{R_i R_o e^{-i\omega(\tau_p + \tau) - \alpha(l_p + 2L)} + R_o e^{-i\omega\tau_q - \alpha l_q}}{1 - R_i R_o e^{-i\omega\tau - 2\alpha L}}, \quad (\text{IV.22})$$

$$\mathcal{R}^- = \frac{e^{-i\omega\tau_r - \alpha l_r} + R_i e^{-i\omega\tau_s - \alpha l_s}}{1 - R_i R_o e^{-i\omega\tau - 2\alpha L}}. \quad (\text{IV.23})$$

IV.2 Bicameral reverberation

So far we have considered a unicameral system, in which there are no reflections apart from those at the inlet and at the outlet. This is not representative of most systems. For example, acoustic waves transmitted through the outlet of the chamber can be reflected further downstream, and be transmitted back into the reverberating chamber, thus affecting the acoustic pressure. Additionally, if one wishes to measure the acoustic waves generated or transmitted downstream of the outlet, reflections occurring further downstream must also be considered.

To account for these effects we can consider a bicameral model consisting of two reverberating chambers separated by an interface: a first chamber upstream, and a second chamber downstream as shown in figure IV.5.

Each chamber is defined by its length L , internal inlet and outlet reflection coefficients (R_i, R_o) , as well as its transmission coefficient across the interface T . The subscripts 1 and 2 are used to denote quantities relating to the first and second chambers respectively. We consider the acoustic pressure in each chambers, at locations x_1 and x_2 .

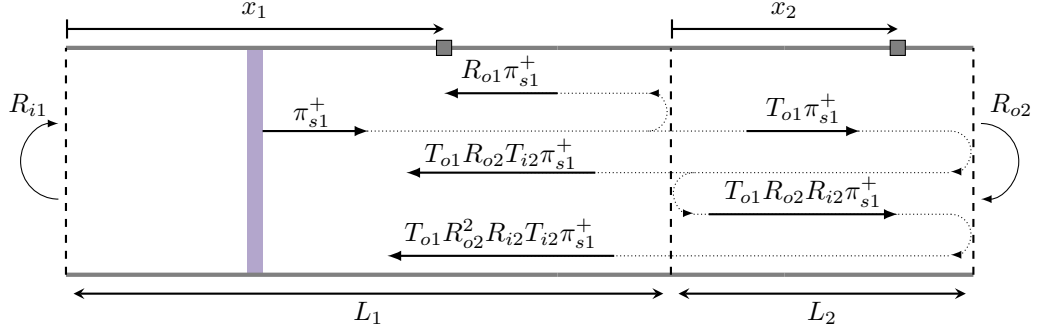


Figure IV.6: The forward-propagating wave π_{s1}^+ generated by the upstream acoustic source is successively reflected at the inlet and outlet of the second chamber, effectively resulting in several reflections.

IV.2.1 Upstream arbitrary source signal

To start, we consider an acoustic source in the first (upstream) chamber, generating acoustic waves $\pi_{s1}^+(t)$ and $\pi_{s1}^-(t)$.

Acoustic pressure in the first chamber

The effect of this source on the acoustic pressure in the first chamber (at location x_1) can be thought of as follows. Forward-propagating waves impinging at the nozzle π_{s1}^+ are reflected with a coefficient R_{o1} , as well as transmitted with a coefficient T_{o1} . The transmitted component $T_{o1}\pi_{s1}^+$ is reflected at the outlet of the second chamber downstream, and returns to the nozzle with an amplitude $T_{o1}R_{o2}\pi_{s1}^+$, and a time delay τ_2 . Part of this wave is transmitted back into the first chamber with an amplitude $T_{o1}R_{o2}T_{o2}\pi_{s1}^+$, while another part is reflected yet again with an amplitude $T_{o1}R_{o2}R_{i2}\pi_{s1}^+$. The latter wave will lead to yet another chain of reflections. This is shown diagrammatically in figure IV.6. The amplitudes and time delays associated to the reflections of π_{s1}^+ are shown in table IV.3.

One way to conceptualise this process is to think of the effective upstream reflection coefficient at the nozzle \dot{R}_{o1} , which corresponds to an immediate reflection R_{o1} , but also subsequent delayed reflections due to the transmitted component. We can write:

$$\dot{R}_{o1} = R_{o1} + T_{o1}R_{o2}T_{i2}e^{-i\omega\tau_2} + T_{o1}R_{o2}^2R_{i2}T_{i2}e^{-2i\omega\tau_2} + T_{o1}R_{o2}^3R_{i2}^2T_{i2}e^{-3i\omega\tau_2} + \dots \quad (\text{IV.24})$$

IV. REVERBERATION

Amplitude	Distance travelled	Time-delay
$R_{o1}\pi_{s1}^+$	0	0
$T_{o1}R_{o2}T_{i2}\pi_{s1}^+$	$2L_2$	τ_2
$T_{o1}R_{i2}R_{o2}^2T_{i2}\pi_{s1}^+$	$4L_2$	$2\tau_2$
$T_{o1}R_{i2}^2R_{o2}^3T_{i2}\pi_{s1}^+$	$6L_2$	$3\tau_2$
\vdots	\vdots	\vdots

Table IV.3: Amplitudes, distances travelled and time-delays associated to the first four reflections of the forward-propagating acoustic wave π_{s1}^+ .

or

$$\dot{R}_{o1} = R_{o1} + T_{o1}T_{i2} \sum_{n=1}^{\infty} \frac{(R_{i2}R_{o2})^n}{R_{i2}} e^{-i\omega n\tau_2}, \quad (\text{IV.25})$$

which can be expressed as:

$$\dot{R}_{o1} = R_{o1} + \frac{T_{o1}T_{i2}R_{o2}}{e^{i\omega\tau_2} - R_{i2}R_{o2}}, \quad (\text{IV.26})$$

for $|R_{i2}R_{o2}| < 1$.

The effective reflection coefficient \dot{R}_{o1} can be implemented in the reverberation transfer functions \mathcal{R}_1^+ and \mathcal{R}_1^- derived in §IV.1.2 to account for downstream reflections. This is done simply by substituting R_{o1} with \dot{R}_{o1} . For example, the upstream reverberation transfer function for the acoustic pressure resulting from an acoustic wave π_{s1}^+ is:

$$\dot{\mathcal{R}}_1^+ = \frac{\widehat{p}'/\gamma\bar{p}|_{s1}}{\widehat{\pi}_{s1}^+} = \frac{e^{-i\omega\tau_{p1}} + \dot{R}_{o1}e^{-i\omega\tau_{q1}}}{1 - R_{i1}\dot{R}_{o1}e^{-i\omega\tau_1}}. \quad (\text{IV.27})$$

If the outlet of the second chamber is anechoic ($R_{o2} = 0$), then we recover $\dot{R}_{o1} = R_{o1}$, and the second chamber has no effect on the first ($\dot{\mathcal{R}}_1 = \mathcal{R}_1$).

Acoustic pressure in the second chamber

In the second chamber, the acoustic pressure is affected by the transmitted component of the upstream acoustic sources π_{s1}^+ and π_{s1}^- .

Forward-propagating waves impinging at the nozzle π_{s1}^+ are transmitted with a coefficient T_{o1} , as well as reflected with a coefficient R_{o1} . The reflected component $R_{o1}\pi_{s1}^+$ is reflected at the inlet of the first chamber, and returns to the interface with an amplitude $R_{o1}R_{i1}\pi_{s1}^+$, and

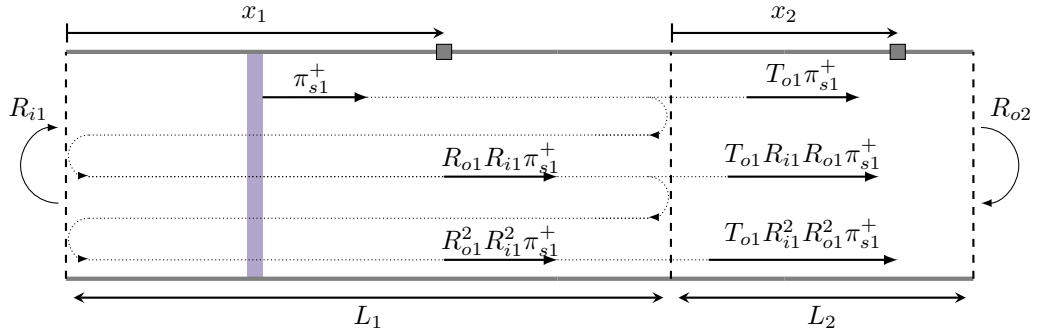


Figure IV.7: The forward-propagating wave π_{s1}^+ generated by the upstream acoustic source is successively reflected at the inlet and outlet of the first chamber, effectively resulting in several transmissions.

Amplitude	Distance travelled	Time-delay
$T_{o1}\pi_{s1}^+$	0	0
$T_{o1}R_{o1}R_{i1}\pi_{s1}^+$	$2L_1$	τ_1
$T_{o1}R_{o1}^2R_{i1}^2\pi_{s1}^+$	$4L_1$	$2\tau_1$
$T_{o1}R_{o1}^3R_{i1}^3\pi_{s1}^+$	$6L_1$	$3\tau_1$
\vdots	\vdots	\vdots

Table IV.4: Amplitudes, distances travelled and time delays associated to the first four transmissions of the forward-propagating acoustic wave π_{s1}^+ .

a time delay τ_1 . Part of this wave is transmitted into the second chamber with an amplitude $T_{o1}R_{o1}R_{i1}\pi_{s1}^+$, while another part is reflected yet again with an amplitude $T_{o1}R_{o2}R_{i2}\pi_{s1}^+$. The latter wave will lead to yet another reflection. This is shown diagrammatically in figure IV.6. These amplitudes and time delays associated to the transmissions of π_{s1}^+ are shown in table IV.3. These effectively act as an acoustic source π_{s2}^+ at the inlet of the second chamber.

We can define an effective transmission coefficient \hat{T}_{o1}^* , to incorporate the effect of upstream reverberation:

$$\hat{T}_{o1}^* = T_{o1} + R_{o1}R_{i1}T_{o1}e^{-i\omega\tau_1} + R_{o1}^2R_{i1}^2T_{o1}e^{-2i\omega\tau_1} + R_{o1}^3R_{i1}^3T_{o1}e^{-3i\omega\tau_1} + \dots \quad (\text{IV.28})$$

or

$$\hat{T}_{o1}^* = T_{o1} \left(1 + \sum_{n=1}^{\infty} (R_{o1}R_{i1})^n e^{-i\omega n\tau_1} \right), \quad (\text{IV.29})$$

IV. REVERBERATION

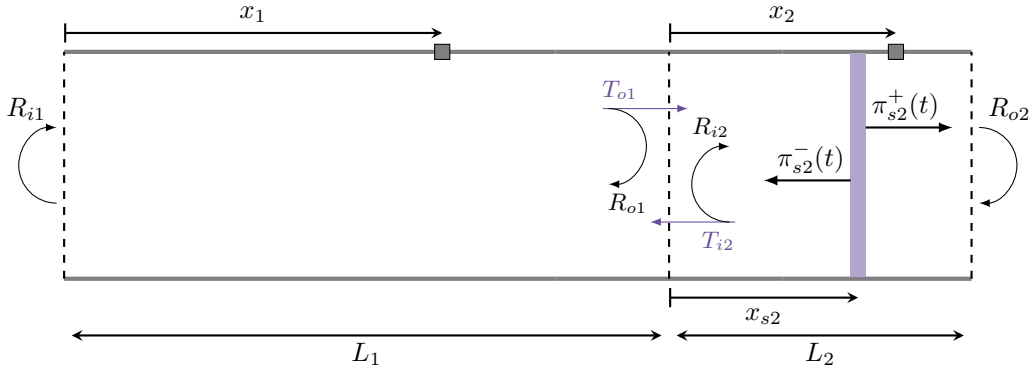


Figure IV.8: Bicameral system: a downstream acoustic source at a location x_{s2} generates forward- and backward-propagating waves $\pi_{s2}^+(t)$ and $\pi_{s2}^-(t)$.

which can be expressed as:

$$\hat{T}_{o1}^* = T_{o1} \left(\frac{1}{1 - R_{o1}R_{i1}e^{-i\omega\tau_1}} \right). \quad (\text{IV.30})$$

for $|R_{i1}R_{o1}| < 1$.

The transmissions of π_{s1}^+ and π_{s1}^- through the interface can be thought of as an acoustic source π_{s2}^+ at the inlet of the second chamber. We can define transmissive transfer functions $\hat{\mathcal{T}}_1^+$ and $\hat{\mathcal{T}}_1^-$ to relate the amplitude of the upstream acoustic sources π_{s1}^+ and π_{s1}^- to the strength of this effective downstream acoustic source π_{s2}^+ :

$$\hat{\mathcal{T}}_1^+ = \hat{T}_{o1}^* e^{-i\omega\tau_{p1}}, \quad (\text{IV.31})$$

$$\hat{\mathcal{T}}_1^- = \hat{T}_{o1}^* R_{i1} e^{-i\omega\tau_{s1}} \quad (\text{IV.32})$$

where τ_{p1} and τ_{s1} are evaluated at $x_1 = L_1$.

IV.2.2 Downstream arbitrary source signal

We now consider an acoustic source located in the second (downstream) chamber, generating forward- and backward-propagating acoustic waves $\pi_{s2}^+(t)$ and $\pi_{s2}^-(t)$ as shown in figure IV.8.

Amplitude	Distance travelled	Time-delay
$T_{i2}\pi_{s2}^-$	0	0
$T_{i2}R_{i2}R_{o2}\pi_{s2}^-$	$2L_2$	τ_2
$T_{i2}R_{i2}^2R_{o2}^2\pi_{s2}^-$	$4L_2$	$2\tau_2$
$T_{i2}R_{i2}^3R_{o2}^3\pi_{s2}^-$	$6L_2$	$3\tau_2$
\vdots	\vdots	\vdots

Table IV.5: Amplitudes, distances travelled and time-delays associated to the first four transmissions of the backward-propagating acoustic wave π_{s2}^- .

Acoustic pressure in the first chamber

The effect of the downstream sources π_{s2}^+ and π_{s2}^- on the pressure in the first chamber can be understood in terms of wave transmissions across the interface. For example, a backward-propagating wave downstream of the nozzle π_{s2}^- will lead to several transmitted waves, as shown in table IV.5.

Once again we can define an effective transmission coefficient from the second chamber to the first:

$$\hat{T}_{i2}^* = T_{i2} \left(\frac{1}{1 - R_{o2}R_{i2}e^{-i\omega\tau_2}} \right). \quad (\text{IV.33})$$

for $|R_{i2}R_{o2}| < 1$.

The transmitted waves due to the downstream wave π_{s2}^- are manifested in the first chamber as a source π_{s1}^- located at the interface, such that $\pi_{s1}^- = \hat{T}_{i2}^*\pi_{s2}^-$. We can define transmissive transfer functions $\hat{\mathcal{T}}_2^+$ and $\hat{\mathcal{T}}_2^-$ to relate the amplitude of the downstream acoustic sources π_{s2}^+ and π_{s2}^- to the strength of this effective downstream acoustic source π_{s1}^- :

$$\hat{\mathcal{T}}_2^+ = \hat{T}_{i2}^*R_{o2}e^{-i\omega\tau_{q2}}, \quad (\text{IV.34})$$

$$\hat{\mathcal{T}}_2^- = \hat{T}_{i2}^*e^{-i\omega\tau_{r2}}, \quad (\text{IV.35})$$

where τ_{q2} and τ_{r2} are evaluated at $x_2 = 0$.

Acoustic pressure in the second chamber

As before, the effect on the first chamber on the second appears in the form of additional reflections at the inlet of the second chamber. These reflections are shown in table IV.6.

IV. REVERBERATION

Amplitude	Distance travelled	Time-delay
$R_{i2}\pi_{s2}^-$	0	0
$T_{i2}R_{i1}T_{o1}\pi_{s2}^-$	$2L_2$	τ_2
$T_{i2}R_{i1}^2R_{o1}T_{o1}\pi_{s2}^-$	$4L_2$	$2\tau_2$
$T_{i2}R_{i1}^3R_{o1}^2T_{o1}\pi_{s2}^-$	$6L_2$	$3\tau_2$
\vdots	\vdots	\vdots

Table IV.6: Amplitudes, distances travelled and time-delays associated to the first four reflections of the backward-propagating acoustic wave π_{s2}^- .

The effective reflection coefficient \dot{R}_{i2}^* is:

$$\dot{R}_{i2}^* = R_{i2} + \frac{T_{i2}T_{o1}R_{o1}}{e^{i\omega\tau_1} - R_{i1}R_{o1}}, \quad (\text{IV.36})$$

for $|R_{i1}R_{o1}| < 1$.

This effective reflection coefficient can be implemented in the reverberation transfer functions \mathcal{R}_2^+ and \mathcal{R}_2^- derived in §IV.1.2 to account for upstream reflections. This is done simply by substituting R_{i2} with \dot{R}_{i2}^* . The downstream reverberation transfer function for the acoustic pressure resulting from an acoustic wave π_{s2}^+ is:

$$\dot{\mathcal{R}}_2^+ = \frac{\widehat{p}'/\gamma\bar{p}}{\widehat{\pi}_{s2}^+} = \frac{e^{-i\omega\tau_{p2}-\alpha l_{p2}} + R_{o2}e^{-i\omega\tau_{q2}-\alpha l_{q2}}}{1 - \dot{R}_{i2}^*R_{o2}e^{-i\omega\tau_2-2\alpha L_2}}. \quad (\text{IV.37})$$

If the inlet of the first chamber is anechoic ($R_{i1} = 0$), then we recover $\dot{R}_{i2}^* = R_{i2}$, and the first chamber has no effect on the second ($\dot{\mathcal{R}}_2^+ = \mathcal{R}_2^+$). If the outlet of the second chamber is anechoic ($R_{o2} = 0$), then $\dot{\mathcal{R}}_2^+$ is simply a time delay representing the propagation of the source wave to the measurement location.

Reverberation and transmission transfer functions

We have derived frequency-dependent acoustic transfer functions $\dot{\mathcal{R}}^+$, $\dot{\mathcal{R}}^-$, $\dot{\mathcal{T}}^+$ and $\dot{\mathcal{T}}^-$, relating acoustic source signals $\widehat{\pi}_{s1}^+$, $\widehat{\pi}_{s1}^-$, $\widehat{\pi}_{s2}^+$ and $\widehat{\pi}_{s2}^-$ to the resulting acoustic pressures upstream and downstream of the interface. The full expressions for these transfer functions (including the effect of acoustic attenuation) are shown in in Appendix B.

The overall acoustic pressures in the first and second chambers are:

$$\left. \frac{\widehat{p}'}{\gamma \bar{p}} \right|_1 (x_1, \omega) = \mathcal{R}_1^+ \widehat{\pi}_{s1}^+ + \mathcal{R}_1^- \widehat{\pi}_{s1}^- + \mathcal{R}_1^- \left(\mathcal{T}_1^+ \widehat{\pi}_{s2}^+ + \mathcal{T}_1^- \widehat{\pi}_{s2}^- \right), \quad (\text{IV.38})$$

$$\left. \frac{\widehat{p}'}{\gamma \bar{p}} \right|_2 (x_2, \omega) = \mathcal{R}_2^+ \widehat{\pi}_{s2}^+ + \mathcal{R}_2^- \widehat{\pi}_{s2}^- + \mathcal{R}_2^- \left(\mathcal{T}_2^+ \widehat{\pi}_{s1}^+ + \mathcal{T}_2^- \widehat{\pi}_{s1}^- \right). \quad (\text{IV.39})$$

DIRECT AND INDIRECT NOISE MODEL

The results presented in §II–IV enable us to assemble a complete model of direct and indirect noise generation in a one-dimensional system. We apply this model to a system containing a wave source with a compact nozzle further downstream as show in in figure V.1.

Owing to the superposition principle, the total acoustic pressure is a sum of the acoustic pressures due to the direct, entropic and compositional noise sources:

$$\frac{p'}{\gamma\bar{p}}(x, t) = \frac{p'}{\gamma\bar{p}}\Big|_d(x, t) + \frac{p'}{\gamma\bar{p}}\Big|_\sigma(x, t) + \frac{p'}{\gamma\bar{p}}\Big|_\xi(x, t). \quad (\text{V.1})$$

In this section, expressions for each of the pressure contributions in (V.1) are shown for both unicameral and bicameral systems. These will be applied to a variety of scenarios, with the goal of comparing the results with data from a model experiment on direct and indirect noise (see §VII–IX). These results are implemented in a set of limit cases to showcase the range of behaviours expected from systems of this type.

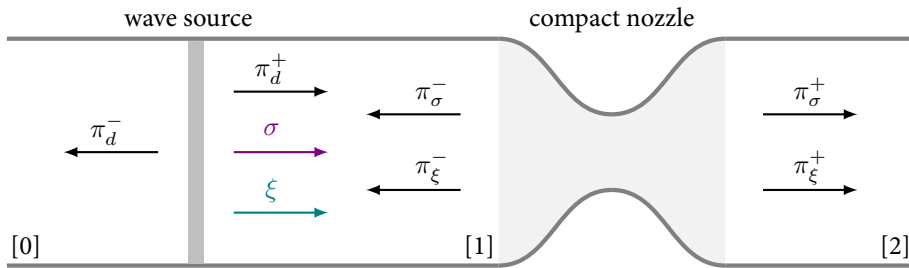


Figure V.1: A one-dimensional wave generator generates forward and backward direct acoustic waves π_d^- and π_d^+ along with entropic and compositional waves σ and ξ . The convected waves generate corresponding forward and backward indirect acoustic waves (π_σ^+ , π_σ^- , π_ξ^+ and π_ξ^-) as they are convected through the nozzle.

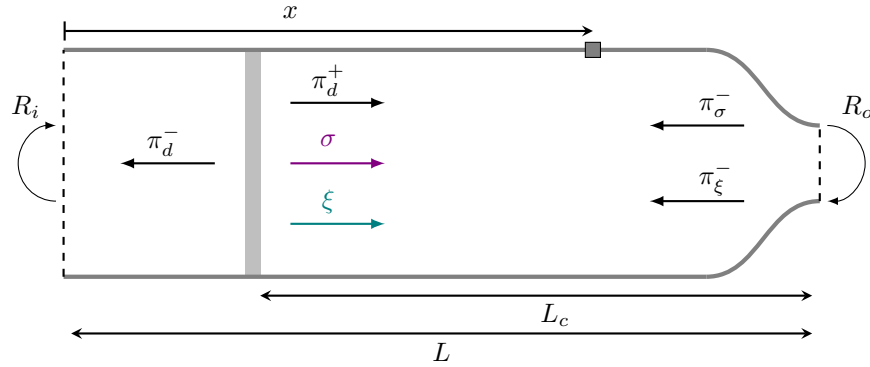


Figure V.2: Unicameral system: a wave generator produces direct noise and convected waves, which produce indirect noise after propagating across a convective length L_c .

The model can also be used to shed some light on the relative importance of direct and indirect noise. Building on the approach of Leyko et al.⁵³, analytical indirect to direct noise ratios are obtained for the simple case of a cold flame (see §II.4.1). Finally, we present a method to extract information about direct and indirect noise sources from acoustic pressure signals. This ‘source identification’ technique can be used to separate direct and indirect noise in experimental data.

V.1 Unicameral model

The results in §IV.1 can be applied to the reverberation of direct and indirect noise. For a unicameral system (i.e. a single reverberating chamber) where the outlet is a nozzle, the system contains a direct noise source (generating π_d^+ and π_d^-), and an indirect noise source (generating π_σ^- and π_ξ^-), as shown in figure V.2.

The indirect noise source is activated once the entropic and compositional waves have propagated from the wave source to the nozzle over a convective length L_c , which corresponds to a convective time delay $\tau_c = L_c/\bar{u}$.

The forward-propagating indirect noise (π_σ^+ , π_ξ^+) is not considered since it propagates downstream of the outlet. Similarly, noise transmitted at the inlet and outlet is not factored into the model. This is good approximation in the cases where the outlet nozzle is choked or supersonic (in which case downstream waves cannot propagate upstream past the nozzle), or if transmitted waves are not reflected once they leave the system.

V.1.1 Rectangular pulses

Assuming the direct and indirect acoustic signals are effectively rectangular pulses, we can employ (IV.6) and (IV.9) to calculate the acoustic pressure in the system. If we consider that the pulse duration is much longer than the system's acoustic time-scale ($t_e \gg \tau$), then the expressions may be approximated and combined to obtain hybrid functions for the acoustic pressure contributions:

$$\frac{p'}{\gamma\bar{p}} \Big|_d (t) \approx \begin{cases} (\pi_d^+ + \pi_d^- R_i)(1 + R_o) \frac{1 - (R_i R_o)^{\lfloor \frac{t+T}{T} \rfloor}}{1 - R_i R_o} & \text{for } t \in [0, t_e] \\ 2\pi_d (R_i R_o)^{\lfloor \frac{t-t_e+\tau}{\tau} \rfloor} & \text{for } t \in]t_e, +\infty[\end{cases} \quad (\text{V.2})$$

$$\frac{p'}{\gamma\bar{p}} \Big|_\sigma (t) \approx \begin{cases} \pi_\sigma^- (1 + R_i) \frac{1 - (R_i R_o)^{\lfloor \frac{t-\tau_c+T}{T} \rfloor}}{1 - R_i R_o} & \text{for } t \in [\tau_c, t_e + \tau_c] \\ 2\pi_\sigma (R_i R_o)^{\lfloor \frac{t-t_e-\tau_c+\tau}{\tau} \rfloor} & \text{for } t \in]t_e + \tau_c, +\infty[\end{cases} \quad (\text{V.3})$$

$$\frac{p'}{\gamma\bar{p}} \Big|_\xi (t) \approx \begin{cases} \pi_\xi^- (1 + R_i) \frac{1 - (R_i R_o)^{\lfloor \frac{t-\tau_c+T}{T} \rfloor}}{1 - R_i R_o} & \text{for } t \in [\tau_c, t_e + \tau_c] \\ \pi_\xi (R_i R_o)^{\lfloor \frac{t-t_e-\tau_c+\tau}{\tau} \rfloor} & \text{for } t \in]t_e + \tau_c, +\infty[\end{cases} \quad (\text{V.4})$$

The wave amplitudes π_d , π_σ and π_ξ describing acoustic decay are determined based on (IV.8). Note that the spatial dependency of $p'/\gamma\bar{p}$ has disappeared due to the low frequency assumption (according to which the acoustic pressure is the same throughout the system).

Equations (V.2), (V.3) and (V.4) are straightforward expressions for the evolution of acoustic pressure due to the successive reflections of direct, entropic and compositional noise respectively. These show that the pressure in the duct closely follows a power law, governed by the acoustic time-scale of the system τ , and the product of the inlet and outlet reflection coefficients $R_i R_o$.

V.1.2 Arbitrary pulses

The reverberation transfer functions can also be used to construct an analytical model for direct and indirect noise. Unlike the rectangular pulse approximation, this model can be applied to arbitrary source signals. Knowledge of the system's dimensions, reflection coefficients, and of the imposed perturbations enables the acoustic pressure due to direct and indirect acoustic

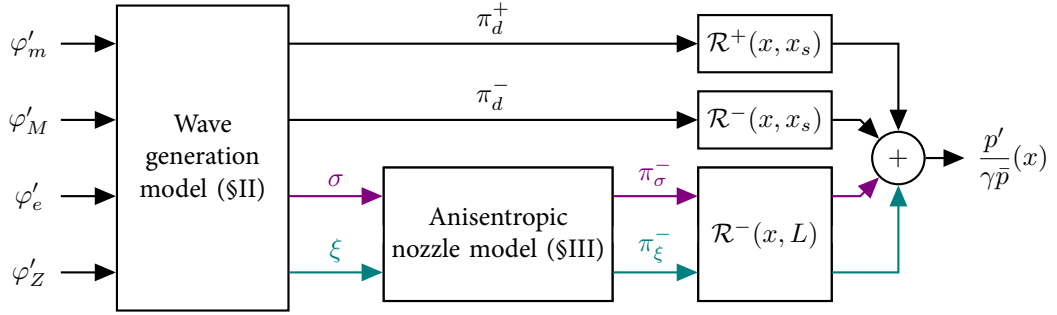


Figure V.3: Block diagram representing the analytical model for a unicameral reverberating system.

waves to be calculated:

$$\left. \frac{\hat{p}'}{\gamma\bar{p}} \right|_d (x, \omega) = \mathcal{R}^+(x, x_s) \widehat{\pi}_d^+(\omega) + \mathcal{R}^-(x, x_s) \widehat{\pi}_d^-(\omega), \quad (\text{V.5})$$

$$\left. \frac{\hat{p}'}{\gamma\bar{p}} \right|_\sigma (x, \omega) = \mathcal{R}^-(x, L) \widehat{\pi}_\sigma^-(\omega), \quad (\text{V.6})$$

$$\left. \frac{\hat{p}'}{\gamma\bar{p}} \right|_\xi (x, \omega) = \mathcal{R}^-(x, L) \widehat{\pi}_\xi^-(\omega), \quad (\text{V.7})$$

where the reverberation transfer functions for indirect noise have been computed for $x_s = L$, since they are generated at the outlet nozzle.

The amplitudes of the direct acoustic waves π_d^+ , π_d^- and convected waves σ , ξ can be computed using the wave generation model presented in §II. The indirect noise generated at the nozzle can be computed using the anisotropic nozzle transfer functions presented in §III using a suitable anisotropy factor Λ . These transfer functions also yield the acoustic reflection coefficients of the nozzle, which are an input of the reverberation transfer functions. The complete analytical model is shown in figure V.3

V.2 Bicameral model

The results in §IV.2 can be applied to the reverberation of direct and indirect noise in bicameral systems. This allows us to account for the forward-propagating components of indirect noise

V. DIRECT AND INDIRECT NOISE MODEL

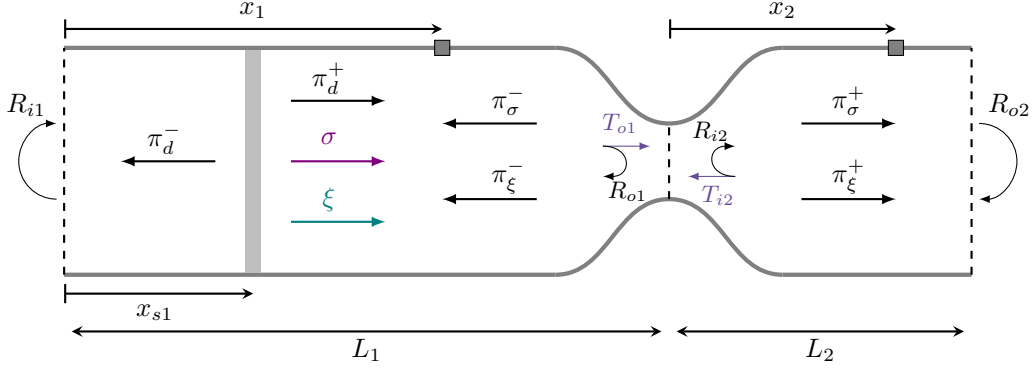


Figure V.4: Bicameral system: a wave generator produces direct noise and convected waves, which produce indirect noise after propagating through a convective length L_c .

π_σ^+ and π_ξ^+ , as shown in figure V.4.

Transmission transfer functions are now required to relate upstream and downstream sound sources. In the first chamber, the acoustic pressure contributions are:

$$\left. \frac{\hat{p}'}{\gamma \bar{p}} \right|_d (x_1, \omega) = \hat{\mathcal{R}}_1^+(x_1, x_{s1}) \hat{\pi}_d^+(\omega) + \hat{\mathcal{R}}_1^-(x_1, x_{s1}) \hat{\pi}_d^-(\omega), \quad (\text{V.8})$$

$$\left. \frac{\hat{p}'}{\gamma \bar{p}} \right|_\sigma (x_1, \omega) = \hat{\mathcal{R}}_1^-(x_1, L_1) \left(\hat{\pi}_\sigma^-(\omega) + \hat{\mathcal{T}}_2^+ \hat{\pi}_\sigma^+(\omega) \right), \quad (\text{V.9})$$

$$\left. \frac{\hat{p}'}{\gamma \bar{p}} \right|_\xi (x_1, \omega) = \hat{\mathcal{R}}_1^-(x_1, L_1) \left(\hat{\pi}_\xi^-(\omega) + \hat{\mathcal{T}}_2^+ \hat{\pi}_\xi^+(\omega) \right). \quad (\text{V.10})$$

For the acoustic pressure in the second chamber, we have:

$$\left. \frac{\hat{p}'}{\gamma \bar{p}} \right|_d (x_2, \omega) = \hat{\mathcal{R}}_2^+(x_2, 0) \left(\hat{\mathcal{T}}_1^+(L_1, x_{s1}) \hat{\pi}_d^+(\omega) + \hat{\mathcal{T}}_1^-(L_1, x_{s1}) \hat{\pi}_d^-(\omega) \right), \quad (\text{V.11})$$

$$\left. \frac{\hat{p}'}{\gamma \bar{p}} \right|_\sigma (x_2, \omega) = \hat{\mathcal{R}}_2^+(x_2, 0) \left(\hat{\pi}_\sigma^+(\omega) + \hat{\mathcal{T}}_1^-(L_1, L_1) \hat{\pi}_\sigma^-(\omega) \right), \quad (\text{V.12})$$

$$\left. \frac{\hat{p}'}{\gamma \bar{p}} \right|_\xi (x_2, \omega) = \hat{\mathcal{R}}_2^+(x_2, 0) \left(\hat{\pi}_\xi^+(\omega) + \hat{\mathcal{T}}_1^-(L_1, L_1) \hat{\pi}_\xi^-(\omega) \right). \quad (\text{V.13})$$

The analytical models for the overall acoustic pressures upstream and downstream of the nozzle are shown diagrammatically in figures V.5 and V.6.

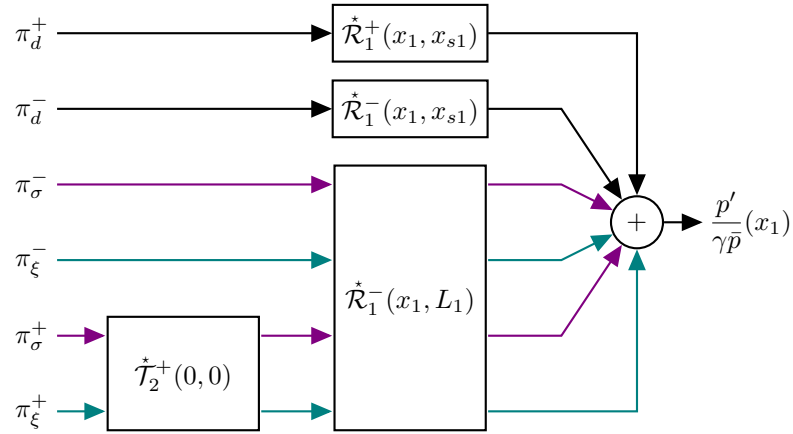


Figure V.5: Block diagram representing the analytical model for the upstream pressure in a bicameral reverberating system.

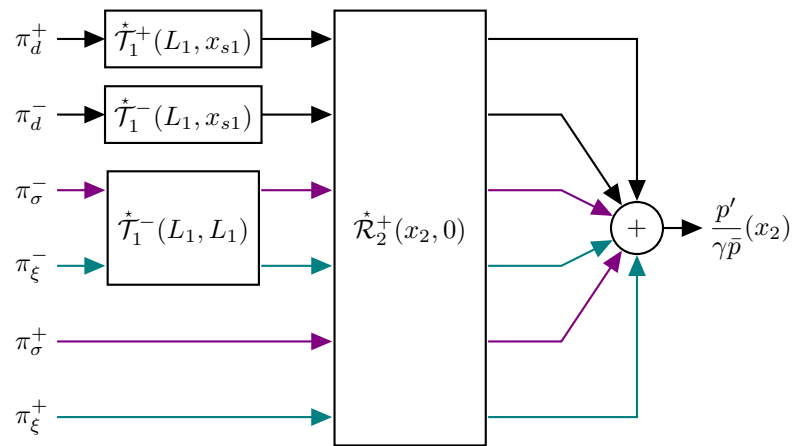


Figure V.6: Block diagram representing the analytical model for the downstream pressure in a bicameral reverberating system.

V.3 Limit cases

The models in §V.1 can be used to compute the acoustic pressure in unicameral reflective systems. While these expressions assume ideal conditions (one-dimensional wave field, localised reflections), they may be used to show some of the limit cases for this type of system.

This section presents eight limit cases showcasing the range of behaviours that may be displayed by model experiments on indirect noise. Cases I–IV examine the influence of acoustic reflections on direct noise, while cases V–VII examine the interaction between direct and indirect noise. Case VIII corresponds to the case where the forcing acoustic pulse is not rectangular. All cases correspond to the geometry shown in figure V.2, where the wave generator is located $x_s = 1$ m downstream of the inlet, and the total length is $L = 3$ m. A pressure sensor is located $x = 2$ m downstream of the inlet. Acoustic reflections occur at the inlet and outlet of the duct (specified by R_i and R_o respectively). Acoustic attenuation is neglected.

The expressions in §V.1.1 assume low-frequency perturbations, which in this case corresponds to $t_e \gg \tau$, i.e. the pulse is much longer than the acoustic time-scale. To place ourselves in this scenario, we take $t_e = 200$ ms for all cases, with $\tau \approx 17.5$ ms depending on the case (the sound speed is taken as $\bar{c} = 345$ m s⁻¹). These values are broadly representative of the DLR EWG⁴ and VWG⁴⁶ experiments, as well as the Cambridge Wave Generator presented in §VI.

As a point of comparison, the acoustic pressures for cases I–VIII are also computed numerically using the general model for arbitrary pulses (§V.1.2). The time-domain formulation of (IV.13) is used rather than the reverberation transfer functions to avoid the Gibbs phenomenon (since in this case the input signal is a discontinuous piecewise function).

V.3.1 Cases I–IV: Direct noise

In cases I–IV, we consider that there is no indirect noise generation at the outlet, meaning that only direct noise is generated ($\pi_\sigma^- = \pi_\xi^- = 0$). For simplicity, the forcing acoustic signal is considered to be a rectangular pulse lasting $t_e = 200$ ms, with $\pi_d^+ = \pi_d^- = 10^{-5}$. The reflection coefficients used for each case are listed in table V.1. These are chosen to cover a range of limit behaviours. The acoustic pressure histories for cases I–IV are shown in figure V.7.

In case I, the system is anechoic ($R_i = R_o = 0$). As a result, the only contribution to the

Limit case	Description	R_i	R_o
I	Anechoic	0	0
II	Fully reflective	0.9999	1
III	Open-ended	0.75	-1
IV	Partial Reflections	0.75	0.25 \rightarrow 0.75

Table V.1: Description of limit cases I-IV with corresponding inlet and outlet reflection coefficients R_i and R_o .

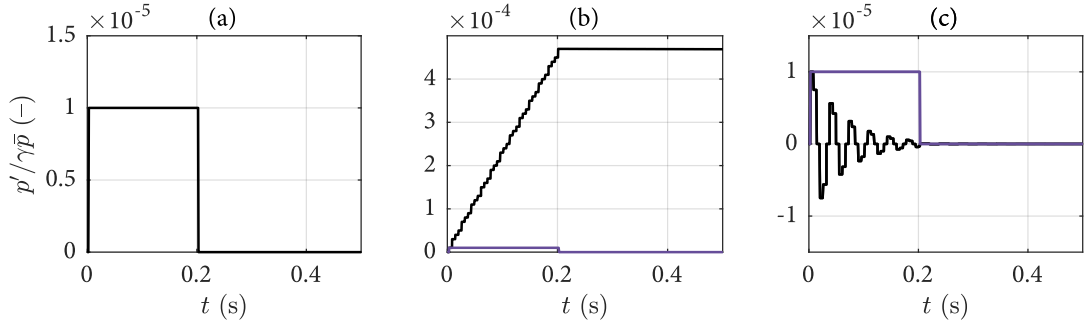


Figure V.7: Acoustic pressure history $p'/\gamma\bar{p}$ at $x = 2$ m (—) and case I results (for reference) (—). (a) case I: Anechoic (b) case II: Fully reflective (c) case III: Open-ended.

acoustic pressure at the pressure measurement location $x = 1$ m is π_d^+ . The acoustic pressure $p'/\gamma\bar{p}(x, t)$ rises sharply to a maximum value of $\pi_d^+ = 10^{-5}$ at $t = \tau_p$, and falls back to 0 at $t = t_e + \tau_p$. As expected, this corresponds to a rectangular pulse (identical to the forcing pulse), with a time shift $\tau_p = \tau_x^+ - \tau_{x_s}^+$ due to the acoustic propagation time delay between the wave generator and the pressure measurement location.

A fully reflective system corresponds to $R_i = R_o = 1$, but the expressions derived in §IV.1.1 are not defined for $R_i R_o = 1$. A virtually identical result is obtained in case II by taking $R_i = 0.9999$ and $R_o = 1$. In this scenario, waves are (nearly) fully reflected at the boundaries of the system, and there are effectively no acoustic losses. Given that waves π_d^+ and π_d^- are being continuously generated for $t \leq t_e$, acoustic energy accumulates inside the system as acoustic waves repeatedly reflect at the boundaries with the same sign. As a result, the acoustic pressure rises gradually to reach a large value (approximately 45 times larger than in the anechoic case here).

Paying close attention to the acoustic pressure history reveals that the pressure does not rise continuously, but instead increases ‘step by step’. Each step corresponds to a wave being reflected at a boundary and adding to the total acoustic pressure. These steps are separated

V. DIRECT AND INDIRECT NOISE MODEL

by the acoustic time-scale τ , which is the time taken for a given acoustic wave to be reflected back to its original position. The ‘staircase’ aspect of the computed signal is not related to a numerical method, but is instead due to the fact that the pulse is perfectly rectangular. In a real situation, the forcing pulse is smoother, and a combination of fluid-mechanical effects (primarily mixing) make this aspect less pronounced. After the end of the pulse (once the wave generator is switched off), internal acoustic energy is conserved as there are no acoustic losses, and the pressure stays constant.

In case III, the inlet of the system is partially reflective ($R_i = 0.5$) and the outlet is open-ended ($R_o = -1$). This means that acoustic waves propagating downstream are reflected with a negative sign; instead of increasing the total acoustic pressure as in case II, these reflected waves decrease the acoustic pressure and interact destructively with incoming waves. The acoustic pressure oscillates around 0, bounded in the interval $[-\pi_d^+, \pi_d^+]$. The amplitude of these oscillations decreases with time. This is due to the partial reflections at the inlet, which make each successively reflected wave slightly smaller in amplitude than the previous one. Once the forcing pulse ends, the acoustic pressure quickly returns to zero. This behaviour is similar to the experimental measurements for case A in De Domenico et al.²⁰.

The results for case IV are shown in figure V.8 for (a) the analytical expressions for arbitrary acoustic signals (IV.13), (b) the full expressions for a rectangular pulse (equations (IV.6) and (IV.9)), and (c) the simplified expressions for a rectangular pulse (equation (V.2)). Case IV corresponds to the case where both the inlet and outlet of the system are partially reflective. As in case II, waves are positively reflected, leading to an overall increase of the acoustic pressure, but as shown in case III, the amplitudes of the partially reflected waves at the inlet decrease as time goes on.

As a result, the acoustic pressure converges towards a maximum value, which is consistent with (IV.7). For all values of R_o , the maximum acoustic pressure is higher than in case I (anechoic), but lower than in case II (fully reflective). Notably, as R_o is increased from 0.25 to 0.75, the acoustic pressure increases. The results given by the model for arbitrary source signals (a) and the the full expressions for rectangular pulses (b) are virtually identical. The simplified expressions for rectangular pulses however, show a coarser signal, due to the fact that small time delays are neglected. However, the signal converges towards the same maximum, and the overall growth rate (neglecting the slightly different step changes) is the same.

Once the wave generator is switched off at $t = 200$ ms, the acoustic pressure decays as acoustic energy leaves the system. Each discontinuous decrease corresponds to an acoustic

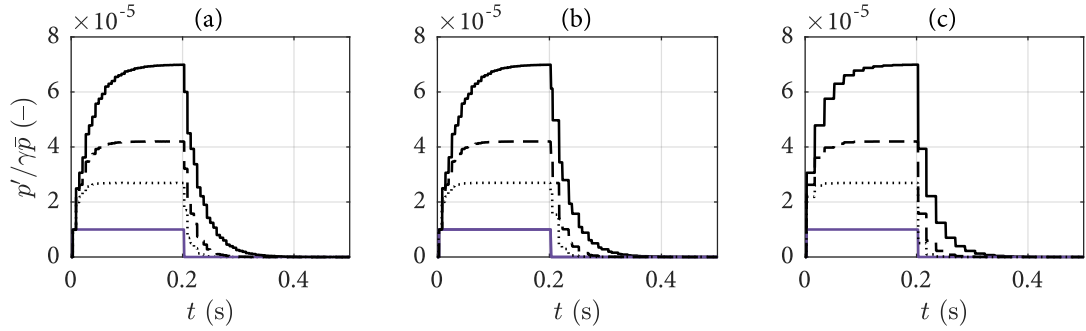


Figure V.8: Acoustic pressure history $p'/\gamma\bar{p}$ at $x = 2$ m and case I results (for reference) (—). (a) case IV: arbitrary source signal for $R_o = 0.25$ (⋯⋯), $R_o = 0.5$ (---), and $R_o = 0.75$ (—), (b) case IV: full expressions for a rectangular pulse, (c) case IV: simplified expression for a rectangular pulse.

wave reaching a boundary, at which point it loses a fraction $(1 - R_i$ or $1 - R_o)$ of its amplitude. Here, the analytical results (figure V.8 b,c) give a coarser result than the arbitrary source method (figure V.8 a). This is because of the simplifying assumptions made in §IV.1.1. Most notably, we have approximated the successive terms of four series as the terms of just two series, which explains why the pressure decays in larger steps in the analytical results. However, the decay rate is identical in all three simulations (e.g. the acoustic pressure falls to 10% of its maximum at $t = 273$ ms in all cases).

V.3.2 Cases V-VII: Direct and indirect noise

Cases V-VII highlight the behaviours of both direct and indirect noise. Here, we assume that there is flow acceleration downstream of the wave generator location, such that indirect noise is generated at the outlet. We consider rectangular pulses with $\pi_d^+ = \pi_d^- = 10^{-5}$ and $\pi_i^- = \pi_\sigma^- + \pi_\xi^- = -10^{-5}$ in all cases regardless of the flow conditions. In a real system, these values would vary based on the flow, but using constant values enables different cases to be compared on an even basis. For each case we vary the reflection coefficients, as well as the Mach number in the duct \bar{M} (which primarily affects the convective time delay τ_c). These parameters are shown in table V.2. The acoustic pressure histories for cases V-VII are shown in figure V.9.

In case V, the Mach number is relatively low, and there is a large convective time delay τ_c between the times at which direct and indirect noise are generated. In this case, we have $\tau_c > t_e$ meaning that entropy waves reach the outlet once direct noise is no longer being generated. This can be seen in the acoustic pressure histories, which shows a very clear temporal

V. DIRECT AND INDIRECT NOISE MODEL

Limit case	Description	R_i	R_o	\bar{M}
V	Anechoic	0	0	0.025
VI	Partial reflections (low Mach)	0.5	0.5	0.025
VII	Partial reflections	0.5	0.5	0.1

Table V.2: Description of limit cases V-VII with corresponding reflection coefficients R_i and R_o and Mach number \bar{M} .

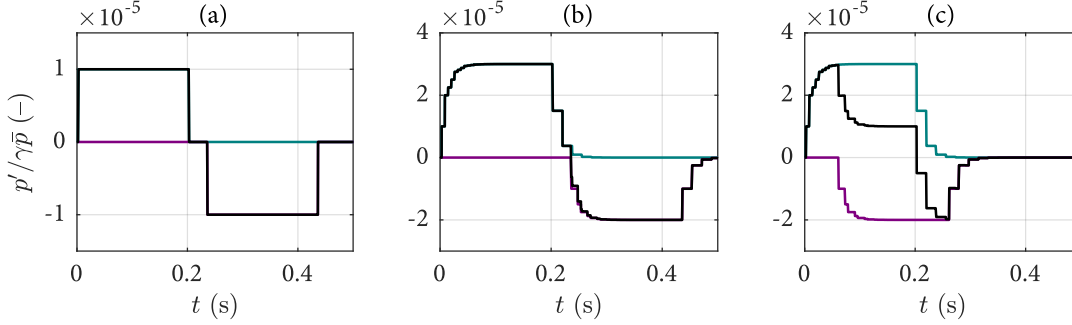


Figure V.9: Acoustic pressure history $p'/\gamma\bar{p}$ at $x = 2$ m of total noise (—), direct noise (—) and indirect noise (—). (a) case V: Anechoic (low Mach) (b) case VI: Partial reflections (low Mach) (c) case VII: Partial reflections.

separation between direct and indirect noise. As in case I, the direct noise appears as a rectangular pulse of duration t_e with a maximum value of $\pi_d = 10^{-5}$. The indirect noise is also a rectangular pulse, but time shifted by τ_c , with a maximum of π_i . The total acoustic pressure in the tube shows a positive pulse (corresponding to the direct noise, followed by a negative pulse (corresponding to indirect noise).

Case VI is identical to case V except that the Mach number in the system is four times larger (and the convective time delay τ_c is four times smaller as a result). We now have $\tau_c < t_e$, meaning that there is an overlap between the generation of direct and indirect noise. Once again, the total acoustic pressure corresponds to a positive pulse followed by a negative pulse. In this case however, direct and indirect noise interact destructively, and the duration of these pulses is reduced to τ_c . At the limit where the convective and acoustic time scales τ_c and τ are 0 (i.e. there is no separation between the entropy wave source and the outlet), then direct and indirect noise cancel each other out completely.

Case VI is a combination of cases IV and V, where direct and indirect noise are clearly separated, and there are partial reflections at the inlet and outlet of the system. As expected, direct and indirect noise are effectively amplified compared to case V (anechoic). Direct and

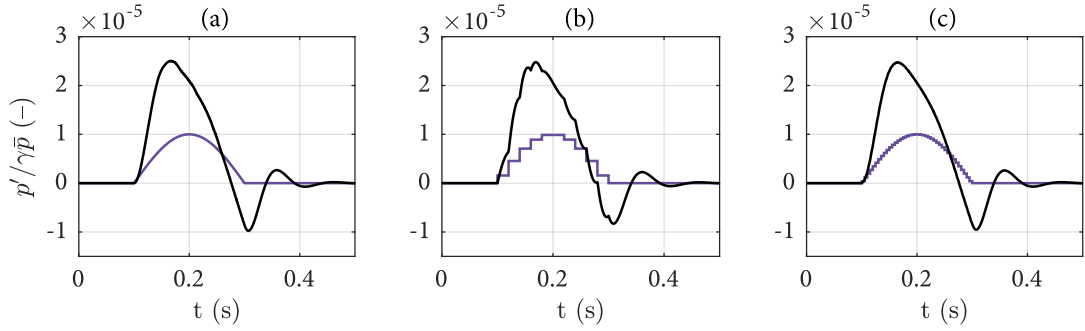


Figure V.10: Acoustic pressure history $p'/\gamma\bar{p}$ at $x = 2$ m for case VIII (—) with acoustic forcing signal (—) obtained with (a) the arbitrary source signal model (b) rectangular approximation for $\delta t = 20$ ms and (c) rectangular approximation for $\delta t = 5$ ms.

indirect noise are not amplified by the same factor however: while both of them give a maximum pressure amplitude of 10^{-5} in the anechoic case, they reach 3×10^{-5} and 2×10^{-5} respectively. This can be explained by the fact that indirect noise is produced directly at the outlet, unlike direct noise. This difference in amplification is made apparent in (V.17).

Case VII is similar to case VI, except that there is now a large overlap between direct and indirect noise due to the decreased convective time delay. This overlap results in a merging effect, whereby direct and indirect noise interact destructively and the overall acoustic pressure is reduced.

V.3.3 Case VIII: Non-rectangular pulse with complex reflections

While the compact nozzle model always gives real-valued reflection coefficients ($R \in \mathbb{R}$), in some cases it is useful to model an acoustic boundary as giving rise to a complex-valued reflection ($R \in \mathbb{C}$). For example, a complex-valued reflection coefficient was used to simulate the DLR Entropy Wave Generator experiment^{4,71,52,25}. The model presented here enables these complex reflections to be taken into account.

For case VIII, we consider an non-rectangular acoustic pulse, of the form $\sin^2(\omega t)$, lasting $t_e = 200$ ms with an amplitude $\pi^+ = 10^{-5}$ (shown in figure IV.4a). The reflection coefficients at the inlet and outlet are taken to be $R_i = 0.75$ and $R_o = 0.75 + 0.65i$ (complex reflection coefficient). The results are shown in figure V.10 for (a) the arbitrary source signal model (b) using a rectangular approximation with $\delta t = 20$ ms, and (c) using a rectangular approximation with $\delta t = 5$ ms.

The acoustic pressures computed using all three methods show an excellent agreement over-

V. DIRECT AND INDIRECT NOISE MODEL

all. Although the shape of the acoustic pressure signal obtained using the true source signal is not entirely replicated for $\delta t = 20$ ms, this small error becomes negligible for $\delta t = 5$ ms. The time step δt used in the semi-analytical method can be further reduced to achieve results virtually identical to those obtained with the arbitrary method. Unlike cases IV, the acoustic signal contains a negative pressure fluctuation even though the forcing signal is positive. This is because R_o is complex-valued; the introduction of a complex reflection coefficient can introduce oscillations not present in the original acoustic signal.

V.3.4 Direct and indirect noise ratios

One of the open questions in the study of combustion noise is the relative importance of direct and indirect noise. This is sometimes estimated by computing a noise ratio.

In their work, Leyko et al.⁵³ and Duran et al.²⁵ define an indirect to direct noise ratio η by considering the acoustic waves brought about by the direct and entropic noise mechanisms: π_d^+ and $\pi_i^+ = \pi_o^+$ respectively. Considering the noise downstream of the nozzle (subscript 2), they define the indirect to direct noise ratio as:

$$\eta_2 = \frac{\pi_i^+}{T_{o1}\pi_d^+} \quad (\text{V.14})$$

where T_{o1} is included to account for the transmission of direct noise through the nozzle.

The formulation above misses out the fact that the backward-propagating waves π_d^- and π_i^- also contribute to the noise downstream of the nozzle. Indeed, these waves are reflected at the inlet of the first chamber and transmitted downstream as $R_{i1}T_{o1}\pi_d^-$ and $R_{i1}T_{o1}\pi_i^-$.

Additionally, we must also take into account that acoustic waves can interfere either constructively or destructively depending on the system's time delays. For example, although π_i^+ and π_i^- are typically of opposite signs, we cannot say a priori that these waves will interfere destructively. For this reason, it is sensible to take the absolute value of individual waves. We can define a new indirect to direct noise ratio ζ to account for both of these effects:

$$\zeta_2 = \frac{|\pi_i^+| + |R_{i1}T_{o1}\pi_i^-|}{|T_{o1}\pi_d^+| + |T_{o1}R_{i1}\pi_d^-|}. \quad (\text{V.15})$$

The ratios η_2 and ζ_2 are only equivalent if $R_{i1} = 0$, which is not a good approximation of a combustion system. In fact, the inlet of a combustion chamber is often modelled as an area expansion²², which typically result in a reflection coefficient R_{i1} of the order of 1.

We can define a similar ratio ζ_1 upstream of the nozzle as :

$$\zeta_1 = \frac{|R_{o2}T_{i2}\pi_i^+| + |\pi_i^-|}{|\pi_d^+| + |R_{i1}\pi_d^-|} \quad (\text{V.16})$$

Analytical expressions for ζ_1 and ζ_2 can be obtained using the appropriate equations in §II–III.

Physically speaking, a more relevant result is the ratio of the direct and indirect pressure contributions p'_d and p'_i to the total acoustic pressure p' . Therefore we define a third indirect to direct noise ratio χ , with:

$$\chi_1 = \frac{p'_{i1}}{p'_{d1}}, \quad \chi_2 = \frac{p'_{i2}}{p'_{d2}}. \quad (\text{V.17})$$

We can compute χ_1 and χ_2 using reverberation transfer functions:

$$\chi_1 = \frac{|\dot{\mathcal{R}}_1^- \pi_i^-| + |\dot{\mathcal{R}}_1^- \dot{\mathcal{T}}_2^+ \pi_i^+|}{|\dot{\mathcal{R}}_1^+ \pi_d^+| + |\dot{\mathcal{R}}_1^- \pi_d^-|}, \quad \chi_2 = \frac{|\dot{\mathcal{R}}_2^+ \pi_i^+| + |\dot{\mathcal{R}}_2^+ \dot{\mathcal{T}}_1^- \pi_i^-|}{|\dot{\mathcal{R}}_2^+ \dot{\mathcal{T}}_1^+ \pi_d^+| + |\dot{\mathcal{R}}_2^+ \dot{\mathcal{T}}_1^- \pi_d^-|}. \quad (\text{V.18})$$

which simplifies to:

$$\chi_1 = \left| \frac{1 + R_{i1}}{1 + R_{o1}} \right| \zeta_1, \quad \chi_2 = \zeta_2. \quad (\text{V.19})$$

Upstream of the nozzle, the ratios χ_1 and ζ_1 are equivalent only if $|1 + R_{i1}| = |1 + R_{o1}|$. This highlights the importance of taking reflection coefficients into account when considering the noise ratio in a real system with acoustic reflections.

If the objective is to estimate the actual ratio of indirect to direct noise in a real system, then the wave ratio η gives the wrong result; the ratio χ must be used instead. This ratio requires the inlet and outlet reflection R_{i1} and R_{o2} to be known.

To examine the evolution of the noise ratio χ with the inlet and outlet reflection coefficients R_{i1} and R_{o1} , we repeat the analysis carried out by Leyko et al.⁵³. We consider the direct and entropic noise produced by a cold flame (see §II.4.1) followed by an isentropic nozzle, neglecting the dispersion and dissipation of entropic waves.

Using the nozzle transfer functions defined in §III, we can compute the entropic to direct noise ratios upstream and downstream of the nozzle χ_1 and χ_2 . These are shown in figure V.11 as a function of R_{i1} for $\bar{M}_1 = [0.025, 0.05, 0.1]$, and $\bar{M}_2 = [0.4, 0.8, 1.2, 1.6]$. The ratio η_2 computed by Leyko et al.⁵³ is shown for comparison (a factor 2 error in the subsonic cases in their original study has been corrected here).

The downstream ratio of indirect to direct noise χ_2 coincides with the ratio η_2 only for

V. DIRECT AND INDIRECT NOISE MODEL

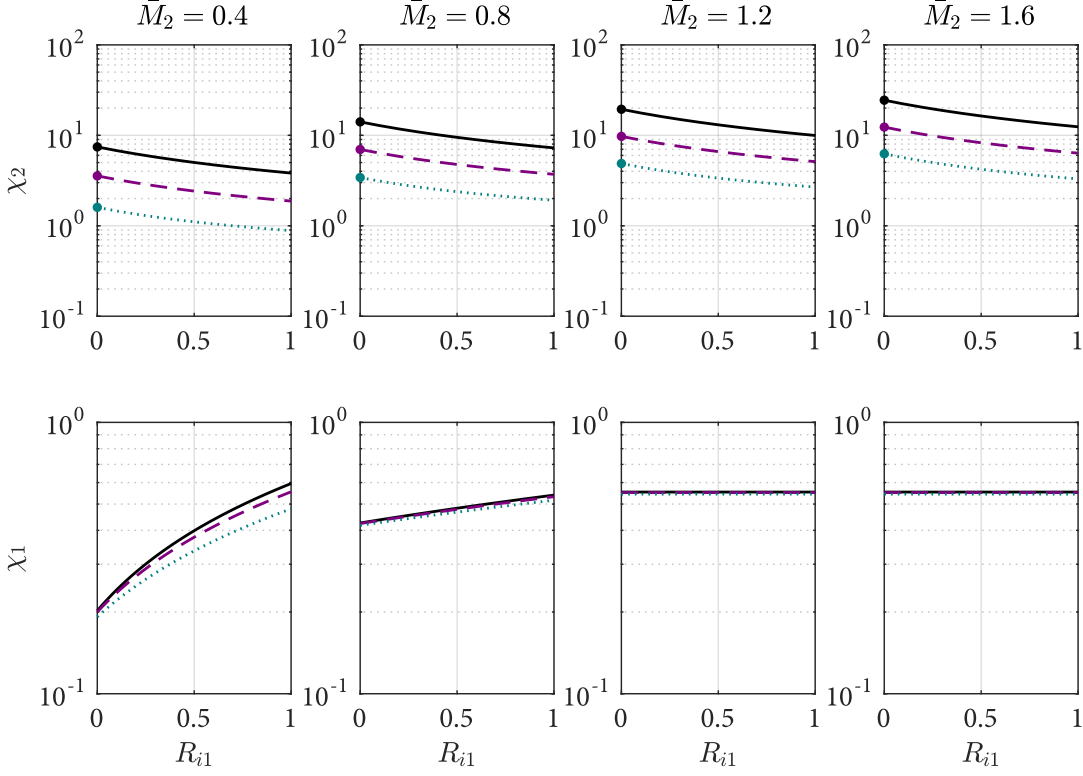


Figure V.11: Upstream and downstream indirect to direct noise ratios χ_1 and χ_2 with $\bar{M}_1 = 0.025$ (—), $\bar{M}_1 = 0.05$ (- - -), $\bar{M}_1 = 0.1$ (.....), and wave ratio η_2 for comparison with $\bar{M}_1 = 0.025$ (●), $\bar{M}_1 = 0.05$ (●), $\bar{M}_1 = 0.1$ (●).

$R_{i1} = 0$. Beyond this value, χ_2 decreases as R_{i1} is increased. This is due to the fact that backward-propagating direct wave π_d^- is larger than the backward-propagating indirect wave π_i^- : their contribution to the signal decreases the noise ratio. Overall, the results show that indirect noise is generally of the same order of magnitude as direct noise in the subsonic cases, and is an order of magnitude larger downstream of the nozzle in sonic or supersonic cases.

Conversely, the upstream ratio χ_1 increases as the inlet reflection R_{i1} is increased. This is not due to the relative amplitudes of direct and indirect waves, but rather to the effect of reverberation, which is responsible for the factor $|1 + R_{i1}|$ in (V.19). This is particularly apparent in the subsonic cases. In the supersonic cases ($\bar{M}_2 \geq 1$), the noise ratio is unaffected by the downstream wave π_i^+ since $T_{i2} = 0$.

V.4 Source and system identification

The results presented in §V.1–V.2 show how the analytical models can be used to simulate model experiments. However, this does not enable us to quantify how much direct, entropic and compositional noise is generated in the experimental cases. Indeed, the measured quantity in an experiment is typically is acoustic pressure, which is dependent on the system's properties and operating conditions. Ideally, we would like to obtain quantitative experimental measurements of direct, entropic and compositional acoustic waves (π_d^+ , π_d^- , π_σ^+ , π_σ^- , π_ξ^+ and π_ξ^-), which are not dependent on a particular system, and could be directly compared to theoretical models from the literature.

This can be achieved by solving an inverse problem, whereby the amplitudes of the acoustic sources π_d^+ , π_d^- , $\pi_i^- = \pi_\sigma^- + \pi_\xi^-$ and $\pi_i^+ = \pi_\sigma^+ + \pi_\xi^+$ are recovered from experimental pressure measurements of p' .

V.4.1 General method

Since the reverberation transfer functions are dependent on the pressure measurement location, then we can use four pressure measurements at different locations to solve for the direct and indirect source waves.

For example, if we have two pressure measurements upstream of the nozzle (at locations x_{11} and x_{22}) and two measurements downstream of the nozzle (at x_{21} and x_{22}), we can write:

$$\begin{bmatrix} \widehat{p}'/\gamma\bar{p}|_{11} \\ \widehat{p}'/\gamma\bar{p}|_{12} \\ \widehat{p}'/\gamma\bar{p}|_{21} \\ \widehat{p}'/\gamma\bar{p}|_{22} \end{bmatrix} = \begin{bmatrix} \mathcal{R}_1^+(x_{11}, xs1) & \mathcal{R}_1^-(x_{11}, xs1) & \mathcal{R}_1^-(x_{11}, L_1) & \mathcal{T}_2^+ \mathcal{R}_1^-(x_{11}, L_1) \\ \mathcal{R}_1^+(x_{12}, xs1) & \mathcal{R}_1^-(x_{12}, xs1) & \mathcal{R}_1^-(x_{12}, L_1) & \mathcal{T}_2^+ \mathcal{R}_1^-(x_{12}, L_1) \\ \mathcal{T}_1^+ \mathcal{R}_2^+(x_{21}, 0) & \mathcal{T}_1^- \mathcal{R}_2^+(x_{21}, 0) & \mathcal{T}_1^- \mathcal{R}_2^+(x_{21}, 0) & \mathcal{R}_2^+(x_{21}, 0) \\ \mathcal{T}_1^+ \mathcal{R}_2^+(x_{22}, 0) & \mathcal{T}_1^- \mathcal{R}_2^+(x_{22}, 0) & \mathcal{T}_1^- \mathcal{R}_2^+(x_{22}, 0) & \mathcal{R}_2^+(x_{22}, 0) \end{bmatrix} \begin{bmatrix} \widehat{\pi}_d^+ \\ \widehat{\pi}_d^- \\ \widehat{\pi}_i^+ \\ \widehat{\pi}_i^- \end{bmatrix}. \quad (\text{V.20})$$

which can be directly inverted to recover values for $\widehat{\pi}_d^+$, $\widehat{\pi}_d^-$, $\widehat{\pi}_i^+$ and $\widehat{\pi}_i^-$. This can be done for each frequency ω of interest to recover the full frequency dependence of the signals. It should be noted that the reverberation transfer functions can take values near zero at certain frequencies (close to the system's antiresonance frequencies in particular). The source identification inversion is likely to lead to spurious solutions in the vicinity of these frequencies.

V. DIRECT AND INDIRECT NOISE MODEL

In general, the problem may be ill-posed in which case some form of regularisation may be required (such as Tikhonov regularisation).

In certain conditions, fewer than four pressure measurements are required to solve the inversion problem. For example, we have shown in §II that the forward and backward-propagating direct noise waves are generally related as:

$$\pi_d^- = \frac{1 + \bar{M}_1}{1 - \bar{M}_1} \pi_d^+. \quad (\text{V.21})$$

Assuming the above allows us to solve for three waves ($\widehat{\pi}_d^+$, $\widehat{\pi}_i^+$, $\widehat{\pi}_i^-$) instead of four, meaning that only three pressure measurements are now required.

Furthermore, if we are dealing with a unicameral system (choked nozzle or no downstream reflections), then we can solve for only two waves in the upstream section of the system ($\widehat{\pi}_d^+$, $\widehat{\pi}_i^-$), which can be identified with only two pressure measurements.

The method above requires the system's length, acoustic reflection and transmission coefficients to be known. Alternatively, these parameters can be recovered as long as the source waves are known (i.e. system identification).

V.4.2 Application to model experiments

The aim of experiments such as the DLR Entropy Wave Generator⁴ and the Cambridge Wave Generator (§VI) is to identify and measure direct and indirect in model conditions. For these systems, several simplifications are appropriate (1) the acoustic frequencies of interest are low i.e. $He \approx 0$, (2) the Mach number upstream of the nozzle is small i.e. $\bar{M}_1 \ll 1$, (3) the measurement section downstream of the nozzle is anechoic i.e. $R_{o2} = 0$.

In the low frequency range ($\omega \approx 0$), the system can be described with a single acoustic transfer function \mathcal{R} , which is not a function of the transducer or source locations:

$$\mathcal{R}(\omega) = \frac{1}{1 - R_{i1}R_{o1}e^{-i\omega\tau_1 - 2\alpha L_1}}. \quad (\text{V.22})$$

The acoustic pressures upstream and downstream of the nozzle are then given by:

$$\left. \begin{aligned} \frac{\widehat{p}'}{\gamma \bar{p}}(x_1, \omega) &= \mathcal{R} \widehat{\pi}_1 \\ \frac{\widehat{p}'}{\gamma \bar{p}}(x_2, \omega) &= \mathcal{R} \widehat{\pi}_2 + \widehat{\pi}_i^+, \end{aligned} \right\} \quad (\text{V.23})$$

where $\widehat{\pi}_1$ and $\widehat{\pi}_2$ are effectively a weighted sum of all the acoustic sources:

$$\left. \begin{aligned} \widehat{\pi}_1 &= (1 + R_{o1})(1 + R_{i1}) \widehat{\pi}_d^+ + (1 + R_{i1}) \widehat{\pi}_i^- \\ \widehat{\pi}_2 &= T_{o1}(1 + R_{i1}) \widehat{\pi}_d^+ + T_{o1}R_{i1} \widehat{\pi}_i^-, \end{aligned} \right\} \quad (\text{V.24})$$

where we have used the fact that $\pi_d^+ = \pi_d^-$ as $\bar{M}_1 \rightarrow 0$.

The equations above can be used to identify direct and indirect noise sources, as well as the acoustic characteristics of the system. This is demonstrated on the Cambridge Wave Generator in §VI.4.2.

VI

THE CAMBRIDGE WAVE GENERATOR

Experiments are carried out on the Cambridge Wave Generator with the objective of investigating the interaction of acoustic, entropic and compositional waves with nozzles. These effects are notoriously difficult to measure in a combustor. Therefore, the Cambridge Wave Generator (CWG) is designed to operate in model conditions. The complexities associated to the presence of a turbulent flame are avoided by generating acoustic, entropic and compositional waves synthetically using interchangeable wave generators. Furthermore, the CWG is modular; its dimensions and boundaries can be varied to manipulate its acoustic properties. These features are used in tandem to generate, identify and measure direct, entropic and compositional noise.

VI.1 Experimental set-up

The CWG is essentially a flow duct, as shown in figure VI.1. A primary flow of air is supplied at up to 7 bar from the laboratory's compressed air supply. The air is filtered and fed through a 250 l tank to dampen unwanted flow oscillations. It is then delivered into the flow duct using a flexible hose (12 mm inner diameter, 0.7 m length) connected to a flat inlet flange. The flow rate of air is controlled using a mass flow controller (the details of which are presented in §VI.3.1). The flow duct itself has an inner diameter of 42.6 mm throughout, and consists of sections of either rigid polyvinyl chloride (PVC) or stainless steel (type 316).

Waves are induced inside the air flow using one of three wave generation modules. These modules are designed to generate a combination of acoustic, entropic and/or compositional waves. The frequency of these waves is kept deliberately low in order for flow elements to be acoustically compact. Depending on the configuration, the flow may be accelerated through

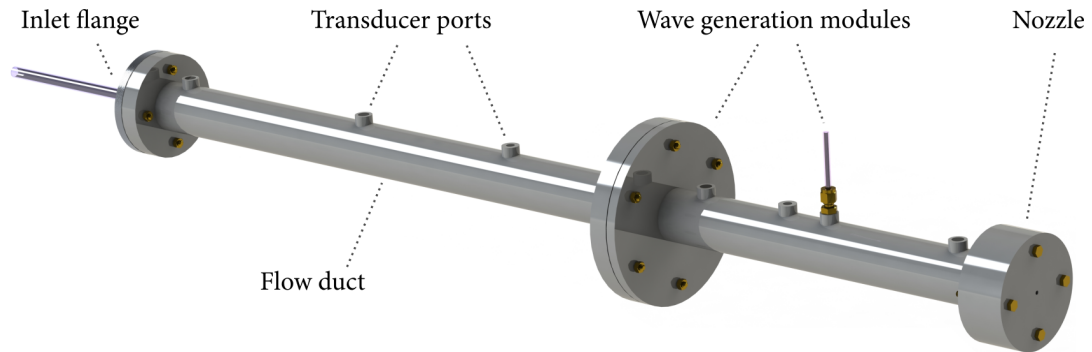


Figure VI.1: The Cambridge Wave Generator: air flows through a duct fitted with wave generation modules and a nozzle.

a nozzle, potentially generating indirect noise. Transducers can be used to measure the flow pressure or temperature at several locations along the duct.

VI.1.1 Configurations

The CWG can be operated in several configurations owing to its modular design. The purpose of these configurations is to modify the lengths governing the acoustic behaviour of the system. These are: (1) the upstream length L_1 from the duct inlet to the nozzle, (2) the downstream length L_2 from the nozzle to the outlet, and (3) the convective length L_c from the wave generator to the nozzle. There are three generic configurations: ‘long’, ‘short’ and ‘short extended’. These are shown in figure VI.2.

The first configuration (‘long’) is designed to minimise the effect of downstream acoustic reflections. This is achieved by placing a 60 m flexible duct downstream of the wave generation module. This has two main effects. First, the acoustic round-trip time is $\tau \approx 360$ ms (since $L_1 \approx 60$ m). In this case, the outlet is effectively anechoic for $t < 360$ ms. This enables individual acoustic pulses to be identified and separated. Second, since the convective length between the wave generation module is of the order of $L_c \approx 60$ m, we can expect any convected wave to have dissipated or dispersed before reaching the outlet, meaning that no indirect noise is generated. Pressure transducers are positioned at short distances upstream and downstream of the wave generation module. In this configuration, the CWG can be considered to be unicameral since there is no duct downstream of the nozzle (i.e. $L_2 = 0$ m).

In the second configuration (‘short’), the length between the wave generator and the nozzle is small (L_1 and L_c are of the order of 1 m). This results in an acoustic round-trip time of

VI. THE CAMBRIDGE WAVE GENERATOR

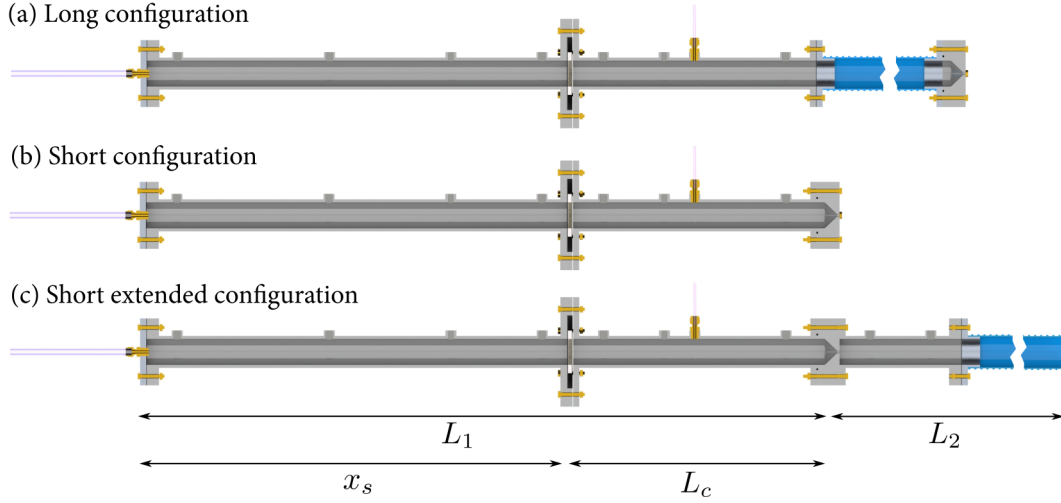


Figure VI.2: Section views of the CWG in its (a) long, (b) short and (c) short extended configurations with upstream length L_1 , downstream length L_2 , wave source location x_s and convective length L_c .

the order of $\tau \approx 10$ ms, which will lead to acoustic reverberation. In addition, the convective distance L_c is reduced, and convected waves are unlikely to have fully dispersed or dissipated before reaching the outlet. If entropic or compositional waves are generated, the measured pressure signal is likely to be a combination of direct and indirect noise. After passing through the nozzle, the flow expands directly into ambient air. Pressure transducers are positioned throughout the duct. Once again, the CWG can be considered to be unicameral since $L_2 = 0$ m.

The third configuration ('short extended') is identical to the short configuration, with the addition of an open-ended 60 m duct downstream of the nozzle ($L_2 \approx 60$ m). This enables the acoustic pressure to be measured both upstream and downstream of the nozzle. Crucially, the forward-propagating indirect noise can now be measured. In addition, the transmissive properties of the nozzle can be determined. In the short extended configuration, the CWG is effectively a bicameral system since there is a chamber downstream of the nozzle. Each configuration enables different noise contributions to be measured, as shown in table VI.1.

VI.1.2 Nozzles

The CWG can be fitted with a nozzle (or an orifice plate) in order to accelerate the flow, thus modifying the system's acoustic boundary conditions. The three most important aspects of

Configuration	Direct noise (π_d^+ , π_d^-)	Indirect noise (π_σ^- , π_ξ^-)	Indirect noise (π_σ^+ , π_ξ^+)
Long	•	-	-
Short	•	•	-
Short extended	•	•	•

Table VI.1: Noise types measured (•) and not measured (-) in each configuration of the Cambridge Wave Generator.

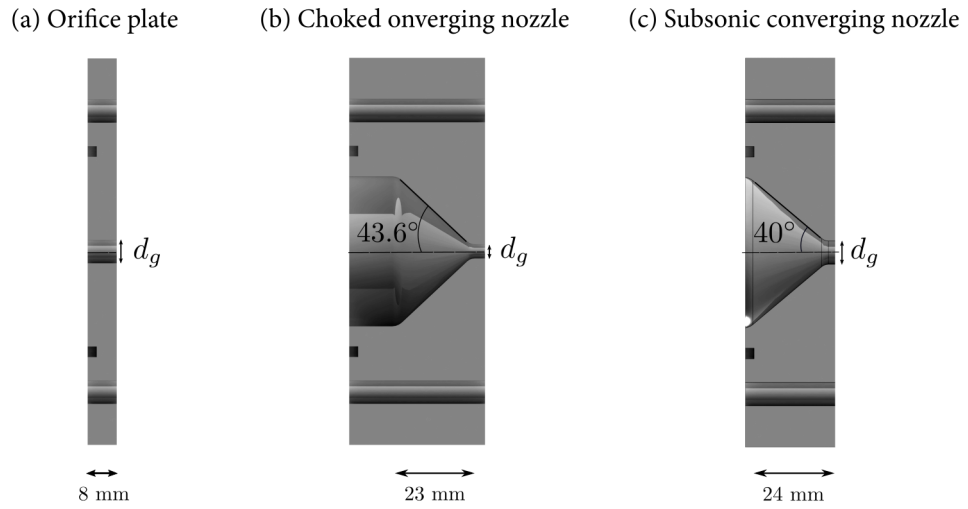


Figure VI.3: Three nozzles used in the Cambridge Wave Generator: (a) orifice plate, (b) choked converging nozzle, (c) subsonic converging nozzle.

each nozzle are: (1) the throat size (which determines the overall acceleration), (2) the length and shape of the acceleration profile (which might result in a different nozzle transfer function due to phasing effects), and (3) the level of anisentropicity (as shown in §III.2). In order to examine the effect of these aspects, we use (a) an orifice plate, (b) a choked converging nozzle and (c) a subsonic converging nozzle, as shown in figure VI.3.

All of the nozzles are manufactured from rigid polyvinyl chloride (PVC). The orifice plate has a geometric throat diameter of $d_g = 6.6$ mm, and a thickness of 8 mm.

The inlet diameter of the converging nozzles match the duct inlet diameter ($d_1 = 42.6$ mm). One of the nozzles has a geometric throat diameter of $d_g = 4$ mm, which enables it to be operated in choked conditions. The choked nozzle has a linear geometric acceleration

VI. THE CAMBRIDGE WAVE GENERATOR

profile with a length of 23 mm (which corresponds to an angle of approximately 43.6°).

The second converging nozzle has a geometric throat diameter of $d_g = 6.6$ mm, and is fully subsonic for the operating conditions considered here. The converging section has a linear geometric profile with a length of 24 mm (which corresponds to an angle of approximately 40°).

Since we are dealing with perturbations with a frequency of the order of $f = 1$ Hz, the Helmholtz number for all of the nozzles is negligible ($He < 0.001$). As such, we expect each of the nozzles considered to be acoustically compact ($He \ll 1$), meaning that their length and acceleration profile will have no effect on their response (assuming the same level of anisentropicity).

VI.2 Wave generators

The CWG can be operated with one of three wave generation modules, performing A: air injection (at ambient temperature), B: heat addition and C: helium injection. Each module generates a different combination of acoustic, entropic and compositional waves, as shown in table VI.2. These perturbations are generated in the form of low-frequency pulses.

Wave generation module	Acoustic wave	Entropic wave	Compositional wave
A: Air injection	●	-	-
B: Heat addition	●	●	-
C: Helium injection	●	●	●

Table VI.2: Wave types generated (●) and not generated (-) by each wave generation module.

VI.2.1 Gas injection/extraction

Flow perturbations can be generated by pulse injecting/extracting a gas into/from the duct. An injection or extraction of air generates acoustic waves as shown in §II.4.2. Injecting helium generates acoustic waves as well as a combined entropic and compositional wave, (see §II.4.3).

The injector nozzle consists of a Swagelok 1/4" fitting, connected to a 0.1 m length of flexible tubing (2 mm inner diameter) through which the injected gas is supplied. The injector can be

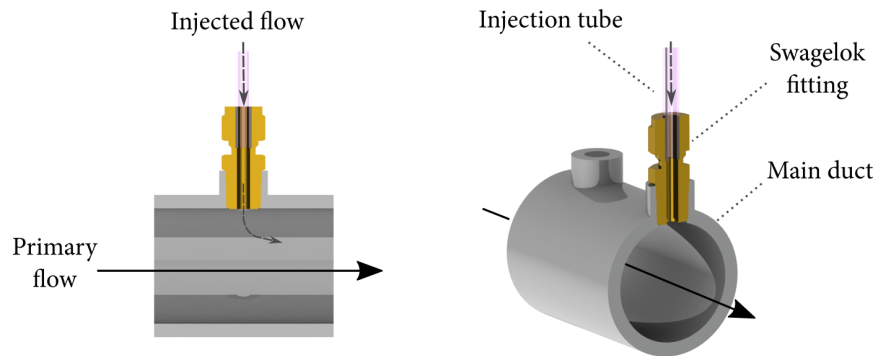


Figure VI.4: Section views of the gas injector/extractor.

mounted via one of several 1/4" ports located along the duct. This enables a range of different source locations x_s to be used (resulting in different convective lengths L_c). The ports are aligned with the duct centreline, so that the injected gas enters the duct in the radial direction, as shown in figure VI.4.

An important consideration is that when gas is not being injected or extracted, the injection line must not have an effect on the acoustics of the main flow duct. Indeed, one might consider that acoustic waves propagating within the duct could be transmitted into the injection flow line through the injector, potentially reflecting and reverberating inside it and modifying the pressure in the duct.

This scenario is avoided due to the geometry of the injector, which is very thin (4 mm internal diameter) and contains a flow constriction (1 mm internal diameter). This flow constriction limits any acoustic transmission between the injection line and the flow duct. This is verified experimentally, by performing tests with different boundary conditions upstream of the injector to show that the injection line has no effect on the duct acoustics.

The injector is connected either to the main air tank, or to a bottle of helium (>99.996% purity), depending on which gas is being injected, as shown in figure VI.5.

The injection itself is carried out using a fast-response micro-solenoid valve (ASCO Numatics HSM2L7H50V). The valve is opened and closed using a Glassman LP 60-20 power supply, which is driven using a computer-generated pulse signal. The injection is a result of the pressure differential across the fast-response valve: when the valve is open, gas flows at a rate determined by the size of the orifice inside it. The amount of gas \dot{m}_i injected into the duct is adjusted using a pressure regulator upstream of the valve, and measured using a mass flow meter (see §VI.3.1).

VI. THE CAMBRIDGE WAVE GENERATOR

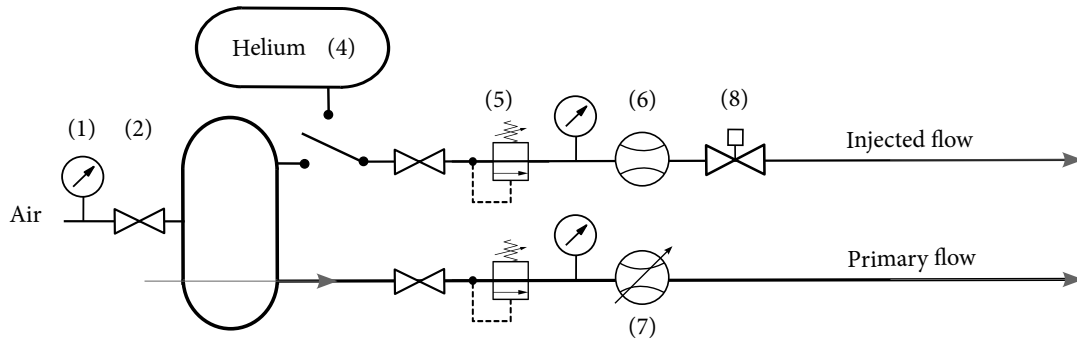


Figure VI.5: Flow lines for air/helium injection with (1) pressure gauge, (2) valve, (3) air tank, (4) helium bottle, (5) pressure regulator, (6) mass flow meter, (7) mass flow controller and (8) fast response valve.

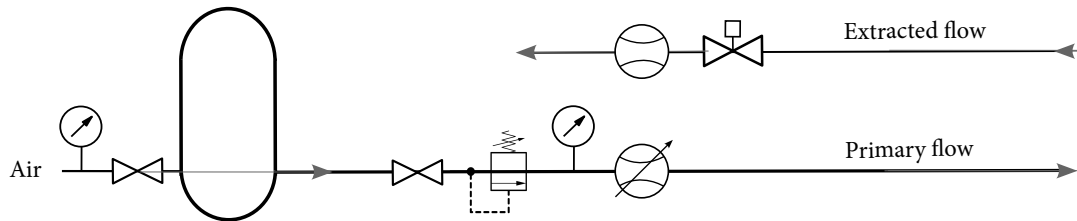


Figure VI.6: Flow lines for air extraction.

Alternatively, air can be extracted from the duct. This is achieved by disconnecting the pressure regulator upstream of the fast-response valve, as shown in figure VI.6. If the duct is pressurised, opening the fast-response valve leads to a portion of the primary air flow escaping the duct through the valve into the atmosphere ($\dot{m}_i < 0$).

The computer-generated signal triggering the gas injection/extraction is essentially a rectangular pulse lasting between $\tau_p=100$ and 500 ms. Each pulse is repeated several times (typically at a rate of 0.25 Hz) to allow for signal averaging (see §VI.3.2).

VI.2.2 Heat addition

Flow perturbations can be generated by heating up the primary air flow unsteadily. This generates acoustic waves, as well as an entropic wave (see §II.4.1).

Heat addition is achieved using a heating device shown in figure VI.7, which was designed by Francesca de Domenico²⁰. The device consists of 7 layers of glass-reinforced epoxy laminate FR4 sheets (roughly 1.4 mm thick each) fitted with a central hole matching the duct inner diameter. Three of these sheets are heating grids connected in series; tungsten wires (58 μm

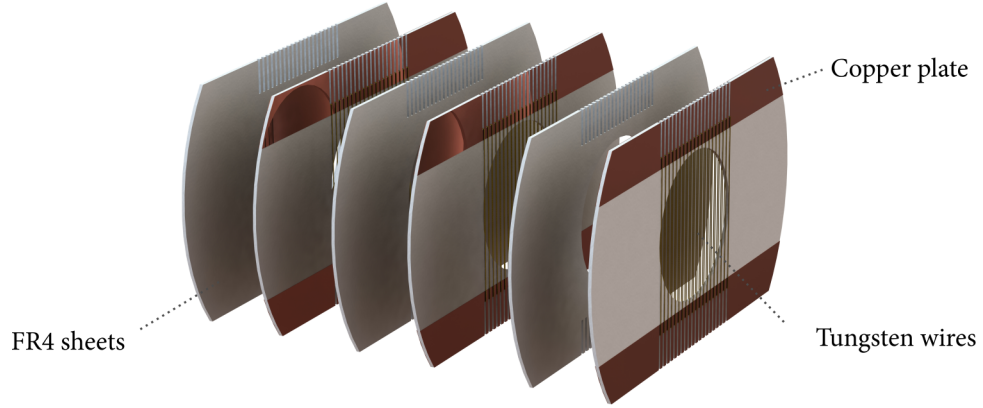


Figure VI.7: Exploded view of the heating device.

diameter) with an overall resistance of 1Ω are wound around a tooth comb structure. These wires connect to copper plating on either sides of the heating grid, through which a current can be delivered.

The device is secured between two PVC flanges to provide electric insulation. The obstruction due to the heating device is minimal: it occupies less than 0.15% of the duct cross section. The total thickness of the heating device is of the order of 10 mm, meaning that it can be considered to be acoustically compact. As such, we consider that it has a negligible effect on acoustic propagation within the duct.

The heating device is driven using an in-house circuit: a computer-generated pulse drives a Glassman LP 60-20 power supply, delivering a current pulse of 21 A through the heating device. This process heats up the heating grid wires via Joule effect, which in turn heats up the air flowing through the heating device (primarily by conduction and convection). This can be thought of as a fluctuating heat release Q' being delivered to the primary air flow, typically for a duration $\tau_p \approx 300$ ms.

The heat flux Q' due to the heating device is expected to be approximately the same for all cases. Given the dissipative losses in the heating device circuit however, it is not possible to compute a priori how much heat is transferred to the flow. Furthermore, the heat exchange process from the heating grids to the flow can be assumed to vary based on the flow conditions.

The heat added to the flow can be deduced by considering the temperature fluctuation ΔT_d generated just downstream of the heating device: $Q' = \dot{m} \bar{c}_p \Delta T_d$.

Similarly, the amplitude of the entropic wave generated by the heating device can be related to the temperature fluctuation ΔT_n associated to it: $\sigma \approx \Delta T_n / \bar{T}$.

VI. THE CAMBRIDGE WAVE GENERATOR

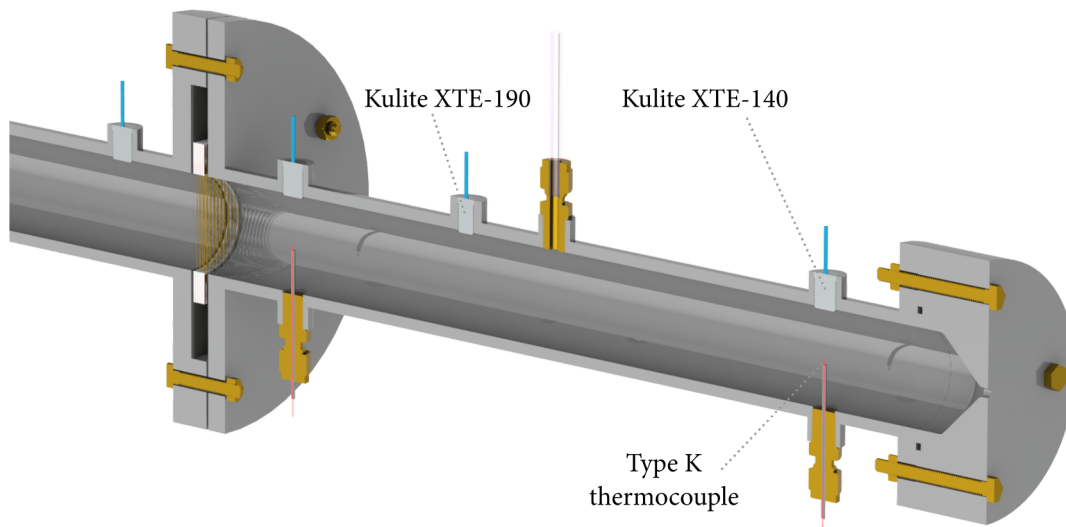


Figure VI.8: Example of pressure transducers and thermocouples mounted on the CWG.

VI.3 Data acquisition and processing

VI.3.1 Mass flow control and measurement

The primary air flow \dot{m} is controlled using an Alicat MCR500 mass flow controller. It enables the mass flow rate to be set to a value between 0 and 10 g s^{-1} , with an accuracy of $\pm 1\%$.

The mass flow rate of injected gas \dot{m}_i is monitored with an Alicat MCR250 mass flow meter (accuracy: $\pm 1\%$). The meter can be calibrated for either air or helium, depending on the gas being injected. For gas extraction, the meter is simply mounted in the reverse direction.

The mass flow controller and meter are connected to a computer via an Alicat BB9 breakout box, which enables primary and injected/extracted mass flow rates to be logged simultaneously at a frequency of roughly 50 Hz. This is sufficient to measure the amplitude of low-frequency pulses with accuracy (for the most part we are dealing with pulses lasting $\tau_p \approx 200 \text{ ms}$).

VI.3.2 Pressure measurements

Acoustic pressure measurements are carried out using Kulite XTE-190M piezoresistive pressure transducers, which can be flush mounted at several $1/4$ " transducer ports along the duct as shown in figure VI.8. The absolute pressure is logged with Kulite XT-140M transducers, flush-mounted at $1/8$ " ports.

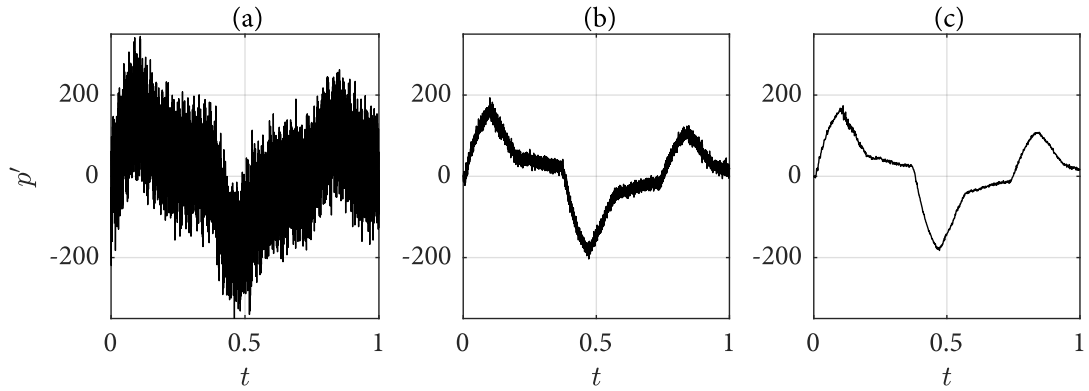


Figure VI.9: Example of acoustic pressure signal conditioning: (a) raw signal, (b) averaged signal (over 100 pulses), (c) averaged and filtered signal.

The pressure transducer signals are amplified using a Fylde FE379-TA amplifier, and acquired with a National Instruments 2090 Digital Acquisition box connected to a National Instruments PCI-5259 card. The signal is sampled at 8192 Hz. Random noise is reduced by performing signal averaging (typically over 100 pulses). Oscillations at 50 Hz (power frequency) and above 400 Hz are filtered out, since the frequencies of interest in this study are low. The effect of averaging and filtering on the raw pressure data is shown in figure VI.9.

VI.3.3 Temperature measurements

If the heating device is used, entropic waves are generated due to a fluctuating heat release Q' . The temperature fluctuations associated to these entropic waves are measured using fast-response type K thermocouples. These are mounted at the duct centreline via 1/4" ports as shown in figure VI.8.

The thermocouple signals are amplified using an in-house circuit, and acquired with a National Instruments 2090 Digital Acquisition box connected to a National Instruments PCI-5259 card. To account for the time-lag inherent to thermocouples, the temperature measurement is corrected using independent anemometer measurements. The temperature measurements and corrections were conducted by Francesca De Domenico²⁰.

The entropic wave can be expected to dissipate, diffuse and disperse as it convects from the grid to the nozzle. As such, temperature fluctuations are measured 40 mm downstream the grid (ΔT_d) as well as 50 mm upstream of the nozzle (ΔT_n).

VI.4 Simulation and source identification

The Cambridge Wave Generator can be modelled as a unicameral system (in the long and short configurations) or as bicameral system (in the short extended configuration). As such, the one-dimensional model presented in §V can be used to simulate the test cases analytically. The results can be compared to experimental measurements or used to perform source identification.

The main inputs required for the direct and indirect noise models are the mass, momentum, energy and composition fluxes ($\varphi'_m, \varphi'_M, \varphi'_e$ and φ'_Z), the mean flow properties, as well as the system's acoustic transfer functions, as shown in figure V.3.

The normalised perturbation fluxes are those outlined in §II.4. The mean flow properties in the duct ($\bar{p}, \bar{T}, \bar{M}$) can be measured using the instruments described in §VI.3. The acoustic transfer functions require the reflection ($R_{i1}, R_{o1}, R_{i2}, R_{o2}$) and transmission coefficients (T_{o1}, T_{i2}) to be known.

VI.4.1 Reflection and transmission coefficients

The reflection coefficient at the inlet of the duct is defined as $R_{i1} = \pi^+ / \pi^-$ where π^+ is the reflection of an impinging backward-propagating wave at the inlet. We assume there are no mass flow rate fluctuations at the mass flow controller ($\dot{m}' = 0$), a condition which is easily met at the current low frequencies. As shown in §II, this condition can be written as a relationship between acoustic and entropic waves at the mass flow controller location:

$$\left(1 + \frac{1}{\bar{M}}\right) \pi^+ + \left(1 - \frac{1}{\bar{M}}\right) \pi^- - \sigma = 0 \quad (\text{VI.1})$$

Assuming that there are no entropic waves upstream of the mass flow controller ($\sigma = 0$), then the reflection coefficient at the mass flow controller can be expressed as:

$$R = \frac{\pi^+}{\pi^-} = \frac{1 - \bar{M}}{1 + \bar{M}} \quad (\text{VI.2})$$

which corresponds to a reflection coefficient of roughly $R \approx 0.99$ for the Mach number range considered here.

Acoustic reflections also occur at the transition between the flexible tube downstream of the mass flow controller (12 mm inner diameter) to the main tube (42.6 mm inner diameter).

Seen from the perspective of a backward-propagating wave π^- , this change in cross-section can be shown to have a reflection coefficient $R \approx 0.85$ ⁸². Given that the distance between this transition and the mass flow controller is small relative to the perturbation wavelength (compactness assumption) we assume that both reflections can be captured by a reflection coefficient of $R_{i1} \approx 0.99$ located at the inlet flange.

In the short extended configuration, the outlet acts as a pressure node, and the reflection coefficient can be taken to be $R_{o2} = -1$.

The nozzle reflection and transmission coefficients (R_{o1} , R_{i2} , T_{o1} , T_{i2}) can be computed using the expressions in §III.2. Some of these values can be verified using experimental data.

For example, in the short extended configuration we have pressure measurements both upstream and downstream of the nozzle (at locations x_1 and x_2 respectively). If only direct noise is considered, then we can obtain the transmission coefficient of the nozzle as:

$$T_{o1} = \frac{p'/\gamma\bar{p}(x_2)}{p'/\gamma\bar{p}(x_1)}(1 + R_{o1}). \quad (\text{VI.3})$$

In the short configuration, if the general wave source π_1 defined in (V.24) is known, then we can recover the reflection coefficient R_{o1} as:

$$R_{o1} = \frac{(\widehat{p}'/\gamma\bar{p}) - \widehat{\pi}_1}{(\widehat{p}'/\gamma\bar{p})R_{i1}e^{-i\omega\tau_1} + \widehat{\pi}_1}. \quad (\text{VI.4})$$

where \mathcal{R} is the overall reverberation function defined in (V.22).

The acoustic attenuation α is not known a priori. It can be deduced from the results in cases A1-A10 (shown in §VII.1.1), in which successive decaying reflections are clearly separated. For most test cases, we obtain $\alpha = 0.0015 \text{ m}^{-1}$.

VI.4.2 Source identification

One of the main challenges associated to model experiments is identifying direct and indirect noise contributions in the overall pressure signal. One way to achieve this is to take advantage of the convective time delay τ_c , which is effectively the time separation between direct and indirect noise generation. By carefully choosing and varying the convective length L_c , we can use time-delay arguments to identify direct and indirect noise.

Alternatively, the source identification methods outlined in §V.4 can be applied to the Cambridge Wave Generator to identify direct and indirect noise. This is accomplished by perform-

VI. THE CAMBRIDGE WAVE GENERATOR

ing experiments in several configurations.

In the long configuration, the system is unicameral with $L_1 \approx 60$ m. Since no indirect noise is generated at the nozzle (due to dissipation and/or dispersion), we can write:

$$\pi_d^+ = \frac{1}{\mathcal{R}} \frac{1}{(1 + R_{i1})(1 + R_{o1})} \frac{p'}{\gamma \bar{p}}(x_1). \quad (\text{VI.5})$$

Since we are dealing with a 60 m duct, downstream acoustic reflections will affect the pressure signal after $\tau \approx 340$ ms. In this situation, we effectively have $R_{o1} = 0$ for $t < 340$ ms (i.e. the duct outlet is anechoic). In that case, (VI.5) simplifies to:

$$\pi_d^+ = \frac{1}{\mathcal{R}} \frac{1}{1 + R_{i1}} \frac{p'}{\gamma \bar{p}}(x_1), \quad (\text{VI.6})$$

from which the direct acoustic wave can be directly recovered.

In the short configuration, a backward-propagating indirect acoustic wave π_i^- is generated at the nozzle. We can write:

$$\pi_i^- = \frac{1}{\mathcal{R}} \frac{1}{1 + R_{i1}} \frac{p'}{\gamma \bar{p}} - (1 + R_{o1})\pi_d^+. \quad (\text{VI.7})$$

Finally, in the short extended configuration, a 60 m duct is installed downstream of the nozzle. Upstream and downstream pressure measurements $p'(x_1)$ and $p'(x_2)$ enable us to identify the forward-propagating indirect acoustic wave:

$$\pi_i^+ = \frac{p'}{\gamma \bar{p}}(x_2) - \frac{T_{o1}}{1 + R_{o1}} \frac{p'}{\gamma \bar{p}}(x_1). \quad (\text{VI.8})$$

VII

AIR INJECTION – DIRECT NOISE

Experiments are carried out on the Cambridge Wave Generator with wave generation module A (air injection/extraction). As shown in §II.4.2, air injection/extraction is expected to generate negligible entropy, meaning that only direct noise is produced.

Sixteen experimental cases are examined in total (A1–A16). Cases A1–A10 are carried out in the long configuration. The corresponding results reveal the direct noise produced by air injection without the effect of reverberation, and enable the acoustic attenuation in the duct to be estimated. Cases A11–A16 are carried out in the short configuration, enabling the effect of repeated acoustic reflections to be examined specifically.

The test cases are simulated using the analytical framework shown in §V, and compared to experimental pressure data. Finally, source identification is performed to extract information regarding the acoustic sources present in the system. The results are compared to analytical predictions.

VII.1 Long configuration

In the long configuration, the flow system is effectively a single duct of length $L = 62.6$ m, as shown in figure VII.1. The injector is located $x_s = 0.95$ m downstream of the inlet. The mean and fluctuating pressures are measured at $x = 0.8$ m.

Acoustic reflections occur at the inlet and outlet with coefficients $R_i = 0.99$ and R_o . (see VI.4.1). If the duct is open-ended we take $R_o = -1$. If it is terminated with a choked nozzle we compute the reflection coefficient using the isentropic compact nozzle model, obtaining $R_o = 0.992$. This is verified a posteriori in §VII.2.4.

Since the system is in its long configuration ($L = 62.6$ m), the acoustic time-scale ($\tau \approx 360$

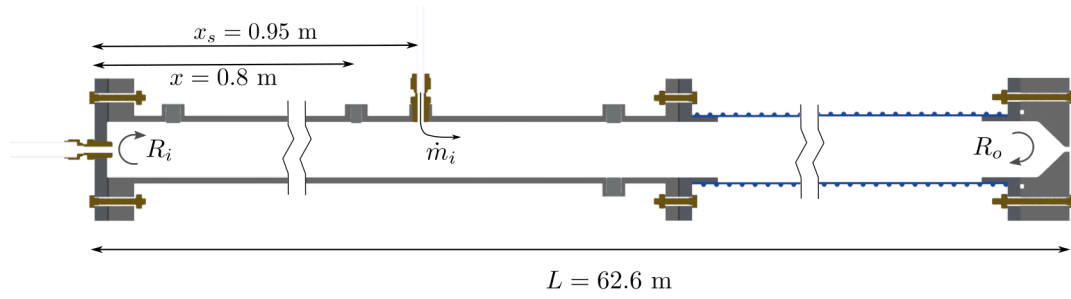


Figure VII.1: Long tube configuration with wave module A: air is injected/extracted into a duct with reflections at the inlet and outlet.

Case	Outlet	\bar{p} [kPa]	\bar{M}_1 [-]	\dot{m} [g s ⁻¹]	\dot{m}_i [g s ⁻¹]
A1	Open	101.6	0.0101	5.92	0.20 → 1.00
A2	Open	101.9	0.0135	7.89	0.20 → 1.00
A3	Open	102.2	0.0168	9.87	0.20 → 1.00
A4	Nozzle	101.3	0	0	0.20 → 1.00
A5	Choked	205.3	0.0052	5.92	0.20 → 1.00
A6	Choked	267.2	0.0052	7.89	0.20 → 1.00
A7	Choked	351.3	0.0052	9.87	0.20 → 1.00
A8	Choked	205.3	0.0052	5.92	-0.67
A9	Choked	267.2	0.0052	7.89	-0.89
A10	Choked	351.3	0.0052	9.87	-1.11

Table VII.1: Experimental cases for wave module A (air injection/extraction) in the long configuration with outlet type, mean pressure \bar{p} , mean Mach number \bar{M}_1 , primary mass flow rate \dot{m} and injected mass flow rate \dot{m}_i .

ms) is sufficiently long for successive acoustic reflections to be distinct.

The test cases for the long configuration are shown in table VII.1. The duct is terminated as an open end (cases A1–A3), or with the convergent nozzle (A4–A10). In the cases where a nozzle is used, the duct can be pressurised, so that the mean pressure \bar{p} is substantially higher than the atmospheric pressure (cases A5–A10). In those cases, the nozzle is choked (i.e. sonic at the throat).

Cases A1–A7 correspond to air injection: in each case, 5 different flow rates of secondary air are injected (0.20, 0.40, 0.60, 0.80 and 1.00 g s⁻¹), meaning that 35 tests are conducted in total. Cases A8–A10 correspond to air extraction. Unlike cases A1–A7, the mass flow rate $\dot{m}_i < 0$ extracted from the duct is a function of the mean internal pressure. As a result, only

VII. AIR INJECTION – DIRECT NOISE

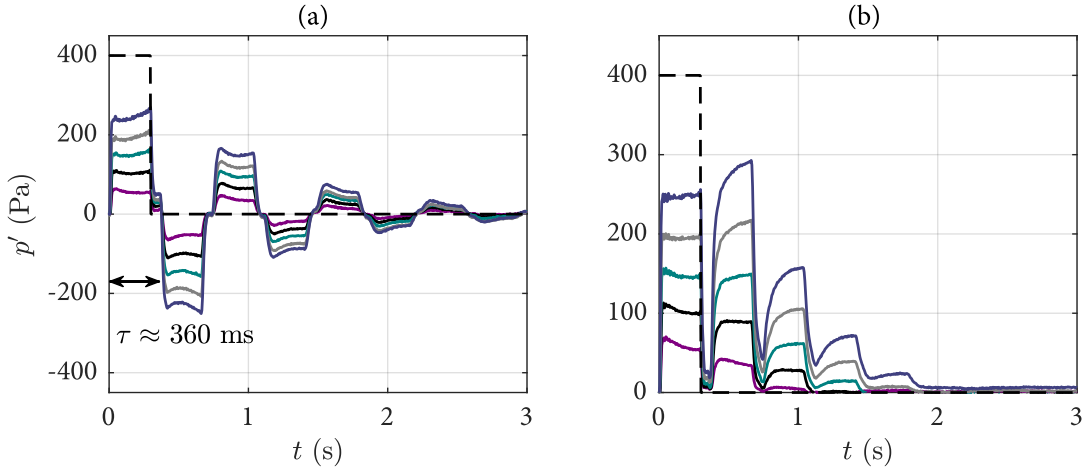


Figure VII.2: Experimental pressure fluctuation $p'(x, t)$ for (a) case A1 and (b) case A4 with $\dot{m}_i = 0.2$ (—), 0.4 (—), 0.6 (—), 0.8 (—), 1.0 g s^{-1} (—). The valve timing signal is shown for reference (---).

one value of \dot{m}_i is used for each case. The duration of the injection/extraction pulse is $\tau_p = 300 \text{ ms}$ for all tests and phase averaging is performed over 100 pulses.

VII.1.1 Experimental results

The pressure measurements $p'(x, t)$ for case A1 are shown in figure VII.2(a). The pressure trace corresponds to a succession of acoustic pulses alternating in sign. The first pulse coincides with the valve pulse signal (starting at $t = 0$ and ending at $\tau_p = 300 \text{ ms}$). This pulse corresponds to the direct acoustic waves π_d^+ and π_d^- generated during the injection. The following pulses are acoustic reflections of the first pulse, which reflects at the outlet of the system, and returns with a time-delay $\tau \approx 2L/\bar{c} \approx 360 \text{ ms}$. Since we have $R_i R_o < 0$, successively reflected pulses alternate in sign. Additionally, there are acoustic losses ($|R_i R_o e^{-2\alpha L}| < 1$), so the amplitude of subsequent pulses decreases exponentially.

The results for case A1 show that the pressure fluctuations increase proportionally to the amount of injected air \dot{m}_i , as predicted by the analytical model in (II.13). Experimental results for cases A2 and A3 are consistent with those for case A1.

In case A4 (shown in figure VII.2(b)), there is no primary air flow ($\bar{M}_1 = 0$), and the duct is terminated with a nozzle. The amplitudes of the first pulses are identical to those in case A1. This confirms that the pressure fluctuation arising from an air injection is independent of both the mean Mach number and mean pressure in the duct, as predicted in (II.13). The

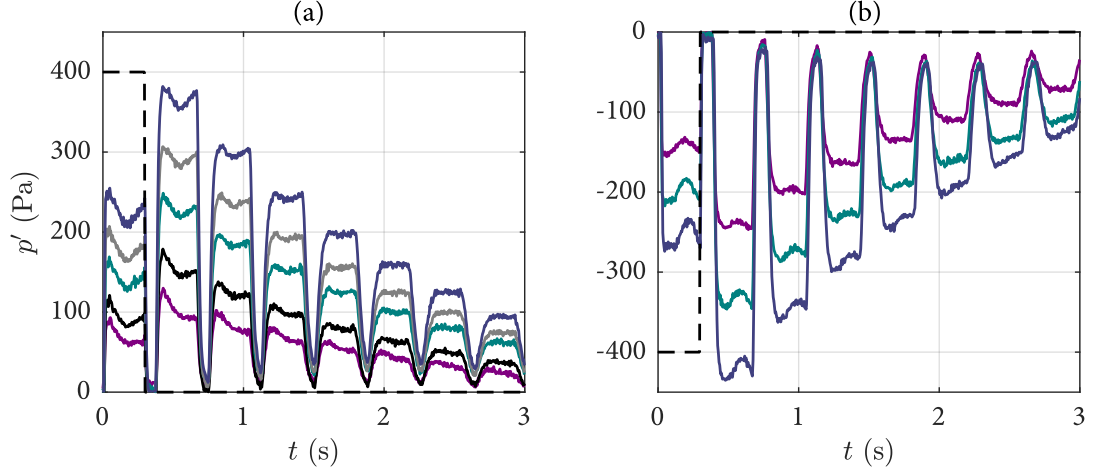


Figure VII.3: Experimental pressure fluctuation $p'(x, t)$ for (a) case A5 with $\dot{m}_i = 0.2$ (—), 0.4 (—), 0.6 (—), 0.8 (—), 1.0 g s^{-1} (—) and (b) cases A8 (—), A9 (—) and A10 (—). The valve timing signal is shown for reference (- - -).

reflected pulses are all positive, since $R_i R_o > 0$.

The results for case A5 are shown in figure VII.3(a). Here, the duct is choked, and the outlet reflection coefficient can be taken as $R_o = 0.992$. Notably, the second acoustic pulse is larger than the first one. This is because the amplitude of the second pulse (given by $(1 + R_i)R_o(\pi_d^+ + R_i\pi_d^-)$) is larger than the first one ($\pi_d^+ + R_i\pi_d^-$) for this value of R_o .

The experimental results for cases A8–A10 (air extraction) are shown in figure VII.3(b). The results are similar to those of previous cases, except that all the acoustic pulses are negative. Once again, this is in agreement with the analytical model: in the case of an extraction, the added energy flux is negative, leading to a negative pressure fluctuation.

In theory, the ratio of the amplitudes of two successive pulses (excluding the first) is $R_i R_o e^{-2\alpha L}$. Since R_i and R_o are known, measuring the amplitudes of successive pulses in the experimental signal gives us an estimation of the effective attenuation α . Since the flow properties vary depending on the case, we can expect to find different values of α for each test. The measured values of the acoustic attenuation α are shown in figure VII.4 for cases A1–A3 and A5–A10.

The results indicate that the attenuation is a function of the mean Mach number \bar{M}_1 (or mean velocity \bar{u}) in the duct. Conversely, the attenuation does not seem to be largely dependent on the mean pressure \bar{p} and density $\bar{\rho}$. Indeed, α is very similar in cases A5–A10, despite the fact that the mean density and pressure are widely different for each test (ranging from $\bar{p}=205.3$ to 351.3 kPa). Conversely, the mean pressure is very similar in cases A1, A2 and A3

VII. AIR INJECTION – DIRECT NOISE

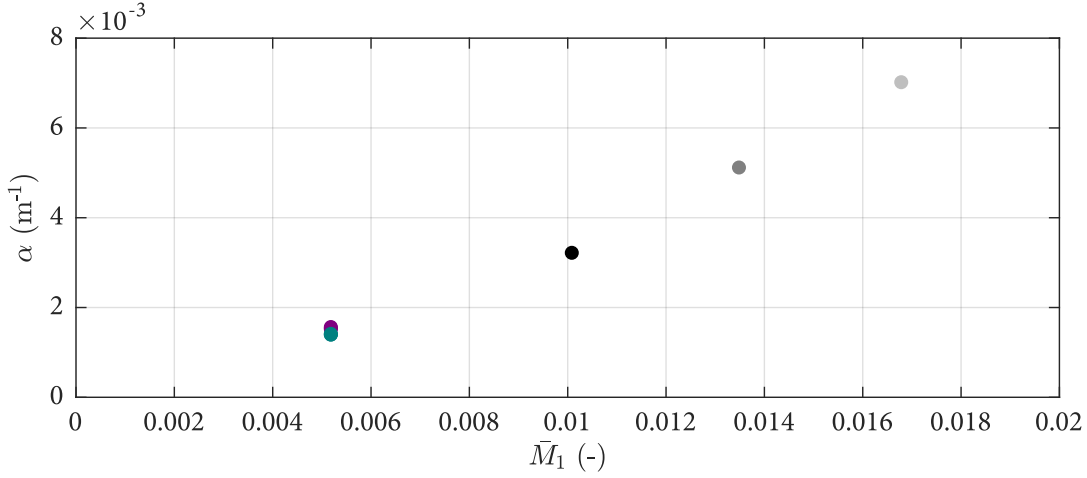


Figure VII.4: Measured acoustic attenuation α as a function of mean Mach number \bar{M}_1 for cases A1 (●), A2 (●), A3 (●), A5-A7 (●) and A8-A10 (●).

($\bar{p} \approx 101.9$ kPa) but these cases lead to widely different values of α (0.03, 0.0045 and 0.006 respectively).

VII.1.2 Simulations

The test cases can be simulated analytically using the model presented in §V (implementing the values of α extracted from experimental data). The analytical results for the acoustic pressure $p'(x, t)$ are shown in figure VII.5 for cases A1 and A3. The analytical results for cases A5 and A8 are shown in figure VII.6.

The simulation results are in good agreement with the experimental data. The amplitude of the first pulse is consistent with the experimental model (with a small error depending on the case). This suggest that the direct noise model is appropriate to compute the acoustic waves generated by an unsteady injection/extraction of air.

Additionally, the amplitudes and time delays between the reflected acoustic pulses are correctly predicted. This indicates that the reflection coefficients, acoustic attenuation and reverberation transfer functions we have implemented are representative of the experimental system.

There is a slight discrepancy in the shape of the acoustic pulses. This could be due to pressure fluctuations inside the injection line, which would affect the measured mass flow rate. Alternatively, the discrepancy could be due to an additional source of noise not accounted

VII. AIR INJECTION – DIRECT NOISE

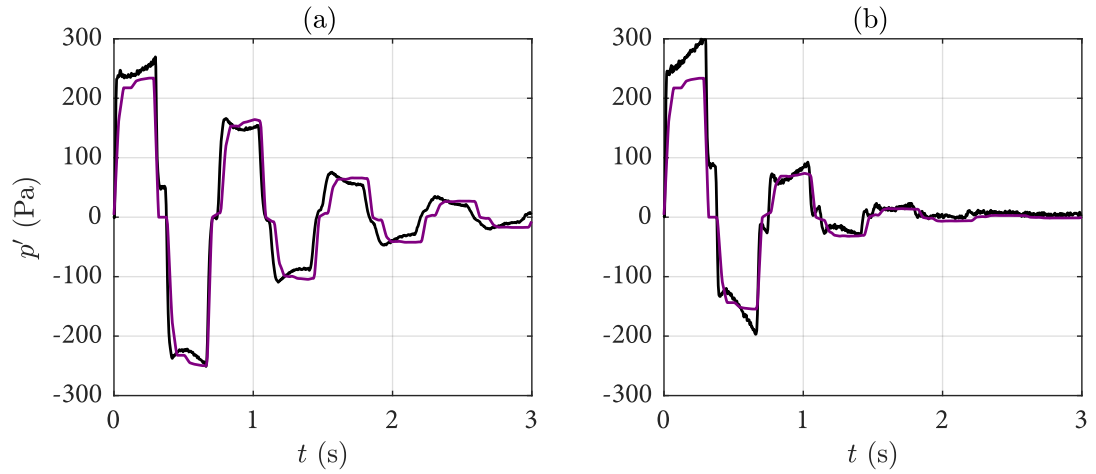


Figure VII.5: Analytical (—) and experimental (—) results for (a) case A1 with $\dot{m}_i = 1 \text{ g s}^{-1}$ and (b) case A3 with $\dot{m}_i = 1 \text{ g s}^{-1}$.

for in the analytical model. For example, two- and three-dimensional effects such as vortical structures produced during the air injection have been neglected in the one-dimensional model.

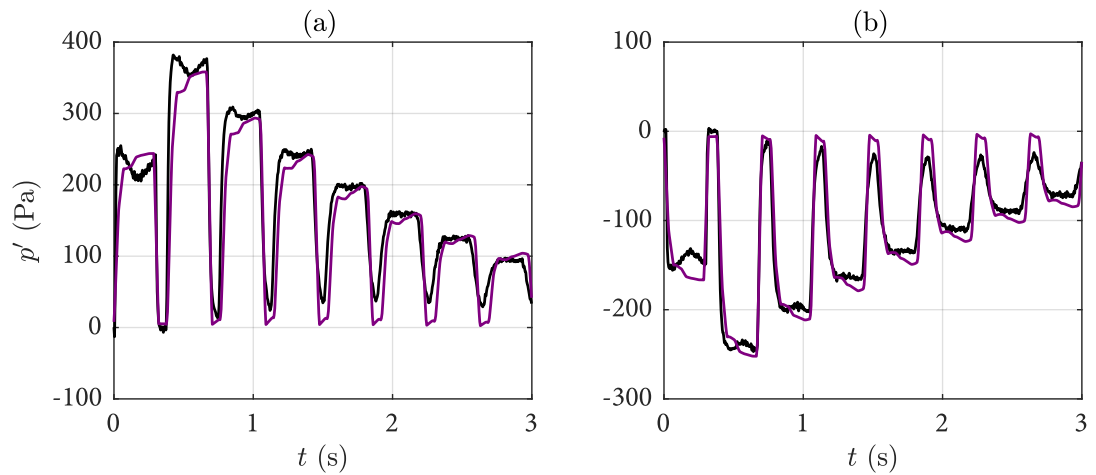


Figure VII.6: Analytical (—) and experimental (—) results for (a) case A5 with $\dot{m}_i = 1 \text{ g s}^{-1}$ and (b) case A8.

VII. AIR INJECTION – DIRECT NOISE

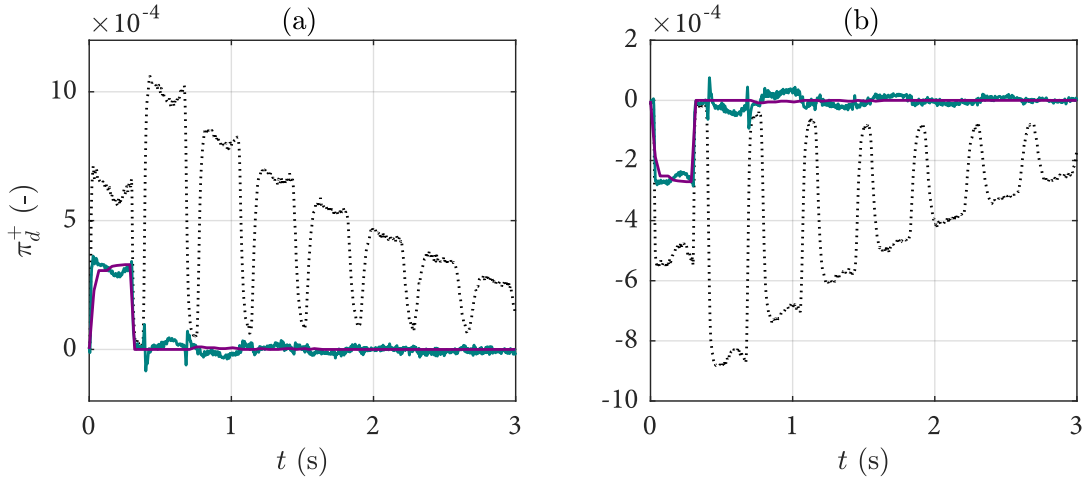


Figure VII.7: Direct acoustic wave π_d^+ extracted from experimental data (—), computed theoretically (—) and normalised experimental acoustic pressure (····) for (a) case A6 with $\dot{m}_i = 1 \text{ g s}^{-1}$ and (b) case A9.

VII.1.3 Source identification

In theory, air injection/extraction generates direct acoustic waves π_d^+ and π_d^- . By using the source identification method outlined in §VI.4.2, we can extract a measurement of these waves from the experimental data. The direct acoustic wave π_d^+ recovered from experimental pressure measurements is shown in figure VII.7 for cases A6 (air injection) and A9 (air extraction). Once again, we can compare this measurement to the theoretical result given by the direct noise model (§II.4.2).

As expected, the acoustic wave π_d^+ is generated only while air is being injected/extracted ($0 < t < 300 \text{ ms}$), and takes a value close to zero for $t > 300 \text{ ms}$. This shows that the subsequent pulses present in the measured acoustic pressure signal are clearly due to acoustic reflections at the outlet. This suggests the source identification method is working as expected.

Furthermore, the measurements of π_d^+ are very close to the theoretical predictions. This is unsurprising. Indeed, the good agreement between simulations and experiments in the previous section indicates that the reverberation and direct noise models are accurate. Since the source identification method relies on these same models, it is also likely to be in good agreement with the experiment. In other words, if the simulations are in good agreement with experiments, the source identification method should successfully recover the acoustic sources.

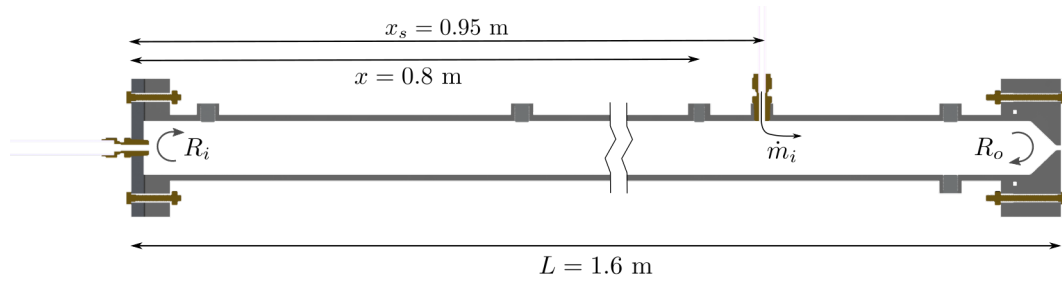


Figure VII.8: Short tube configuration with wave module A: air is injected/extracted into a duct with reflections at the inlet and outlet.

VII.2 Short configuration

In the short configuration, the flow system is effectively a single duct of length $L = 1.6$ m, as shown in figure VII.8. The injector is located at a location $x_s = 0.95$ m downstream of the inlet. The mean and fluctuating pressures are measured at $x = 0.8$ m.

Acoustic reflections occur at the inlet and outlet, with reflection coefficients $R_i = 0.99$ and $R_o = 0.992$ (since the outlet is a choked isentropic nozzle in all cases).

Since the duct is in its short configuration ($L = 1.6$ m), the acoustic round-trip time is now $\tau \approx 10$ ms, which is much shorter than the pulse duration ($\tau_p = 300$ ms). Therefore, the reflections now overlap the initial acoustic signal (i.e. reverberation occurs).

The test cases for the short configuration are shown in table VII.2.

Case	Outlet	\bar{p} [kPa]	\bar{M}_1 [-]	\dot{m} [g s ⁻¹]	\dot{m}_i [g s ⁻¹]
A11	Choked	205.3	0.0052	5.92	0.20 → 1.00
A12	Choked	267.2	0.0052	7.89	0.20 → 1.00
A13	Choked	351.3	0.0052	9.87	0.20 → 1.00
A14	Choked	205.3	0.0052	5.92	-0.64
A15	Choked	267.2	0.0052	7.89	-0.88
A16	Choked	351.3	0.0052	9.87	-1.12

Table VII.2: Experimental cases for wave module A (air injection/extraction) in the short configuration with outlet type, mean pressure \bar{p} , mean Mach number \bar{M}_1 , primary mass flow rate \dot{m} and injected mass flow rate \dot{m}_i .

Cases A11–A13 correspond to air injection: in each case, 5 different flow rates of secondary air are injected (0.20, 0.40, 0.60, 0.80 and 1.00 g s⁻¹), corresponding to 15 tests in total. Cases

VII. AIR INJECTION – DIRECT NOISE

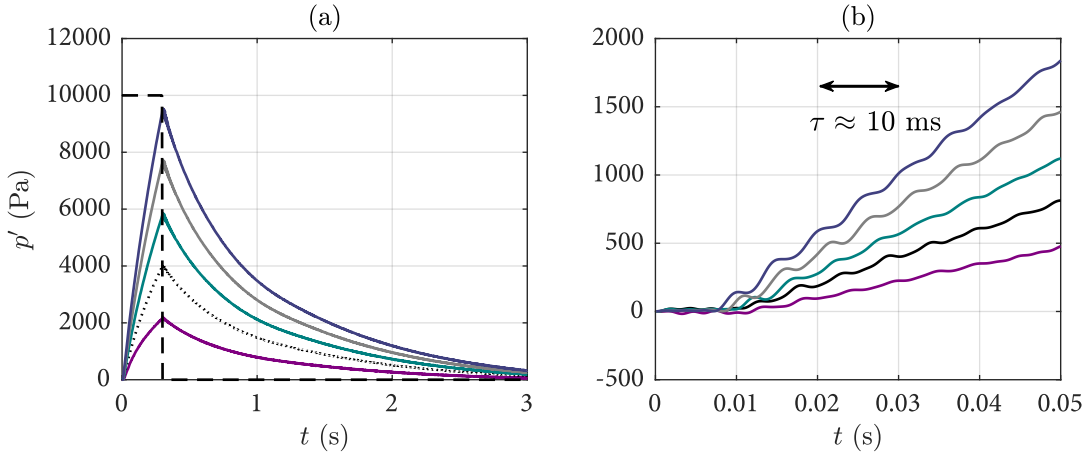


Figure VII.9: Experimental pressure fluctuation $p'(x, t)$ for case A11 with $\dot{m}_i=0.2$ (—), 0.4 (—), 0.6 (—), 0.8 (—), 1.0 g s^{-1} (—). The valve timing signal is shown for reference (- - -).

A14–A16 correspond to air extraction, with a single value of $\dot{m}_i < 0$ for each case. The duration of the injection/extraction pulse is $\tau_p = 300 \text{ ms}$ for all tests and phase averaging is performed over 100 pulses.

VII.2.1 Experimental results

The pressure measurements $p'(x, t)$ for case A11 (air injection) are shown in figure VII.9.

In case A11, the acoustic pressure rises sharply during the injection pulse (for $0 < t < 300 \text{ ms}$). This can be explained as follows: during the injection, acoustic waves are generated and reflected at the inlet and outlet with a time delay $\tau \approx 10 \text{ ms}$, meaning that roughly $\tau_p/\tau \approx 30$ reflections occur before the end of the injection at $t = \tau_p$. As such, the pressure signal corresponds to a superposition of several acoustic pulses, each with a small time delay.

Observing the experimental signal closely reveals the pressure does not rise continuously, but rather in discrete steps, where each step is an acoustic reflection as shown in figure VII.9(b).

Once the valve is closed at $\tau_p = 300 \text{ ms}$, acoustic waves are no longer being generated. The acoustic pulses being reflected inside the duct progressively decay due to acoustic losses ($|R_1 R_2 e^{-2\alpha L}| < 1$), until the acoustic pressure reaches zero.

The pressure measurements for case A14–A16 (air extraction) are shown in figure VII.10. The results are similar to those for cases A11–A13, except that the pressure fluctuation is now negative. This is consistent with the theoretical prediction that an air extraction generates negative pressure waves (while an injection generates positive ones).

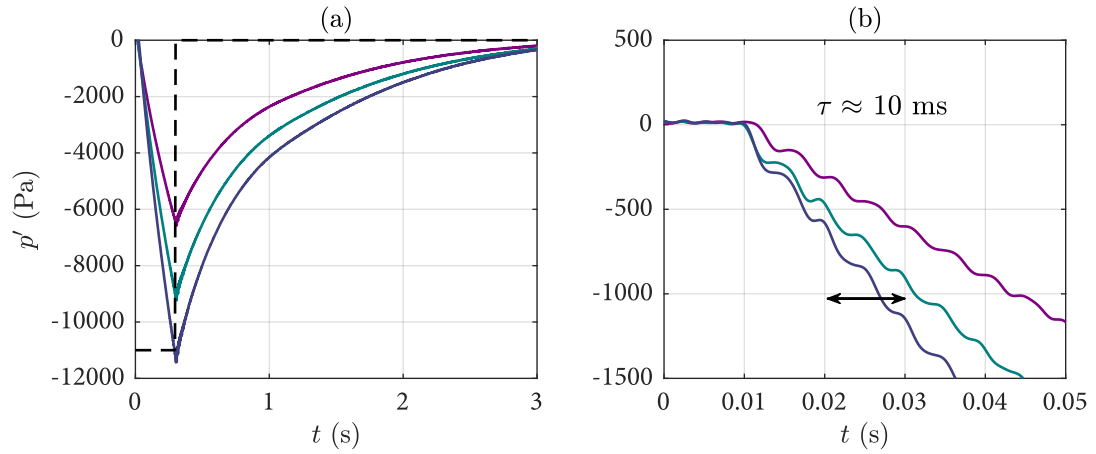


Figure VII.10: Experimental pressure fluctuation $p'(x, t)$ for cases A14 (—), A15 (—) and A16 (—). The valve timing signal is shown for reference (---).

During the air extraction, the pressure decreases in increments corresponding to individual acoustic reflections of π_d^+ and π_d^- , as shown in figure VII.10(b). The pressure fluctuation then decays progressively after the valve is closed.

VII.2.2 Simulations

The analytical results for the acoustic pressure $p'(x, t)$ are shown in figure VII.11 for cases A13 (air injection) and A14 (air extraction).

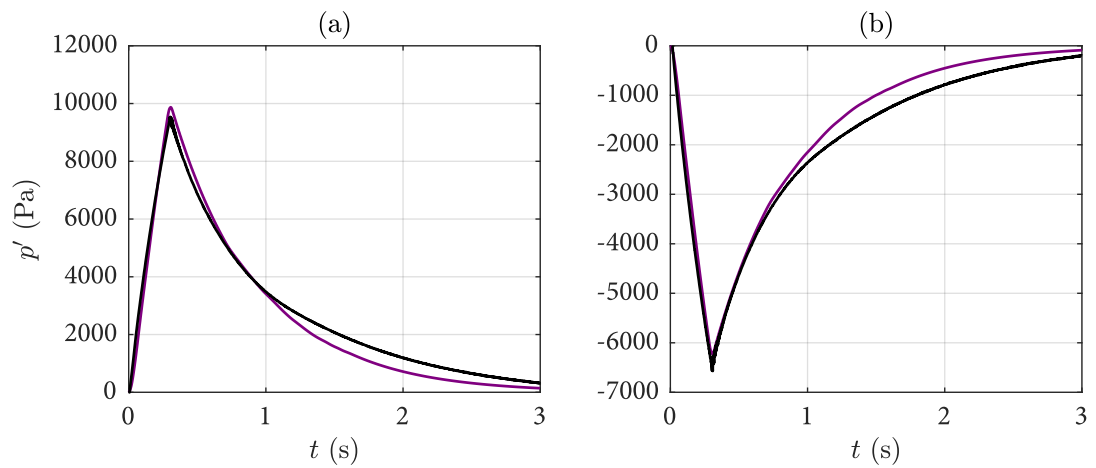


Figure VII.11: Analytical (—) and experimental (—) pressure fluctuation $p'(x, t)$ for (a) case A13 with $\dot{m}_i = 1 \text{ g s}^{-1}$ and (b) case A14.

VII. AIR INJECTION – DIRECT NOISE

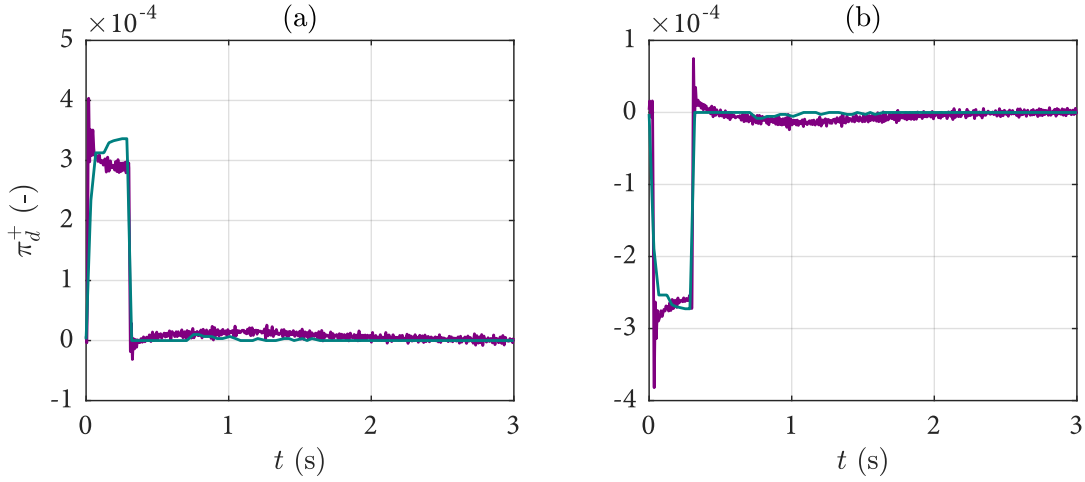


Figure VII.12: Direct acoustic wave π_d^+ extracted from experimental data (—), computed theoretically (—) for (a) case A12 with $\dot{m}_i = 1 \text{ g s}^{-1}$ and (b) case A16.

The analytical results are once again in good agreement with the experimental data, and the system's behaviour is correctly predicted. Once the injection is stopped at $\tau_p = 300 \text{ ms}$, the analytical model suggests the pressure should decrease exponentially, as $(R_i R_o e^{-2\alpha L})^{t/\tau}$. In the experiment however, the pressure appears to decay at a slightly different rate. This difference is small; a deviation in the value of $R_i R_o e^{-2\alpha L}$ by as little as 0.5% would explain the decay rate discrepancy.

VII.2.3 Source identification

As with the long configuration cases, we can perform source identification to extract acoustic sources from the experimental data. The direct acoustic wave π_d^+ recovered from experimental pressure measurements is shown in figure VII.12 for cases A12 (air injection) and A16 (air extraction), and compared to the theoretical result given by the direct noise model (§II.4.2).

The extracted acoustic source is consistent with theoretical predictions. Crucially, the measurement of π_d^+ is also in agreement with the corresponding measurements in the long configuration (cases A6 and A9 shown in figure VII.7).

This confirms that the effect of acoustic reflections is being correctly eliminated. Indeed, the measured acoustic pressure is very different in the long and short configurations (see figures VII.3 and VII.9 for example). By performing source identification, we have shown that these differences are due entirely to the acoustic properties of the system (L, R_i, R_o, α), but that the

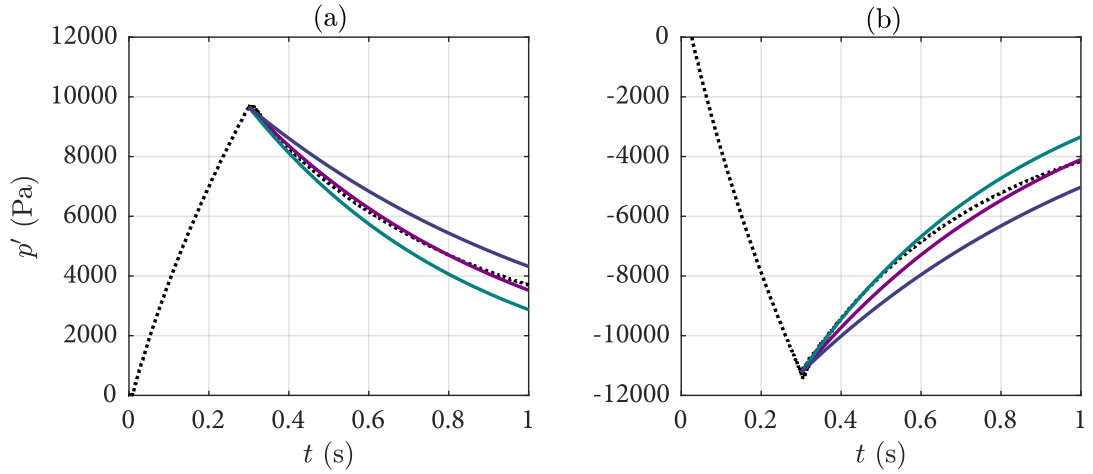


Figure VII.13: Experimental acoustic pressure (.....) and theoretical decay for $R_o = 0.982$ (—), $R_o = 0.985$ (—) and $R_o = 0.988$ (—) for (a) case A12 with $\dot{m}_i = 1 \text{ g s}^{-1}$ and (b) case A16.

acoustic source π_d^+ is actually identical. This is consistent with our analytical model.

VII.2.4 System identification

So far, we have assumed the outlet reflection coefficient to be $R_o = 0.992$, as predicted by the isentropic compact nozzle model. We can now verify this assumption.

Indeed, (VI.4) shows that R_o can be recovered from the experimental pressure signal, as long as the acoustic source π_d^+ is known. Using our analytical prediction for π_d^+ , extracting the outlet reflection coefficient R_o for $\omega = 0$ (compactness hypothesis) gives $R_o = 0.995$ ($\pm 0.7\%$ depending on the test case). This measurement is in good agreement with the isentropic compact model for a choked nozzle.

Alternatively, we can estimate the value of R_o by taking advantage of the fact that the pressure fluctuations in cases A11–A16 are predicted to decay exponentially as $(R_i R_o e^{-2\alpha L})^{t/\tau}$. Each value of R_o leads to a different decay rate, as shown in figure VII.13.

There is good agreement between the experimental signal and the exponential decay model for $R_o = 0.995$ ($\pm 0.2\%$ depending on the experimental case). The decay rate is very sensitive to the value of R_o , suggesting that our estimation of this value is likely to be precise.

VII. AIR INJECTION – DIRECT NOISE

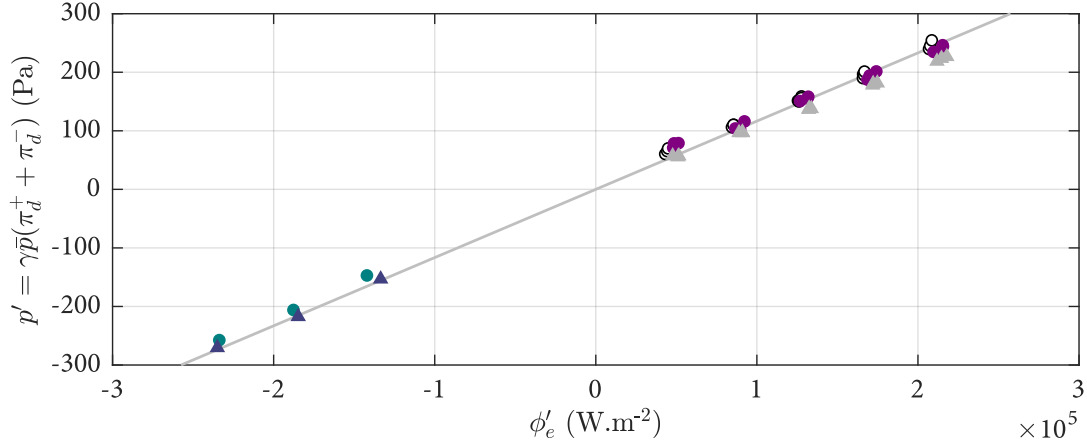


Figure VII.14: Analytical (—) and experimental results for the peak direct noise pressure $p' = \gamma \bar{p}(\pi_d^+ + \pi_d^-)$ for cases A1-A4 (○), A5-A7 (●), A8-A10 (●), A11-A13 (▲) and A14-A16 (▲).

VII.3 Comparison to the direct noise model

For each of the experimental cases (A1–A16), we can identify the acoustic sources π_d^+ and π_d^- . We can then compute the peak pressure fluctuation associated to these acoustic sources: $p' = \gamma \bar{p}(\pi_d^+ + \pi_d^-)$. This peak pressure is plotted as a function of the added energy flux $\phi'_e = \dot{m}_i \bar{c}_p \bar{T} / A_1$ in figure VII.14. These measurements can be directly compared to the analytical direct noise model (§II.4.2).

The experimental measurements are in good agreement with the analytical model. As predicted in (II.14), the direct noise fluctuation p' is proportional to the added energy flux ϕ'_e , such that $p' \approx \frac{\gamma-1}{c} \phi'_e$. This confirms that the direct noise model is correct.

VIII

HEAT ADDITION – ENTROPIC NOISE

Experiments are carried out on the Cambridge Wave Generator with wave module B (heat addition). This is expected to generate direct noise as well as convected entropic waves (as shown in §II.4.1). If these entropic waves are not fully dispersed or dissipated before reaching the outlet of the duct they will lead to the generation of entropic noise.

Twenty experimental cases are carried out in total (B1–B20). Cases B1–B6 correspond to the long duct configuration, in which acoustic pulses are separated by a large time delay, and no entropic noise is produced. The results of these tests are used to determine the direct noise generated by unsteady heat addition. Cases B7–B20 are carried out in the short configuration, meaning that reverberation occurs and that entropic waves are convected through the outlet nozzle. The resulting entropic noise is measured for a choked nozzle (B7–B12) and a subsonic orifice (B13–B20).

The experimental results are then compared to simulations carried out using the analytical model presented in §V. Source identification enables the contributions of direct and entropic noise to be identified clearly in the experimental signal. This enables us to shed light on the suitability of the isentropic and anisentropic nozzle transfer functions derived in §III.

The experiments presented in this chapter were carried out either by Francesca de Domenico (B13–B20), or in collaboration with her (B1–B12). The interpretation and analysis of the experimental data was performed by the author.

VIII.1 Long configuration

In the long configuration, the system is effectively a duct of length $L = 62.6$ m as shown in figure VIII.1. The heating device is located at a distance $x_s = 0.7$ m downstream of the inlet,

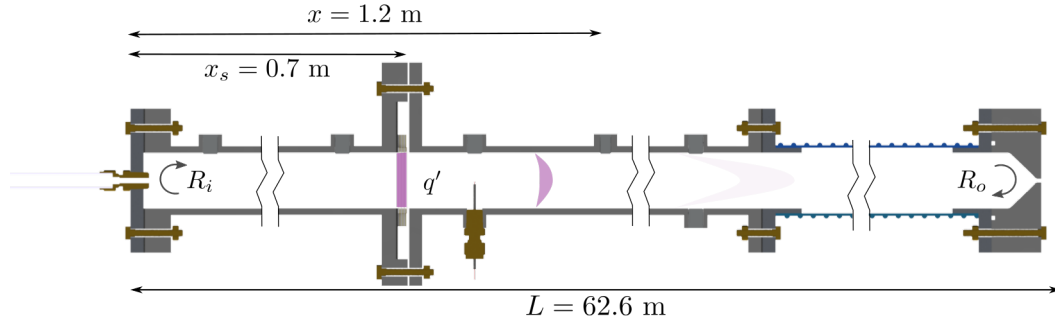


Figure VIII.1: Long tube configuration with wave module B: heat is generated in a duct with reflections at the inlet and outlet.

Case	Outlet	\bar{p} [kPa]	\bar{M}_1 [-]	\dot{m} [g s ⁻¹]	ΔT_d [K]
B1	Open	101.6	0.0101	5.92	5.1
B2	Open	101.8	0.0135	7.89	3.9
B3	Open	102.2	0.0168	9.87	3.2
B4	Choked	205.3	0.0052	5.92	5.7
B5	Choked	267.2	0.0052	7.89	4.1
B6	Choked	351.3	0.0052	9.87	3.3

Table VIII.1: Experimental cases for wave module B (heat addition) in the long configuration with outlet type, mean pressure \bar{p} , mean Mach number \bar{M}_1 , primary mass flow rate \dot{m} and average grid temperature fluctuation ΔT_d .

and the mean and fluctuating pressures are measured at $x = 1.2$ m.

The fluctuating temperature ΔT_d is measured 0.04 m downstream of the heating device. This is used as an indication of how much heat has been added to the flow (see §VI.2.2).

Acoustic reflections occur at the inlet of the duct with $R_i = 0.99$. The outlet is either open-ended (with $R_o = -1$), or fitted with a choked converging nozzle ($R_o = 0.992$). As a consequence of the duct length ($L = 62.6$ m), reverberation does not occur and only direct noise is generated.

The test cases are shown in table VIII.1. Cases B1–B3 are carried out near atmospheric pressure with an open end. The duct is pressurised in cases B4–B6, in which the outlet is a choked converging nozzle. In all cases, the heating device is activated for a pulse duration of $\tau_p = 300$ ms and phase averaging is performed over 50 pulses.

VIII. HEAT ADDITION – ENTROPIC NOISE

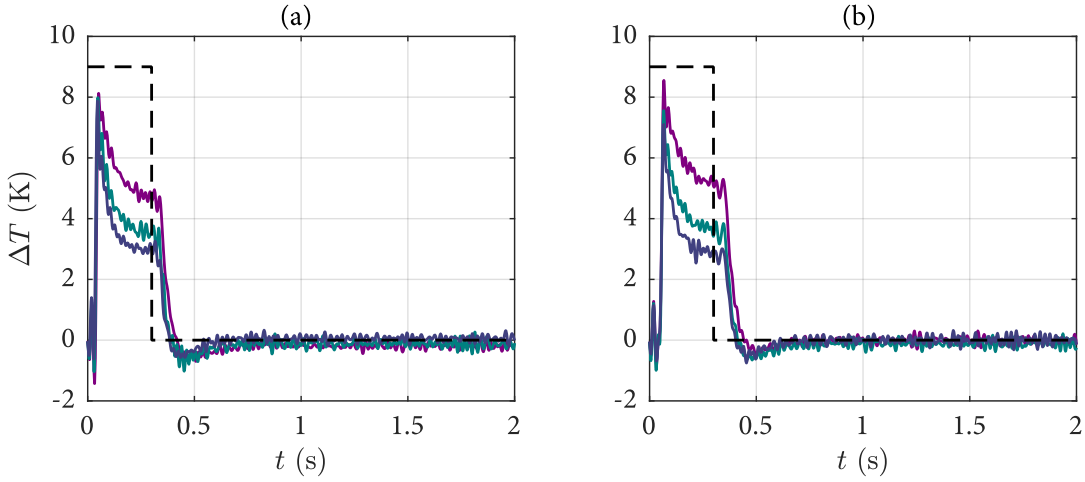


Figure VIII.2: Experimental temperature fluctuation ΔT_d downstream of the heating device for (a) cases B1 (—), B2 (—), B3 (—) and (b) cases B4 (—), B5 (—), B6 (—). The heating device signal is shown for reference (---).

VIII.1.1 Experimental results

The temperature fluctuations ΔT_d measured just downstream of the heating device are shown in figure VIII.2 for cases B1–B6.

The temperature fluctuation measured is consistent with the activation of the heating device for $0 < t < 300$ ms. There is small time delay since ΔT_d is measured 40 mm downstream of the device itself. The temperature rises sharply when the heating device is switched on at $t = 0$ and heat is transferred to the flow by convection. The induced temperature fluctuation then decreases until $t = 300$ ms, at which point the device is switched off and the temperature fluctuation falls. The temperature fluctuation appears to be negative for a short duration after the heating device is switched off, after which it progressively returns to zero.

For all cases, we see that the amplitude of the induced temperature fluctuation is inversely proportional to the mass flow rate. This is consistent with the fact that we have a nearly constant heat flux $Q' \approx \dot{m} \bar{c}_p \Delta T_d$.

The acoustic pressure measurements $p'(x, t)$ for cases B1–B3 and B4–B6 are shown in figures VIII.3(a) and (b) respectively.

The results for cases B1–B6 are reminiscent of those for cases A1–A6 (long configuration, air injection). The pressure signal corresponds to several time-separated acoustic pulses. The duration of the pulses coincides with the heating device pulse duration $\tau_p = 300$ ms.

The shape of the acoustic pulses is very similar to the shape of the temperature fluctua-

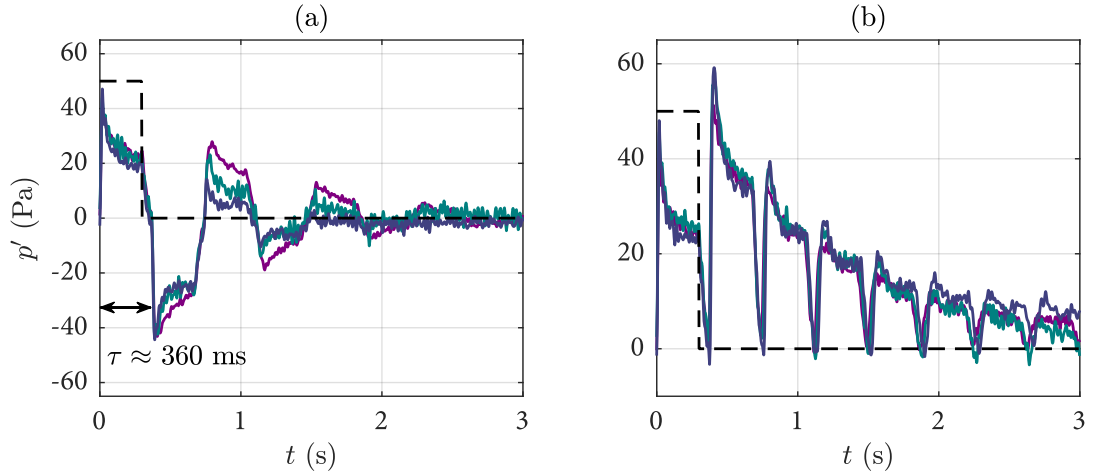


Figure VIII.3: Experimental pressure fluctuation $p'(x, t)$ for (a) cases B1 (—), B2 (—), B3 (—) and (b) cases B4 (—), B5 (—), B6 (—). The heating device signal is shown for reference (---).

tions shown in figure VIII.2. This is consistent with the analytical model for an unsteady heat addition (§II.4.1), which predicts that the direct noise pulse is directly proportional to the normalised heat flux $q' = \Delta T_d / \bar{T}$.

Once again, the sign of the reflected pulses is given by the sign of the outlet reflection coefficient R_o . Notably, the amplitude of the pulses is roughly the same for all cases. This is consistent with the theory, which shows that for a given heat input Q' (equivalent to a constant energy flux ϕ'), the resulting direct pressure fluctuation p' is independent of the mean pressure and Mach number, as shown in (II.14).

In cases B1–B3 shown in figure VIII.3(a) the first acoustic pulse is identical but the reflections decay at slightly different rates. This is consistent with a change in acoustic attenuation α due to the Mach number in the duct (see figure VII.4).

VIII.1.2 Simulations

Analytical results for cases B1 and B4 are shown in figure VIII.4 along with the corresponding experimental measurements. The input used for the heat flux at the heating device is the temperature measurement ΔT_d . We use the acoustic attenuation factors α measured in §VII.1.1.

The analytical results are in very good agreement with the experimental measurements. The shape of the pressure pulses is finely predicted by the analytical model, which suggests that the temperature measurements used as an input are accurate.

VIII. HEAT ADDITION – ENTROPIC NOISE

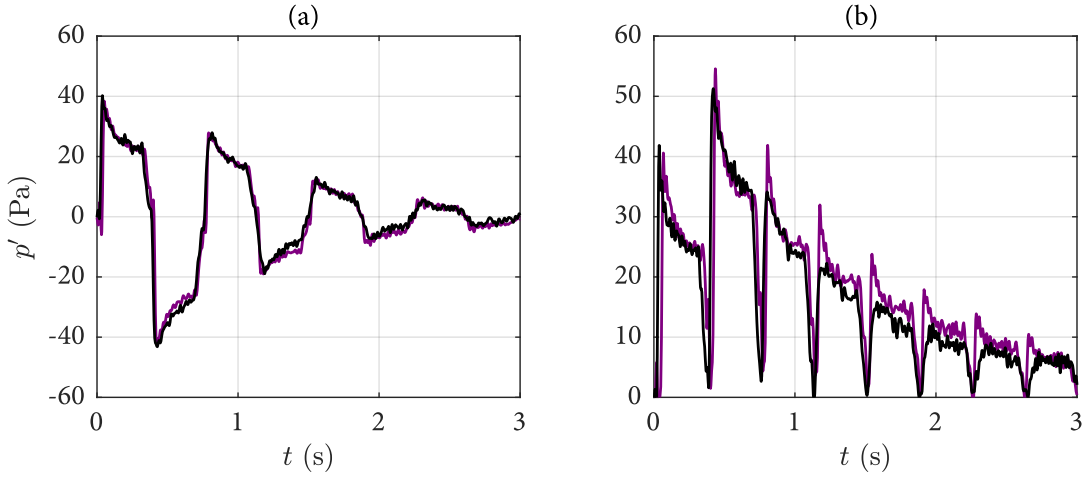


Figure VIII.4: Analytical (—) and experimental results (—) for the pressure fluctuation $p'(x, t)$ for (a) case B1 (b) case B4.

VIII.2 Short configuration – choked nozzle

Six cases are carried out in the short configuration with a choked converging nozzle. The length of the duct is either $L = 1.1$ m or $L = 1.6$ m. This corresponds to acoustic time-scales of less than 10 ms (much shorter than the heat pulse duration), meaning that reverberation occurs.

The convective length $L_c = L - x_s$ between the heating device and the outlet nozzle is $L_c = 0.4$ m or $L_c = 0.9$ m depending on the case. These relatively short lengths ensure that entropic waves are not fully dispersed or dissipated before reaching the outlet nozzle, meaning that entropic noise will be generated.

The heating device is located at $x_s = 0.7$ m, and the mean and fluctuating pressures are measured at $x = 1.2$ m. Temperature fluctuations are measured 40 mm downstream of the heating device (ΔT_d) and 50 mm upstream of the outlet (ΔT_n). The latter provides a measurement of the amplitude of the entropic wave $\sigma \approx \Delta T_n / \bar{T}$ convected through the nozzle.

The operating conditions for cases B7–B11 are shown in table VIII.2. The heating device is activated for a pulse duration of $\tau_p = 200$ ms in all cases and phase averaging is performed over 50 pulses.

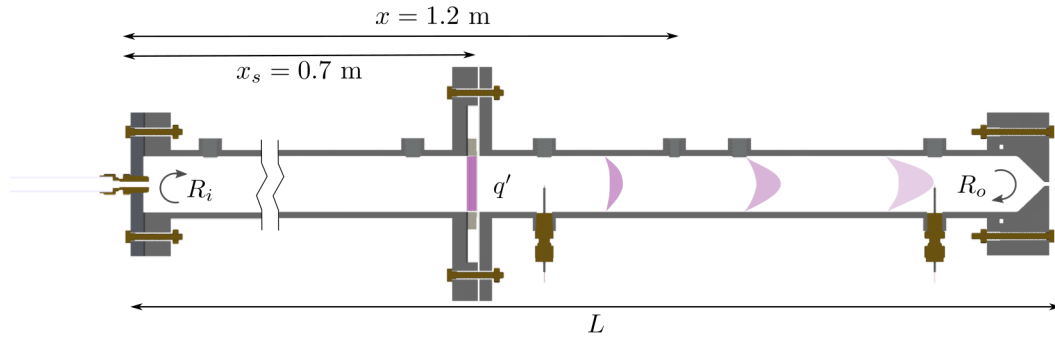


Figure VIII.5: Short tube configuration with wave module B: heat is generated in a duct with reflections at the inlet and outlet. An entropic wave is generated at the heating device and convected through the duct.

Case	L [m]	L_c [m]	\bar{p} [kPa]	\bar{M}_1 [-]	\dot{m} [g s ⁻¹]	ΔT_d [K]	ΔT_n [K]
B7	1.6	0.9	205.3	0.0052	5.92	5.7	4.8
B8	1.6	0.9	267.2	0.0052	7.89	4.1	3.6
B9	1.6	0.9	351.3	0.0052	9.87	3.3	2.9
B10	1.1	0.4	205.3	0.0052	5.92	5.7	4.5
B11	1.1	0.4	267.2	0.0052	7.89	4.1	3.5
B12	1.1	0.4	351.3	0.0052	9.87	3.3	2.8

Table VIII.2: Experimental cases for wave module B (heat addition) in the short configuration with a choked nozzle, convective length L_c , mean pressure \bar{p} , mean Mach number \bar{M}_1 , primary mass flow rate \dot{m} , average grid temperature fluctuation ΔT_d and average nozzle temperature fluctuation ΔT_n .

VIII. HEAT ADDITION – ENTROPIC NOISE

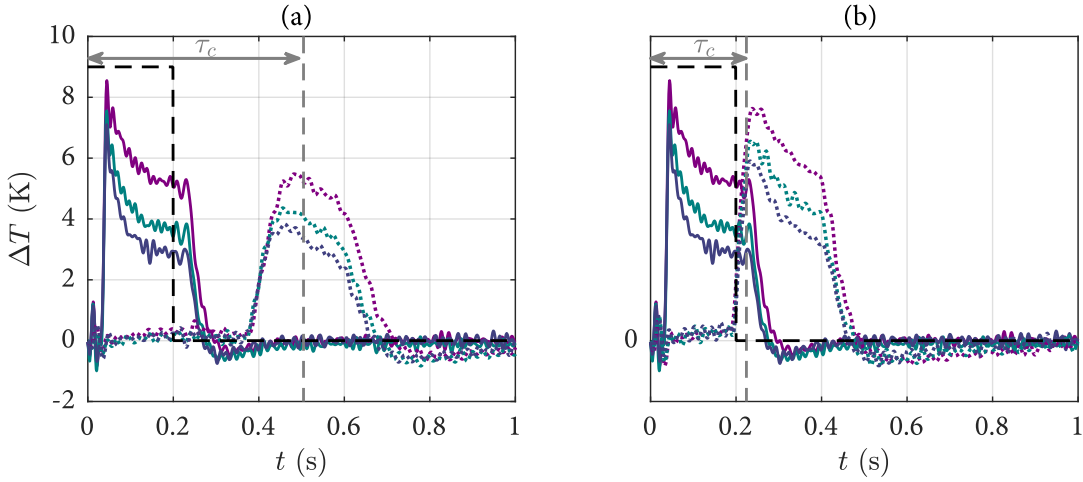


Figure VIII.6: Experimental temperature fluctuations downstream of the heating device and upstream of the nozzle ($\Delta T_d, \Delta T_n$) for (a) cases B7 (—, ····), B8 (—, ····), B9 (—, ····) and (b) cases B10 (—, ····), B11 (—, ····), B12 (—, ····). The convective time delay (---) and heating device signal (- - -) are shown for reference.

VIII.2.1 Experimental results

The temperature measurements downstream of the heating device and upstream of the nozzle are shown for cases B7–B12 in figure VIII.6.

The temperature fluctuations ΔT_d measured near the heating device are very similar to those obtained in the corresponding long tube cases (B4–B6); the main difference is the shorter pulse duration ($\tau_p = 200$ ms). As before, the temperature fluctuation ΔT_d briefly falls below zero just after the heating device is switched off.

For cases B7–B9, an entropic wave is measured at the nozzle starting at $t \approx 0.4$ s. This is consistent with the convective time delay $\tau_c = L_c/\bar{u} \approx 0.5$ s. Similarly, in cases B10–B12 the entropic wave is measured at the nozzle at $t \approx 0.2$ s, which is close to the mean convective time delay $\tau_c = L_c/\bar{u} \approx 0.22$ s. The slight discrepancy in these two values can be explained by the fact that the entropic wave is measured at the duct centreline (at which the flow speed is higher than the mean flow speed). As such, it is measured earlier than indicated by the convective time delay τ_c , which is based on the mean flow speed \bar{u} .

In all cases the shape of the temperature fluctuation at the nozzle is slightly different to the one at the heating device, and its amplitude is reduced. This is indicative of diffusion, dissipation and dispersion⁶⁹.

The acoustic pressures for cases B7–B9 and B10–B12 are shown in figures VIII.7(a) and (b)

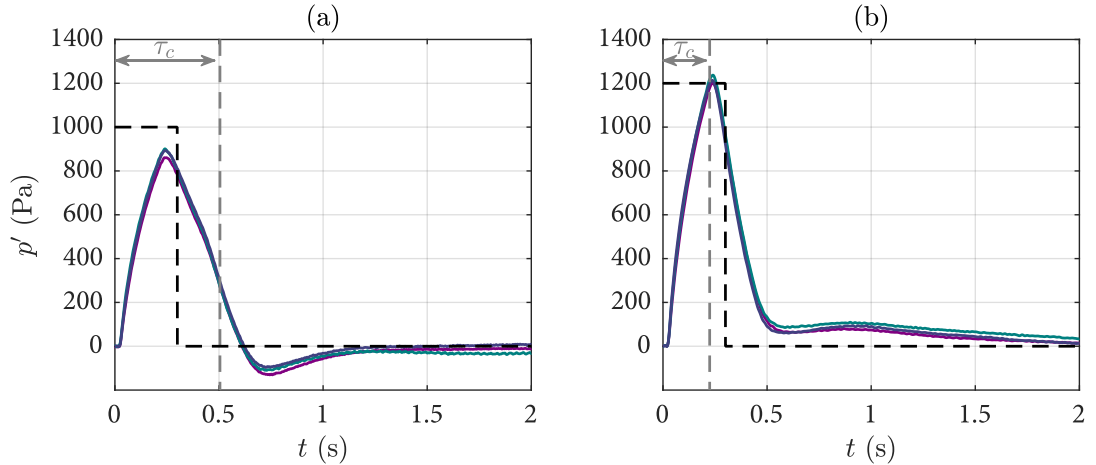


Figure VIII.7: Experimental pressure fluctuation $p'(x, t)$ for (a) cases B7 (—), B8 (—), B9 (—) and (b) cases B10 (—), B11 (—), B12 (—). The convective time delay (---) and heating device signal are shown for reference (---).

respectively.

We know from the results for configuration A (§VII.2) that in the case of a short duct, the acoustic time-scale is shorter than the pulse duration ($\tau \ll \tau_p$), and the acoustic pressure builds up and decreases exponentially. The results for cases B7–B9 show a slightly different picture. During the heat addition ($0 < t < 200$ ms), the pressure rises sharply to reach a maximum at $t = 200$ ms. The pressure then appears to decrease exponentially. At $t = \tau_c \approx 500$ ms (when the entropic wave reaches the nozzle), the pressure appears to decrease at a different rate. Once the temperature disturbance has completely convected through the nozzle (at $t = \tau_c + \tau_p \approx 700$ ms), the pressure disturbance appears to decay exponentially once again. These results suggest that the pressure fluctuation visible from $t = 0$ to $t = \tau_p$ is direct noise due to heat addition, while the change in slope at $t = \tau_c$ is due to entropic noise as the entropic wave is accelerated through the nozzle.

In cases B10–B12, the duct is shorter than in cases B7–B9, meaning that the acoustic round-trip time τ is also shorter. This explains why the maximum pressure is higher than in cases B7–B9: the repeated acoustic reflections accumulate faster. The convection time $\tau_c \approx 220$ ms nearly coincides with the pulse duration τ_p . As a result, the change in slope associated to indirect noise appears sooner in the experimental signal, and the entropic noise does not cause the overall acoustic pressure to become negative.

VIII. HEAT ADDITION – ENTROPIC NOISE

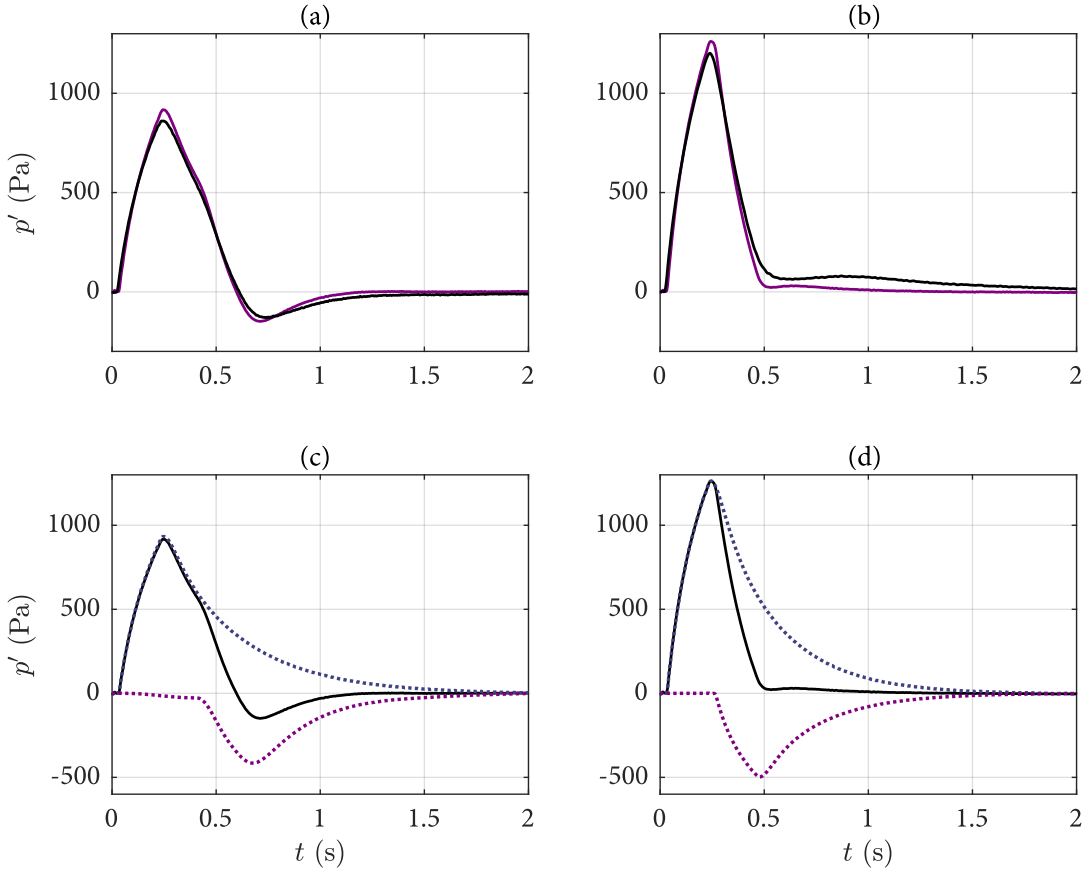


Figure VIII.8: Analytical (—) and experimental results (—) for the pressure fluctuation $p'(x, t)$: (a) case B7 (b) case B10. Contributions of direct (····) and entropic (····) noise to the overall analytical pressure (—) for (c) case B7 and (d) case B10.

VIII.2.2 Simulations

The analytical results for cases B7 and B10 are in good agreement with the experimental measurements, as shown in figure VIII.8. In both cases, the peak pressure is slightly higher than expected. In case B10, the change in slope is more pronounced than in the experimental signal, which suggests that the entropic noise may have been slightly over-predicted.

While the individual contributions of direct and entropic noise are merged in the experimental results, they can be computed separately in the analytical model. These contributions are shown in figures VIII.8(c) and (d) for cases B7 and B10. The results clearly show that the change in slope which occurs after a convective time delay is due to entropic noise. In the cases shown here, entropic noise is approximately half as large as direct noise.

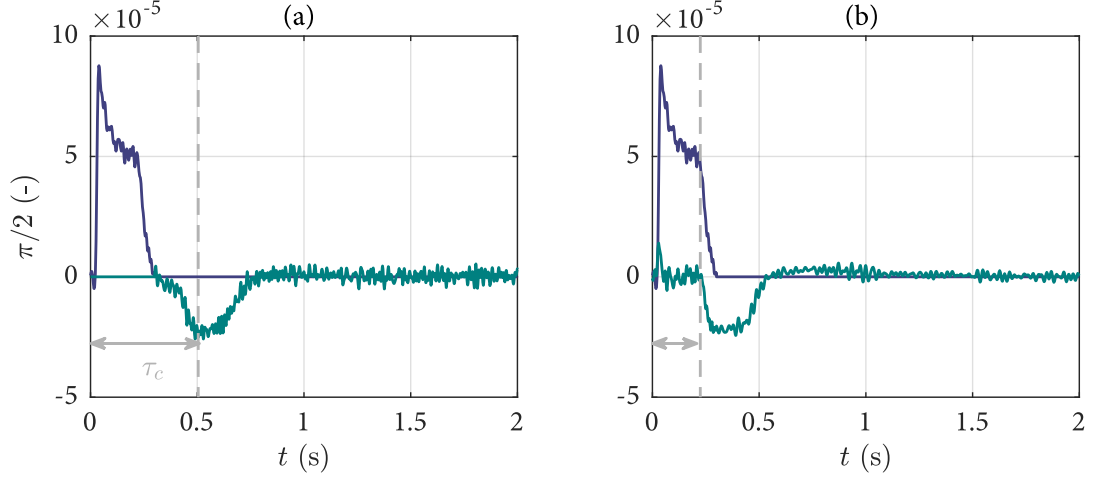


Figure VIII.9: Acoustic source $\pi/2$ for direct (—) and entropic acoustic waves (—) generated for (a) case B7 and (b) case B10. Convective time delay τ_c (- -).

VIII.2.3 Source identification

The experimental results can be dereverberated using the method outlined in §V.4.2 and §VI.4.2. As shown in (V.24), the resulting acoustic source signal π is a combination of direct and entropic sound waves such that $\pi \approx 4\pi_d^+ + 2\pi_\sigma^-$, or $\pi/2 \approx 2\pi_d^+ + \pi_\sigma^-$ (since $R_i \approx R_o \approx 1$ in this case). The source signals $\pi/2$ for cases B7 and B10 are shown in figure VIII.9.

The source signals closely match what one would expect. In case B7, a positive acoustic pulse can be seen for $0 < t < \tau_p$, coinciding with the heating device pulse. Clearly, this corresponds to the direct sound source (π_d^+, π_d^-). The shape of the pressure pulse is consistent with the results for cases B1–B6 (figure VIII.3), in which direct acoustic pulses are separated.

A negative pulse occurs after the convective time delay, which can be identified as the entropic sound source (π_σ^-). Since the convective time delay τ_c is longer than the pulse duration τ_p , we can clearly separate the direct and indirect sound waves here (direct noise is generated for $t < \tau_p$, and indirect noise is generated for $t \geq \tau_c$).

In cases B10, the direct and indirect noise appear to be merged since we have $\tau_p > \tau_c$. However, these contributions can be separated by subtracting the direct noise signal from case B7 from the results in case B10 ($\pi_\sigma^- = \pi/2 - 2\pi_d^+$). Once again, the resulting indirect noise source signal appears at a time corresponding to the convective time delay τ_c .

VIII. HEAT ADDITION – ENTROPIC NOISE

Case	L [m]	L_c [m]	\bar{p} [kPa]	\bar{M}_1 [-]	\bar{M}_t [-]	\dot{m} [g s ⁻¹]	ΔT_d [K]	ΔT_n [K]
B13	2.1	1.4	102.78	0.0026	0.128	1.52	26.7	7.9
B14	2.1	1.4	103.54	0.0033	0.170	2.95	21.1	8.2
B15	2.1	1.4	104.00	0.0036	0.187	2.17	19.5	8.0
B16	2.1	1.4	105.19	0.0043	0.221	2.64	15.9	7.5
B17	2.1	1.4	106.64	0.0051	0.262	3.14	13.3	6.8
B18	2.1	1.4	108.34	0.0058	0.304	3.61	11.7	6.1
B19	2.1	1.4	110.86	0.0066	0.354	4.26	10.5	5.9
B20	2.1	1.4	113.65	0.0075	0.411	4.89	9.2	5.7

Table VIII.3: Experimental cases for wave module B (heat addition) in the short configuration with the orifice, convective length L_c , mean pressure \bar{p} , mean Mach number \bar{M}_1 , orifice throat Mach number \bar{M}_t , primary mass flow rate \dot{m} , average grid temperature fluctuation ΔT_d and average nozzle temperature fluctuation ΔT_n .

VIII.3 Short configuration – orifice

We have shown in §III that the transfer functions of anisentropic nozzles are substantially different to those of the isentropic nozzles we have considered so far. To investigate this, we perform experiments on the Cambridge Wave Generator with a subsonic orifice, which is one of the limit cases of an anisentropic nozzle (see §III.2.1).

This enables us to examine the influence of anisentropy on the acoustic reflection coefficient R_o , as well as the entropic-acoustic reflection coefficient π_{σ}^-/σ .

The experimental details are identical to those in §VIII.2 (short configuration – choked nozzle) unless otherwise stated. Notably, the thermocouples used to measure the temperature fluctuations at the heating device and at the nozzle have a longer response time than those used in cases B1–B12. As a result, the temperature measurements can be expected to be less accurate than those in cases B1–B12.

We perform eight tests in the short configuration with an orifice (B13–B20). The operating conditions for these cases are shown in table VIII.3. The mean Mach number at the throat M_t is calculated by solving the mean flow jump equations for an orifice in (III.1) and (III.19) (for $\Lambda = 1$ and $\Gamma = 0.83$).

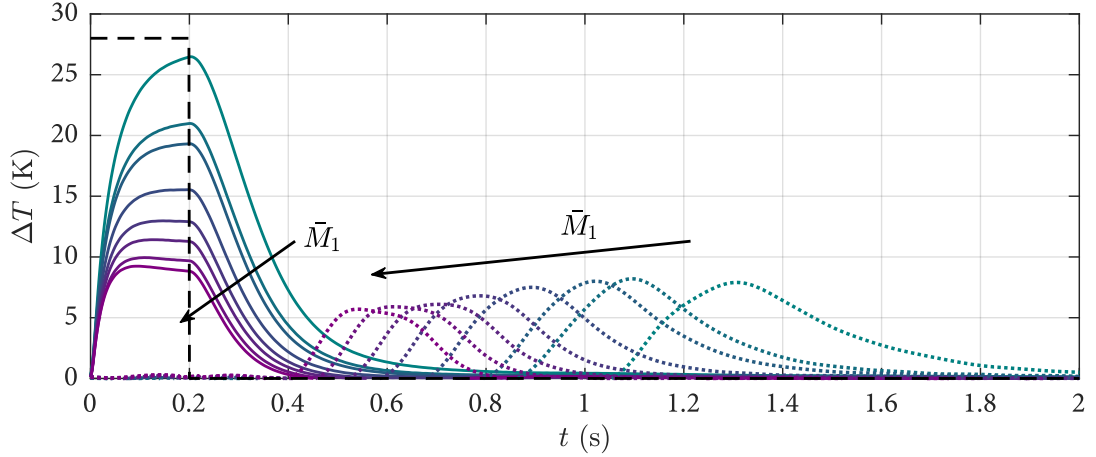


Figure VIII.10: Experimental temperature fluctuations downstream of the heating device and upstream of the nozzle ($\Delta T_d, \Delta T_n$) for cases B12 (—, ···) to B20 (—, ···). The heating device signal is shown for reference (---).

VIII.3.1 Experiments

The temperature measurements just downstream of the heating device and just upstream of the orifice are shown in figure VIII.10.

As in cases B1–B12, the temperature fluctuation ΔT_d induced by the heating device decreases as the Mach number \bar{M}_1 (and mass flow rate \dot{m}) increases. Nevertheless, the shape of the temperature fluctuation ΔT_d is substantially different to the one measured in previous cases (see figures VIII.2 and VIII.6).

Crucially, the current measurements of ΔT_d do not show the negative oscillation seen in cases B1–B12. Given that the thermocouples used in cases B1–B12 had a faster response time than those used in cases B13–B20, this oscillation is likely present in cases B13–B20, although it has not been recovered in the measurements.

An entropic wave is detected upstream of the orifice in the form of a temperature fluctuation ΔT_n . The time at which it is measured is consistent with the convective time delays $\tau_c = L_c/\bar{u}$, which decrease as the Mach number in the duct is increased. The entropic waves with the longest convective time delays (i.e. the longest residence times) appear to be most affected by dispersion and dissipation, which is physically intuitive.

The acoustic pressure measurements for cases B13–B20 are shown in figure VIII.11.

The acoustic pressure increases while the heating device pulse signal is active ($0 < t < 200$ ms), and decays thereafter. This can be attributed to the reverberation of direct noise. The

VIII. HEAT ADDITION – ENTROPIC NOISE

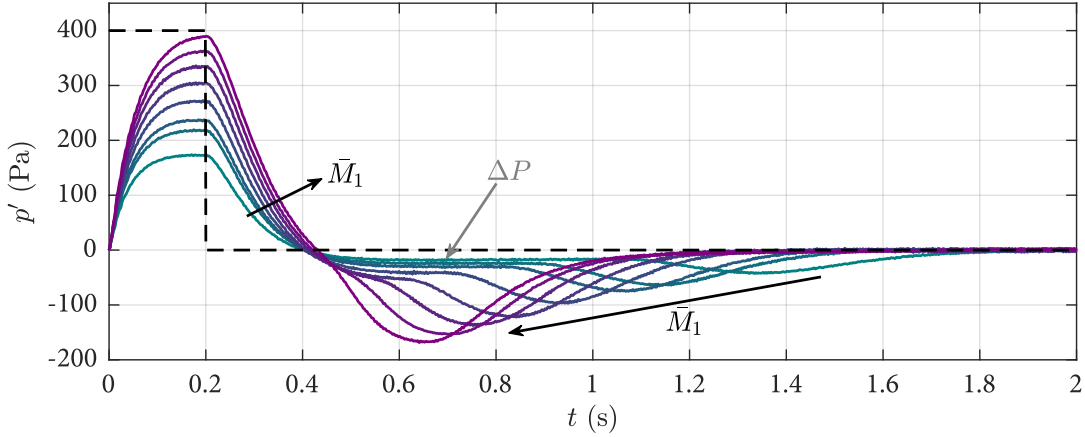


Figure VIII.11: Experimental pressure fluctuations $p'(x, t)$ for cases B12 (—) to B20 (—). The heating device signal is shown for reference (- - -).

shape of the pressure signal is very similar to limit case III (§V.3): the acoustic pressure appears to converge towards a limit as t approaches 200 ms. This is consistent with the predictions of the reverberation model (see (IV.7)).

After the direct noise pulse (for $t < 200$ ms), the acoustic pressure signal decays and appears to reach a negative plateau ($\Delta P < 0$) instead of falling to zero.

A negative pressure pulse appears in the measured signal after a time delay. This time delay is consistent with the convective time delay τ_c for each case, and decreases as the Mach number \bar{M}_1 is increased. Comparing figures VIII.11 and VIII.10 shows that the negative pulse appears at the same time as an entropic wave is detected at the orifice. This indicates that the negative pressure pulse is in fact entropic noise. The amplitudes of the direct and entropic noise signals both increase with the Mach number \bar{M}_1 .

VIII.3.2 Simulations

One of the objectives of this thesis is to validate the anisentropic nozzle model derived in §III. As such, simulation of cases B13–B20 are carried out using the anisentropic nozzle model (for the limit case of an orifice with $\Lambda = 1$). For comparison, we also perform simulations using the isentropic nozzle model previously derived by Marble & Candel⁶¹, which is applied to a convergent nozzle of dimensions identical to those of the orifice (A_1, A_t).

The anisentropic nozzle model makes predictions concerning the mean pressure drop $\bar{p}_1 - \bar{p}_2$ across the orifice. Taking \bar{p}_1 as the mean pressure measured in the duct and \bar{p}_2 as atmo-

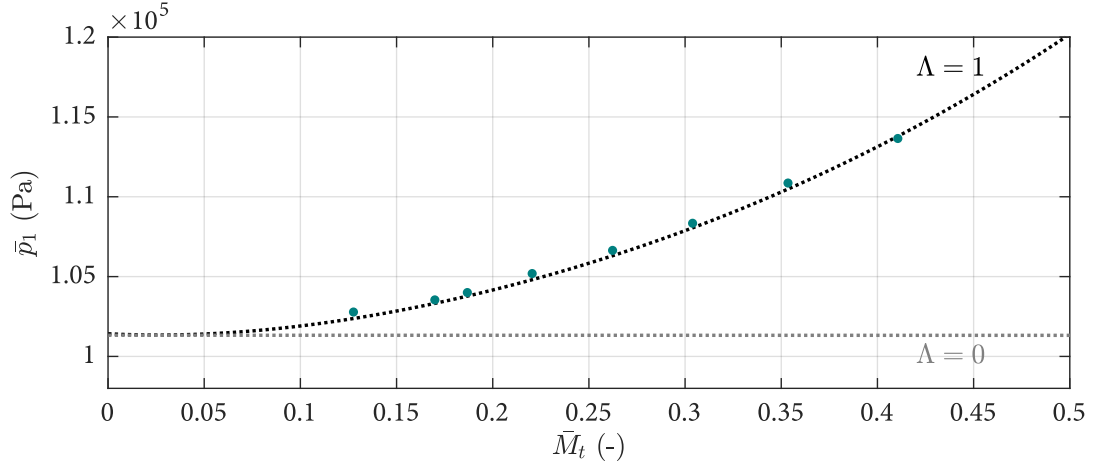


Figure VIII.12: Upstream mean pressure \bar{p}_1 as a function of the throat Mach number \bar{M}_t . Experimental measurements for cases B13–B20 (●), isentropic limit case for $\Lambda = 0$ (.....), orifice limit case for $\Lambda = 1$ (.....).

spheric, we can compare these predictions to our experimental results. This is shown in figure VIII.12 for cases B13–B20.

The upstream pressures \bar{p}_1 measured experimentally are very close to the analytical solution obtained with the anisentropic model for the orifice plate limit case ($\Lambda = 1$, $\Gamma = 0.83$). Conversely, the isentropic model is inadequate here (since it assumes that there is no mean pressure drop across the orifice).

The theoretical acoustic ($R_o = \pi_1^- / \pi_1^+$) and entropic-acoustic ($R_\sigma = \pi_1^- / \sigma_1$) reflection coefficients of the anisentropic orifice and isentropic convergent nozzle are shown in figure VIII.13.

The reflection coefficients of the anisentropic orifice are substantially different from those of the equivalent isentropic nozzle. The acoustic reflection coefficient of the orifice is much lower than that for the isentropic nozzle. The opposite is true for the entropic-acoustic reflection coefficient; the orifice plate is predicted to generate a larger amount of entropic noise than the isentropic nozzle.

The simulation results for cases B13–B20 using the isentropic model are shown in figure VIII.14.

The simulation results are not in agreement with the experimental measurements. The pressure peak reached at $t \approx 200$ ms is over predicted by up to 160 % depending on the case. This is consistent with an overestimation of the acoustic reflection coefficient R_o .

Conversely, entropic noise is significantly under-predicted in the isentropic simulation.

VIII. HEAT ADDITION – ENTROPIC NOISE

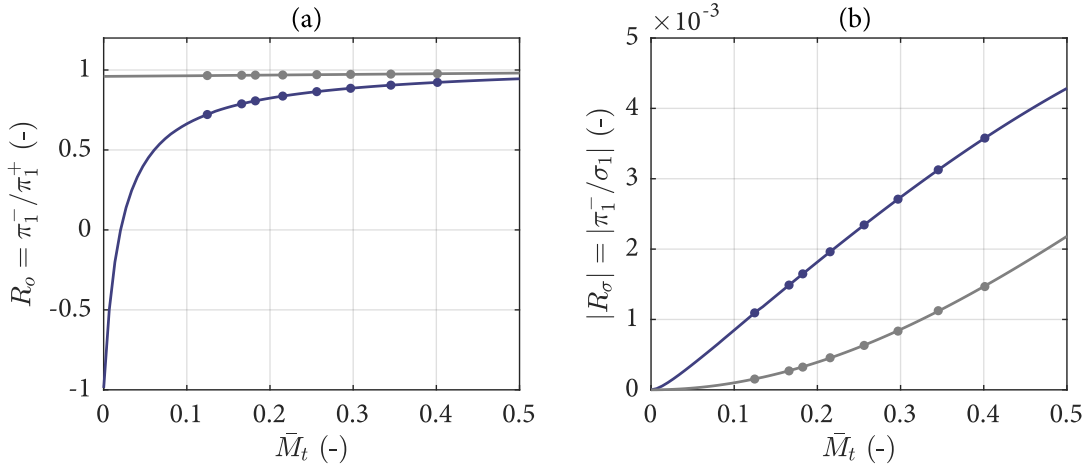


Figure VIII.13: Reflection coefficients of the orifice (—) and of an isentropic convergent nozzle of identical dimensions (—). Values corresponding to cases B13–B20 (●,●).

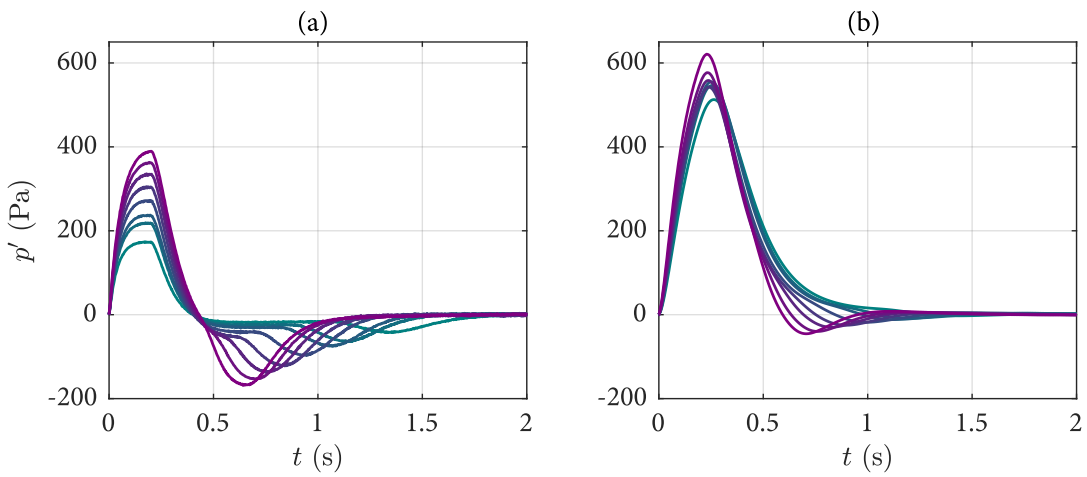


Figure VIII.14: Acoustic pressure fluctuation $p'(x, t)$ for cases B13 (—) to B20 (—): (a) Experimental measurements (b) analytical results with the isentropic nozzle model.

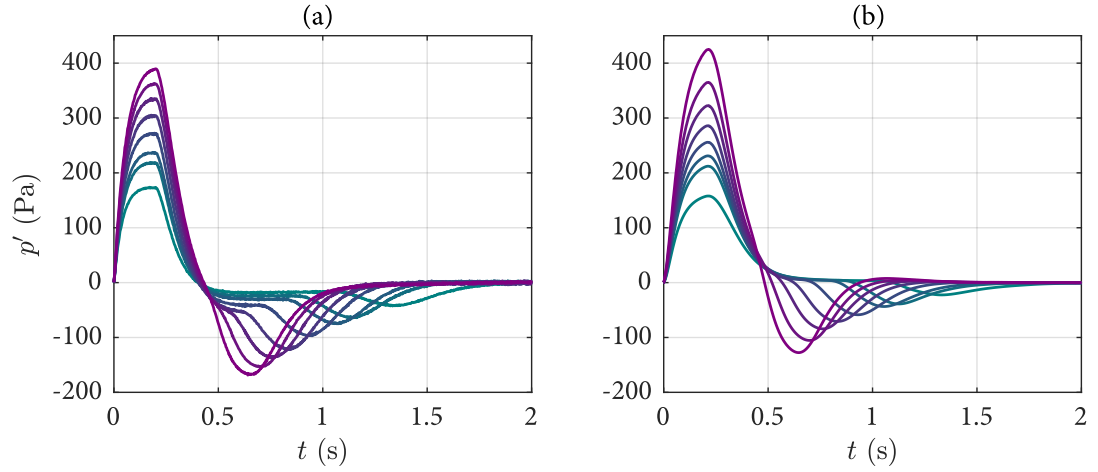


Figure VIII.15: Acoustic pressure fluctuation $p'(x, t)$ for cases B13 (—) to B20 (—): (a) Experimental measurements (b) analytical results with the anisentropic nozzle model.

While negative entropic pressure pulses can clearly be seen in the experimental signal, the acoustic pressure barely falls below zero in the simulations. The significant under-prediction of the entropic noise amplitude suggest that the entropic-acoustic reflection coefficient R_σ has been underestimated. Overall, the comparison shows that the isentropic nozzle model employed here is not adapted to an orifice.

The simulation results for cases B13–B20 using the anisentropic nozzle model are shown in figure VIII.15.

The simulations carried out with the anisentropic model are in good agreement with the experiment. The amplitudes and shapes of both the direct and entropic noise signals are correctly recovered. This confirms that the anisentropic nozzle transfer functions are much more representative of the experiment than the isentropic ones.

The negative pressure plateau ΔP after the direct noise pulse identified in the experimental measurements is not recovered in the simulations. Potential explanations for this difference are addressed in VIII.3.3.

VIII.3.3 Source identification

The acoustic sources in cases B13–B20 are identified using the method outlined in §V.4.2 and §VI.4.2. The resulting acoustic source signal π is a combination of direct and entropic sound waves such that $\pi \approx (1 + R_i)(1 + R_o)\pi_d^+ + (1 + R_i)\pi_\sigma^-$. The source signal π is shown in figure VIII.16(a) for cases B13–B20.

VIII. HEAT ADDITION – ENTROPIC NOISE

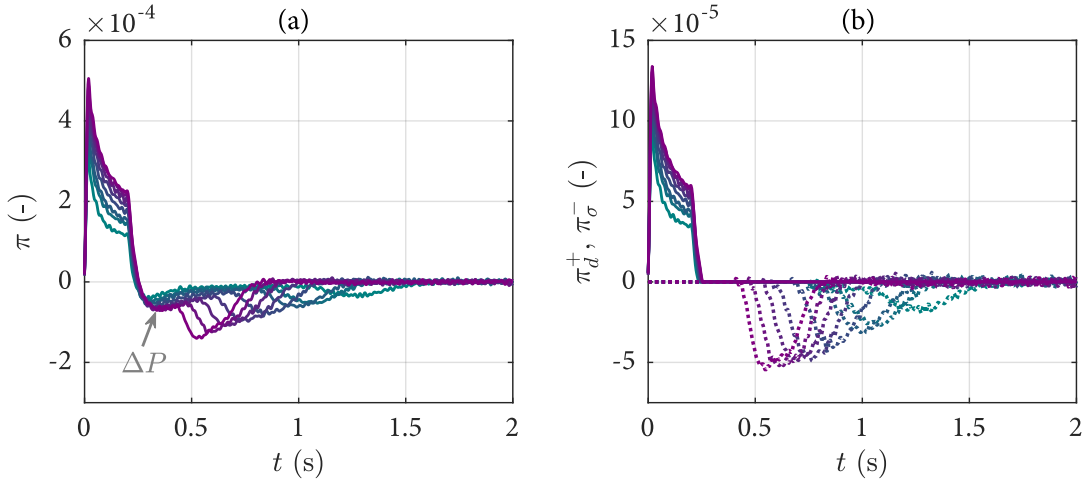


Figure VIII.16: Cases B13 to B20: (a) Overall acoustic source π (—to —), (b) direct and entropic acoustic sources π_d^+ (—to —) and π_σ^- (.....to).

The results clearly show a direct noise pulse for $0 < t < 200$ ms, and an entropic noise pulse after a convective time delay. The shape of the direct noise pulse is quite different from that of the temperature measured downstream of the grid shown in figure VIII.10. However, it is very similar to the temperature measurements for cases B1–B12, which were carried out with a different method. This confirms that the thermocouple used for cases B1–B12 is more accurate than the one used for cases B13–B20.

Notably, the direct acoustic source shows a negative oscillation (from $t = 200$ ms) before the entropic source appears. This oscillation is consistent with the temperature measurements of ΔT_d in cases B1–B12, and is likely to be responsible for the negative pressure plateau ΔP seen in the experimental results. An alternative explanation is that the negative pressure plateau is actually a mean flow effect (rather than an acoustic one). Since the source identification process assumes all pressure fluctuations are acoustic, this mean flow effect is then wrongly identified as an acoustic source. However, this first explanation is most consistent with the negative temperature fluctuation we measure downstream of the grid.

In order to separate the direct and indirect acoustic sources, the negative oscillation responsible for ΔP is eliminated from the signal using a polynomial fitting algorithm, based on the assumption that the direct acoustic source is strictly positive. Since the direct and entropic noise sources are clearly separated in signal, they can be separated as shown in figure VIII.16(b).

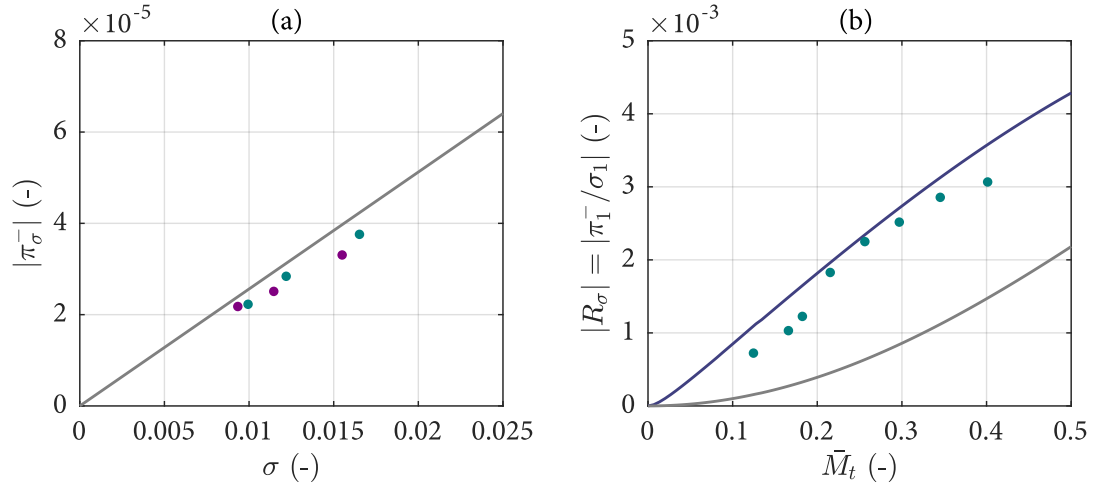


Figure VIII.17: (a) Entropic sound wave $|\pi_\sigma^-|$ for cases B7–B9 (●) and cases B10–B12 (●) compared to the isentropic model (—) and (b) Entropic-acoustic transfer function $|R_\sigma| = |\pi_1^-/\sigma_1|$ for cases B13–B20 (●) compared to the anisentropic orifice model (—) and isentropic model (—).

VIII.4 Comparison to the entropic noise models

The entropic noise waves π_σ^- extracted from cases B7–B12 (choked nozzle) can be compared to the theoretical model for the entropic noise generated at an isentropic choked nozzle (III.14). This is shown in figure VIII.17(a).

Similarly, we can extract the transfer functions $R_\sigma = \pi_\sigma^-/\sigma$ from the experimental results for cases B13–B20 (subsonic orifice). These are compared to the isentropic model as well as the anisentropic model in VIII.17(b).

The experimental measurements of the entropic sound wave π_σ^- in cases B7–B12 are in good agreement with isentropic theory. The entropic noise produced by a choked nozzle increases almost linearly with the incoming entropic wave σ , as predicted by (III.14). The entropic noise is slightly over-predicted. This may be due to the one-dimensional approximation we have made for the entropic wave: we assume that the temperature disturbance is uniformly distributed as it convects through the nozzle, yet this is not the case in reality.

The experimental results for the entropic-acoustic reflection coefficient R_σ in cases B13–B20 are in relatively good agreement with the anisentropic model. Conversely, R_σ is measured to be several times larger than predicted by the isentropic model. This demonstrates that isentropic models inadequately predict the response of nozzles with losses such as orifices.

IX

HELIUM INJECTION – COMPOSITIONAL NOISE

Experiments are carried out on the Cambridge Wave Generator with wave module C (helium injection). As shown in §II.4.3, this generates direct noise as well as a convected entropic and compositional wave. If this convected wave is not fully dispersed or diffused before reaching the outlet nozzle, entropic and compositional noise are generated.

Twenty-two cases are carried out in total (C1–C22). Cases C1–C6 are carried in the long configuration. Since the convective length is long, the helium mixes with the air before reaching the outlet, and only noise resulting from the helium injection itself is detectable. In cases C7–C12, the short configuration is used with a choked nozzle, and entropic and compositional noise are generated. Finally, cases C13–C22 are carried out using the short-extended configuration fitted with a subsonic convergent nozzle, meaning that forward-propagating entropic and compositional noise generated downstream of the nozzle can be measured.

Simulations of each test case are performed using the framework shown in §V, and compared to experimental results. Source identification is then applied to experimental data. The results are used as a basis to validate theoretical models for the compositional noise generated at isentropic and anisentropic nozzles.

IX.1 Long configuration

In cases C1–C6, the convective length is $L_c = 61.65$ m, and the helium disturbances generated by the CWG can be expected to have dispersed and diffused into the primary air flow before reaching the nozzle. The only acoustic waves generated are those associated to the helium injection. The experimental set-up is shown in figure IX.1.

The test cases for wave module C in the long configuration are shown in table IX.1. For

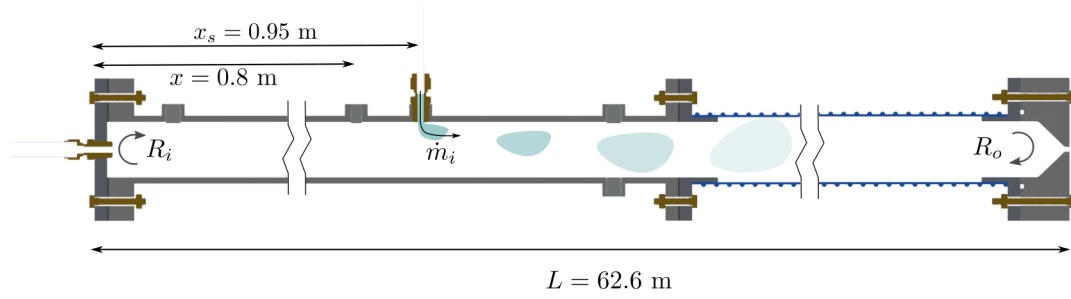


Figure IX.1: Long tube configuration with wave module C: helium is injected into a duct with reflections at the inlet and outlet.

Case	Outlet	\bar{p} [kPa]	\bar{M}_1 [-]	\dot{m} [g s ⁻¹]	\dot{m}_i [g s ⁻¹]
C1	Open	101.3	0.0101	5.92	0.027 → 0.136
C2	Open	101.6	0.0135	7.89	0.027 → 0.136
C3	Open	102.0	0.0168	9.87	0.027 → 0.136
C4	Choked	205.3	0.0052	5.92	0.027 → 0.136
C5	Choked	267.2	0.0052	7.89	0.027 → 0.136
C6	Choked	351.3	0.0052	9.87	0.027 → 0.136

Table IX.1: Experimental cases for wave module C (helium injection) in the long configuration with outlet type, mean pressure \bar{p} , mean Mach number \bar{M}_1 , primary mass flow rate \dot{m} and injected helium mass flow rate \dot{m}_i .

each case, 5 different flow rates of helium are injected (0.027, 0.055, 0.082, 0.109 and 0.136 g.s⁻¹), meaning that 30 tests are conducted in total. The pulse duration is $\tau_p = 100$ ms in all cases.

IX.1.1 Experimental results

The acoustic pressure measurements $p'(x, t)$ for cases C1 and C4 are shown in figure IX.2.

The results for cases C1 and C4 show a similar trend to the corresponding cases in configurations A and B. An acoustic pulse is generated for $0 < t < 100$ ms while the valve is open. As the mass flow rate of injected helium increases, the amplitude of the acoustic pulses increases accordingly.

Notably, the amplitude of the first pulse is not the same in cases C1 and C4; it reaches 300 Pa for case C1, while it reaches only 250 Pa for case C4. This appears to contradict the direct noise model, which suggests that the direct noise is independent of the mean Mach number

IX. HELIUM INJECTION – COMPOSITIONAL NOISE

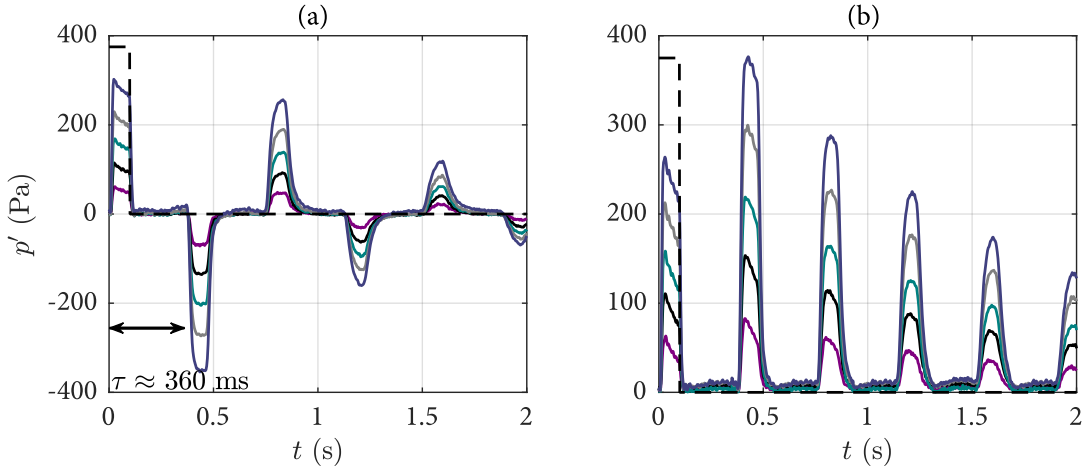


Figure IX.2: Experimental pressure fluctuation $p'(x, t)$ for (a) case C1 and (b) case C4, with $\dot{m}_i=0.027$ (—), 0.055 (—), 0.082 (—), 0.109 (—), 0.136 g s^{-1} (—).

and pressure (which are the only differences between cases C1 and C4). However, this would be overlooking the fact that we are injecting helium, which has a different composition and entropy to air. This generates not only direct noise due to the mass and energy flux at the dispensing valve, but also indirect noise at the same location, which may be responsible for the small difference in amplitude between cases C1 and C4.

IX.1.2 Simulations

The experimental and analytical results for case C6 (long tube, choked) are shown in figure IX.3(a).

The general acoustic behaviour is captured by the analytical model. Unlike the results for configurations A and B, the amplitude of the experimentally measured acoustic pulse is larger than the one predicted with the analytical model. This is expected: the indirect noise generated when the helium flows through the valve and decelerates into the duct is not taken into account by the direct noise model described in §II.

The amplitude of the first pulses in cases C2, C3 (atmospheric pressure) and C5, C6 (pressurised duct) are compared to the direct noise model in figure IX.3(b). The results for cases C2 and C3 are proportional to the total energy flux perturbation, and are consistently 55% higher than predicted if only direct noise is taken into account. The results for cases C5 and C6 also increase linearly with the energy flux ϕ_e , but they are only 22% higher than predicted by the direct noise model.

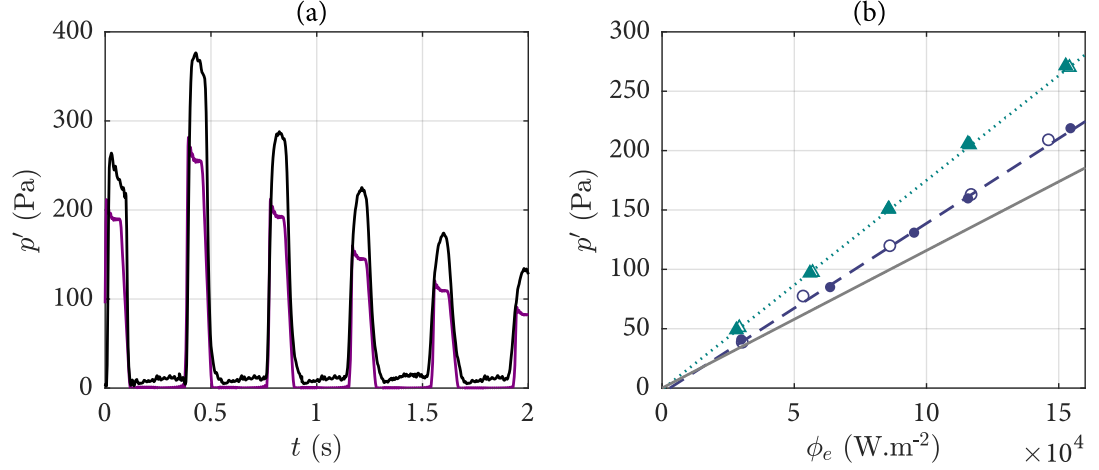


Figure IX.3: (a) Analytical (—) and experimental (—) results for case C6 with $\dot{m}_i = 0.136$ g/s and (b) Experimental peak pressure fluctuation: for cases C2 (Δ), C3 (\blacktriangle) with linear fit (.....), and C5 (\circ), C6 (\bullet) with linear fit (- - -) and analytical prediction of direct noise (—).

The direct noise model for a helium injection depends on two measured inputs: (1) \dot{m}_{He} the mass flow rate of helium being injected (which is measured with a mass flow meter) and (2) on the mean Mach number \bar{M} in the duct (which is computed based on the duct cross section and mass flow rate \dot{m} , which is controlled with a mass flow controller). Neither of these measurements appears to be unreliable. As a result, the discrepancy between the experimental results and the theoretical prediction is likely to be inherent to the direct noise model itself.

As highlighted in §II.4.3, the direct noise model does not account for the production of indirect noise that can be expected during the injection of helium at a high speed into a flow of air. Although it is not possible to apply the one-dimensional indirect noise transfer functions to the inherently two-dimensional helium injection process, the discrepancies between the direct noise prediction and the experimental results are consistent with the indirect noise mechanism.

IX.2 Short configuration

In cases C7–C9 and C10–C12, the tube is short ($L = 1.6$ m), as are the convective lengths ($L_c = 0.65$ m and 0.05 m respectively). The experimental set-up is shown in figure IX.4. Given the short convective lengths, we expect entropic and compositional noise to be generated at the nozzle.

IX. HELIUM INJECTION – COMPOSITIONAL NOISE

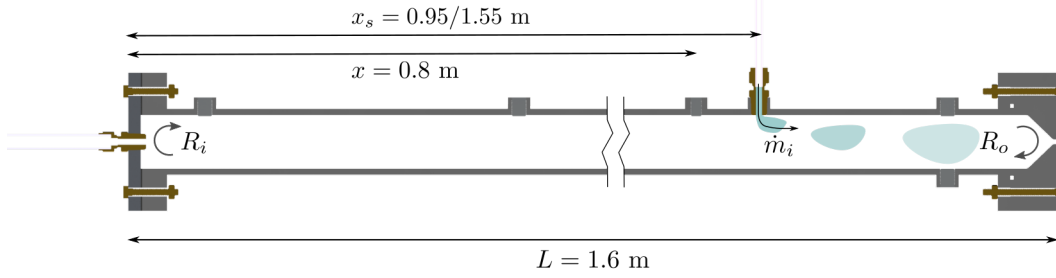


Figure IX.4: Long tube configuration with wave module C: helium is injected into a duct with reflections at the inlet and outlet.

Case	L [m]	\bar{p} [kPa]	\bar{M}_1 [-]	\dot{m} [g s ⁻¹]	\dot{m}_i [g s ⁻¹]
C7	0.65	205.3	0.0052	5.92	0.027 → 0.136
C8	0.65	267.2	0.0052	7.89	0.027 → 0.136
C9	0.65	351.3	0.0052	9.87	0.027 → 0.136
C10	0.05	205.3	0.0052	5.92	0.027 → 0.136
C11	0.05	267.2	0.0052	7.89	0.027 → 0.136
C12	0.05	351.3	0.0052	9.87	0.027 → 0.136

Table IX.2: Experimental cases for wave module C (helium injection) in the short configuration with a choked nozzle, convective length L_c , mean pressure \bar{p} , mean Mach number \bar{M}_1 , primary mass flow rate \dot{m} and injected helium mass flow rate \dot{m}_i .

The operating conditions for cases C7–C12 are shown in table IX.2. The pulse duration is $\tau_p = 100$ ms and phase averaging is performed over 100 pulses.

IX.2.1 Experimental results

The experimental results for cases C7 ($L_c = 0.65$ m) and cases C10 ($L_c = 0.05$ m) are shown in figure IX.5.

For cases C7–C9, the pressure rises sharply during the injection ($0 < t < 100$ ms), and decreases exponentially thereafter. At $t = \tau_c \approx 365$ ms (when the helium reaches the nozzle), the slope changes sharply, and reaches a plateau. Once the helium disturbance has completely convected through the nozzle (at $t = \tau_c + \tau_p \approx 465$ ms), the pressure decays exponentially once more. These results suggest that the pressure from $t = 0$ to $t = \tau_p$ is entirely due to the helium injection, while the change in slope at $t = \tau_c$ is due to indirect noise as the helium disturbance is convected through the nozzle.

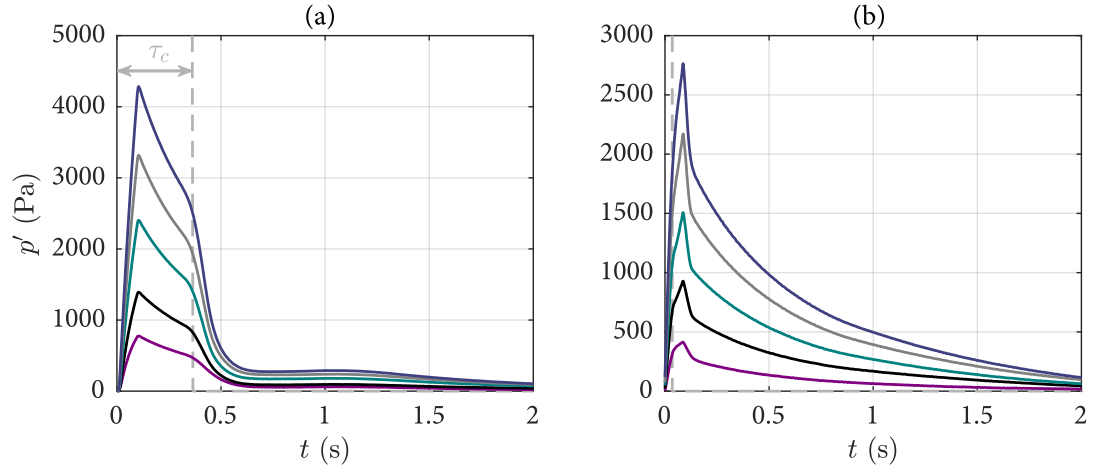


Figure IX.5: Experimental pressure fluctuation $p'(x, t)$ for (a) case C7 and (b) case C10, with $\dot{m}_i=0.027$ (—), 0.055 (—), 0.082 (—), 0.109 (—), 0.136 g s^{-1} (—). Convective time delay τ_c (---).

For cases C10–C12, the convective time delay is shorter ($\tau_c \approx 30 \text{ ms}$). As such, the noise due to the helium injection ($0 < t < 100 \text{ ms}$) and the indirect noise ($t > \tau_c$) overlap. Indeed, the pressure rises sharply, until its slope decreases at $t = \tau_c$. The pressure reaches a maximum at $t = \tau_p$ and decays at a high rate. The decay rate is modified once again at $t = \tau_c + \tau_p$, once the helium has completely convected through the nozzle, and indirect noise is no longer generated.

IX.2.2 Simulations

For cases C7–C12, we adjust the direct noise model in order to incorporate the ‘excess’ noise measured in cases C4–C6. This is done simply by increasing the output of the direct noise model by 22%, which based on IX.3(b), appears to correctly predict the injection noise. The analytical and experimental results for cases C7 and C10 are shown in figure IX.6(a) and IX.6(b) respectively.

The analytical and experimental results for case C7 are in good agreement overall. There is a substantial difference for $t > \tau_c$, when the indirect noise is generated. At first glance, the results appear to suggest that the indirect noise is over-predicted by the model. However, this is expected. Indeed, we have not accounted for advective-diffusive effects. As a result, we can expect the helium disturbance to have diffused and dispersed substantially over the convective length from the injection to the nozzle. This is consistent with the overestimation

IX. HELIUM INJECTION – COMPOSITIONAL NOISE

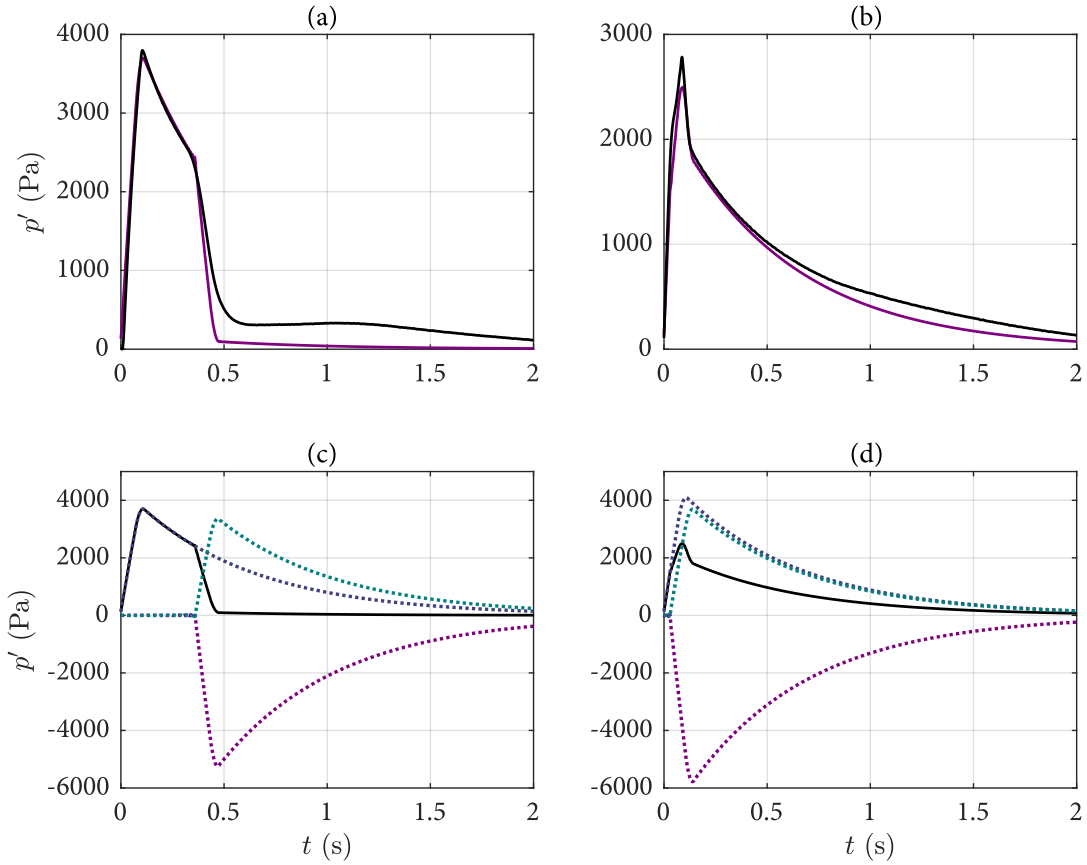


Figure IX.6: Analytical (—) and experimental results (—) for the pressure fluctuation $p'(x, t)$: (a) case C7 (b) case C10. Contributions of direct (.....), entropic (.....) and compositional (.....) noise to the overall analytical pressure (—) for (c) case C7 and (d) case C10.

of the peak indirect noise amplitude. In case C10, the convective distance is short ($L_c = 0.05$ m), and we expect significantly less diffusion and dispersion will have taken place. As a result, the analytical results are in better agreement than in case C7. There is slight discrepancy in the decay rate, as discussed in §VII.2.

The individual contributions of direct, entropic and compositional noise to the analytical signal are shown in figures IX.6(c,d) for cases C7 and C10 respectively. The results show that entropic noise is actually the dominant source of sound in this configuration. Compositional and direct noise are of comparable amplitudes for the test cases considered here. However, since compositional and entropic noise add up destructively, the direct noise is larger than the overall indirect noise. Most importantly, if compositional noise had been not taken into account in the analytical model, the experimental result would differ widely from the theoretical prediction. In other words, compositional noise contributes significantly to the experimental signal. This demonstrates that the compositional mechanism contributes significantly to the overall indirect noise.

IX.2.3 Source identification

The experimental results for configuration C can be dereverberated using (V.22). The resulting signal is a combination of direct noise, entropic and compositional noise $\pi = (1 + R_o)(1 + R_i)\pi_d^+ + (1 + R_i)(\pi_\sigma^- + \pi_\xi^-)$. The direct and indirect source signals are separated by a time delay for case C7–C9, as shown in figure IX.7(a).

The shape of the dereverberated direct noise signal closely matches that of the acoustic pulse measured in cases C1–C6 (figure IX.2a). The indirect noise signal ($\pi_\sigma^- + \pi_\xi^-$) appears at a time consistent with the convective time delay τ_c . The indirect noise source signal resembles a Gaussian, indicating that the helium disturbance has diffused and dispersed during the convection process.

The only difference between cases C7 and C10 is the convective length L_c between the valve and the outlet nozzle: the generated direct noise is the same in both cases. We can take advantage of this by isolating the direct noise in case C7, and subtracting it from the signal in case C10, leaving us with the indirect noise signal for case C10 ($\pi_\sigma^- + \pi_\xi^- = \pi/(1 + R_i) - (1 + R_o)\pi_d^+$). The resulting direct and indirect noise signals for case C10 are shown in figure IX.7(b). Here, the indirect noise signal appears earlier due to the reduced convective length, and the shape of the signal suggests that less diffusion and dispersion has occurred than in case C7.

IX. HELIUM INJECTION – COMPOSITIONAL NOISE

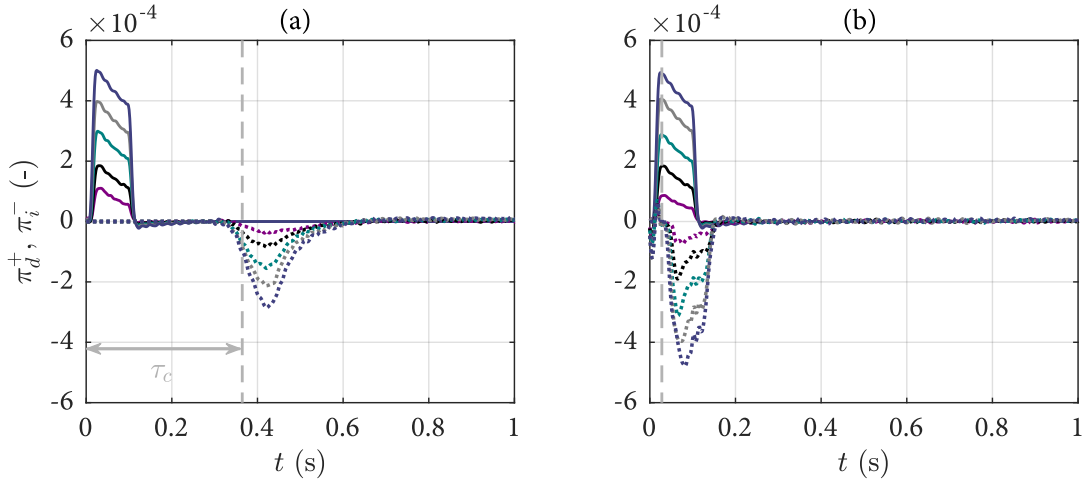


Figure IX.7: Dereverberated experimental signal for direct (π_d^+ , —) and indirect acoustic waves ($\pi_i^- = \pi_\sigma^- + \pi_\xi^-$,), generated for $\dot{m}_i = 0.027$ (—), 0.055 (—), 0.082 (—), 0.109 (—), 0.136 g s^{-1} (—) in (a) case C7 and (b) case C10. Convective time delay τ_c (---).

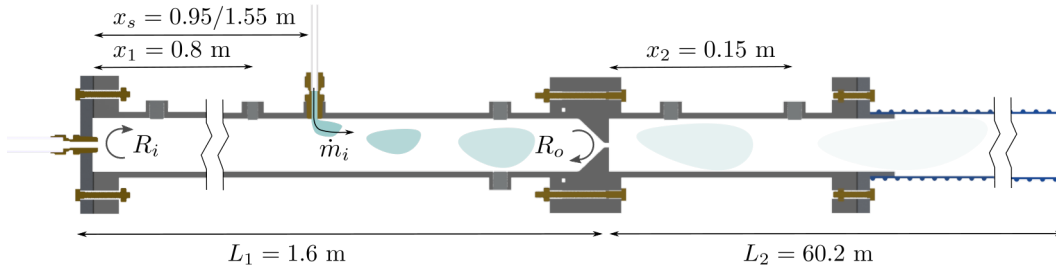


Figure IX.8: Short extended configuration with wave module C: helium is injected/extracted into a duct with reflections at the inlet and outlet.

IX.3 Short extended configuration

In the short extended configuration, a duct of length $L_2 = 60.2 \text{ m}$ is fitted downstream of the subsonic convergent nozzle (described in §VI.1.2), as shown in figure IX.8. This enables pressure measurements to be conducted both upstream and downstream of the nozzle (at locations $x_1 = 0.8 \text{ m}$ and $x_2 = 0.15 \text{ m}$ respectively), permitting the nozzle's transmissive properties to be measured.

As with the short tube cases (C7–C12), we expect entropic and compositional noise to be generated at the nozzle, aside from the noise resulting from the helium injection.

We perform ten experimental cases in the short-extended configuration (C13–C22). Cases

Case	L_c [m]	\bar{p} [kPa]	\bar{M}_1 [-]	\bar{M}_t [-]	\dot{m} [g s ⁻¹]	\dot{m}_i [g s ⁻¹]
C13	0.65	102.93	0.0033	0.155	1.97	0.068
C14	0.65	107.56	0.0063	0.310	3.95	0.068
C15	0.65	115.14	0.0089	0.467	5.92	0.068
C16	0.65	125.85	0.0108	0.629	7.89	0.068
C17	0.65	139.69	0.0122	0.821	9.87	0.068
C18	0.05	102.93	0.0033	0.155	1.97	0.068
C19	0.05	107.56	0.0063	0.310	3.95	0.068
C20	0.05	115.14	0.0089	0.467	5.92	0.068
C21	0.05	125.85	0.0108	0.629	7.89	0.068
C22	0.05	139.69	0.0122	0.821	9.87	0.068

Table IX.3: Experimental cases for wave module C (helium injection) in the short extended configuration with a subsonic convergent nozzle: convective length L_c , mean pressure \bar{p} , mean Mach number \bar{M}_1 , mean throat Mach number \bar{M}_t , primary mass flow rate \dot{m} and injected helium mass flow rate \dot{m}_i .

C13–C17 are executed with a ‘long’ convective length $L_c = 0.65$ m, while cases C18–C22 are performed with a ‘short’ convective length $L_c = 0.05$ m. Together, these two sets of cases will be used to identify the entropic and compositional noise reflected and transmitted through the nozzle. The operating conditions for the experimental cases are shown in table IX.3. The pulse duration is $\tau_p = 100$ ms in all cases and phase averaging is performed over 100 pulses.

IX.3.1 Experimental results

The experimental pressure measurements upstream ($p'(x_1)$) and downstream of the nozzle ($p'(x_2)$) are shown in figure IX.9(a,b) for cases C13–C17, and IX.9(c,d) for cases C18–C22.

The experimental results are less straightforward to interpret directly than those obtained in the short and long configurations. It should be noted that the only effective difference between cases C13–C17 and C18–C22 are the convective time delays τ_c after which indirect noise is generated. As such, differences in the acoustic pressures between these two sets of cases are manifestations of the indirect noise mechanism.

One easily recognised feature in all of the measured signals is the effect of the acoustic reflections occurring at the outlet of the second chamber ($R_{o2} = -1$). Since these reflections occur at a distance of $L \approx 60$ m from the inlet of the duct, they appear at intervals of $\tau \approx 2L/\bar{c} \approx 360$ ms, and alternate in sign (since $R_{o2} < 0$). The reflections are more easily

IX. HELIUM INJECTION – COMPOSITIONAL NOISE

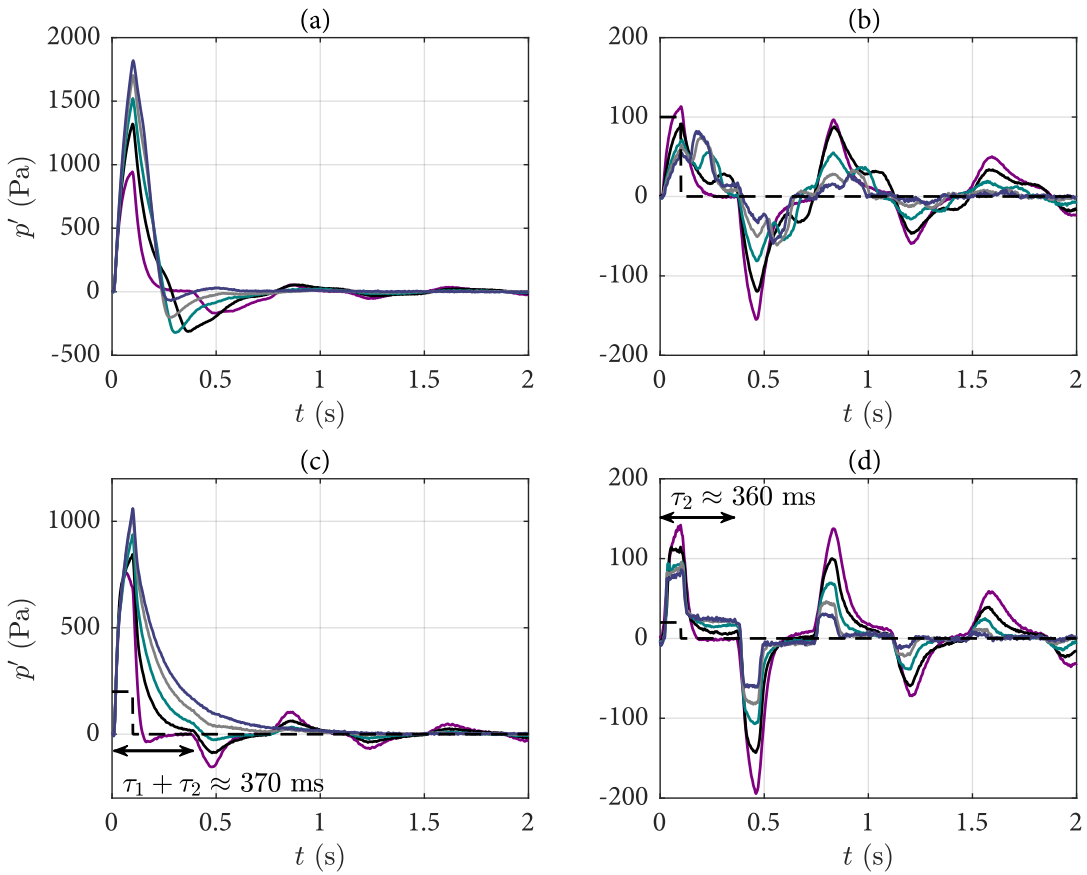


Figure IX.9: Experimental pressure fluctuations (a) $p'(x_1)$ upstream of the nozzle and (b) $p'(x_2)$ downstream of the nozzle for cases C13 (—), C14 (—), C15 (—), C16 (—), C17 (—) and (c) $p'(x_1)$ upstream of the nozzle and (d) $p'(x_2)$ downstream of the nozzle for cases C18 (—), C19 (—), C20 (—), C21 (—), C22 (—). The valve timing signal is shown for reference (---).

discerned in the downstream pressure $p'(x_2)$ (figure IX.9b,d) than in the upstream pressure $p'(x_1)$ (figure IX.9a,c). This is because the downstream reflections are attenuated as they are transmitted upstream through the nozzle (with a coefficient T_{i2}).

As with the short tube cases, the pressure upstream of the nozzle $p'(x_1)$ (figure IX.9a,c) increases sharply during the helium injection (for $0 < t < 100$ ms). This is due to the reverberation of the noise generated by the helium injection. In cases C18–C22, the convective time delay is smaller than the pulse duration ($\tau_c < \tau_p$). As such, indirect noise is generated concomitantly with the injection noise. We know from the results of cases C7–C12 that injection noise is positive, while indirect noise is negative for this configuration. As such, these sound sources interact destructively in cases C18–C22. Conversely, in cases C13–C17, the convective time delay is larger than the pulse duration ($\tau_c > \tau_p$) and these sound sources do not interact. This explains why the maximum pressure is higher in cases C13–C17 than in cases C18–C22.

To obtain further insight regarding the experimental results, one can perform source identification. The source identification model requires information about the experimental set-up (reflection and transmission coefficients, level of anisentropicity) which are not known a priori. These can be obtained using system identification.

IX.3.2 System identification

The experimental results can be used as a basis to perform system identification. We limit our analysis to the experimental signal measured for $t < 0.36$ s, which is the time sequence during which the second chamber downstream of the nozzle can be considered anechoic (since $\tau_2 \approx 360$ ms). This enables us to use the simplified identification methods outlined in §VI.4.2.

One of the main parameters of the anisentropic nozzle model is the anisentropicity factor $\Lambda = (A_2 - A_j)/(A_2 - A_t)$. The value of Λ can be determined by considering the experimental measurements of the mean pressure upstream of the nozzle \bar{p}_1 and using a least-squares fitting for Λ . These measurements are consistent with $\Lambda \approx 0.9988$, as shown in figure IX.10. This corresponds to a case somewhere between a fully isentropic nozzle ($\Lambda = 0$), and one with a fully dissipative divergent section ($\Lambda = 1$).

As shown in VII.2.4, the reflection coefficient of the nozzle R_{o1} can be extracted from the upstream pressure measurements $p'(x_1)$ in cases C13–C17. Indeed, we know that reverberated pulses decay exponentially as $(R_{i1}R_{o1}e^{-2\alpha L_1})^t/\tau_1$. Each value of R_{o1} leads to a different decay rate, as shown in figure IX.11(a). Using this method, the nozzle reflection coefficient

IX. HELIUM INJECTION – COMPOSITIONAL NOISE

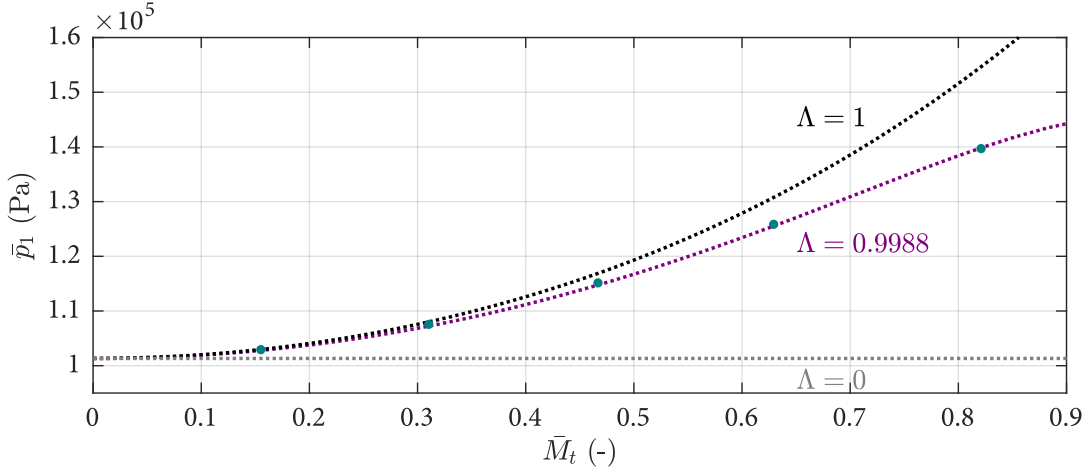


Figure IX.10: Upstream mean pressure \bar{p}_1 as a function of the throat Mach number \bar{M}_t . Experimental measurements for cases C13–C22 (●), isentropic limit case for $\Lambda = 0$ (.....), fully dissipative limit case for $\Lambda = 1$ (.....) and best fit for $\Lambda = 0.9988$ (.....).

R_{o1} can be recovered for all experimental cases.

Furthermore, the transmission coefficient across the nozzle T_{o1} can be recovered by considering the pressures upstream and downstream of the nozzle. In the absence of indirect noise, the ratio between the upstream and downstream pressures $p'/\gamma\bar{p}(x_1)$ and $p'/\gamma\bar{p}(x_2)$ is $T_{o1}/(1 + R_{o1})$, as shown in (VI.3). Since there is no indirect noise for $t < 0.2$ s in cases C13–C17, we can recover the value of T_{o1} by measuring this ratio. This is shown in figure IX.11(b).

The nozzle reflection and transmission coefficients R_{o1} and T_{o1} recovered from the experimental data can be compared to the anisentropic nozzle model for $\Lambda = 0.9988$. This is shown in figure IX.12. The model is in good agreement with the measured values.

IX.3.3 Source identification

The acoustic sources upstream (π_1) and downstream (π_2) of the nozzle for cases C13–C22 can be recovered from the experimental pressure measurements using source identification (see §VI.4.2).

The upstream signal π_1 is combination of direct noise and backward-propagating indirect noise: $\pi_1 = (1 + R_{o1})(1 + R_{i1})\pi_d^+ + (1 + R_{i1})\pi_i^-$. Here, the indirect noise source is a combination of entropic and compositional noise; $\pi_i^- = \pi_\sigma^- + \pi_\xi^-$. As with the short configuration results, we can separate the direct and indirect acoustic sources by taking advantage of the

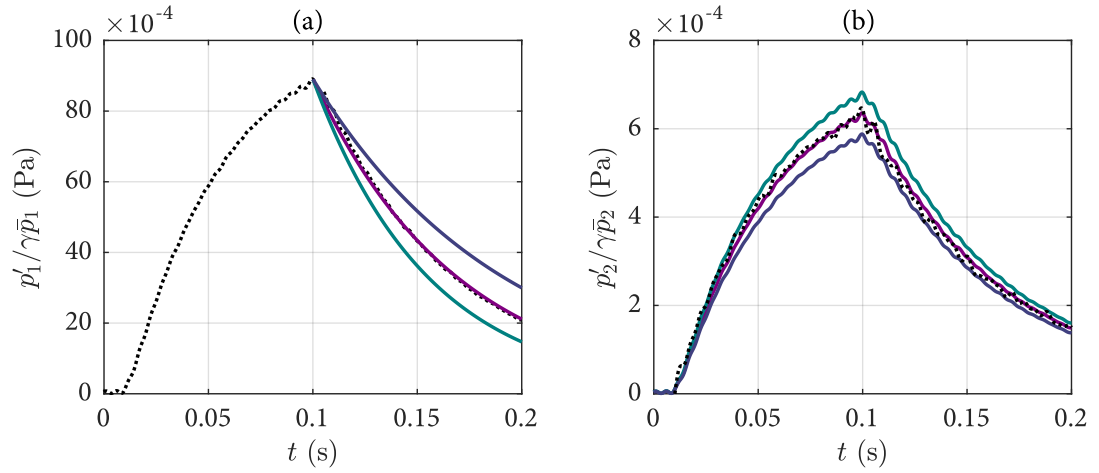


Figure IX.11: Case C14: (a) Upstream experimental acoustic pressure $p'(x_1)$ (.....) and theoretical decay for $R_{o1} = 0.870$ (—), $R_{o1} = 0.873$ (—) and $R_{o1} = 0.867$ (—) and (b) downstream experimental acoustic pressure $p'(x_2)$ (.....) and theoretical upstream transmission for $T_{o1} = 0.131$ (—), $T_{o1} = 0.141$ (—) and $T_{o1} = 0.121$ (—).

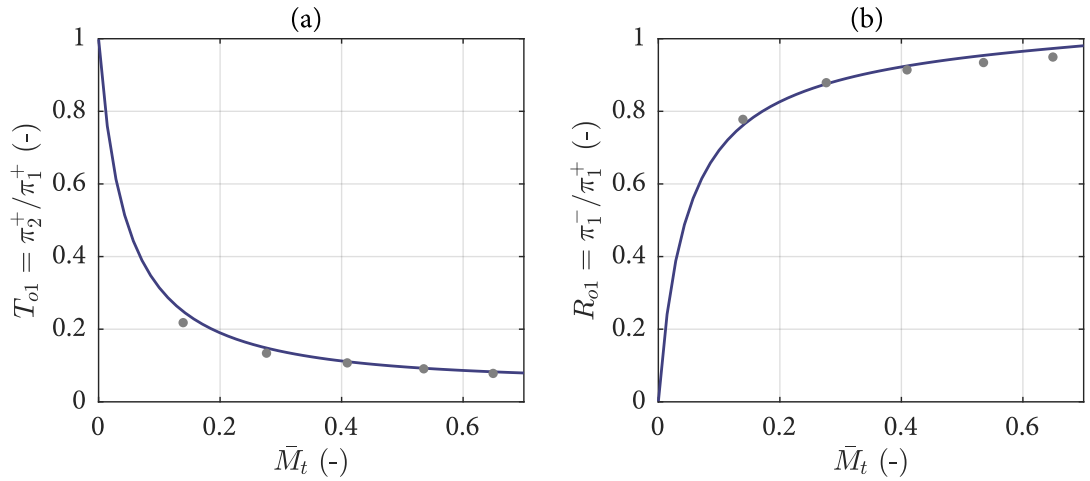


Figure IX.12: (a) Acoustic transmission coefficient T_{o1} and (b) acoustic reflection coefficient R_{o1} extracted from experimental data (●), and computed using the anisentropic nozzle model (—).

IX. HELIUM INJECTION – COMPOSITIONAL NOISE

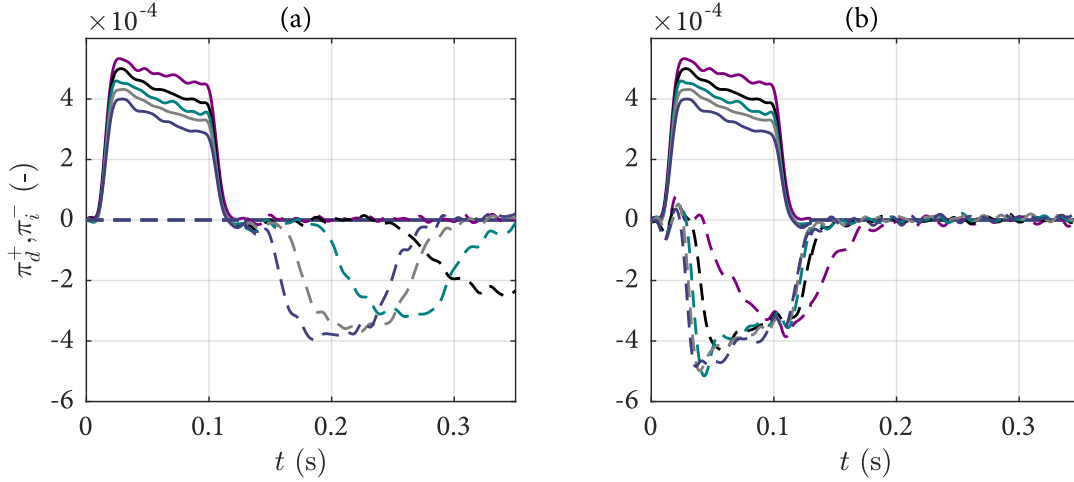


Figure IX.13: Dereverberated experimental signal for direct (π_d^+ , —) and indirect acoustic waves (π_i^- ,), generated for (a) cases C13 (—), C14 (—), C15 (—), C16 (—), C17 (—) and (b) cases C18 (—), C19 (—), C20 (—), C21 (—), C22 (—).

difference in convective time delays between cases C13–C17 and cases C18–C22. The direct and indirect acoustic sources upstream of the nozzle are shown in figure IX.13.

The dereverberated signals correspond to injection noise followed by an indirect noise source. The injection noise appears as a positive pulse for $0 < t < 100$ ms. The indirect noise source is manifested as a negative pulse. In cases C13–C17, it appears after a convective time delay $\tau_c = L_c/\bar{u}$ which depends on the case. In cases C18–C22, the convective time delay is extremely small, meaning that the indirect noise pulse occurs almost simultaneously with the injection.

Pressure measurements downstream of the nozzle can also be used to identify the forward-propagating indirect noise wave $\pi_i^+ = \pi_\sigma^+ + \pi_\xi^+$. As shown in (VI.8), π_i^+ is simply the component of the downstream pressure $p'/\gamma\bar{p}(x_2)$ not resulting from transmissions of the upstream acoustic pressure $(T_{o1}/(1 + R_{o1}))p'/\gamma\bar{p}(x_1)$. This enables the forward-propagating indirect sound wave to be identified, as shown in figure IX.14.

The forward-propagating indirect noise wave π_i^+ manifests itself as a positive acoustic source. It appears with a time delay consistent with the small convective time delays τ_c for each case.

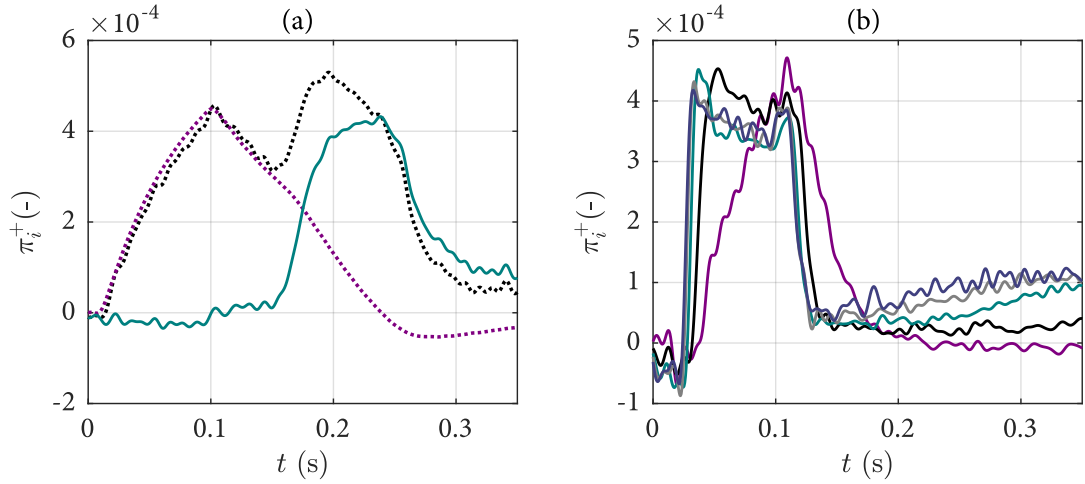


Figure IX.14: (a) Downstream pressure $p'/\gamma\bar{p}(x_2)$ (.....), transmitted upstream pressure $p'/\gamma\bar{p}(x_1) T_{o1}/(1 + R_{o1})$ (.....) and resulting indirect sound wave π_i^+ (—) for case C21. (b) Indirect sound wave π_i^+ for cases C13 (—), C14 (—), C15 (—), C16 (—), C17 (—).

IX.4 Comparison to compositional noise models

The backward-propagating entropic and compositional noise wave $\pi_i^- = \pi_\sigma^- + \pi_\xi^-$ extracted from cases C7-C12 (choked nozzle) can be compared to the theoretical model for the entropic noise generated at an isentropic choked nozzle (III.14). This is shown in figure IX.15.

The experimental results for the combined entropic and compositional sound waves $|\pi_\sigma^- + \pi_\xi^-|$ are in good agreement with the theoretical isentropic model. The favourable agreement found for independently measured entropic noise (§VIII.4) suggests that the isentropic model derived by Magri et al.⁵⁸ for the upstream-propagating compositional noise generated at a compact choked nozzle is representative of the experiment.

We can also extract the indirect noise transfer functions $|\pi_\sigma^- + \pi_\xi^-|/\xi$ and $|\pi_\sigma^+ + \pi_\xi^+|/\xi$ from the experimental results for cases C13–C17 (subsonic convergent nozzle). These are compared to the anisentropic model in IX.16.

Once again, the experimental results are in good agreement with the predictions of the theoretical model. This demonstrates that the anisentropic model enables one to accurately predict the entropic and compositional noise produced both upstream and downstream of a nozzle with losses.

IX. HELIUM INJECTION – COMPOSITIONAL NOISE

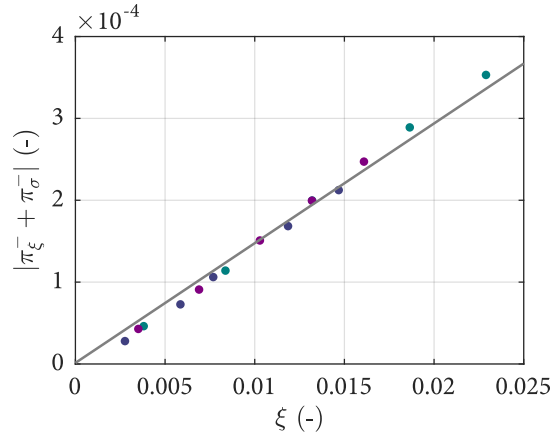


Figure IX.15: Indirect sound wave $|\pi_{\xi}^{-} + \pi_{\sigma}^{-}|$ for cases C10 (●), C11 (●) and C12 (●) compared to the isentropic model (—).

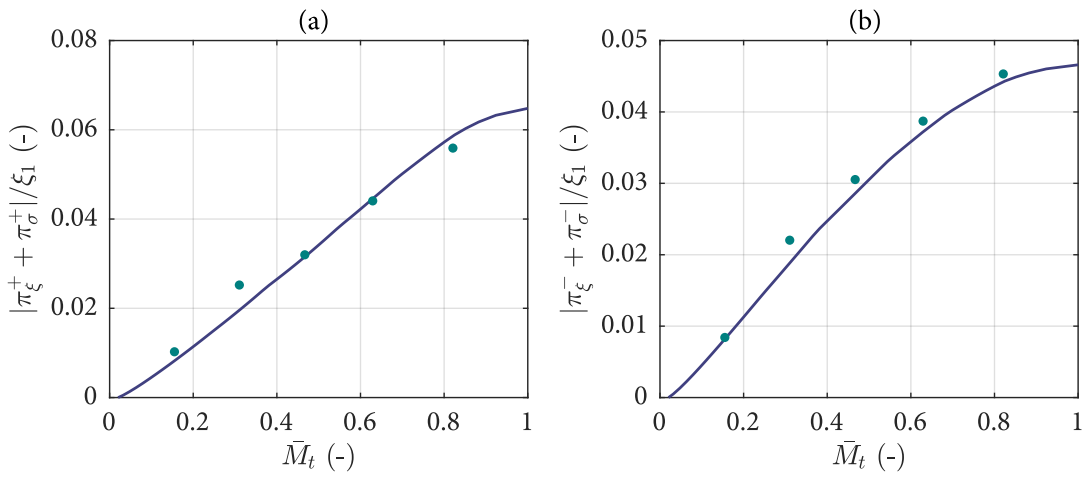


Figure IX.16: Indirect noise transfer functions (a) $|\pi_{\xi}^{+} + \pi_{\sigma}^{+}|/\xi_1$ and (b) $|\pi_{\xi}^{-} + \pi_{\sigma}^{-}|/\xi_1$ for cases C13–C17 (●) compared to the anisentropic nozzle model for $\Lambda = 0.9988$ (—).

CONCLUSIONS AND FUTURE WORK

In this thesis the entropic and compositional noise generated at compact nozzles has been investigated both analytically and experimentally. To do so a complete one-dimensional model of direct and indirect noise generation has been produced, accounting for the effect of anisotropic nozzles and acoustic reverberation. The model enables direct and indirect noise to be identified, separated and quantified using system and source identification techniques. These techniques were successfully applied to experimental results obtained on the Cambridge Wave Generator, in which direct, entropic and compositional noise were generated in model conditions. The main findings and conclusions of this work are presented here along with possible avenues for future work.

Conclusions

The main contributions of this thesis can be organised into four main themes: (1) reverberation and source identification, (2) direct noise, (3) entropic noise and (4) compositional noise.

Reverberation and source identification

Prior to the present work, experimental data had been largely unable to shed a light on the validity of indirect noise models. While the generation of entropic and vortical noise had been demonstrated experimentally^{4,46}, quantitative comparisons with theoretical predictions were not usually carried out^{46,48,47,77}. In the cases where such a comparison was performed^{4,90}, the results were inconclusive, so that it was unclear exactly how much indirect noise had been produced.

The difficulty of making these comparisons stems from the fact that indirect noise models are formulated in terms of acoustic source waves^{61,57,44}. In contrast, in an experiment the

measured quantity is the acoustic pressure which is a convolution of acoustic source waves and their subsequent reflections.

To bridge this gap, a one-dimensional model accounting for the effect of repeated acoustic reflections was presented in chapter IV. For rectangular acoustic source pulses in reverberating systems (in which acoustic wavelengths are longer than the system's length), it was shown that acoustic sources can result in a pressure accumulation (during the pulse), followed by exponential decay (after the pulse). For the more general case (arbitrary acoustic sources), we derived two-way acoustic transfer functions relating acoustic sources to the resulting acoustic pressure.

In chapter V, this model was applied to the case of two chambers separated by a nozzle, in which both direct and indirect noise are produced. The results show that acoustic reflections (1) greatly affect the shape and amplitude of the measured signal, and (2) affect direct and indirect noise differently depending on the acoustic properties of the system. Practically speaking, this means that the effect of repeated acoustic reflections must be eliminated for the experimental data to be interpreted meaningfully. One way to do this is to eliminate acoustic reflections in the experimental set-up — though this is usually unattainable, particularly at low frequencies. Alternatively, the acoustic transfer functions derived here can be applied to the experimental data to perform source and system identification, revealing the acoustic sources and the acoustic properties of the experimental system respectively.

The reverberation and source identification models were validated experimentally in chapter VII. Rectangular acoustic source pulses were generated in the Cambridge Wave Generator using air injection. As predicted by the reverberation model, these acoustic sources were amplified, and the shape of the acoustic pressure was in very good agreement with theoretical predictions. Source identification was achieved by applying the acoustic transfer functions to the measured pressure signal. The resulting rectangular acoustic source pulse was identical to the acoustic wave produced by the air injection, which was measured in another experiment.

Direct noise

Indirect noise is generated by the convection of an entropic, vortical or compositional wave. Practically speaking, the generation of these waves is typically accompanied by the generation of direct noise, although this has not always been taken into account previously^{4,48}. As such, direct noise generation must be understood in order to interpret the results of experiments on indirect noise.

CONCLUSIONS AND FUTURE WORK

Direct noise is usually defined as the noise generated by unsteady heat addition^{86,8,21}. Here, it is defined more generally as the noise resulting from a mass, momentum and/or energy addition, which covers a wider range of relevant scenarios.

In chapter II, a one-dimensional model for the generation of direct noise was derived, assuming a compact acoustic source at which mass, momentum, energy and species fluctuations are imposed on the flow. The results enable the direct noise produced in a variety of cases to be computed.

The model can be reduced to the case of heat addition, in which case the equations first derived by Cumpsty¹⁸ are recovered. The direct noise produced by heat addition was measured experimentally on the Cambridge Wave Generator in chapter VIII, in which heat was added to the flow using a heating device. The results were in excellent agreement with the theory, thus validating the direct noise model for the first time. This lends additional credibility to theoretical studies built upon this model, such as the comparison of direct and entropic noise performed by Leyko et al.⁵³.

The direct noise model was also applied to the case of air injection/extraction, in which mass, momentum and energy are added/removed from the flow. Once again, the results were in excellent agreement with data obtained on the Cambridge Wave Generator in chapter VII, further validating the model.

Finally, the direct noise model can be implemented for the special case of an injection of helium into a flow of air. Clearly the model can only be partially representative of this case, since an injection of helium into air can be also be expected to produce indirect noise. Experiments on the Cambridge Wave Generator in chapter IX confirm this, showing that the noise produced by the helium injection is larger than one would expect if only direct noise were generated.

Entropic noise

Predictions of entropic noise generated at nozzles are typically computed using the Marble & Candel⁶¹ transfer functions developed for quasi-one-dimensional compact isentropic nozzles, sometimes extended to account for nozzle non-compactness²⁴. For these predictions to be trusted, empirical evidence is required to show that real nozzles behave in accordance to these models.

Up till now, experiments have demonstrated the entropic noise mechanism by measuring the downstream-propagating entropic noise generated at a nozzle⁴. Nevertheless, these mea-

measurements were not sufficient to confirm or refute the Marble & Candel⁶¹ model. Furthermore, the upstream-propagating entropic noise (which may play a part in thermoacoustic instabilities) had yet to be measured. Both of these points have been addressed in this thesis.

In the Cambridge Wave Generator experiment reported in chapter VIII, low-frequency entropic noise was produced by generating an entropic wave with a heating device and accelerating it through a choked compact nozzle. The reverberation and source identification framework was then applied to the resulting pressure measurements, revealing the amplitude of the entropic noise generated upstream of the nozzle. The results are in good agreement with the Marble & Candel⁶¹ model. The model also makes predictions for the acoustic reflection coefficient of the nozzle, which once again was in good agreement with the experiment. These observations provide validation for the Marble & Candel⁶¹ model, showing that it is an appropriate tool to predict the response of choked compact nozzles.

In another set of experiments on the CWG, the entropic noise generated at a subsonic orifice plate was also measured. Contrary to the previous experiments, the measurements were in strong disagreement with the Marble & Candel⁶¹ transfer functions. In a sense this is unsurprising since the model assumes an isentropic nozzle whereas an orifice plate is not isentropic.

To account for this difference, transfer functions for subsonic anisentropic compact nozzles were derived by De Domenico et al.¹⁹. These transfer functions were recast in a non-dimensional form directly comparable to the Marble & Candel⁶¹ transfer functions in chapter III. The anisentropic model was found to be in good agreement with the entropic noise measurements obtained with a subsonic orifice plate. Crucially, it was demonstrated that anisentropic nozzles produce more entropic noise than the corresponding isentropic nozzles.

Outlet nozzles in gas turbines are designed to be nearly isentropic in most operating conditions, so the effect of anisentropy can typically be assumed to be small. However, this effect may be of importance in other combustion systems in which entropic noise occurs. Furthermore, laboratory-scale nozzles used in model experiments on indirect noise are unlikely to be fully isentropic due to the reduced dimensions and Reynolds numbers. The present findings show that the nozzle response cannot be predicted correctly unless this effect is taken into account.

Compositional noise

Magri⁵⁷ and Ihme⁴⁴ recently theorised the existence of an additional indirect noise mechanism: compositional noise generated by convected compositional inhomogeneities. They

CONCLUSIONS AND FUTURE WORK

developed one-dimensional transfer functions for isentropic compact⁵⁷ and non-compact⁶⁰ nozzles analogous to those obtained by Marble & Candel⁶¹ for entropic noise. This was an important finding, particularly as compositional noise is thought to be comparable or larger than direct and entropic noise for certain operating conditions⁵⁷. Nonetheless, the compositional noise mechanisms had never been demonstrated experimentally.

An experimental demonstration of compositional noise generation is reported for the first time in chapter IX. A compositional and entropic wave was produced in the Cambridge Wave Generator by injecting helium in a flow of air, and convected through a choked compact nozzle to produce compositional (and entropic) noise. Using source identification, the compositional noise was shown to be in good agreement with the one-dimensional isentropic compact nozzle transfer functions^{57,44}. The results show that the indirect noise generated by a compositional and entropic wave cannot be explained using entropic noise models alone, and that compositional noise can be of the same order of magnitude as entropic noise. This highlights the need to take compositional noise into account if indirect combustion noise is to be predicted accurately.

Finally, the response of an anisentropic compact nozzle to impinging compositional waves was derived for the first time in chapter III. The results reveal the existence of a previously unreported mode transfer mechanism from compositional waves to entropic waves. Further experiments were carried out on the CWG with an anisentropic subsonic nozzle. The resulting upstream- and downstream-propagating compositional and entropic noise were identified in the pressure measurements. These were found to be in good agreement with the anisentropic nozzle transfer functions. Once again, the results diverged largely from the isentropic predictions, showing that nozzle anisentropy should be taken into account when dealing with nozzles with losses.

Future work

This thesis has focused on the experimental validation of one-dimensional transfer functions of compact nozzles. This has been achieved, showing that direct, entropic and compositional noise can be generated, separated and measured in model conditions, with results consistent with analytical models. The analytical framework and experimental methods developed here can be used to obtain further insight into indirect noise mechanisms. Promising approaches for future work on this theme are presented here.

Supersonic nozzles

The work presented in this thesis has been limited to subsonic nozzles and choked (sonic) nozzles. Supersonic nozzles have not been tested owing to limitations in the current experimental set-up. In principle a converging-diverging supersonic nozzle could be designed and adapted to be used on the Cambridge Wave Generator. The results would shed some light on the behaviour of supersonic nozzles with shocks, for which isentropic transfer functions have already been derived analytically⁶⁶. The source identification and separation techniques developed here could be directly applied to the resulting measurements.

Subsonic isentropic nozzles

The nozzle model shown in chapter III makes predictions for nozzles with varying levels of anisentropy, including the limit case of a fully isentropic nozzle. A choked nozzle (which is fully isentropic in the converging section) was tested to verify these predictions. However, subsonic isentropic nozzles could not be tested. This was due to the difficulty of designing and manufacturing an isentropic divergent section at the low flow rates accessible with the current experimental set-up (up to 10 g s^{-1}). Preliminary experiments were carried out with a divergent section with an angle of 4.5° . Even with this moderate angle the nozzle was found to have a high level of anisentropy (presumably due to flow separation). By extending the range of the Cambridge Wave Generator to achieve higher flow rates, it may be possible to explore the behaviour of fully isentropic subsonic nozzles.

Vortical noise

In this thesis we examined the generation of entropic and compositional noise. Indirect noise is also thought to be generated by the convection of vortical perturbations. This has been previously investigated on the Vorticity Wave Generator (VWG) at the DLR by Kings & Bake⁴⁶, in which vortical waves were generated by injecting air tangentially into a flow duct. To corroborate these results, a similar set-up was tested on the Cambridge Wave Generator. The results did not indicate any generation of vortical noise, though this may have been due to small differences in the CWG set-up compared to the VWG. Further experiments could be conducted on the CWG to shed some light on the vortical noise mechanism, particularly

CONCLUSIONS AND FUTURE WORK

given that the methods used here to identify entropic and compositional noise should be directly applicable.

Effect of dispersion and dissipation

The dissipation and dispersion of entropic and compositional waves can be observed in some of the results shown in chapters VIII and IX. These effects were, for the most part, eliminated by minimising the convective length, with the objective of isolating the effect of the nozzle transfer functions on indirect noise generation. Nevertheless, dispersive, dissipative and diffusive effects are interesting in themselves, and they have important consequences for the emergence of indirect noise in combustion systems^{69,33}.

As a starting point, these effects could be investigated on the current experimental set-up with minor adjustments. The convection of entropic waves could be examined using a set of thermocouple measurements along the duct. Furthermore, the addition of an optical access section to the CWG would open the door to a large array of diagnostics (such as Rayleigh scattering⁸⁰ or laser induced thermal grating spectroscopy³⁵) enabling the amplitude of entropic and compositional waves to be examined. The measurements could then be directly compared to quasi-one-dimensional analytical models for wave propagation^{92,69,31}.

Effect of nozzle non-compactness

The experiments conducted on the CWG have been limited to compact nozzles with low-frequency perturbations (of the order of 1 Hz). This was due to shortcomings of the wave generation modules, which were limited by wire cooling time (for the heating device) and valve response time (for the gas injection). Analytical models show that the nozzle transfer functions for indirect noise are frequency-dependent^{24,60}. This is likely to be important in real combustion systems.

The effect of frequency could be investigated on the current rig using improved wave generation methods. Fast response micro-solenoid valves have been obtained, which in principle can be operated at up to 600 Hz. These could be used to generate compositional waves at high frequencies. The source identification method presented in chapter V is not limited to low-frequency sources, and could be implemented directly to interpret the results.

Realistic flow geometries

While not described in this thesis, a new experimental rig was designed and manufactured during the course of the Ph.D. project. The rig is modular, water cooled, visually accessible, and intended to be operated in both non-reacting and reacting configurations. In the non-reacting configuration, the wave generation methods used on the CWG could be implemented with minimal adjustments to generate entropic and compositional noise. This would enable indirect noise to be investigated in a system closer to a realistic gas turbine combustor. This would also enable dispersion and dissipation to be measured in a two- or three-dimensional flow field. The effect of the flow field on the generation of indirect noise could also be investigated, and compared to two-dimensional models developed by others⁹⁴. Finally, these experiments could act as a stepping stone towards conducting experiments on indirect noise in a fully reacting configuration.

⊖

A

NOZZLE TRANSFER FUNCTIONS

A.1 Matrix permutations

The matrix permutations used in §III.1.2 to relate inlet and outlet matrices \mathbf{X}_1 and \mathbf{X}_2 to ingoing and outgoing matrices \mathbf{X}_i and \mathbf{X}_o are:

$$\mathbf{X}_i = \begin{bmatrix} X_1(1,1) & -X_2(1,2) & X_1(1,3) & X_1(1,4) \\ X_1(2,1) & -X_2(2,2) & X_1(2,3) & X_1(1,4) \\ X_1(3,1) & -X_2(3,2) & X_1(3,3) & X_1(4,4) \\ X_1(4,1) & -X_2(4,2) & X_1(4,3) & X_1(3,4) \end{bmatrix}, \quad (\text{A.1})$$

and

$$\mathbf{X}_o = \begin{bmatrix} X_2(1,1) & -X_1(1,2) & X_2(1,3) & X_2(1,4) \\ X_2(2,1) & -X_1(2,2) & X_2(2,3) & X_2(1,4) \\ X_2(3,1) & -X_1(3,2) & X_2(3,3) & X_2(4,4) \\ X_2(4,1) & -X_1(4,2) & X_2(4,3) & X_2(3,4) \end{bmatrix}. \quad (\text{A.2})$$

The same permutation is used in §III.2.3, replacing \mathbf{X}_2 with $\mathbf{X}_j \mathbf{Y}_j^{-1} \mathbf{Y}_2$.

A.2 Supersonic compact isentropic nozzle

If the flow in the nozzle is supersonic ($\bar{M}_2 > 1$), then the backward-propagating downstream wave π_2^- actually propagates in the forward direction since the flow is faster than sound ($\bar{u} > \bar{c}$). This is shown in figure A.1.

As such, π_2^- is no longer an incoming wave, and cannot be imposed. We are left with only

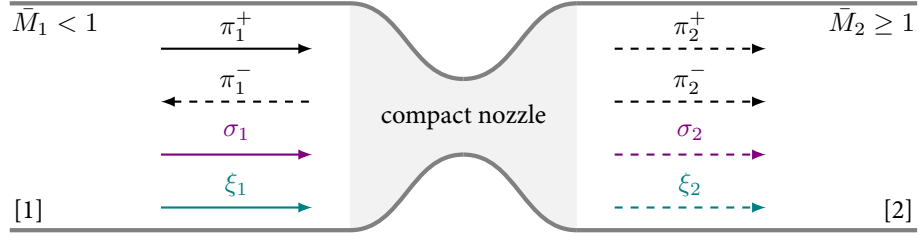


Figure A.1: Forward and backward acoustic (π^+ , π^-), entropic (σ) and compositional waves (ξ) upstream [1] and downstream [2] of a supersonic compact nozzle.

two incoming waves w_i , and four unknown outgoing waves w_o :

$$\mathbf{w}_i = \begin{bmatrix} \pi_1^+ \\ \sigma_1 \\ \xi_1 \end{bmatrix}, \quad \mathbf{w}_o = \begin{bmatrix} \pi_2^+ \\ \pi_2^- \\ \pi_1^- \\ \sigma_2 \\ \xi_2 \end{bmatrix}. \quad (\text{A.3})$$

To solve for the outgoing waves, an additional jump condition is required. For a supersonic nozzle, the flow is constrained by the sonic flow rate at the throat, which can be equated to the mass flow condition in (III.2) to yield:

$$\frac{\gamma - 1}{2} \frac{p'}{\gamma \bar{p}} - \frac{1}{\bar{M}} \frac{u'}{\bar{c}} + \frac{1}{2} \frac{s'}{\bar{c}_p} + \frac{\Psi}{2} Z' = 0, \quad (\text{A.4})$$

which is true throughout the compact nozzle. We can use this as the basis for a jump condition for the waves upstream and downstream of the nozzle:

$$\left[\left(\frac{\gamma - 1}{2} - \frac{1}{\bar{M}} \right) \pi^+ + \left(\frac{\gamma - 1}{2} + \frac{1}{\bar{M}} \right) \pi^- + \frac{\sigma}{2} + \frac{\Psi \xi}{2} \right]_1^2 = 0. \quad (\text{A.5})$$

As before, we can write $\mathbf{X}_i \mathbf{w}_i = \mathbf{X}_o \mathbf{w}_o$, where \mathbf{X}_i and \mathbf{X}_o are permutations of an aug-

A. NOZZLE TRANSFER FUNCTIONS

mented transfer matrix \mathbf{X} :

$$\mathbf{X} = \begin{bmatrix} 1 + \frac{1}{\bar{M}} & 1 - \frac{1}{\bar{M}} & -1 & -\Psi \\ \frac{(\gamma - 1)(1 + \bar{M})}{1 + \frac{\gamma-1}{2}\bar{M}^2} & \frac{(\gamma - 1)(1 - \bar{M})}{1 + \frac{\gamma-1}{2}\bar{M}^2} & 1 & \Psi \\ 0 & 0 & 1 & 0 \\ 0 & 0 & 0 & 1 \\ \gamma - 1 - \frac{2}{\bar{M}} & \gamma - 1 + \frac{2}{\bar{M}} & 1 & \Psi \end{bmatrix}. \quad (\text{A.6})$$

The relationship can be inverted to yield $\mathbf{w}_o = \mathbf{X}_o^{-1} \mathbf{X}_i \mathbf{w}_i = \mathbf{T} \mathbf{w}_i$ where \mathbf{T} is the matrix of supersonic nozzle transfer functions:

$$\mathbf{T} = \begin{bmatrix} \frac{\pi_2^+}{\pi_1^+} & \frac{\pi_2^+}{\sigma_1} & \frac{\pi_2^+}{\xi_1} \\ \frac{\pi_1^-}{\pi_1^+} & \frac{\pi_1^-}{\sigma_1} & \frac{\pi_1^-}{\xi_1} \\ \frac{\pi_2^-}{\pi_1^+} & \frac{\pi_2^-}{\sigma_1} & \frac{\pi_2^-}{\xi_1} \\ \frac{\sigma_2}{\pi_1^+} & \frac{\sigma_2}{\sigma_1} & \frac{\sigma_2}{\xi_1} \\ \frac{\xi_2}{\pi_1^+} & \frac{\xi_2}{\sigma_1} & \frac{\xi_2}{\xi_1} \end{bmatrix}. \quad (\text{A.7})$$

Compared to the subsonic case, we now have an additional transmitted wave π_2^- , meaning that we have two transmission coefficients. The acoustic-acoustic transmission coefficients of the nozzle are:

$$\frac{\pi_2^+}{\pi_1^+} = \frac{1 + \frac{\gamma-1}{2}\bar{M}_2}{1 + \frac{\gamma-1}{2}\bar{M}_1}, \quad \frac{\pi_2^-}{\pi_1^+} = \frac{1 - \frac{\gamma-1}{2}\bar{M}_2}{1 + \frac{\gamma-1}{2}\bar{M}_1}. \quad (\text{A.8})$$

The acoustic-acoustic reflection coefficient is:

$$\frac{\pi_1^-}{\pi_1^+} = \frac{1 - \frac{\gamma-1}{2}\bar{M}_1}{1 + \frac{\gamma-1}{2}\bar{M}_1}. \quad (\text{A.9})$$

The entropic-acoustic transmission coefficients read:

$$\frac{\pi_2^+}{\sigma_1} = \frac{1}{4} \frac{\bar{M}_2 - \bar{M}_1}{1 + \frac{\gamma-1}{2} \bar{M}_1}, \quad \frac{\pi_2^-}{\sigma_1} = -\frac{1}{4} \frac{\bar{M}_2 + \bar{M}_1}{1 + \frac{\gamma-1}{2} \bar{M}_1}, \quad (\text{A.10})$$

and the entropic-acoustic reflection coefficient is:

$$\frac{\pi_1^-}{\sigma_1} = -\frac{1}{2} \frac{\bar{M}_1}{1 + \frac{\gamma-1}{2} \bar{M}_1}. \quad (\text{A.11})$$

The compositional-acoustic transmission coefficients are:

$$\frac{\pi_2^+}{\xi_1} = \frac{1}{2(\gamma-1)} \left[\frac{1 + \frac{\gamma-1}{2} \bar{M}_2}{1 + \frac{\gamma-1}{2} \bar{M}_1} \Psi_1 - \Psi_2 \right], \quad (\text{A.12})$$

$$\frac{\pi_2^-}{\xi_1} = -\frac{1}{2(\gamma-1)} \left[\Psi_2 - \frac{1 - \frac{\gamma-1}{2} \bar{M}_2}{1 + \frac{\gamma-1}{2} \bar{M}_1} \Psi_1 \right], \quad (\text{A.13})$$

and the compositional-acoustic transmission coefficient is:

$$\frac{\pi_1^-}{\xi_1} = -\frac{1}{2} \frac{\bar{M}_1}{1 + \frac{\gamma-1}{2} \bar{M}_1} \Psi_1. \quad (\text{A.14})$$

A.3 Anisentropic compact nozzle

Explicit analytical expressions for the transfer functions of a subsonic compact anisentropic nozzle are presented here.

A.3.1 Downstream acoustic wave

The upstream acoustic transmission coefficient is:

$$\frac{\pi_2^+}{\pi_1^+} = 2\bar{M}_2 \left(\frac{\bar{M}_1 + 1}{\bar{M}_2 + 1} \right) \frac{A}{Y}, \quad (\text{A.15})$$

A. NOZZLE TRANSFER FUNCTIONS

with

$$\begin{aligned}
A = & 2\bar{M}_j^2 \bar{c}_j - \bar{M}_j^4 \bar{c}_j - \bar{M}_2^3 \bar{M}_j^3 \bar{c}_2 - 2\bar{M}_2^2 \bar{M}_j^2 \bar{c}_j + \bar{M}_2^2 \bar{M}_j^4 \bar{c}_j - 2\bar{M}_2 \bar{M}_j \bar{c}_2 \\
& + \frac{2A_2 \bar{c}_j}{A_j} + 2\bar{M}_2 \bar{M}_j^3 \bar{c}_2 + \bar{M}_2^3 \bar{M}_j \bar{c}_2 - 4\bar{M}_j^2 \bar{c}_j \gamma + \bar{M}_j^4 \bar{c}_j \gamma - 2\bar{M}_2 \bar{M}_j^3 \bar{c}_2 \gamma \\
& - 2\bar{M}_2^3 \bar{M}_j \bar{c}_2 \gamma - \frac{3A_2 \bar{M}_j^2 \bar{c}_j}{A_j} + \bar{M}_2^3 \bar{M}_j \bar{c}_2 \gamma^2 + 2\bar{M}_2^3 \bar{M}_j^3 \bar{c}_2 \gamma + 4\bar{M}_2^2 \bar{M}_j^2 \bar{c}_j \gamma \\
& - 2\bar{M}_2^2 \bar{M}_j^4 \bar{c}_j \gamma + 2\bar{M}_2 \bar{M}_j \bar{c}_2 \gamma - \bar{M}_2^3 \bar{M}_j^3 \bar{c}_2 \gamma^2 - 2\bar{M}_2^2 \bar{M}_j^2 \bar{c}_j \gamma^2 + \bar{M}_2^2 \bar{M}_j^4 \bar{c}_j \gamma^2 \\
& + \frac{3A_2 \bar{M}_j^2 \bar{c}_j \gamma}{A_j} + \frac{A_2 \bar{M}_2^2 \bar{M}_j^2 \bar{c}_j}{A_j} - \frac{2A_2 \bar{M}_2^2 \bar{M}_j^2 \bar{c}_j \gamma}{A_j} + \frac{A_2 \bar{M}_2^2 \bar{M}_j^2 \bar{c}_j \gamma^2}{A_j},
\end{aligned} \tag{A.16}$$

$$\begin{aligned}
Y = & 2\bar{M}_j \bar{c}_2 - 2\bar{M}_j^3 \bar{c}_2 - 4\bar{M}_j^2 \bar{c}_j + 2\bar{M}_j^4 \bar{c}_j + \bar{M}_1^2 \bar{M}_j^3 \bar{c}_2 + 2\bar{M}_2^2 \bar{M}_j^3 \bar{c}_2 \\
& + 2\bar{M}_1^2 \bar{M}_j^2 \bar{c}_j - \bar{M}_1^2 \bar{M}_j^4 \bar{c}_j + 2\bar{M}_1 \bar{M}_j \bar{c}_2 + 2\bar{M}_2 \bar{M}_j \bar{c}_2 - \bar{M}_1^2 \bar{M}_j \bar{c}_2 \\
& - 2\bar{M}_1 \bar{M}_j^3 \bar{c}_2 - 2\bar{M}_2^2 \bar{M}_j \bar{c}_2 - 2\bar{M}_2 \bar{M}_j^3 \bar{c}_2 - 2\bar{M}_1 \bar{M}_j^2 \bar{c}_j + 4\bar{M}_2 \bar{M}_j^2 \bar{c}_j \\
& + \bar{M}_1 \bar{M}_j^4 \bar{c}_j - 2\bar{M}_2 \bar{M}_j^4 \bar{c}_j - \bar{M}_1 \bar{M}_2^2 \bar{M}_j \bar{c}_2 - \bar{M}_1^2 \bar{M}_2 \bar{M}_j \bar{c}_2 + 2\bar{M}_1 \bar{M}_2 \bar{M}_j^2 \bar{c}_j \\
& - \bar{M}_1 \bar{M}_2 \bar{M}_j^4 \bar{c}_j + \bar{M}_1^2 \bar{M}_j \bar{c}_2 \gamma + 2\bar{M}_1 \bar{M}_j^3 \bar{c}_2 \gamma + 2\bar{M}_2^2 \bar{M}_j \bar{c}_2 \gamma - 4\bar{M}_2 \bar{M}_j^2 \bar{c}_j \gamma \\
& - \bar{M}_1 \bar{M}_j^4 \bar{c}_j \gamma + 2\bar{M}_2 \bar{M}_j^4 \bar{c}_j \gamma + \frac{2A_2 \bar{M}_j^2 \bar{c}_j}{A_j} + \bar{M}_1^2 \bar{M}_2^2 \bar{M}_j \bar{c}_2 + \bar{M}_1 \bar{M}_2^2 \bar{M}_j^3 \bar{c}_2 \\
& + \bar{M}_1^2 \bar{M}_2 \bar{M}_j^3 \bar{c}_2 - 2\bar{M}_1^2 \bar{M}_2 \bar{M}_j^2 \bar{c}_j + \bar{M}_1^2 \bar{M}_2 \bar{M}_j^4 \bar{c}_j - \bar{M}_1^2 \bar{M}_j^3 \bar{c}_2 \gamma - 2\bar{M}_2^2 \bar{M}_j^3 \bar{c}_2 \gamma \\
& - 2\bar{M}_1^2 \bar{M}_j^2 \bar{c}_j \gamma + \bar{M}_1^2 \bar{M}_j^4 \bar{c}_j \gamma - 2\bar{M}_1 \bar{M}_j \bar{c}_2 \gamma - \bar{M}_1^2 \bar{M}_2^2 \bar{M}_j^3 \bar{c}_2 + \frac{2A_2 \bar{M}_1 \bar{c}_j}{A_j} \\
& + \bar{M}_1^2 \bar{M}_2^2 \bar{M}_j \bar{c}_2 \gamma^2 + \bar{M}_1 \bar{M}_2^2 \bar{M}_j^3 \bar{c}_2 \gamma^2 + 2\bar{M}_1^2 \bar{M}_2^2 \bar{M}_j^3 \bar{c}_2 \gamma - 2\bar{M}_1^2 \bar{M}_2 \bar{M}_j^2 \bar{c}_j \gamma^2 \\
& + \bar{M}_1^2 \bar{M}_2 \bar{M}_j^4 \bar{c}_j \gamma^2 - \frac{2A_2 \bar{M}_1 \bar{M}_2 \bar{c}_j}{A_j} + 2\bar{M}_1 \bar{M}_2^2 \bar{M}_j \bar{c}_2 \gamma + \bar{M}_1^2 \bar{M}_2 \bar{M}_j \bar{c}_2 \gamma \\
& - 2\bar{M}_1 \bar{M}_2 \bar{M}_j^2 \bar{c}_j \gamma + 2\bar{M}_1 \bar{M}_2 \bar{M}_j^4 \bar{c}_j \gamma - \bar{M}_1^2 \bar{M}_2^2 \bar{M}_j^3 \bar{c}_2 \gamma^2 - \frac{A_2 \bar{M}_1 \bar{M}_j^2 \bar{c}_j}{A_j} \\
& - \frac{2A_2 \bar{M}_2 \bar{M}_j^2 \bar{c}_j}{A_j} - \bar{M}_1 \bar{M}_2^2 \bar{M}_j \bar{c}_2 \gamma^2 - 2\bar{M}_1^2 \bar{M}_2^2 \bar{M}_j \bar{c}_2 \gamma - 2\bar{M}_1 \bar{M}_2^2 \bar{M}_j^3 \bar{c}_2 \gamma \\
& - \bar{M}_1^2 \bar{M}_2 \bar{M}_j^3 \bar{c}_2 \gamma + 4\bar{M}_1^2 \bar{M}_2 \bar{M}_j^2 \bar{c}_j \gamma - \bar{M}_1 \bar{M}_2 \bar{M}_j^4 \bar{c}_j \gamma^2 - 2\bar{M}_1^2 \bar{M}_2 \bar{M}_j^4 \bar{c}_j \gamma \\
& - \frac{A_2 \bar{M}_1^2 \bar{M}_j^2 \bar{c}_j}{A_j} + \frac{A_2 \bar{M}_1 \bar{M}_j^2 \bar{c}_j \gamma}{A_j} + \frac{2A_2 \bar{M}_2 \bar{M}_j^2 \bar{c}_j \gamma}{A_j} + \frac{A_2 \bar{M}_1^2 \bar{M}_2 \bar{M}_j^2 \bar{c}_j}{A_j} \\
& + \frac{A_2 \bar{M}_1^2 \bar{M}_j^2 \bar{c}_j \gamma}{A_j} + \frac{2A_2 \bar{M}_1 \bar{M}_2 \bar{c}_j \gamma}{A_j} + \frac{A_2 \bar{M}_1 \bar{M}_2 \bar{M}_j^2 \bar{c}_j}{A_j} + \frac{A_2 \bar{M}_1^2 \bar{M}_2 \bar{M}_j^2 \bar{c}_j \gamma^2}{A_j} \\
& - \frac{2A_2 \bar{M}_1 \bar{M}_2 \bar{M}_j^2 \bar{c}_j \gamma}{A_j} + \frac{A_2 \bar{M}_1 \bar{M}_2 \bar{M}_j^2 \bar{c}_j \gamma^2}{A_j} - \frac{2A_2 \bar{M}_1^2 \bar{M}_2 \bar{M}_j^2 \bar{c}_j \gamma}{A_j}.
\end{aligned} \tag{A.17}$$

The downstream acoustic reflection coefficient is:

$$\frac{\pi_2^+}{\pi_2^-} = - \left(\frac{1 - \bar{M}_2}{1 + \bar{M}_2} \right) \frac{B}{Y}, \quad (\text{A.18})$$

with

$$\begin{aligned} B = & 2\bar{M}_j\bar{c}_2 - 2\bar{M}_j^3\bar{c}_2 + 4\bar{M}_j^2\bar{c}_j - 2\bar{M}_j^4\bar{c}_j + \bar{M}_1^2\bar{M}_j^3\bar{c}_2 + 2\bar{M}_2^2\bar{M}_j^3\bar{c}_2 \\ & - 2\bar{M}_1^2\bar{M}_j^2\bar{c}_j + \bar{M}_1^2\bar{M}_j^4\bar{c}_j + 2\bar{M}_1\bar{M}_j\bar{c}_2 - 2\bar{M}_2\bar{M}_j\bar{c}_2 - \bar{M}_1^2\bar{M}_j\bar{c}_2 \\ & - 2\bar{M}_1\bar{M}_j^3\bar{c}_2 - 2\bar{M}_2^2\bar{M}_j\bar{c}_2 + 2\bar{M}_2\bar{M}_j^3\bar{c}_2 + 2\bar{M}_1\bar{M}_j^2\bar{c}_j + 4\bar{M}_2\bar{M}_j^2\bar{c}_j \\ & - \bar{M}_1\bar{M}_j^4\bar{c}_j - 2\bar{M}_2\bar{M}_j^4\bar{c}_j - \bar{M}_1\bar{M}_2^2\bar{M}_j\bar{c}_2 + \bar{M}_1^2\bar{M}_2\bar{M}_j\bar{c}_2 + 2\bar{M}_1\bar{M}_2\bar{M}_j^2\bar{c}_j \\ & - \bar{M}_1\bar{M}_2\bar{M}_j^4\bar{c}_j + \bar{M}_1^2\bar{M}_j\bar{c}_2\gamma + 2\bar{M}_1\bar{M}_j^3\bar{c}_2\gamma + 2\bar{M}_2^2\bar{M}_j\bar{c}_2\gamma - 4\bar{M}_2\bar{M}_j^2\bar{c}_j\gamma \\ & + \bar{M}_1\bar{M}_j^4\bar{c}_j\gamma + 2\bar{M}_2\bar{M}_j^4\bar{c}_j\gamma - \frac{2A_2\bar{M}_j^2\bar{c}_j}{A_j} + \bar{M}_1^2\bar{M}_2^2\bar{M}_j\bar{c}_2 + \bar{M}_1\bar{M}_2^2\bar{M}_j^3\bar{c}_2 \\ & - \bar{M}_1^2\bar{M}_2\bar{M}_j^3\bar{c}_2 - 2\bar{M}_1^2\bar{M}_2\bar{M}_j^2\bar{c}_j + \bar{M}_1^2\bar{M}_2\bar{M}_j^4\bar{c}_j - \bar{M}_1^2\bar{M}_j^3\bar{c}_2\gamma - 2\bar{M}_2^2\bar{M}_j^3\bar{c}_2\gamma \\ & + 2\bar{M}_1^2\bar{M}_j^2\bar{c}_j\gamma - \bar{M}_1^2\bar{M}_j^4\bar{c}_j\gamma - 2\bar{M}_1\bar{M}_j\bar{c}_2\gamma - \bar{M}_1^2\bar{M}_2^2\bar{M}_j^3\bar{c}_2 - \frac{2A_2\bar{M}_1\bar{c}_j}{A_j} \\ & + \bar{M}_1^2\bar{M}_2^2\bar{M}_j\bar{c}_2\gamma^2 + \bar{M}_1\bar{M}_2^2\bar{M}_j^3\bar{c}_2\gamma^2 + 2\bar{M}_1^2\bar{M}_2^2\bar{M}_j^3\bar{c}_2\gamma - 2\bar{M}_1^2\bar{M}_2\bar{M}_j^2\bar{c}_j\gamma^2 \\ & + \bar{M}_1^2\bar{M}_2\bar{M}_j^4\bar{c}_j\gamma^2 - \frac{2A_2\bar{M}_1\bar{M}_2\bar{c}_j}{A_j} + 2\bar{M}_1\bar{M}_2^2\bar{M}_j\bar{c}_2\gamma - \bar{M}_1^2\bar{M}_2\bar{M}_j\bar{c}_2\gamma \\ & - 2\bar{M}_1\bar{M}_2\bar{M}_j^2\bar{c}_j\gamma + 2\bar{M}_1\bar{M}_2\bar{M}_j^4\bar{c}_j\gamma - \bar{M}_1^2\bar{M}_2^2\bar{M}_j^3\bar{c}_2\gamma^2 + \frac{A_2\bar{M}_1\bar{M}_j^2\bar{c}_j}{A_j} \\ & - \frac{2A_2\bar{M}_2\bar{M}_j^2\bar{c}_j}{A_j} - \bar{M}_1\bar{M}_2^2\bar{M}_j\bar{c}_2\gamma^2 - 2\bar{M}_1^2\bar{M}_2^2\bar{M}_j\bar{c}_2\gamma - 2\bar{M}_1\bar{M}_2^2\bar{M}_j^3\bar{c}_2\gamma \\ & + \bar{M}_1^2\bar{M}_2\bar{M}_j^3\bar{c}_2\gamma + 4\bar{M}_1^2\bar{M}_2\bar{M}_j^2\bar{c}_j\gamma - \bar{M}_1\bar{M}_2\bar{M}_j^4\bar{c}_j\gamma^2 - 2\bar{M}_1^2\bar{M}_2\bar{M}_j^4\bar{c}_j\gamma \\ & + \frac{A_2\bar{M}_1^2\bar{M}_j^2\bar{c}_j}{A_j} - \frac{A_2\bar{M}_1\bar{M}_j^2\bar{c}_j\gamma}{A_j} + \frac{2A_2\bar{M}_2\bar{M}_j^2\bar{c}_j\gamma}{A_j} + \frac{A_2\bar{M}_1^2\bar{M}_2\bar{M}_j^2\bar{c}_j}{A_j} \\ & - \frac{A_2\bar{M}_1^2\bar{M}_j^2\bar{c}_j\gamma}{A_j} + \frac{2A_2\bar{M}_1\bar{M}_2\bar{c}_j\gamma}{A_j} + \frac{A_2\bar{M}_1\bar{M}_2\bar{M}_j^2\bar{c}_j}{A_j} + \frac{A_2\bar{M}_1^2\bar{M}_2\bar{M}_j^2\bar{c}_j\gamma^2}{A_j} \\ & - \frac{2A_2\bar{M}_1\bar{M}_2\bar{M}_j^2\bar{c}_j\gamma}{A_j} + \frac{A_2\bar{M}_1\bar{M}_2\bar{M}_j^2\bar{c}_j\gamma^2}{A_j} - \frac{2A_2\bar{M}_1^2\bar{M}_2\bar{M}_j^2\bar{c}_j\gamma}{A_j}. \end{aligned} \quad (\text{A.19})$$

The entropic-acoustic transmission coefficient is:

$$\frac{\pi_2^+}{\sigma_1} = \left(\frac{\bar{M}_2}{1 + \bar{M}_2} \right) \frac{C}{Y}, \quad (\text{A.20})$$

A. NOZZLE TRANSFER FUNCTIONS

with

$$\begin{aligned}
C = & \bar{M}_j^4 \bar{c}_j - 2\bar{M}_j^2 \bar{c}_j + \bar{M}_2^3 \bar{M}_j^3 \bar{c}_2 + 2\bar{M}_2^2 \bar{M}_j^2 \bar{c}_j - \bar{M}_2^2 \bar{M}_j^4 \bar{c}_j + 2\bar{M}_2 \bar{M}_j \bar{c}_2 \\
& - 2\bar{M}_2 \bar{M}_j^3 \bar{c}_2 - \bar{M}_2^3 \bar{M}_j \bar{c}_2 - 2\bar{M}_1 \bar{M}_j^2 \bar{c}_j + \bar{M}_1 \bar{M}_j^4 \bar{c}_j - 2\bar{M}_1 \bar{M}_2 \bar{M}_j^3 \bar{c}_2 \\
& - \bar{M}_1 \bar{M}_2^3 \bar{M}_j \bar{c}_2 + \bar{M}_2^3 \bar{M}_j \bar{c}_2 \gamma + 2\bar{M}_1 \bar{M}_j^2 \bar{c}_j \gamma - \bar{M}_1 \bar{M}_j^4 \bar{c}_j \gamma - \frac{A_2 \bar{M}_1^2 \bar{c}_j}{A_j} + \frac{A_2 \bar{M}_j^2 \bar{c}_j}{A_j} \\
& + \bar{M}_1 \bar{M}_2^3 \bar{M}_j^3 \bar{c}_2 + 2\bar{M}_1 \bar{M}_2^2 \bar{M}_j^2 \bar{c}_j - \bar{M}_1 \bar{M}_2^2 \bar{M}_j^4 \bar{c}_j - \bar{M}_2^3 \bar{M}_j^3 \bar{c}_2 \gamma + \bar{M}_1^2 \bar{M}_j^2 \bar{c}_j \gamma \\
& - 2\bar{M}_2^2 \bar{M}_j^2 \bar{c}_j \gamma + \bar{M}_2^2 \bar{M}_j^4 \bar{c}_j \gamma + 2\bar{M}_1 \bar{M}_2 \bar{M}_j \bar{c}_2 - 2\bar{M}_1 \bar{M}_2 \bar{M}_j \bar{c}_2 \gamma + \bar{M}_1 \bar{M}_2^3 \bar{M}_j^3 \bar{c}_2 \gamma^2 \\
& + \bar{M}_1 \bar{M}_2^2 \bar{M}_j^2 \bar{c}_j \gamma^2 - \bar{M}_1 \bar{M}_2^2 \bar{M}_j^4 \bar{c}_j \gamma^2 + 2\bar{M}_1 \bar{M}_2 \bar{M}_j^3 \bar{c}_2 \gamma + 2\bar{M}_1 \bar{M}_2^3 \bar{M}_j \bar{c}_2 \gamma \\
& - \frac{A_2 \bar{M}_1 \bar{M}_2^2 \bar{c}_j}{A_j} + \frac{A_2 \bar{M}_1 \bar{M}_j^2 \bar{c}_j}{A_j} - \bar{M}_1 \bar{M}_2^3 \bar{M}_j \bar{c}_2 \gamma^2 - 2\bar{M}_1 \bar{M}_2^3 \bar{M}_j^3 \bar{c}_2 \gamma \\
& - 3\bar{M}_1 \bar{M}_2^2 \bar{M}_j^2 \bar{c}_j \gamma + 2\bar{M}_1 \bar{M}_2^2 \bar{M}_j^4 \bar{c}_j \gamma + \frac{A_2 \bar{M}_1^2 \bar{M}_j^2 \bar{c}_j}{A_j} - \frac{A_2 \bar{M}_2^2 \bar{M}_j^2 \bar{c}_j}{A_j} \\
& + \frac{A_2 \bar{M}_1 \bar{M}_2^2 \bar{c}_j \gamma}{A_j} - \frac{A_2 \bar{M}_1 \bar{M}_j^2 \bar{c}_j \gamma}{A_j} - \frac{A_2 \bar{M}_1^2 \bar{M}_j^2 \bar{c}_j \gamma}{A_j} + \frac{A_2 \bar{M}_2^2 \bar{M}_j^2 \bar{c}_j \gamma}{A_j}.
\end{aligned} \tag{A.21}$$

The compositional-acoustic transmission coefficient is:

$$\frac{\pi_2^+}{\xi_1} = \left(\frac{\bar{M}_2}{1 + \bar{M}_2} \right) \left(\frac{1}{\gamma - 1} \right) \frac{D}{Y}, \tag{A.22}$$

with

$$\begin{aligned}
D = & 2\bar{M}_j^2 \bar{c}_j \Psi_1 - \bar{M}_j^4 \bar{c}_j \Psi_1 + \frac{2A_2 \bar{c}_j \Psi_1}{A_j} - \frac{2A_2 \bar{c}_j \Psi_j}{A_j} + 2\bar{M}_2 \bar{M}_j^3 \bar{c}_2 \Psi_1 + \bar{M}_2^3 \bar{M}_j \bar{c}_2 \Psi_1 \\
& + 2\bar{M}_1 \bar{M}_j^2 \bar{c}_j \Psi_1 - \bar{M}_1 \bar{M}_j^4 \bar{c}_j \Psi_1 - 4\bar{M}_j^2 \bar{c}_j \gamma \Psi_1 + \bar{M}_j^4 \bar{c}_j \gamma \Psi_1 + 2\bar{M}_j^2 \bar{c}_j \gamma \Psi_j - \bar{M}_2^3 \bar{M}_j^3 \bar{c}_2 \Psi_1 \\
& - 2\bar{M}_2^2 \bar{M}_j^2 \bar{c}_j \Psi_1 + \bar{M}_2^2 \bar{M}_j^4 \bar{c}_j \Psi_1 - 2\bar{M}_2 \bar{M}_j \bar{c}_2 \Psi_1 - 2\bar{M}_1 \bar{M}_2 \bar{M}_j \bar{c}_2 \Psi_1 + 2\bar{M}_2 \bar{M}_j \bar{c}_2 \gamma \Psi_1 \\
& - \bar{M}_2^3 \bar{M}_j^3 \bar{c}_2 \gamma^2 \Psi_1 - 2\bar{M}_2^2 \bar{M}_j^2 \bar{c}_j \gamma^2 \Psi_1 + \bar{M}_2^2 \bar{M}_j^4 \bar{c}_j \gamma^2 \Psi_1 + \bar{M}_1^2 \bar{M}_j^2 \bar{c}_j \gamma^2 \Psi_j + \frac{2A_2 \bar{M}_1 \bar{c}_j \Psi_1}{A_j} \\
& - \frac{2A_2 \bar{M}_1 \bar{c}_j \Psi_j}{A_j} + 2\bar{M}_1 \bar{M}_2 \bar{M}_j^3 \bar{c}_2 \Psi_1 + \bar{M}_1 \bar{M}_2^3 \bar{M}_j \bar{c}_2 \Psi_1 - 2\bar{M}_2 \bar{M}_j^3 \bar{c}_2 \gamma \Psi_1 - 2\bar{M}_2^3 \bar{M}_j \bar{c}_2 \gamma \Psi_1 \\
& - 6\bar{M}_1 \bar{M}_j^2 \bar{c}_j \gamma \Psi_1 + 2\bar{M}_1 \bar{M}_j^4 \bar{c}_j \gamma \Psi_1 + 2\bar{M}_1 \bar{M}_j^2 \bar{c}_j \gamma \Psi_j + \frac{A_2 \bar{M}_1^2 \bar{c}_j \Psi_j}{A_j} - \frac{3A_2 \bar{M}_j^2 \bar{c}_j \Psi_1}{A_j} \\
& + \frac{2A_2 \bar{M}_j^2 \bar{c}_j \Psi_j}{A_j} - \bar{M}_1 \bar{M}_2^3 \bar{M}_j^3 \bar{c}_2 \Psi_1 - 2\bar{M}_1 \bar{M}_2^2 \bar{M}_j^2 \bar{c}_j \Psi_1 + \bar{M}_1 \bar{M}_2^2 \bar{M}_j^4 \bar{c}_j \Psi_1 \\
& + \bar{M}_2^3 \bar{M}_j \bar{c}_2 \gamma^2 \Psi_1 + 2\bar{M}_2^3 \bar{M}_j^3 \bar{c}_2 \gamma \Psi_1 + 4\bar{M}_1 \bar{M}_j^2 \bar{c}_j \gamma^2 \Psi_1 + 4\bar{M}_2^2 \bar{M}_j^2 \bar{c}_j \gamma \Psi_1 \\
& - \bar{M}_1 \bar{M}_j^4 \bar{c}_j \gamma^2 \Psi_1 - 2\bar{M}_2^2 \bar{M}_j^4 \bar{c}_j \gamma \Psi_1 - 2\bar{M}_1 \bar{M}_j^2 \bar{c}_j \gamma^2 \Psi_j - \bar{M}_1^2 \bar{M}_j^2 \bar{c}_j \gamma \Psi_j + \frac{A_2 \bar{M}_1 \bar{M}_2^2 \bar{c}_j \Psi_j}{A_j} \\
& - \frac{3A_2 \bar{M}_1 \bar{M}_j^2 \bar{c}_j \Psi_1}{A_j} + \frac{2A_2 \bar{M}_1 \bar{M}_j^2 \bar{c}_j \Psi_j}{A_j} - \frac{A_2 \bar{M}_1^2 \bar{c}_j \gamma \Psi_j}{A_j} + \frac{3A_2 \bar{M}_j^2 \bar{c}_j \gamma \Psi_1}{A_j} \\
& - \frac{2A_2 \bar{M}_j^2 \bar{c}_j \gamma \Psi_j}{A_j} + 2\bar{M}_1 \bar{M}_2 \bar{M}_j^3 \bar{c}_2 \gamma^2 \Psi_1 + 3\bar{M}_1 \bar{M}_2^3 \bar{M}_j \bar{c}_2 \gamma^2 \Psi_1 - \bar{M}_1 \bar{M}_2^3 \bar{M}_j \bar{c}_2 \gamma^3 \Psi_1 \\
& + 3\bar{M}_1 \bar{M}_2^3 \bar{M}_j^3 \bar{c}_2 \gamma \Psi_1 + 6\bar{M}_1 \bar{M}_2^2 \bar{M}_j^2 \bar{c}_j \gamma \Psi_1 - 3\bar{M}_1 \bar{M}_2^2 \bar{M}_j^4 \bar{c}_j \gamma \Psi_1 - \bar{M}_1 \bar{M}_2^2 \bar{M}_j^2 \bar{c}_j \gamma \Psi_j \\
& + \frac{A_2 \bar{M}_2^2 \bar{M}_j^2 \bar{c}_j \Psi_1}{A_j} - \frac{A_2 \bar{M}_1^2 \bar{M}_j^2 \bar{c}_j \Psi_j}{A_j} + 4\bar{M}_1 \bar{M}_2 \bar{M}_j \bar{c}_2 \gamma \Psi_1 - 3\bar{M}_1 \bar{M}_2^3 \bar{M}_j^3 \bar{c}_2 \gamma^2 \Psi_1 \\
& + \bar{M}_1 \bar{M}_2^3 \bar{M}_j^3 \bar{c}_2 \gamma^3 \Psi_1 - 6\bar{M}_1 \bar{M}_2^2 \bar{M}_j^2 \bar{c}_j \gamma^2 \Psi_1 + 2\bar{M}_1 \bar{M}_2^2 \bar{M}_j^2 \bar{c}_j \gamma^3 \Psi_1 + 3\bar{M}_1 \bar{M}_2^2 \bar{M}_j^4 \bar{c}_j \gamma^2 \Psi_1 \\
& - \bar{M}_1 \bar{M}_2^2 \bar{M}_j^4 \bar{c}_j \gamma^3 \Psi_1 + 2\bar{M}_1 \bar{M}_2^2 \bar{M}_j^2 \bar{c}_j \gamma^2 \Psi_j - \bar{M}_1 \bar{M}_2^2 \bar{M}_j^2 \bar{c}_j \gamma^3 \Psi_j - \frac{2A_2 \bar{M}_1 \bar{c}_j \gamma \Psi_1}{A_j} \\
& + \frac{2A_2 \bar{M}_1 \bar{c}_j \gamma \Psi_j}{A_j} - 2\bar{M}_1 \bar{M}_2 \bar{M}_j \bar{c}_2 \gamma^2 \Psi_1 - 4\bar{M}_1 \bar{M}_2 \bar{M}_j^3 \bar{c}_2 \gamma \Psi_1 - 3\bar{M}_1 \bar{M}_2^3 \bar{M}_j \bar{c}_2 \gamma \Psi_1 \\
& + \frac{A_2 \bar{M}_2^2 \bar{M}_j^2 \bar{c}_j \gamma^2 \Psi_1}{A_j} - \frac{A_2 \bar{M}_1^2 \bar{M}_j^2 \bar{c}_j \gamma^2 \Psi_j}{A_j} - \frac{2A_2 \bar{M}_1 \bar{M}_2^2 \bar{c}_j \gamma \Psi_j}{A_j} + \frac{6A_2 \bar{M}_1 \bar{M}_j^2 \bar{c}_j \gamma \Psi_1}{A_j} \\
& - \frac{4A_2 \bar{M}_1 \bar{M}_j^2 \bar{c}_j \gamma \Psi_j}{A_j} + \frac{A_2 \bar{M}_1 \bar{M}_2^2 \bar{M}_j^2 \bar{c}_j \Psi_1}{A_j} - \frac{A_2 \bar{M}_1 \bar{M}_2^2 \bar{M}_j^2 \bar{c}_j \Psi_j}{A_j} + \frac{A_2 \bar{M}_1 \bar{M}_2^2 \bar{c}_j \gamma^2 \Psi_j}{A_j} \\
& - \frac{3A_2 \bar{M}_1 \bar{M}_j^2 \bar{c}_j \gamma^2 \Psi_1}{A_j} - \frac{2A_2 \bar{M}_2^2 \bar{M}_j^2 \bar{c}_j \gamma \Psi_1}{A_j} + \frac{2A_2 \bar{M}_1 \bar{M}_j^2 \bar{c}_j \gamma^2 \Psi_j}{A_j} + \frac{2A_2 \bar{M}_1^2 \bar{M}_j^2 \bar{c}_j \gamma \Psi_j}{A_j} \\
& - \frac{3A_2 \bar{M}_1 \bar{M}_2^2 \bar{M}_j^2 \bar{c}_j \gamma \Psi_1}{A_j} + \frac{3A_2 \bar{M}_1 \bar{M}_2^2 \bar{M}_j^2 \bar{c}_j \gamma \Psi_j}{A_j} + \frac{3A_2 \bar{M}_1 \bar{M}_2^2 \bar{M}_j^2 \bar{c}_j \gamma^2 \Psi_1}{A_j} \\
& - \frac{A_2 \bar{M}_1 \bar{M}_2^2 \bar{M}_j^2 \bar{c}_j \gamma^3 \Psi_1}{A_j} - \frac{3A_2 \bar{M}_1 \bar{M}_2^2 \bar{M}_j^2 \bar{c}_j \gamma^2 \Psi_j}{A_j} + \frac{A_2 \bar{M}_1 \bar{M}_2^2 \bar{M}_j^2 \bar{c}_j \gamma^3 \Psi_j}{A_j}.
\end{aligned} \tag{A.23}$$

A.3.2 Upstream acoustic wave

The upstream acoustic-acoustic reflection coefficient is:

$$\frac{\pi_1^-}{\pi_1^+} = \left(\frac{1 + \bar{M}_1}{1 - \bar{M}_1} \right) \frac{E}{Y}, \quad (\text{A.24})$$

with

$$\begin{aligned} E = & 2\bar{M}_j\bar{c}_2 - 2\bar{M}_j^3\bar{c}_2 - 4\bar{M}_j^2\bar{c}_j + 2\bar{M}_j^4\bar{c}_j + \bar{M}_1^2\bar{M}_j^3\bar{c}_2 + 2\bar{M}_2^2\bar{M}_j^3\bar{c}_2 \\ & + 2\bar{M}_1^2\bar{M}_j^2\bar{c}_j - \bar{M}_1^2\bar{M}_j^4\bar{c}_j - 2\bar{M}_1\bar{M}_j\bar{c}_2 + 2\bar{M}_2\bar{M}_j\bar{c}_2 - \bar{M}_1^2\bar{M}_j\bar{c}_2 + 2\bar{M}_1\bar{M}_j^3\bar{c}_2 \\ & - 2\bar{M}_2^2\bar{M}_j\bar{c}_2 - 2\bar{M}_2\bar{M}_j^3\bar{c}_2 + 2\bar{M}_1\bar{M}_j^2\bar{c}_j + 4\bar{M}_2\bar{M}_j^2\bar{c}_j - \bar{M}_1\bar{M}_j^4\bar{c}_j \\ & - 2\bar{M}_2\bar{M}_j^4\bar{c}_j + \bar{M}_1\bar{M}_2^2\bar{M}_j\bar{c}_2 - \bar{M}_1^2\bar{M}_2\bar{M}_j\bar{c}_2 - 2\bar{M}_1\bar{M}_2\bar{M}_j^2\bar{c}_j + \bar{M}_1\bar{M}_2\bar{M}_j^4\bar{c}_j \\ & + \bar{M}_1^2\bar{M}_j\bar{c}_2\gamma - 2\bar{M}_1\bar{M}_j^3\bar{c}_2\gamma + 2\bar{M}_2^2\bar{M}_j\bar{c}_2\gamma - 4\bar{M}_2\bar{M}_j^2\bar{c}_j\gamma + \bar{M}_1\bar{M}_j^4\bar{c}_j\gamma \\ & + 2\bar{M}_2\bar{M}_j^4\bar{c}_j\gamma + \frac{2A_2\bar{M}_j^2\bar{c}_j}{A_j} + \bar{M}_1^2\bar{M}_2^2\bar{M}_j\bar{c}_2 - \bar{M}_1\bar{M}_2^2\bar{M}_j^3\bar{c}_2 + \bar{M}_1^2\bar{M}_2\bar{M}_j^3\bar{c}_2 \\ & - 2\bar{M}_1^2\bar{M}_2\bar{M}_j^2\bar{c}_j + \bar{M}_1^2\bar{M}_2\bar{M}_j^4\bar{c}_j - \bar{M}_1^2\bar{M}_j^3\bar{c}_2\gamma - 2\bar{M}_2^2\bar{M}_j^3\bar{c}_2\gamma \\ & - 2\bar{M}_1^2\bar{M}_j^2\bar{c}_j\gamma + \bar{M}_1^2\bar{M}_j^4\bar{c}_j\gamma + 2\bar{M}_1\bar{M}_j\bar{c}_2\gamma - \bar{M}_1^2\bar{M}_2^2\bar{M}_j^3\bar{c}_2 - \frac{2A_2\bar{M}_1\bar{c}_j}{A_j} \\ & + \bar{M}_1^2\bar{M}_2^2\bar{M}_j\bar{c}_2\gamma^2 - \bar{M}_1\bar{M}_2^2\bar{M}_j^3\bar{c}_2\gamma^2 + 2\bar{M}_1^2\bar{M}_2^2\bar{M}_j^3\bar{c}_2\gamma - 2\bar{M}_1^2\bar{M}_2\bar{M}_j^2\bar{c}_j\gamma^2 \\ & + \bar{M}_1^2\bar{M}_2\bar{M}_j^4\bar{c}_j\gamma^2 + \frac{2A_2\bar{M}_1\bar{M}_2\bar{c}_j}{A_j} - 2\bar{M}_1\bar{M}_2^2\bar{M}_j\bar{c}_2\gamma + \bar{M}_1^2\bar{M}_2\bar{M}_j\bar{c}_2\gamma \\ & + 2\bar{M}_1\bar{M}_2\bar{M}_j^2\bar{c}_j\gamma - 2\bar{M}_1\bar{M}_2\bar{M}_j^4\bar{c}_j\gamma - \bar{M}_1^2\bar{M}_2^2\bar{M}_j^3\bar{c}_2\gamma^2 + \frac{A_2\bar{M}_1\bar{M}_j^2\bar{c}_j}{A_j} \\ & - \frac{2A_2\bar{M}_2\bar{M}_j^2\bar{c}_j}{A_j} + \bar{M}_1\bar{M}_2^2\bar{M}_j\bar{c}_2\gamma^2 - 2\bar{M}_1^2\bar{M}_2^2\bar{M}_j\bar{c}_2\gamma + 2\bar{M}_1\bar{M}_2^2\bar{M}_j^3\bar{c}_2\gamma \\ & - \bar{M}_1^2\bar{M}_2\bar{M}_j^3\bar{c}_2\gamma + 4\bar{M}_1^2\bar{M}_2\bar{M}_j^2\bar{c}_j\gamma + \bar{M}_1\bar{M}_2\bar{M}_j^4\bar{c}_j\gamma^2 - 2\bar{M}_1^2\bar{M}_2\bar{M}_j^4\bar{c}_j\gamma \\ & - \frac{A_2\bar{M}_1^2\bar{M}_j^2\bar{c}_j}{A_j} - \frac{A_2\bar{M}_1\bar{M}_j^2\bar{c}_j\gamma}{A_j} + \frac{2A_2\bar{M}_2\bar{M}_j^2\bar{c}_j\gamma}{A_j} + \frac{A_2\bar{M}_1^2\bar{M}_2\bar{M}_j^2\bar{c}_j}{A_j} \\ & + \frac{A_2\bar{M}_1^2\bar{M}_j^2\bar{c}_j\gamma}{A_j} - \frac{2A_2\bar{M}_1\bar{M}_2\bar{c}_j\gamma}{A_j} - \frac{A_2\bar{M}_1\bar{M}_2\bar{M}_j^2\bar{c}_j}{A_j} + \frac{A_2\bar{M}_1^2\bar{M}_2\bar{M}_j^2\bar{c}_j\gamma^2}{A_j} \\ & + \frac{2A_2\bar{M}_1\bar{M}_2\bar{M}_j^2\bar{c}_j\gamma}{A_j} - \frac{A_2\bar{M}_1\bar{M}_2\bar{M}_j^2\bar{c}_j\gamma^2}{A_j} - \frac{2A_2\bar{M}_1^2\bar{M}_2\bar{M}_j^2\bar{c}_j\gamma}{A_j}. \end{aligned} \quad (\text{A.25})$$

The downstream acoustic-acoustic transmission coefficient is:

$$\frac{\pi_1^-}{\pi_2^-} = 2 \left(\frac{\bar{M}_1}{\bar{M}_2} \right) \left(\frac{1 - \bar{M}_2}{1 - \bar{M}_1} \right) \frac{F}{Y}, \quad (\text{A.26})$$

with

$$F = \bar{M}_j \bar{c}_2 \left(1 - \bar{M}_j^2 \right) \left(2 + (\gamma - 1) \bar{M}_1^2 \right). \quad (\text{A.27})$$

The entropic-acoustic reflection coefficient is:

$$\frac{\pi_1^-}{\sigma_1} = \left(\frac{\bar{M}_1}{1 - \bar{M}_1} \right) \frac{G}{Y}, \quad (\text{A.28})$$

with

$$\begin{aligned} G = & 2\bar{M}_j^2 \bar{c}_j - \bar{M}_j^4 \bar{c}_j - \bar{M}_1^2 \bar{M}_j^3 \bar{c}_2 - \bar{M}_2^2 \bar{M}_j^3 \bar{c}_2 - 2\bar{M}_1^2 \bar{M}_j^2 \bar{c}_j + \bar{M}_1^2 \bar{M}_j^4 \bar{c}_j \\ & - 2\bar{M}_2 \bar{M}_j \bar{c}_2 + \bar{M}_1^2 \bar{M}_j \bar{c}_2 + \bar{M}_2^2 \bar{M}_j \bar{c}_2 + 2\bar{M}_2 \bar{M}_j^3 \bar{c}_2 - 2\bar{M}_2 \bar{M}_j^2 \bar{c}_j \\ & + \bar{M}_2 \bar{M}_j^4 \bar{c}_j + \bar{M}_1^2 \bar{M}_2 \bar{M}_j \bar{c}_2 - \bar{M}_1^2 \bar{M}_j \bar{c}_2 \gamma - \bar{M}_2^2 \bar{M}_j \bar{c}_2 \gamma + 2\bar{M}_2 \bar{M}_j^2 \bar{c}_j \gamma \\ & - \bar{M}_2 \bar{M}_j^4 \bar{c}_j \gamma + \frac{A_2 \bar{M}_1^2 \bar{c}_j}{A_j} - \frac{A_2 \bar{M}_j^2 \bar{c}_j}{A_j} - \bar{M}_1^2 \bar{M}_2^2 \bar{M}_j \bar{c}_2 - \bar{M}_1^2 \bar{M}_2 \bar{M}_j^3 \bar{c}_2 \\ & + 2\bar{M}_1^2 \bar{M}_2 \bar{M}_j^2 \bar{c}_j - \bar{M}_1^2 \bar{M}_2 \bar{M}_j^4 \bar{c}_j + \bar{M}_1^2 \bar{M}_j^3 \bar{c}_2 \gamma + \bar{M}_2^2 \bar{M}_j^3 \bar{c}_2 \gamma + \bar{M}_1^2 \bar{M}_j^2 \bar{c}_j \gamma \\ & - \bar{M}_1^2 \bar{M}_j^4 \bar{c}_j \gamma + \bar{M}_1^2 \bar{M}_2^2 \bar{M}_j^3 \bar{c}_2 - \bar{M}_1^2 \bar{M}_2^2 \bar{M}_j \bar{c}_2 \gamma^2 - 2\bar{M}_1^2 \bar{M}_2^2 \bar{M}_j^3 \bar{c}_2 \gamma \\ & + \bar{M}_1^2 \bar{M}_2 \bar{M}_j^2 \bar{c}_j \gamma^2 - \bar{M}_1^2 \bar{M}_2 \bar{M}_j^4 \bar{c}_j \gamma^2 - \bar{M}_1^2 \bar{M}_2 \bar{M}_j \bar{c}_2 \gamma + \bar{M}_1^2 \bar{M}_2^2 \bar{M}_j^3 \bar{c}_2 \gamma^2 \\ & - \frac{A_2 \bar{M}_1^2 \bar{M}_2 \bar{c}_j}{A_j} + \frac{A_2 \bar{M}_2 \bar{M}_j^2 \bar{c}_j}{A_j} + 2\bar{M}_1^2 \bar{M}_2^2 \bar{M}_j \bar{c}_2 \gamma + \bar{M}_1^2 \bar{M}_2 \bar{M}_j^3 \bar{c}_2 \gamma \\ & - 3\bar{M}_1^2 \bar{M}_2 \bar{M}_j^2 \bar{c}_j \gamma + 2\bar{M}_1^2 \bar{M}_2 \bar{M}_j^4 \bar{c}_j \gamma + \frac{A_2 \bar{M}_1^2 \bar{M}_2 \bar{c}_j \gamma}{A_j} - \frac{A_2 \bar{M}_2 \bar{M}_j^2 \bar{c}_j \gamma}{A_j}. \end{aligned} \quad (\text{A.29})$$

The compositional-acoustic reflection coefficient is:

$$\frac{\pi_1^-}{\xi_1} = - \left(\frac{\bar{M}_1}{1 - \bar{M}_1} \right) \left(\frac{1}{\gamma - 1} \right) \frac{H}{Y}, \quad (\text{A.30})$$

A. NOZZLE TRANSFER FUNCTIONS

with

$$\begin{aligned}
H = & 2\bar{M}_j^2 \bar{c}_j \Psi_1 - \bar{M}_j^4 \bar{c}_j \Psi_1 + \frac{2A_2 \bar{c}_j \Psi_1}{A_j} - \frac{2A_2 \bar{c}_j \Psi_j}{A_j} + \bar{M}_1^2 \bar{M}_j \bar{c}_2 \Psi_1 + \bar{M}_2^2 \bar{M}_j \bar{c}_2 \Psi_1 \\
& + 2\bar{M}_2 \bar{M}_j^3 \bar{c}_2 \Psi_1 - 2\bar{M}_2 \bar{M}_j^2 \bar{c}_2 \Psi_1 + \bar{M}_2 \bar{M}_j^4 \bar{c}_2 \Psi_1 - 4\bar{M}_j^2 \bar{c}_j \gamma \Psi_1 + \bar{M}_j^4 \bar{c}_j \gamma \Psi_1 \\
& + 2\bar{M}_j^2 \bar{c}_j \gamma \Psi_j - \bar{M}_1^2 \bar{M}_j^3 \bar{c}_2 \Psi_1 - \bar{M}_2^2 \bar{M}_j^3 \bar{c}_2 \Psi_1 - 2\bar{M}_1^2 \bar{M}_j^2 \bar{c}_j \Psi_1 + \bar{M}_1^2 \bar{M}_j^4 \bar{c}_j \Psi_1 \\
& - 2\bar{M}_2 \bar{M}_j \bar{c}_2 \Psi_1 + 2\bar{M}_2 \bar{M}_j \bar{c}_2 \gamma \Psi_1 + \bar{M}_1^2 \bar{M}_2^2 \bar{M}_j^3 \bar{c}_2 \Psi_1 - \bar{M}_1^2 \bar{M}_j^3 \bar{c}_2 \gamma^2 \Psi_1 - \bar{M}_2^2 \bar{M}_j^3 \bar{c}_2 \gamma^2 \Psi_1 \\
& - 2\bar{M}_1^2 \bar{M}_j^2 \bar{c}_j \gamma^2 \Psi_1 + \bar{M}_1^2 \bar{M}_j^4 \bar{c}_j \gamma^2 \Psi_1 + \bar{M}_1^2 \bar{M}_j^2 \bar{c}_j \gamma^2 \Psi_j - \frac{2A_2 \bar{M}_2 \bar{c}_j \Psi_1}{A_j} + \frac{2A_2 \bar{M}_2 \bar{c}_j \Psi_j}{A_j} \\
& + \bar{M}_1^2 \bar{M}_2 \bar{M}_j \bar{c}_2 \Psi_1 - 2\bar{M}_1^2 \bar{M}_j \bar{c}_2 \gamma \Psi_1 - 2\bar{M}_2^2 \bar{M}_j \bar{c}_2 \gamma \Psi_1 - 2\bar{M}_2 \bar{M}_j^3 \bar{c}_2 \gamma \Psi_1 + 6\bar{M}_2 \bar{M}_j^2 \bar{c}_j \gamma \Psi_1 \\
& - 2\bar{M}_2 \bar{M}_j^4 \bar{c}_j \gamma \Psi_1 - 2\bar{M}_2 \bar{M}_j^2 \bar{c}_j \gamma \Psi_j + \frac{A_2 \bar{M}_1^2 \bar{c}_j \Psi_j}{A_j} - \frac{3A_2 \bar{M}_j^2 \bar{c}_j \Psi_1}{A_j} + \frac{2A_2 \bar{M}_j^2 \bar{c}_j \Psi_j}{A_j} \\
& - \bar{M}_1^2 \bar{M}_2^2 \bar{M}_j \bar{c}_2 \Psi_1 - \bar{M}_1^2 \bar{M}_2 \bar{M}_j^3 \bar{c}_2 \Psi_1 + 2\bar{M}_1^2 \bar{M}_2 \bar{M}_j^2 \bar{c}_j \Psi_1 - \bar{M}_1^2 \bar{M}_2 \bar{M}_j^4 \bar{c}_j \Psi_1 \\
& + \bar{M}_1^2 \bar{M}_j \bar{c}_2 \gamma^2 \Psi_1 + 2\bar{M}_1^2 \bar{M}_j^3 \bar{c}_2 \gamma \Psi_1 + \bar{M}_2^2 \bar{M}_j \bar{c}_2 \gamma^2 \Psi_1 + 2\bar{M}_2^2 \bar{M}_j^3 \bar{c}_2 \gamma \Psi_1 + 4\bar{M}_1^2 \bar{M}_j^2 \bar{c}_j \gamma \Psi_1 \\
& - 4\bar{M}_2 \bar{M}_j^2 \bar{c}_j \gamma^2 \Psi_1 - 2\bar{M}_1^2 \bar{M}_j^4 \bar{c}_j \gamma \Psi_1 + \bar{M}_2 \bar{M}_j^4 \bar{c}_j \gamma^2 \Psi_1 - \bar{M}_1^2 \bar{M}_j^2 \bar{c}_j \gamma \Psi_j + 2\bar{M}_2 \bar{M}_j^2 \bar{c}_j \gamma^2 \Psi_j \\
& + 3\bar{M}_1^2 \bar{M}_2^2 \bar{M}_j^3 \bar{c}_2 \gamma^2 \Psi_1 - \bar{M}_1^2 \bar{M}_2^2 \bar{M}_j^3 \bar{c}_2 \gamma^3 \Psi_1 - \frac{A_2 \bar{M}_1^2 \bar{M}_2 \bar{c}_j \Psi_j}{A_j} + \frac{3A_2 \bar{M}_2 \bar{M}_j^2 \bar{c}_j \Psi_1}{A_j} \\
& - \frac{2A_2 \bar{M}_2 \bar{M}_j^2 \bar{c}_j \Psi_j}{A_j} - \frac{A_2 \bar{M}_1^2 \bar{c}_j \gamma \Psi_j}{A_j} + \frac{3A_2 \bar{M}_j^2 \bar{c}_j \gamma \Psi_1}{A_j} - \frac{2A_2 \bar{M}_j^2 \bar{c}_j \gamma \Psi_j}{A_j} + \bar{M}_1^2 \bar{M}_2 \bar{M}_j \bar{c}_2 \gamma^2 \Psi_1 \\
& + 3\bar{M}_1^2 \bar{M}_2^2 \bar{M}_j \bar{c}_2 \gamma \Psi_1 + 2\bar{M}_1^2 \bar{M}_2 \bar{M}_j^3 \bar{c}_2 \gamma \Psi_1 - 6\bar{M}_1^2 \bar{M}_2 \bar{M}_j^2 \bar{c}_j \gamma \Psi_1 + 3\bar{M}_1^2 \bar{M}_2 \bar{M}_j^4 \bar{c}_j \gamma \Psi_1 \\
& + \bar{M}_1^2 \bar{M}_2 \bar{M}_j^2 \bar{c}_j \gamma \Psi_j + \frac{A_2 \bar{M}_1^2 \bar{M}_j^2 \bar{c}_j \Psi_1}{A_j} - \frac{A_2 \bar{M}_1^2 \bar{M}_j^2 \bar{c}_j \Psi_j}{A_j} - 3\bar{M}_1^2 \bar{M}_2^2 \bar{M}_j \bar{c}_2 \gamma^2 \Psi_1 \\
& - \bar{M}_1^2 \bar{M}_2 \bar{M}_j^3 \bar{c}_2 \gamma^2 \Psi_1 + \bar{M}_1^2 \bar{M}_2^2 \bar{M}_j \bar{c}_2 \gamma^3 \Psi_1 - 3\bar{M}_1^2 \bar{M}_2^2 \bar{M}_j^3 \bar{c}_2 \gamma \Psi_1 + 6\bar{M}_1^2 \bar{M}_2 \bar{M}_j^2 \bar{c}_j \gamma^2 \Psi_1 \\
& - 2\bar{M}_1^2 \bar{M}_2 \bar{M}_j^2 \bar{c}_j \gamma^3 \Psi_1 - 3\bar{M}_1^2 \bar{M}_2 \bar{M}_j^4 \bar{c}_j \gamma^2 \Psi_1 + \bar{M}_1^2 \bar{M}_2 \bar{M}_j^4 \bar{c}_j \gamma^3 \Psi_1 - 2\bar{M}_1^2 \bar{M}_2 \bar{M}_j^2 \bar{c}_j \gamma^2 \Psi_j \\
& + \bar{M}_1^2 \bar{M}_2 \bar{M}_j^2 \bar{c}_j \gamma^3 \Psi_j + \frac{2A_2 \bar{M}_2 \bar{c}_j \gamma \Psi_1}{A_j} - \frac{2A_2 \bar{M}_2 \bar{c}_j \gamma \Psi_j}{A_j} - 2\bar{M}_1^2 \bar{M}_2 \bar{M}_j \bar{c}_2 \gamma \Psi_1 \\
& + \frac{A_2 \bar{M}_1^2 \bar{M}_j^2 \bar{c}_j \gamma^2 \Psi_1}{A_j} - \frac{A_2 \bar{M}_1^2 \bar{M}_j^2 \bar{c}_j \gamma^2 \Psi_j}{A_j} + \frac{2A_2 \bar{M}_1^2 \bar{M}_2 \bar{c}_j \gamma \Psi_j}{A_j} - \frac{6A_2 \bar{M}_2 \bar{M}_j^2 \bar{c}_j \gamma \Psi_1}{A_j} \\
& + \frac{4A_2 \bar{M}_2 \bar{M}_j^2 \bar{c}_j \gamma \Psi_j}{A_j} - \frac{A_2 \bar{M}_1^2 \bar{M}_2 \bar{M}_j^2 \bar{c}_j \Psi_1}{A_j} + \frac{A_2 \bar{M}_1^2 \bar{M}_2 \bar{M}_j^2 \bar{c}_j \Psi_j}{A_j} - \frac{A_2 \bar{M}_1^2 \bar{M}_2 \bar{c}_j \gamma^2 \Psi_j}{A_j} \\
& - \frac{2A_2 \bar{M}_1^2 \bar{M}_j^2 \bar{c}_j \gamma \Psi_1}{A_j} + \frac{3A_2 \bar{M}_2 \bar{M}_j^2 \bar{c}_j \gamma^2 \Psi_1}{A_j} + \frac{2A_2 \bar{M}_1^2 \bar{M}_j^2 \bar{c}_j \gamma \Psi_j}{A_j} - \frac{2A_2 \bar{M}_2 \bar{M}_j^2 \bar{c}_j \gamma^2 \Psi_j}{A_j} \\
& + \frac{3A_2 \bar{M}_1^2 \bar{M}_2 \bar{M}_j^2 \bar{c}_j \gamma \Psi_1}{A_j} - \frac{3A_2 \bar{M}_1^2 \bar{M}_2 \bar{M}_j^2 \bar{c}_j \gamma \Psi_j}{A_j} - \frac{3A_2 \bar{M}_1^2 \bar{M}_2 \bar{M}_j^2 \bar{c}_j \gamma^2 \Psi_1}{A_j} \\
& + \frac{A_2 \bar{M}_1^2 \bar{M}_2 \bar{M}_j^2 \bar{c}_j \gamma^3 \Psi_1}{A_j} + \frac{3A_2 \bar{M}_1^2 \bar{M}_2 \bar{M}_j^2 \bar{c}_j \gamma^2 \Psi_j}{A_j} - \frac{A_2 \bar{M}_1^2 \bar{M}_2 \bar{M}_j^2 \bar{c}_j \gamma^3 \Psi_j}{A_j}.
\end{aligned} \tag{A.31}$$

The entropic-acoustic transmission coefficient is:

$$\frac{\sigma_2}{\pi_1^+} = 2(\gamma - 1) (1 + \bar{M}_1) \frac{I}{Y}, \quad (\text{A.32})$$

with

$$\begin{aligned} I = & 2\bar{M}_j\bar{c}_2 - 2\bar{M}_j^3\bar{c}_2 - 4\bar{M}_j^2\bar{c}_j + 2\bar{M}_j^4\bar{c}_j + \bar{M}_2^2\bar{M}_j^3\bar{c}_2 + \bar{M}_2^3\bar{M}_j^3\bar{c}_2 + 2\bar{M}_2^2\bar{M}_j^2\bar{c}_j \\ & - \bar{M}_2^2\bar{M}_j^4\bar{c}_j + 2\bar{M}_2\bar{M}_j\bar{c}_2 - \bar{M}_2^2\bar{M}_j\bar{c}_2 - 2\bar{M}_2\bar{M}_j^3\bar{c}_2 - \bar{M}_2^3\bar{M}_j\bar{c}_2 + 2\bar{M}_2\bar{M}_j^2\bar{c}_j \\ & - \bar{M}_2\bar{M}_j^4\bar{c}_j + \bar{M}_2^2\bar{M}_j\bar{c}_2\gamma + \bar{M}_2^3\bar{M}_j\bar{c}_2\gamma + \bar{M}_2\bar{M}_j^4\bar{c}_j\gamma + \frac{2A_2\bar{M}_j^2\bar{c}_j}{A_j} \\ & - \bar{M}_2^2\bar{M}_j^3\bar{c}_2\gamma - \bar{M}_2^3\bar{M}_j^3\bar{c}_2\gamma - 2\bar{M}_2^2\bar{M}_j^2\bar{c}_j\gamma + \bar{M}_2^2\bar{M}_j^4\bar{c}_j\gamma - \frac{2A_2\bar{M}_2\bar{c}_j}{A_j} \\ & + \frac{A_2\bar{M}_2\bar{M}_j^2\bar{c}_j}{A_j} - \frac{A_2\bar{M}_2^2\bar{M}_j^2\bar{c}_j}{A_j} - \frac{A_2\bar{M}_2\bar{M}_j^2\bar{c}_j\gamma}{A_j} + \frac{A_2\bar{M}_2^2\bar{M}_j^2\bar{c}_j\gamma}{A_j}. \end{aligned} \quad (\text{A.33})$$

A.3.3 Downstream entropic wave

The entropic-acoustic reflection coefficient is:

$$\frac{\sigma_2}{\pi_2} = -2(\gamma - 1) \left(\frac{1 - \bar{M}_2}{\bar{M}_2} \right) \frac{J}{Y}, \quad (\text{A.34})$$

with

$$\begin{aligned} J = & 2\bar{M}_1\bar{M}_j^3\bar{c}_2 - 2\bar{M}_1\bar{M}_j\bar{c}_2 - 2\bar{M}_2^2\bar{M}_j^3\bar{c}_2 + 2\bar{M}_2^2\bar{M}_j\bar{c}_2 - 4\bar{M}_2\bar{M}_j^2\bar{c}_j \\ & + 2\bar{M}_2\bar{M}_j^4\bar{c}_j + \bar{M}_1\bar{M}_2^2\bar{M}_j\bar{c}_2 - 2\bar{M}_1\bar{M}_2\bar{M}_j^2\bar{c}_j + \bar{M}_1\bar{M}_2\bar{M}_j^4\bar{c}_j \\ & - \bar{M}_1^2\bar{M}_2^2\bar{M}_j\bar{c}_2 - \bar{M}_1\bar{M}_2^2\bar{M}_j^3\bar{c}_2 + 2\bar{M}_1^2\bar{M}_2\bar{M}_j^2\bar{c}_j - \bar{M}_1^2\bar{M}_2\bar{M}_j^4\bar{c}_j \\ & + \bar{M}_1^2\bar{M}_2^2\bar{M}_j^3\bar{c}_2 - \bar{M}_1^2\bar{M}_2^2\bar{M}_j^3\bar{c}_2\gamma + \frac{2A_2\bar{M}_1\bar{M}_2\bar{c}_j}{A_j} - \bar{M}_1\bar{M}_2^2\bar{M}_j\bar{c}_2\gamma \\ & - \bar{M}_1\bar{M}_2\bar{M}_j^4\bar{c}_j\gamma + \frac{2A_2\bar{M}_2\bar{M}_j^2\bar{c}_j}{A_j} + \bar{M}_1^2\bar{M}_2^2\bar{M}_j\bar{c}_2\gamma + \bar{M}_1\bar{M}_2^2\bar{M}_j^3\bar{c}_2\gamma \\ & - 2\bar{M}_1^2\bar{M}_2\bar{M}_j^2\bar{c}_j\gamma + \bar{M}_1^2\bar{M}_2\bar{M}_j^4\bar{c}_j\gamma - \frac{A_2\bar{M}_1^2\bar{M}_2\bar{M}_j^2\bar{c}_j}{A_j} \\ & - \frac{A_2\bar{M}_1\bar{M}_2\bar{M}_j^2\bar{c}_j}{A_j} + \frac{A_2\bar{M}_1\bar{M}_2\bar{M}_j^2\bar{c}_j\gamma}{A_j} + \frac{A_2\bar{M}_1^2\bar{M}_2\bar{M}_j^2\bar{c}_j\gamma}{A_j}. \end{aligned} \quad (\text{A.35})$$

A. NOZZLE TRANSFER FUNCTIONS

The entropic-entropic transmission coefficient is:

$$\frac{\sigma_2}{\sigma_1} = \frac{K}{Y} \quad (\text{A.36})$$

with

$$\begin{aligned}
K = & 2\bar{M}_j\bar{c}_2 - 2\bar{M}_j^3\bar{c}_2 - 4\bar{M}_j^2\bar{c}_j + 2\bar{M}_j^4\bar{c}_j + \bar{M}_2^2\bar{M}_j^3\bar{c}_2 + \bar{M}_2^3\bar{M}_j^3\bar{c}_2 + 2\bar{M}_2^2\bar{M}_j^2\bar{c}_j \\
& - \bar{M}_2^2\bar{M}_j^4\bar{c}_j + 2\bar{M}_1\bar{M}_j\bar{c}_2 + 2\bar{M}_2\bar{M}_j\bar{c}_2 - 2\bar{M}_1\bar{M}_j^3\bar{c}_2 - \bar{M}_2^2\bar{M}_j\bar{c}_2 \\
& - 2\bar{M}_2\bar{M}_j^3\bar{c}_2 - \bar{M}_2^3\bar{M}_j\bar{c}_2 - 4\bar{M}_1\bar{M}_j^2\bar{c}_j + 2\bar{M}_2\bar{M}_j^2\bar{c}_j + 2\bar{M}_1\bar{M}_j^4\bar{c}_j \\
& - \bar{M}_2\bar{M}_j^4\bar{c}_j - \bar{M}_1\bar{M}_2^2\bar{M}_j\bar{c}_2 - 2\bar{M}_1\bar{M}_2\bar{M}_j^3\bar{c}_2 - \bar{M}_1\bar{M}_2^3\bar{M}_j\bar{c}_2 + 2\bar{M}_1\bar{M}_2\bar{M}_j^2\bar{c}_j \\
& - \bar{M}_1\bar{M}_2\bar{M}_j^4\bar{c}_j + 2\bar{M}_1\bar{M}_j^3\bar{c}_2\gamma + \bar{M}_2^2\bar{M}_j\bar{c}_2\gamma + \bar{M}_2^3\bar{M}_j\bar{c}_2\gamma + 2\bar{M}_1\bar{M}_j^2\bar{c}_j\gamma \\
& - 2\bar{M}_2\bar{M}_j^2\bar{c}_j\gamma - 2\bar{M}_1\bar{M}_j^4\bar{c}_j\gamma + \bar{M}_2\bar{M}_j^4\bar{c}_j\gamma + \frac{2A_2\bar{M}_j^2\bar{c}_j}{A_j} + \bar{M}_1\bar{M}_2^2\bar{M}_j^3\bar{c}_2 \\
& + \bar{M}_1\bar{M}_2^3\bar{M}_j^3\bar{c}_2 + 2\bar{M}_1\bar{M}_2^2\bar{M}_j^2\bar{c}_j - \bar{M}_1\bar{M}_2^2\bar{M}_j^4\bar{c}_j - \bar{M}_2^2\bar{M}_j^3\bar{c}_2\gamma - \bar{M}_2^3\bar{M}_j^3\bar{c}_2\gamma \\
& - 2\bar{M}_2^2\bar{M}_j^2\bar{c}_j\gamma + \bar{M}_2^2\bar{M}_j^4\bar{c}_j\gamma + 2\bar{M}_1\bar{M}_2\bar{M}_j\bar{c}_2 - 2\bar{M}_1\bar{M}_j\bar{c}_2\gamma + \frac{2A_2\bar{M}_1\bar{c}_j}{A_j} \\
& - 2\bar{M}_1\bar{M}_2\bar{M}_j\bar{c}_2\gamma + \bar{M}_1\bar{M}_2^2\bar{M}_j^3\bar{c}_2\gamma^2 + \bar{M}_1\bar{M}_2^3\bar{M}_j^3\bar{c}_2\gamma^2 + \bar{M}_1\bar{M}_2^2\bar{M}_j^2\bar{c}_j\gamma^2 \\
& - \bar{M}_1^2\bar{M}_2\bar{M}_j^2\bar{c}_j\gamma^2 - \bar{M}_1\bar{M}_2^2\bar{M}_j^4\bar{c}_j\gamma^2 - \frac{2A_2\bar{M}_1\bar{M}_2\bar{c}_j}{A_j} + 2\bar{M}_1\bar{M}_2^2\bar{M}_j\bar{c}_2\gamma \\
& + 2\bar{M}_1\bar{M}_2\bar{M}_j^3\bar{c}_2\gamma + 2\bar{M}_1\bar{M}_2^3\bar{M}_j\bar{c}_2\gamma - 2\bar{M}_1\bar{M}_2\bar{M}_j^2\bar{c}_j\gamma + 2\bar{M}_1\bar{M}_2\bar{M}_j^4\bar{c}_j\gamma \\
& - \frac{A_2\bar{M}_1\bar{M}_2^2\bar{c}_j}{A_j} - \frac{A_2\bar{M}_1^2\bar{M}_2\bar{c}_j}{A_j} - \frac{A_2\bar{M}_2\bar{M}_j^2\bar{c}_j}{A_j} - \bar{M}_1\bar{M}_2^2\bar{M}_j\bar{c}_2\gamma^2 \\
& - 2\bar{M}_1\bar{M}_2^2\bar{M}_j^3\bar{c}_2\gamma - \bar{M}_1\bar{M}_2^3\bar{M}_j\bar{c}_2\gamma^2 - 2\bar{M}_1\bar{M}_2^3\bar{M}_j^3\bar{c}_2\gamma - 3\bar{M}_1\bar{M}_2^2\bar{M}_j^2\bar{c}_j\gamma \\
& + \bar{M}_1^2\bar{M}_2\bar{M}_j^2\bar{c}_j\gamma - \bar{M}_1\bar{M}_2\bar{M}_j^4\bar{c}_j\gamma^2 + 2\bar{M}_1\bar{M}_2^2\bar{M}_j^4\bar{c}_j\gamma - \frac{A_2\bar{M}_2^2\bar{M}_j^2\bar{c}_j}{A_j} \\
& + \frac{A_2\bar{M}_1\bar{M}_2^2\bar{c}_j\gamma}{A_j} + \frac{A_2\bar{M}_1^2\bar{M}_2\bar{c}_j\gamma}{A_j} + \frac{A_2\bar{M}_2\bar{M}_j^2\bar{c}_j\gamma}{A_j} + \frac{A_2\bar{M}_1^2\bar{M}_2\bar{M}_j^2\bar{c}_j}{A_j} \\
& + \frac{A_2\bar{M}_2^2\bar{M}_j^2\bar{c}_j\gamma}{A_j} + \frac{2A_2\bar{M}_1\bar{M}_2\bar{c}_j\gamma}{A_j} + \frac{A_2\bar{M}_1\bar{M}_2\bar{M}_j^2\bar{c}_j}{A_j} + \frac{A_2\bar{M}_1^2\bar{M}_2\bar{M}_j^2\bar{c}_j\gamma^2}{A_j} \\
& - \frac{2A_2\bar{M}_1\bar{M}_2\bar{M}_j^2\bar{c}_j\gamma}{A_j} + \frac{A_2\bar{M}_1\bar{M}_2\bar{M}_j^2\bar{c}_j\gamma^2}{A_j} - \frac{2A_2\bar{M}_1^2\bar{M}_2\bar{M}_j^2\bar{c}_j\gamma}{A_j}.
\end{aligned} \quad (\text{A.37})$$

The compositional-entropic transmission coefficient is:

$$\frac{\sigma_2}{\xi_1} = \frac{L + M}{Y}, \quad (\text{A.38})$$

with

$$\begin{aligned}
L = & 2\bar{M}_j\bar{c}_2\Psi_1 - 2\bar{M}_j\bar{c}_2\Psi_2 - 2\bar{M}_j^3\bar{c}_2\Psi_1 + 2\bar{M}_j^3\bar{c}_2\Psi_2 - 4\bar{M}_j^2\bar{c}_j\Psi_1 + 4\bar{M}_j^2\bar{c}_j\Psi_2 \\
& + 2\bar{M}_j^4\bar{c}_j\Psi_1 - 2\bar{M}_j^4\bar{c}_j\Psi_2 - 2\bar{M}_1\bar{M}_j^3\bar{c}_2\Psi_1 + \bar{M}_1^2\bar{M}_j\bar{c}_2\Psi_2 - \bar{M}_2^2\bar{M}_j\bar{c}_2\Psi_1 \\
& + 2\bar{M}_1\bar{M}_j^3\bar{c}_2\Psi_2 - 2\bar{M}_2\bar{M}_j^3\bar{c}_2\Psi_1 + 2\bar{M}_2^2\bar{M}_j\bar{c}_2\Psi_2 - \bar{M}_2^3\bar{M}_j\bar{c}_2\Psi_1 \\
& + 2\bar{M}_2\bar{M}_j^3\bar{c}_2\Psi_2 - 4\bar{M}_1\bar{M}_j^2\bar{c}_j\Psi_1 + 2\bar{M}_1\bar{M}_j^2\bar{c}_j\Psi_2 + 2\bar{M}_2\bar{M}_j^2\bar{c}_j\Psi_1 \\
& + 2\bar{M}_1\bar{M}_j^4\bar{c}_j\Psi_1 - 4\bar{M}_2\bar{M}_j^2\bar{c}_j\Psi_2 - \bar{M}_1\bar{M}_j^4\bar{c}_j\Psi_2 - \bar{M}_2\bar{M}_j^4\bar{c}_j\Psi_1 \\
& + 2\bar{M}_2\bar{M}_j^4\bar{c}_j\Psi_2 - \bar{M}_1^2\bar{M}_j^3\bar{c}_2\Psi_2 + \bar{M}_2^2\bar{M}_j^3\bar{c}_2\Psi_1 - 2\bar{M}_2^2\bar{M}_j^3\bar{c}_2\Psi_2 \\
& + \bar{M}_2^3\bar{M}_j^3\bar{c}_2\Psi_1 - 2\bar{M}_1^2\bar{M}_j^2\bar{c}_j\Psi_2 + 2\bar{M}_2^2\bar{M}_j^2\bar{c}_j\Psi_1 + \bar{M}_1^2\bar{M}_j^4\bar{c}_j\Psi_2 \\
& - \bar{M}_2^2\bar{M}_j^4\bar{c}_j\Psi_1 + 2\bar{M}_1\bar{M}_j\bar{c}_2\Psi_1 - 2\bar{M}_1\bar{M}_j\bar{c}_2\Psi_2 + 2\bar{M}_2\bar{M}_j\bar{c}_2\Psi_1 - 2\bar{M}_2\bar{M}_j\bar{c}_2\Psi_2 \\
& + 2\bar{M}_1\bar{M}_2\bar{M}_j\bar{c}_2\Psi_1 - 2\bar{M}_1\bar{M}_j\bar{c}_2\gamma\Psi_1 + 2\bar{M}_1\bar{M}_j\bar{c}_2\gamma\Psi_2 + \bar{M}_1^2\bar{M}_2^2\bar{M}_j^3\bar{c}_2\Psi_2 \\
& - \frac{2A_2\bar{M}_1\bar{c}_j\Psi_2}{A_j} - \frac{2A_2\bar{M}_2\bar{c}_j\Psi_1}{A_j} + \frac{2A_2\bar{M}_1\bar{c}_j\Psi_j}{A_j} + \frac{2A_2\bar{M}_2\bar{c}_j\Psi_j}{A_j} \\
& - \bar{M}_1\bar{M}_2^2\bar{M}_j\bar{c}_2\Psi_1 - 2\bar{M}_1\bar{M}_2\bar{M}_j^3\bar{c}_2\Psi_1 + \bar{M}_1\bar{M}_2^2\bar{M}_j\bar{c}_2\Psi_2 - \bar{M}_1\bar{M}_2^3\bar{M}_j\bar{c}_2\Psi_1 \\
& + \bar{M}_1^2\bar{M}_2\bar{M}_j\bar{c}_2\Psi_2 + 2\bar{M}_1\bar{M}_2\bar{M}_j^2\bar{c}_j\Psi_1 - 2\bar{M}_1\bar{M}_2\bar{M}_j^2\bar{c}_j\Psi_2 - \bar{M}_1\bar{M}_2\bar{M}_j^4\bar{c}_j\Psi_1 \\
& + \bar{M}_1\bar{M}_2\bar{M}_j^4\bar{c}_j\Psi_2 + 2\bar{M}_1\bar{M}_j^3\bar{c}_2\gamma\Psi_1 - \bar{M}_1^2\bar{M}_j\bar{c}_2\gamma\Psi_2 + \bar{M}_2^2\bar{M}_j\bar{c}_2\gamma\Psi_1 \\
& - 2\bar{M}_1\bar{M}_j^3\bar{c}_2\gamma\Psi_2 - 2\bar{M}_2^2\bar{M}_j\bar{c}_2\gamma\Psi_2 + \bar{M}_2^3\bar{M}_j\bar{c}_2\gamma\Psi_1 + 4\bar{M}_1\bar{M}_j^2\bar{c}_j\gamma\Psi_1 \\
& - 2\bar{M}_1\bar{M}_j^4\bar{c}_j\gamma\Psi_1 + 4\bar{M}_2\bar{M}_j^2\bar{c}_j\gamma\Psi_2 + \bar{M}_1\bar{M}_j^4\bar{c}_j\gamma\Psi_2 + \bar{M}_2\bar{M}_j^4\bar{c}_j\gamma\Psi_1 \\
& - 2\bar{M}_2\bar{M}_j^4\bar{c}_j\gamma\Psi_2 - 2\bar{M}_1\bar{M}_j^2\bar{c}_j\gamma\Psi_j - 2\bar{M}_2\bar{M}_j^2\bar{c}_j\gamma\Psi_j + \frac{2A_2\bar{M}_j^2\bar{c}_j\Psi_1}{A_j} \\
& - \frac{2A_2\bar{M}_j^2\bar{c}_j\Psi_2}{A_j} + \bar{M}_1\bar{M}_2^2\bar{M}_j^3\bar{c}_2\Psi_1 - \bar{M}_1^2\bar{M}_2^2\bar{M}_j\bar{c}_2\Psi_2 - \bar{M}_1\bar{M}_2^2\bar{M}_j^3\bar{c}_2\Psi_2 \\
& + \bar{M}_1\bar{M}_2^3\bar{M}_j^3\bar{c}_2\Psi_1 - \bar{M}_1^2\bar{M}_2\bar{M}_j^3\bar{c}_2\Psi_2 + 2\bar{M}_1\bar{M}_2^2\bar{M}_j^2\bar{c}_j\Psi_1 + 2\bar{M}_1^2\bar{M}_2\bar{M}_j^2\bar{c}_j\Psi_2 \\
& - \bar{M}_1\bar{M}_2^2\bar{M}_j^4\bar{c}_j\Psi_1 - \bar{M}_1^2\bar{M}_2\bar{M}_j^4\bar{c}_j\Psi_2 + \bar{M}_1^2\bar{M}_j^3\bar{c}_2\gamma\Psi_2 - \bar{M}_2^2\bar{M}_j^3\bar{c}_2\gamma\Psi_1 \\
& + 2\bar{M}_2^2\bar{M}_j^3\bar{c}_2\gamma\Psi_2 - \bar{M}_2^3\bar{M}_j^3\bar{c}_2\gamma\Psi_1 + 2\bar{M}_1^2\bar{M}_j^2\bar{c}_j\gamma\Psi_2 - 2\bar{M}_2^2\bar{M}_j^2\bar{c}_j\gamma\Psi_1 \\
& - \bar{M}_1^2\bar{M}_j^4\bar{c}_j\gamma\Psi_2 + \bar{M}_2^2\bar{M}_j^4\bar{c}_j\gamma\Psi_1 + \bar{M}_1^2\bar{M}_2^2\bar{M}_j^3\bar{c}_2\gamma^2\Psi_2 - \frac{A_2\bar{M}_1\bar{M}_2^2\bar{c}_j\Psi_j}{A_j} \\
& - \frac{A_2\bar{M}_1^2\bar{M}_2\bar{c}_j\Psi_j}{A_j} + \frac{2A_2\bar{M}_1\bar{M}_j^2\bar{c}_j\Psi_1}{A_j} + \frac{A_2\bar{M}_1\bar{M}_j^2\bar{c}_j\Psi_2}{A_j} + \frac{A_2\bar{M}_2\bar{M}_j^2\bar{c}_j\Psi_1}{A_j},
\end{aligned} \quad (\text{A.39})$$

A. NOZZLE TRANSFER FUNCTIONS

$$\begin{aligned}
M = & + \frac{2A_2\bar{M}_2\bar{M}_j^2\bar{c}_j\Psi_2}{A_j} - \frac{2A_2\bar{M}_1\bar{M}_j^2\bar{c}_j\Psi_j}{A_j} - \frac{2A_2\bar{M}_2\bar{M}_j^2\bar{c}_j\Psi_j}{A_j} - \bar{M}_1\bar{M}_2^2\bar{M}_j\bar{c}_2\gamma^2\Psi_1 \\
& + \bar{M}_1\bar{M}_2^2\bar{M}_j\bar{c}_2\gamma^2\Psi_2 - 2\bar{M}_1\bar{M}_2^2\bar{M}_j^3\bar{c}_2\gamma\Psi_1 - \bar{M}_1\bar{M}_2^3\bar{M}_j\bar{c}_2\gamma^2\Psi_1 \\
& + 2\bar{M}_1^2\bar{M}_2^2\bar{M}_j\bar{c}_2\gamma\Psi_2 + 2\bar{M}_1\bar{M}_2^2\bar{M}_j^3\bar{c}_2\gamma\Psi_2 - 2\bar{M}_1\bar{M}_2^3\bar{M}_j^3\bar{c}_2\gamma\Psi_1 \\
& + \bar{M}_1^2\bar{M}_2\bar{M}_j^3\bar{c}_2\gamma\Psi_2 - 4\bar{M}_1\bar{M}_2^2\bar{M}_j^2\bar{c}_j\gamma\Psi_1 - 4\bar{M}_1^2\bar{M}_2\bar{M}_j^2\bar{c}_j\gamma\Psi_2 \\
& - \bar{M}_1\bar{M}_2\bar{M}_j^4\bar{c}_j\gamma^2\Psi_1 + 2\bar{M}_1\bar{M}_2^2\bar{M}_j^4\bar{c}_j\gamma\Psi_1 + \bar{M}_1\bar{M}_2\bar{M}_j^4\bar{c}_j\gamma^2\Psi_2 \\
& + 2\bar{M}_1^2\bar{M}_2\bar{M}_j^4\bar{c}_j\gamma\Psi_2 + \bar{M}_1\bar{M}_2^2\bar{M}_j^2\bar{c}_j\gamma\Psi_j + \bar{M}_1^2\bar{M}_2\bar{M}_j^2\bar{c}_j\gamma\Psi_j + \frac{A_2\bar{M}_1^2\bar{M}_j^2\bar{c}_j\Psi_2}{A_j} \\
& - \frac{A_2\bar{M}_2^2\bar{M}_j^2\bar{c}_j\Psi_1}{A_j} - 2\bar{M}_1\bar{M}_2\bar{M}_j\bar{c}_2\gamma\Psi_1 + \bar{M}_1\bar{M}_2^2\bar{M}_j^3\bar{c}_2\gamma^2\Psi_1 - \bar{M}_1^2\bar{M}_2^2\bar{M}_j\bar{c}_2\gamma^2\Psi_2 \\
& - \bar{M}_1\bar{M}_2^2\bar{M}_j^3\bar{c}_2\gamma^2\Psi_2 + \bar{M}_1\bar{M}_2^3\bar{M}_j^3\bar{c}_2\gamma^2\Psi_1 - 2\bar{M}_1^2\bar{M}_2^2\bar{M}_j^3\bar{c}_2\gamma\Psi_2 \\
& + 2\bar{M}_1\bar{M}_2^2\bar{M}_j^2\bar{c}_j\gamma^2\Psi_1 + 2\bar{M}_1^2\bar{M}_2\bar{M}_j^2\bar{c}_j\gamma^2\Psi_2 - \bar{M}_1\bar{M}_2^2\bar{M}_j^4\bar{c}_j\gamma^2\Psi_1 \\
& - \bar{M}_1^2\bar{M}_2\bar{M}_j^4\bar{c}_j\gamma^2\Psi_2 - \bar{M}_1\bar{M}_2^2\bar{M}_j^2\bar{c}_j\gamma^2\Psi_j - \bar{M}_1^2\bar{M}_2\bar{M}_j^2\bar{c}_j\gamma^2\Psi_j \\
& - \frac{2A_2\bar{M}_1\bar{M}_2\bar{c}_j\Psi_1}{A_j} + \frac{2A_2\bar{M}_1\bar{M}_2\bar{c}_j\Psi_2}{A_j} + 2\bar{M}_1\bar{M}_2^2\bar{M}_j\bar{c}_2\gamma\Psi_1 + 2\bar{M}_1\bar{M}_2\bar{M}_j^3\bar{c}_2\gamma\Psi_1 \\
& - 2\bar{M}_1\bar{M}_2^2\bar{M}_j\bar{c}_2\gamma\Psi_2 + 2\bar{M}_1\bar{M}_2^3\bar{M}_j\bar{c}_2\gamma\Psi_1 - \bar{M}_1^2\bar{M}_2\bar{M}_j\bar{c}_2\gamma\Psi_2 - 2\bar{M}_1\bar{M}_2\bar{M}_j^2\bar{c}_j\gamma\Psi_1 \\
& + 2\bar{M}_1\bar{M}_2\bar{M}_j^2\bar{c}_j\gamma\Psi_2 + 2\bar{M}_1\bar{M}_2\bar{M}_j^4\bar{c}_j\gamma\Psi_1 - 2\bar{M}_1\bar{M}_2\bar{M}_j^4\bar{c}_j\gamma\Psi_2 + \frac{2A_2\bar{M}_1\bar{M}_2\bar{c}_j\gamma\Psi_1}{A_j} \\
& - \frac{2A_2\bar{M}_1\bar{M}_2\bar{c}_j\gamma\Psi_2}{A_j} + \frac{A_2\bar{M}_1\bar{M}_2\bar{M}_j^2\bar{c}_j\Psi_1}{A_j} - \frac{A_2\bar{M}_1\bar{M}_2\bar{M}_j^2\bar{c}_j\Psi_2}{A_j} \\
& + \frac{A_2\bar{M}_1\bar{M}_2^2\bar{c}_j\gamma\Psi_j}{A_j} + \frac{A_2\bar{M}_1^2\bar{M}_2\bar{c}_j\gamma\Psi_j}{A_j} - \frac{2A_2\bar{M}_1\bar{M}_j^2\bar{c}_j\gamma\Psi_1}{A_j} - \frac{A_2\bar{M}_1\bar{M}_j^2\bar{c}_j\gamma\Psi_2}{A_j} \\
& - \frac{A_2\bar{M}_2\bar{M}_j^2\bar{c}_j\gamma\Psi_1}{A_j} - \frac{2A_2\bar{M}_2\bar{M}_j^2\bar{c}_j\gamma\Psi_2}{A_j} + \frac{2A_2\bar{M}_1\bar{M}_j^2\bar{c}_j\gamma\Psi_j}{A_j} + \frac{2A_2\bar{M}_2\bar{M}_j^2\bar{c}_j\gamma\Psi_j}{A_j} \\
& - \frac{A_2\bar{M}_1\bar{M}_2^2\bar{M}_j^2\bar{c}_j\Psi_1}{A_j} - \frac{A_2\bar{M}_1^2\bar{M}_2\bar{M}_j^2\bar{c}_j\Psi_2}{A_j} + \frac{A_2\bar{M}_1\bar{M}_2^2\bar{M}_j^2\bar{c}_j\Psi_j}{A_j} \\
& + \frac{A_2\bar{M}_1^2\bar{M}_2\bar{M}_j^2\bar{c}_j\Psi_j}{A_j} - \frac{A_2\bar{M}_1^2\bar{M}_j^2\bar{c}_j\gamma\Psi_2}{A_j} + \frac{A_2\bar{M}_2^2\bar{M}_j^2\bar{c}_j\gamma\Psi_1}{A_j} \\
& + \frac{A_2\bar{M}_1\bar{M}_2\bar{M}_j^2\bar{c}_j\gamma^2\Psi_1}{A_j} + \frac{2A_2\bar{M}_1\bar{M}_2^2\bar{M}_j^2\bar{c}_j\gamma\Psi_1}{A_j} - \frac{A_2\bar{M}_1\bar{M}_2\bar{M}_j^2\bar{c}_j\gamma^2\Psi_2}{A_j} \\
& + \frac{2A_2\bar{M}_1^2\bar{M}_2\bar{M}_j^2\bar{c}_j\gamma\Psi_2}{A_j} - \frac{2A_2\bar{M}_1\bar{M}_2^2\bar{M}_j^2\bar{c}_j\gamma\Psi_j}{A_j} - \frac{2A_2\bar{M}_1^2\bar{M}_2\bar{M}_j^2\bar{c}_j\gamma\Psi_j}{A_j} \\
& - \frac{A_2\bar{M}_1\bar{M}_2^2\bar{M}_j^2\bar{c}_j\gamma^2\Psi_1}{A_j} - \frac{A_2\bar{M}_1^2\bar{M}_2\bar{M}_j^2\bar{c}_j\gamma^2\Psi_2}{A_j} + \frac{A_2\bar{M}_1\bar{M}_2^2\bar{M}_j^2\bar{c}_j\gamma^2\Psi_j}{A_j} \\
& + \frac{A_2\bar{M}_1^2\bar{M}_2\bar{M}_j^2\bar{c}_j\gamma^2\Psi_j}{A_j} - \frac{2A_2\bar{M}_1\bar{M}_2\bar{M}_j^2\bar{c}_j\gamma\Psi_1}{A_j} + \frac{2A_2\bar{M}_1\bar{M}_2\bar{M}_j^2\bar{c}_j\gamma\Psi_2}{A_j}.
\end{aligned} \tag{A.40}$$

B

BICAMERAL TRANSFER FUNCTIONS

Analytical expressions for the reverberation and transmissive transfer functions of a bicameral system with attenuation are presented here.

B.1 First chamber

The reverberation transfer functions for an acoustic source in the first chamber are $\dot{\mathcal{R}}_1^+$ and $\dot{\mathcal{R}}_1^-$. If the pressure transducer is located downstream of the acoustic source ($x_1 > x_{s1}$), we have:

$$\dot{\mathcal{R}}_1^+ = \frac{e^{-i\omega\tau_{p1}-\alpha l_{p1}} + \dot{R}_{o1}e^{-i\omega\tau_{q1}-\alpha l_{q1}}}{1 - R_{i1}\dot{R}_{o1}e^{-i\omega\tau_1-2\alpha L_1}}, \quad (\text{B.1})$$

$$\dot{\mathcal{R}}_1^- = \frac{R_{i1}\dot{R}_{o1}e^{-i\omega(\tau_{r1}+\tau)-\alpha(l_{r1}+2L_1)} + R_i e^{-i\omega\tau_{s1}-\alpha l_{s1}}}{1 - R_{i1}\dot{R}_{o1}e^{-i\omega\tau_1-2\alpha L_1}}. \quad (\text{B.2})$$

If the pressure transducer is located upstream of the acoustic source ($x < x_{s1}$), we have:

$$\dot{\mathcal{R}}_1^+ = \frac{R_{i1}\dot{R}_{o1}e^{-i\omega(\tau_{p1}+\tau_1)-\alpha(l_{p1}+2L_1)} + \dot{R}_{o1}e^{-i\omega\tau_{p1}-\alpha l_{q1}}}{1 - R_{i1}\dot{R}_{o1}e^{-i\omega\tau_1-2\alpha L_1}}, \quad (\text{B.3})$$

$$\dot{\mathcal{R}}_1^- = \frac{e^{-i\omega\tau_{r1}-\alpha l_{r1}} + R_{i1}e^{-i\omega\tau_{s1}-\alpha l_{s1}}}{1 - R_{i1}\dot{R}_{o1}e^{-i\omega\tau_1-2\alpha L_1}}, \quad (\text{B.4})$$

where

$$\dot{R}_{o1}^* = R_{o1} + \frac{T_{o1}T_{i2}R_{o2}}{e^{i\omega\tau_2-2\alpha L_2} - \dot{R}_{i2}R_{o2}}, \quad (\text{B.5})$$

and $\tau_{p1} = \tau_{x_1}^+ - \tau_{x_{s1}}^+$, $\tau_{q1} = \tau_1 - \tau_{x_1}^- - \tau_{x_{s1}}^+$, $\tau_{r1} = \tau_{x_{s1}}^- - \tau_{x_1}^-$, and $\tau_{s1} = \tau_{x_{s1}}^- + \tau_{x_1}^+$.

The transmissive transfer functions $\dot{\mathcal{T}}_2^+$ and $\dot{\mathcal{T}}_2^-$ enable an acoustic source in the second chamber to be expressed as an acoustic source at the outlet of the first chamber. We have:

$$\dot{\mathcal{T}}_2^+ = \dot{T}_{i2}^* R_{o2} e^{-i\omega\tau_{q2} - \alpha l_{q2}}, \quad (\text{B.6})$$

$$\dot{\mathcal{T}}_2^- = \dot{T}_{i2}^* e^{-i\omega\tau_{r2} - \alpha l_{r2}}. \quad (\text{B.7})$$

where τ_{q2} and τ_{r2} are evaluated at $x_2 = 0$ (at the inlet of the second chamber), and

$$\dot{T}_{i2}^* = \frac{T_{i2}}{1 - R_{o2}\dot{R}_{i2}e^{-i\omega\tau_2-2\alpha L_2}}. \quad (\text{B.8})$$

B.2 Second chamber

The reverberation transfer functions (for an acoustic source in the second chamber) are $\dot{\mathcal{R}}_2^+$ and $\dot{\mathcal{R}}_2^-$. If the pressure transducer is located downstream of the acoustic source ($x_2 > x_{s2}$), we have:

$$\dot{\mathcal{R}}_2^+ = \frac{e^{-i\omega\tau_{p2} - \alpha l_{p2}} + R_{o2}e^{-i\omega\tau_{q2} - \alpha l_{q2}}}{1 - \dot{R}_{i2}R_{o2}e^{-i\omega\tau_2-2\alpha L_2}}, \quad (\text{B.9})$$

$$\dot{\mathcal{R}}_2^- = \frac{\dot{R}_{i2}R_{o2}e^{-i\omega(\tau_{r2} + \tau) - \alpha(l_{r2} + 2L_2)} + \dot{R}_{i2}e^{-i\omega\tau_{s2} - \alpha l_{s2}}}{1 - \dot{R}_{i2}R_{o2}e^{-i\omega\tau_2-2\alpha L_2}}. \quad (\text{B.10})$$

If the pressure transducer is located upstream of the acoustic source ($x_2 < x_{s2}$), we have:

$$\dot{\mathcal{R}}_2^+ = \frac{\dot{R}_{i2}R_{o2}e^{-i\omega(\tau_{p2} + \tau_2) - \alpha(l_{p2} + 2L_2)} + R_{o2}e^{-i\omega\tau_{p2} - \alpha l_{q2}}}{1 - \dot{R}_{i2}R_{o2}e^{-i\omega\tau_2-2\alpha L_2}}, \quad (\text{B.11})$$

B. BICAMERAL TRANSFER FUNCTIONS

$$\mathcal{R}_2^* = \frac{e^{-i\omega\tau_{r2}-\alpha l_{r2}} + \mathcal{R}_{i2}^* e^{-i\omega\tau_{s2}-\alpha l_{s2}}}{1 - \mathcal{R}_{i2}^* R_{o2} e^{-i\omega\tau_2-2\alpha L_2}}, \quad (\text{B.12})$$

where

$$\mathcal{R}_{i2}^* = R_{i2} + \frac{T_{i2} T_{o1} R_{o1}}{e^{i\omega\tau_1-2\alpha L_1} - R_{i1} R_{o1}}. \quad (\text{B.13})$$

and $\tau_{p2} = \tau_{x_2}^+ - \tau_{x_{s2}}^+$, $\tau_{q2} = \tau_2 - \tau_{x_2}^- - \tau_{x_{s2}}^+$, $\tau_{r2} = \tau_{x_{s2}}^- - \tau_{x_2}^-$, and $\tau_{s2} = \tau_{x_{s2}}^- + \tau_{x_2}^+$.

The transmissive transfer functions \mathcal{T}_1^* and \mathcal{T}_1^* enable an acoustic source in the first chamber to be expressed as an acoustic source at the inlet of the second chamber.

We have:

$$\mathcal{T}_1^{*+} = T_{o1}^* e^{-i\omega\tau_{p1}-\alpha l_{p1}}, \quad (\text{B.14})$$

$$\mathcal{T}_1^{*-} = T_{o1}^* R_{i1} e^{-i\omega\tau_{s1}-\alpha l_{s1}} \quad (\text{B.15})$$

where τ_{p1} and τ_{s1} are evaluated at $x_1 = L_1$ (at the outlet of the first chamber), and

$$T_{o1}^* = \frac{T_{o1}}{1 - R_{o1} R_{i1} e^{-i\omega\tau_1-2\alpha L_1}}. \quad (\text{B.16})$$

REFERENCES

- [1] Bailly, C., Bogey, C., & Candel, S. M. (2010). Modelling of sound generation by turbulent reacting flows. *International Journal of Aeroacoustics*, 9(4), 461–490.
- [2] Bake, F., Michel, U., & Roehle, I. (2007). Investigation of Entropy Noise in Aero-Engine Combustors. *Journal of Engineering for Gas Turbines and Power*, 129(2), 370.
- [3] Bake, F., Michel, U., Röhle, I., Richter, C., Thiele, F., Liu, M., & Noll, B. (2005). Indirect Combustion Noise Generation in Gas Turbines. In *11th AIAA/CEAS Aeroacoustics Conference* Reston, Virginia: American Institute of Aeronautics and Astronautics.
- [4] Bake, F., Richter, C., Mühlbauer, B., Kings, N., Röhle, I., Thiele, F., & Noll, B. (2009). The Entropy Wave Generator (EWG): A reference case on entropy noise. *Journal of Sound and Vibration*, 326(3-5), 574–598.
- [5] Bechert, D. (1979). Sound absorption caused by vorticity shedding, demonstrated with a jet flow. In *5th Aeroacoustics Conference* Reston, Virginia: American Institute of Aeronautics and Astronautics.
- [6] Bednarek, J. R. D. (2005). *Ideas into Hardware: A History of the Rocket Engine Test Facility at the NASA Glenn Research Center*. Routledge.
- [7] Bohn, M. S. (1977). Response of a subsonic nozzle to acoustic and entropy disturbances. *Journal of Sound and Vibration*, 52(2), 283–297.
- [8] Bragg, S. L. (1963). Combustion Noise. *Journal of the Institute of Fuel*, 36(264), 12–16.
- [9] Brear, M. J., Nicoud, F., Talei, M., Giauque, A., & R, H. E. (2012). Disturbance energy transport and sound production in gaseous combustion. *Journal of Fluid Mechanics*, 707.

- [10] Candel, S., Durox, D., Ducruix, S., Birbaud, A.-L., Noiray, N., & Schuller, T. (2009). Flame Dynamics and Combustion Noise: Progress and Challenges. *International Journal of Aeroacoustics*, 8(1), 1–56.
- [11] Candel, S. M. (2002). Combustion dynamics and control: Progress and challenges. In *Proceedings of the Combustion Institute*, volume 29 (pp. 1–28).
- [12] Chu, B.-T. (1965). On the energy transfer to small disturbances in fluid flow (Part I). *Acta Mechanica*, 1(3), 215–234.
- [13] Chu, B. T. & Kovásznay, L. S. G. (1958). Non-linear interactions in a viscous heat-conducting compressible gas. *Journal of Fluid Mechanics*, 3(05), 494–514.
- [14] Correa, S. M. (1998). Power generation and aeropropulsion gas turbines: From combustion science to combustion technology. *Symposium (International) on Combustion*, 27(2), 1793–1807.
- [15] Cuadra, E. (1967). Acoustic Wave Generation by Entropy Discontinuities Flowing Past an Area Change. *The Journal of the Acoustical Society of America*, 42(4), 725–730.
- [16] Cumpsty, N. & Marble, F. (1977a). Core noise from gas turbine exhausts. *Journal of Sound and Vibration*, 54(2), 297–309.
- [17] Cumpsty, N. & Marble, F. (1977b). The Interaction of Entropy Fluctuations with Turbine Blade Rows; A Mechanism of Turbojet Engine Noise. *Proceedings of the Royal Society A: Mathematical, Physical and Engineering Sciences*, 357(1690), 323–344.
- [18] Cumpsty, N. A. (1979). Jet engine combustion noise: Pressure, entropy and vorticity perturbations produced by unsteady combustion or heat addition. *Journal of Sound and Vibration*, 66(4), 527–544.
- [19] De Domenico, F., Rolland, E., & Hochgreb, S. (2017a). Acoustic and entropic transfer functions of a generalised subsonic nozzle. In *24th International congress on sound and vibration* London.
- [20] De Domenico, F., Rolland, E. O., & Hochgreb, S. (2017b). Detection of direct and indirect noise generated by synthetic hot spots in a duct. *Journal of Sound and Vibration*, 394, 220–236.

REFERENCES

- [21] Dowling, A. P. & Mahmoudi, Y. (2015). Combustion noise. *Proceedings of the Combustion Institute*, 35(1), 65–100.
- [22] Dowling, A. P. & Stow, S. R. (2003). Acoustic Analysis of Gas Turbine Combustors. *Journal of Propulsion and Power*, 19(5), 751–764.
- [23] Ducruix, S., Schuller, T., Durox, D., & Candel, B. (2003). Combustion Dynamics and Instabilities: Elementary Coupling and Driving Mechanisms. *Journal of Propulsion and Power*, 19(5), 722–734.
- [24] Duran, I. & Moreau, S. (2013). Solution of the quasi-one-dimensional linearized Euler equations using flow invariants and the Magnus expansion. *Journal of Fluid Mechanics*, 723, 190–231.
- [25] Duran, I., Moreau, S., & Poinot, T. (2013). Analytical and Numerical Study of Combustion Noise Through a Subsonic Nozzle. *AIAA Journal*, 51(1), 42–52.
- [26] Durrieu, P., Hofmans, G., Ajello, G., Boot, R., Aurégan, Y., Hirschberg, A., & Peters, M. C. A. M. (2001). Quasisteady aero-acoustic response of orifices. *The Journal of the Acoustical Society of America*, 110(4), 1859–1872.
- [27] Eckstein, J. & Sattelmayer, T. (2006). Low-order modeling of low-frequency combustion instabilities in aeroengines. *Journal of Propulsion and Power*, 22(2), 425–432.
- [28] Ffowcs Williams, J. E. & Howe, M. S. (1975). The generation of sound by density inhomogeneities in low Mach number nozzle flows. *Journal of Fluid Mechanics*, 70(03), 605–622.
- [29] Giauque, A., Huet, M., & Clero, F. (2012). Analytical Analysis of Indirect Combustion Noise in Subcritical Nozzles. *Journal of Engineering for Gas Turbines and Power*, 134(11), 111202.
- [30] Giuliani, F., Gajan, P., Diers, O., & Ledoux, M. (2002). Influence of pulsed entries on a spray generated by an air-blast injection device: An experimental analysis on combustion instability processes in aeroengines. *Proceedings of the Combustion Institute*, 29(1), 91–98.
- [31] Giusti, A., Worth, N. A., Mastorakos, E., & Dowling, A. P. (2017). Experimental and Numerical Investigation into the Propagation of Entropy Waves. In *Proceedings of the*

- Mechanical Engineering Congress, Japan*, volume 55 (pp. 446–458).: American Institute of Aeronautics and Astronautics.
- [32] Goh, C. S. & Morgans, A. S. (2011). Phase prediction of the response of choked nozzles to entropy and acoustic disturbances. *Journal of Sound and Vibration*, 330(21), 5184–5198.
- [33] Goh, C. S. & Morgans, A. S. (2013). The Influence of Entropy Waves on the Thermoacoustic Stability of a Model Combustor. *Combustion Science and Technology*, 185(2), 249–268.
- [34] Hansell, A. L., Blangiardo, M., Fortunato, L., Floud, S., de Hoogh, K., Fecht, D., Ghosh, R. E., Laszlo, H. E., Pearson, C., Beale, L., Beevers, S., Gulliver, J., Best, N., Richardson, S., & Elliott, P. (2013). Aircraft noise and cardiovascular disease near Heathrow airport in London: small area study. *BMJ*, 347.
- [35] Hayakawa, A., Gao, Y., Lowe, S., & Hochgreb, S. (2016). Quantitative Temperature Measurement of Toluene/air Mixture using Laser Induced Thermal Grating Spectroscopy (LITGS). *The Proceedings of Mechanical Engineering Congress, Japan*, 2016(0), G0600101.
- [36] Hochgreb, S., Dennis, D., Ayranci, I., Bainbridge, W., & Cant, S. (2013). Forced and Self-Excited Instabilities from Lean Premixed, Liquid-Fuelled Aeroengine Injectors at High Pressures and Temperatures. In *Proceedings of the ASME Turbo Expo IGTI, June 3-7, 2013, San Antonio, Texas, USA* (pp. 95311).
- [37] Howe, M. S. (1975a). Contributions to the theory of aerodynamic sound, with application to excess jet noise and the theory of the flute. *Journal of Fluid Mechanics*, 71(04), 625.
- [38] Howe, M. S. (1975b). The generation of sound by aerodynamic sources in an inhomogeneous steady flow. *Journal of Fluid Mechanics*, 67(03), 597.
- [39] Howe, M. S. (1979). Attenuation of sound in a low Mach Number nozzle flow. *Journal of Fluid Mechanics*, 91(02), 209.
- [40] Howe, M. S. & Liu, J. T. C. (1977). The generation of sound by vorticity waves in swirling duct flows. *Journal of Fluid Mechanics*, 81(02), 369.

REFERENCES

- [41] Huet, M. (2016). Nonlinear indirect combustion noise for compact supercritical nozzle flows. *Journal of Sound and Vibration*, 374, 211–227.
- [42] Huet, M. & Giauque, A. (2013). A nonlinear model for indirect combustion noise through a compact nozzle. *Journal of Fluid Mechanics*, 733, 268–301.
- [43] ICAO (2013). *Global air transport outlook to 2030 and trends to 2040*. Technical report, International Civil Aviation Organization.
- [44] Ihme, M. (2017). Combustion and Engine-Core Noise. *Annual Review of Fluid Mechanics*, 49(1), 277–310.
- [45] Keller, J. J., Egli, W., & Hellat, J. (1985). Thermally induced low-frequency oscillations. *ZAMP Zeitschrift fur angewandte Mathematik und Physik*, 36(2), 250–274.
- [46] Kings, N. & Bake, F. (2010). Indirect combustion noise: noise generation by accelerated vorticity in a nozzle flow. *International Journal of Spray and Combustion Dynamics*, 2(3), 253–266.
- [47] Knobloch, K., Neuhaus, L., Bake, F., Gaetani, P., & Persico, G. (2017). Experimental Assessment of Noise Generation and Transmission in a High-Pressure Transonic Turbine Stage. *Journal of Turbomachinery*, 139(10), 101006.
- [48] Knobloch, K., Werner, T., & Bake, F. (2015). Noise Generation in Hot Nozzle Flow. In *Proceedings of ASME Turbo Expo 2015: Turbine Technical Conference and Exposition*: ASME.
- [49] Leconte, J. (1858). On the influence of musical sounds on the flame of a jet of coal-gas. *Philosophical Magazine*, 15(99), 235–239.
- [50] Lee, D. S., Fahey, D. W., Forster, P. M., Newton, P. J., Wit, R. C., Lim, L. L., Owen, B., & Sausen, R. (2009). Aviation and global climate change in the 21st century. *Atmospheric Environment*, 43(22), 3520–3537.
- [51] Leyko, M., Duran, I., Moreau, S., Nicoud, F., & Poinsot, T. (2014). Simulation and modelling of the waves transmission and generation in a stator blade row in a combustion-noise framework. *Journal of Sound and Vibration*, 333(23), 6090–6106.

- [52] Leyko, M., Moreau, S., Nicoud, F., & Poinso, T. (2011). Numerical and analytical modelling of entropy noise in a supersonic nozzle with a shock. *Journal of Sound and Vibration*, 330(16), 3944–3958.
- [53] Leyko, M., Nicoud, F., & Poinso, T. (2009). Comparison of Direct and Indirect Combustion Noise Mechanisms in a Model Combustor. *AIAA Journal*, 47(11), 2709–2716.
- [54] Lieuwen, T. (2003). Modeling Premixed Combustion-Acoustic Wave Interactions: A Review. *Journal of Propulsion and Power*, 19(5), 765–781.
- [55] Lighthill, M. J. (1952). On Sound Generated Aerodynamically. I. General Theory. *Proceedings of the Royal Society A: Mathematical, Physical and Engineering Sciences*, 211(1107), 564–587.
- [56] Lourier, J. M., Huber, A., Noll, B., & Aigner, M. (2014). Numerical Analysis of Indirect Combustion Noise Generation Within a Subsonic Nozzle. *AIAA Journal*, 52(10), 2114–2126.
- [57] Magri, L. (2017). On indirect noise in multi-component nozzle flows. *Journal of Fluid Mechanics*, 828, R2.
- [58] Magri, L., O'Brien, J., & Ihme, M. (2016a). Compositional inhomogeneities as a source of indirect combustion noise. *Journal of Fluid Mechanics*, 799, R4.
- [59] Magri, L., O'Brien, J., & Ihme, M. (2016b). Compositional inhomogeneities as a source of indirect noise in subsonic and supersonic nozzle. In *Annual Research Briefs* (pp. 235–246).: Center for Turbulence Research.
- [60] Magri, L., O'Brien, J., & Ihme, M. (2017). Effects of nozzle Helmholtz number on indirect combustion noise by compositional perturbations. *Journal of Engineering for Gas Turbines and Power*, 140(3), 0.31501.
- [61] Marble, F. E. & Candel, S. M. (1977). Acoustic disturbance from gas non-uniformities convected through a nozzle. *Journal of Sound and Vibration*, 55(2), 225–243.
- [62] Miles, J. H. (2009). Time Delay Analysis of Turbofan Engine Direct and Indirect Combustion Noise Sources. *Journal of Propulsion and Power*, 25(1), 218–227.
- [63] Miles, J. H. (2010a). Core Noise Diagnostics of Turbofan Engine Noise Using Correlation and Coherence Functions. *Journal of Propulsion and Power*, 26(2), 303–316.

REFERENCES

- [64] Miles, J. H. (2010b). Separating Direct and Indirect Turbofan Engine Combustion Noise Using the Correlation Function. *Journal of Propulsion and Power*, 26(5), 1144–1152.
- [65] Mills, A. K. (1999). The Historic Rocket Engine Test Facility (RETF): Trial and error.
- [66] Moase, W. H., Brear, M. J., & Manzie, C. (2007). The forced response of choked nozzles and supersonic diffusers. *Journal of Fluid Mechanics*, 585, 281–304.
- [67] Morfey, C. L. (1973). Amplification of aerodynamic noise by convected flow inhomogeneities. *Journal of Sound and Vibration*, 31(4), 391–397.
- [68] Morgans, A. S. & Duran, I. (2016). Entropy noise: A review of theory, progress and challenges. *International Journal of Spray and Combustion Dynamics*, 8(4), 285–298.
- [69] Morgans, A. S., Goh, C. S., & Dahan, J. A. (2013). The dissipation and shear dispersion of entropy waves in combustor thermoacoustics. *Journal of Fluid Mechanics*, 733, R2.
- [70] Motheau, E., Nicoud, F., & Poinso, T. (2014). Mixed acoustic–entropy combustion instabilities in gas turbines. *Journal of Fluid Mechanics*, 749, 542–576.
- [71] Mühlbauer, B., Noll, B., & Aigner, M. (2009). Numerical Investigation of the Fundamental Mechanism for Entropy Noise Generation in Aero-Engines. *Acta Acustica united with Acustica*, 95(3), 470–478.
- [72] Muthukrishnan, M., Strahle, W. C., & Neale, D. H. (1978). Separation of Hydrodynamic, Entropy, and Combustion Noise in a Gas Turbine Combustor. *AIAA Journal*, 16(4), 320–327.
- [73] Noiray, N., Durox, D., Schuller, T., & Candel, S. (2012). Mode Conversion in Acoustically Modulated Confined Jets. *AIAA Journal*, 47(2053-2062).
- [74] Oosthuizen, P. H. & Carscallen, W. E. (2013). *Introduction to Compressible Fluid Flow, Second Edition*. CRC Press.
- [75] O'Brien, J., Magri, L., & Ihme, M. (2017). Species dependency of the compositional indirect noise mechanism. In *ASME Turbo Expo 2017: Turbomachinery Technical Conference and Exposition* (pp. 63076).

- [76] Palies, P., Durox, D., Schuller, T., & Candel, S. (2011). Acoustic–convective mode conversion in an aerofoil cascade. *Journal of Fluid Mechanics*, 672, 545–569.
- [77] Persico, G., Gaetani, P., & Spinelli, A. (2017). Assessment of synthetic entropy waves for indirect combustion noise experiments in gas turbines. *Experimental Thermal and Fluid Science*, 88, 376–388.
- [78] Poinso, T. & Veynante, D. (2005). *Theoretical and Numerical Combustion*. R.T. Edwards, Inc.
- [79] Polifke, W., Paschereit, C. O., & Dobbeling, K. (2001). Constructive and Destructive Interference of Acoustic and Entropy Waves in a Premixed Combustor with a Choked Exit. *International Journal of Acoustics and Vibration*, 6(3), 135–146.
- [80] Rausch, A., Fischer, A., Konle, H., Gaertlein, A., Nitsch, S., Knobloch, K., Bake, F., & Röhle, I. (2011). Measurements of Density Pulsations in the Outlet Nozzle of a Combustion Chamber by Rayleigh-Scattering Searching Entropy Waves. *Journal of Engineering for Gas Turbines and Power*, 133(3), 31601.
- [81] Rayleigh, J. (1878). Chapter XVI: Maintenance by heat of aerial vibrations. In *The Theory of Sound* (pp. 226–227). Cambridge: Macmillan and co.
- [82] Rienstra, S. & Hirschberg, A. (2015). *An Introduction to Acoustics*.
- [83] Sattelmayer, T. (2003). Influence of the combustor aerodynamics on combustion instabilities from equivalence ratio fluctuations. *Journal of Engineering for Gas Turbines and Power*, 125(1), 11–19.
- [84] Schemel, C., Thiele, F., Bake, F., Lehmann, B., & Michel, U. (2004). Sound Generation in the Outlet Section of Gas Turbine Combustion Chambers. In *10th AIAA/CEAS Aeroacoustics Conference*, Aeroacoustics Conferences. American Institute of Aeronautics and Astronautics.
- [85] Stow, S. R., Dowling, A. P., & Hynes, T. P. (2002). Reflection of circumferential modes in a choked nozzle. *Journal of Fluid Mechanics*, 467, 215–239.
- [86] Strahle, W. C. (1978). Combustion noise. *Progress in Energy and Combustion Science*, 4(3), 157–176.

REFERENCES

- [87] Summerfield, M. (1960). The Liquid Propellant Rocket Engine. In *Liquid Propellant Rockets* (pp. 108–189). Princeton University Press.
- [88] Tam, C. K., Parrish, S. A., Xu, J., & Schuster, B. (2013). Indirect combustion noise of auxiliary power units. *Journal of Sound and Vibration*, 332(17), 4004–4020.
- [89] Tao, W., Mazur, M., Huet, M., & Richecoeur, F. (2016). Indirect Combustion Noise Contributions in a Gas Turbine Model Combustor with a Choked Nozzle. *Combustion Science and Technology*, 188(4-5), 793–804.
- [90] Tao, W., Schuller, T., Huet, M., & Richecoeur, F. (2017). Coherent entropy induced and acoustic noise separation in compact nozzles. *Journal of Sound and Vibration*, 394, 237–255.
- [91] Taylor, G. (1954). The Dispersion of Matter in Turbulent Flow through a Pipe. *Proceedings of the Royal Society of London A: Mathematical, Physical and Engineering Sciences*, 223(1155).
- [92] Wassmer, D., Schuermans, B., Paschereit, C. O., & Moeck, J. P. (2017). Measurement and modeling of the generation and the transport of entropy waves in a model gas turbine combustor. *International Journal of Spray and Combustion Dynamics*, 9, 1–11.
- [93] Yao, Z., Gao, Y., Zhu, M., Dowling, A. P., & Bray, K. C. (2012). Combustion Rumble Prediction with Integrated Computational-Fluid-Dynamics/Low-Order-Model Methods. *Journal of Propulsion and Power*, 28(5), 1015–1025.
- [94] Zheng, J. (2016). *Analytical and Numerical study of indirect combustion noise generated by entropy disturbances in nozzle flows*. PhD thesis, Université Paris-Saclay.
- [95] Zhu, M., Dowling, A. P., & Bray, K. N. C. (2001). Self-Excited Oscillations in Combustors With Spray Atomizers. *Journal of Engineering for Gas Turbines and Power*, 123(4), 779.
- [96] Zinn, B. T., Bell, W. A., Daniel, B. R., & Smith, Jr., A. J. (1973). Experimental determination of three-dimensional liquid rocket nozzle admittances. *AIAA Journal*, 11(3), 267–272.

REFERENCES

- [97] Zukoski, E. E. & Auerbach, J. M. (1976). Experiments Concerning the Response of Supersonic Nozzles to Fluctuating Inlet Conditions. *Journal of Engineering for Power*, 98(1), 60–64.